Constrained Magnetism in the Niobates

Synthesis and Characterization of Constrained Magnetism in Niobates

By

Timothy John Sagan Munsie, CD, M.Sc., B.A.Sc.(Hons. Spec)

A Thesis

Submitted to the School of Graduate Studies

in Partial Fulfilment of the Requirements

for the Degree

Doctorate of Philosophy

McMaster University

DOCTORATE OF PHILOSOPHY (2017) McMaster University

(Department of Physics and Astronomy) Hamilton, Ontario

TITLE: Synthesis and Characterization of Constrained Magnetism in Niobates

AUTHOR: Timothy Munsie, CD, M.Sc., B.A.Sc.(Hons. Spec)

SUPERVISOR: Dr. Graeme M. Luke

NUMBER OF PAGES: xxvi, 246

Lay Abstract

This thesis examines two different niobium-based compounds: cobalt niobate ($CoNb_2O_6$) and nickel niobate ($NiNb_2O_6$). In these systems the cobalt and nickel atoms provide interesting magnetic properties.

Within a magnetic material, the magnetic atoms tend to have their spins align in certain ways. The atoms themselves are fixed to particular sites by the way the material is assembled; an atomic framework.

In the case of cobalt niobate, the magnetic atoms are arranged in well-separated chains so that a magnetic atom interacts strongly with its magnetic neighbours within a chain, and weakly with ones that are further away. This is an example of a material that is called 'low dimensional'. The chains themselves form triangular patterns, and the interactions between chains are both weaker and antialigned, which creates a frustrated competition between the chains, protecting the low dimensional state by creating conditions where it is hard for all the spins in the material to order.

For nickel niobate, the magnetic moments all want to anti-align, or be pointing in the opposite direction as its nearest neighbour. The magnetism is 'frustrated' because each magnetic atom is tetrahedrally connected to three other atoms, so it cannot meet that condition. This can be visualized by drawing a triangle and trying to make each corner have an arrow pointing up or down. The third corner of the triangle cannot satisfy this requirement for its neighbours (one up and one down arrow).

Both decreased dimensionality and frustration can lead to the emergence of novel quantum states of matter at low temperature. This thesis explores these materials with that in mind.

Abstract

This thesis contains the results of the extensive study into the synthesis of nickel niobate ($NiNb_2O_6$) including the formation of what was a previously unreported polymorph of the material, as well as the magnetic properties of both cobalt niobate ($CoNb_2O_6$) and nickel niobate using techniques including SQUID magnetometry, powder and single crystal x-ray scattering, powder and single crystal neutron scattering and muon spin rotation/relaxation.

In cobalt niobate we found extremely long relaxation times in the heat capacity which showed up strongly in muon spin rotation experiments but not in neutron measurements. Additionally, with field applied to the system we see the emergence of spin-wave like structures in the neutron scattering data. Within cobalt niobate the strongest interaction is ferromagnetic and along the chain. The chains themselves are laid out on a triangular fashion and interact, although far more weakly, in an antiferromagnetic manner. This triangular patterning as well as an antiferromagnetic interaction results in interchain frustration, which protects the quasi-1D nature of the system due to the difficulty generated in creating 3D order.

In nickel niobate we found that growth conditions caused highly variable changes, and we were able to create two different polymorphs. One polymorph was in the same space group as cobalt niobate, which gave us an opportunity to explore the magnetic difference between a spin-$\frac{1}{2}$ and spin-1 magnetic system and in nickel niobate in the new space group we performed an ab initio characterization solving the unit cell structure, the magnetic structure with neutron scattering as well as a magnetic characterization with SQUID magnetometry

and muon spin rotation, allowing us to contrast the significant crystallographic differences. For the new polymorph we were able to determine its magnetic structure, characterized by Ising-like spins arranged in frustrated tetrahedra with three of the four points lying in the same plane as the spin, and for both materials we were able to use zero-field μSR data to estimate behaviour near the critical point and determine a critical exponent near the magnetic transitions. In both polymorphs there is evidence of constrained magnetism or reduced dimensionality, although the evidence for low dimensionality is much stronger in the columbite polymorph.

Acknowledgements

"But I don't want to go among mad people," Alice remarked.

"Oh, you can't help that," said the Cat: "We're all made here. I'm mad. You're mad."

"How do you know I'm mad?" said Alice.

"You must be," said the cat, "or you wouldn't have come here."

~ Lewis Carroll, Alice in Wonderland

When it takes you over seven years to write up your work, looking back there are a lot of people who deserve a lot of thanks for getting me to this point. I'm certain that I'm going to be forgetting several of those people, so to the forgotten, my apologies and my thanks.

No person is an island, and a doctoral degree is no exception to that. The long list of co-authors is the perfect proof that collaboration is key. In particular, however, the group that you work with influences the final outcome, and I have had the opportunity to work with some remarkable and uniquely talented people. Top of that list is Dr. Travis Williams. For putting up with me for years and helping me throughout the process I am perpetually indebted. For this work in particular, Ms. Alannah Hallas and Mr. Murray Wilson not only did a significant amount of work and rightfully earned a place in the co-authorship, but did much more through being the first two to volunteer to edit this manuscript; a not-insignificant task. I became a better author and created a better final work directly because of this help. Additionally, Dr. Eteri Svanidze and Dr. Benjamin Fransden lent not only kind words and their final theses, but their keen eyes to the editing endeavour as well. A significant re-organization for flow was inspired through decent debate; the heart of any good collaborative effort.

I've been given the good fortune to become something of a generalist as a doctoral candidate. This is a little bit unique; typically a graduate student focuses on one technique. I was never able to quite master that aspect and I owe a number of people thanks for teaching me various techniques.

Dr. Jim Britten, Dr. Hilary Jenkins and Dr. Scott Forbes all helped me through learning the techniques involved with powder and single crystal x-ray diffraction. I regret never having time to volunteer in Dr. Britten's lab to learn more about acquisition and analysis of x-ray data.

Dr. Paul Dube was a good friend and someone who always had time to talk, especially when it came to lab equipment breaking. He taught me most of what I know about analyzing susceptibility data, helped me through using the ExaLab including a lot of rewriting of the software; between the two of us we finally made VdP measurements work correctly. And he taught me a lot about keeping the lab equipment working. I think that is the most valuable skill I'll leave with.

Dr. Hanna Dabkowska and Dr. Antoni Dabkowski are two of the finest collegues and friends that one could ask for. Between the two of them I became as close to mastering the Chemistry and the art of synthesizing and preparing materials. Either would drop everything at a moments notice to help, and were willing to invest into you whatever you were willing to invest in yourself. The lab techniques I have developed are owed solely to them. The confidence I've learned in synthesis was because they nurtured that talent. Because of that my crystals have gone to groups all over North America, and my publication list has swelled. They've made me feel truly accomplished as a scientist.

The staff at TRIUMF National Lab is some of the best that you will find. Dr. Bassam Hitti taught me how to make a DR run, and always had experimental advice

when needed. Dr. Donald Arsenault taught me enough that when the electronics broke, I had at least a vague idea how to fix them, and between him and Dr. Gerald Morris I became highly self-sufficient, or at least knew when something was very wrong with my data. Gerald was always around to help correct some of my misconceptions and helped me to evolve as an experimenter. Mr. Deepak Vyas and Mr. Rahim Abasalti made sure that everything always worked, and ensured the success of my experiments. This team made me feel like I was a part of the facility. Additionally, Dr. Iain McKenzie had seemingly infinite patience and was always there to help when I needed it most even if my experiment needed it least. Dr. Fanlong Ning deserves special note here as well: he and his students helped significantly with the work, and aside from volunteering comments and edits, he has been a good friend throughout the entirety of my Masters and Doctorate. In addition to this group, my constant collaborator, Dr. Sarah Dunsiger, aside from correcting misconceptions and explaining things to me (often more than once) has my extreme gratitude for being the very first person to make me feel like a scientist and that my opinions had both weight and merit. When a graduate student starts working at a large facility, it is generally in the capacity of a 'data monkey'. Sarah made it so that that description no longer applied to me.

The neutron work I performed and the understanding of its analysis are in no small part to Dr. Travis Williams, Dr. Adam Aczel, Dr. Huibo Cai and Dr. Corey Thompson. The patience, dedication and time commitment was valued and appreciated.

I have had the good fortune to work with a number of exceptional undergraduate thesis students who helped immensely with the synthesis and characterization: Ms. Alison Kinross with the cobalt niobate crystals as well as some μSR measurements, Ms. Casey Marjerrison with a little bit of everything in the crystal growth lab, and

Ms. Anna Millington who stuck with the nickel niobate project well past the end of her undergraduate thesis and in spite of less-than-instantaneous success.

Although never a formal part of my committee, Dr. John Greedan is someone who I cannot thank enough. I don't think there is a piece of published writing that I have done that he hasn't critiqued, edited or improved. The same is likely true for my understanding of the Chemistry behind what I've done. I don't know where he has ever found the time to mentor me, but I'm certainly glad that he did.

Dr. Takashi Imai and Dr. Bruce Gaulin have both been very supportive and helpful members of my committee; Bruce especially with the neutron scattering. They've given timely advice and let me have the freedom and academic license to explore these topics that I have found so interesting. I've been fortunate to have such a strong and knowledgable committee guiding my research. Even if we've never actually all been in the same place at the same time for any of my committee meetings or my Masters defense. I believe that Dr. Imai is the only person who has been physically present every time (myself included in that).

And to the one who I owe the most, I need only say the least: Dr. Graeme Luke, thank you for the privilege of letting me be one of your graduate students. I hope this work is a testament to your guidance, knowledge and faith.

And lastly, Dr. Meaghan Burford. I wouldn't be here, now, at this point, without your help, your kindness and your caring. I don't know if they teach patience when you complete a doctorate in theology, but yours has certainly been saintlike and I can no longer imagine being without the richness you bring me.

Co-Authorship

This section is written to meet the requirement for the 'Declaration of Academic Achievement' required as part of the thesis.

The growth of the samples of cobalt niobate used in this thesis were the product of a collaboration with Ms. A. Kinross and Dr. H.A. Dabkowska. This was done as part of both an undergraduate thesis project for Ms. Kinross and as part of my Masters thesis.

The growth of the samples of pseudo-rutile nickel niobate used in this thesis were the product of a collaboration with Ms. A. Millington and Dr. H.A. Dabkowska. This was done as part of both an undergraduate thesis project for Ms. Millington as well as for this thesis. The samples of columbite nickel niobate were synthesized without Ms. Millington.

Heat capacity measurements of cobalt niobate were done with Dr. P.A. Dube at McMaster. The low temperature data (below 2K) reported was collected by Mr. D. Pomaranski and Dr. J. Kycia at the University of Waterloo.

The SQUID Magnetometry presented was done without assistance. Some initial measurements with the ^{4}He system used to guide crystal growth were done by myself, Ms. A. Millington and Dr. P. Dube. All ^{3}He measurements were done independently. Some of the original SQUID data on cobalt niobate was taken with Ms. A. Kinross and Dr. P. Dube. SQUID analysis was done with the assistance of Dr. P. Dube and Dr. J.E. Greedan.

All powder x-ray scattering and Laue x-ray scattering and alignment was performed and analyzed independently. Some initial powder measurements were done with Ms. A. Kinross or Ms. A. Millington for their respective theses. All single

crystal x-ray scattering was done with or by Dr. J. Britten, who also provided the final refinements.

Sample alignments and cutting of nickel niobate was done independently. Preparation of some powders for analysis was done with Ms. A. Millington.

Powder neutron scattering, which was integral to the understanding of this work and is being formally published separately, was done by with Dr. R. Flacau at Chalk River National Labs with Dr. C. Thompson and Dr. J.E. Greedan from the Chemistry Department at McMaster University.

Single Crystal neutron scattering was done with Dr. A.A. Aczel and Dr. H. Cao at Oak Ridge National Lab. The analysis was done independently and was confirmed by Dr. A.A. Aczel and Dr. H. Cao.

Muon Spin Rotation measurements were done at TRIUMF National Lab and were done in collaboration with Dr. T. Williams, Mr. R. D'Ortenzio, Ms. T. Medina, Mr. M. Wilson, Ms. A. Hallas and Ms. A. Kinross from McMaster University, Dr. B. Fransden and Dr. L. Liu from Columbia University and Ms. C. Ding, Mr. S. Guo and Mr. Z. Gong from Zhejiang University.

Supervision and project direction were given by Dr. G.M. Luke (Physics), Dr. B. Gaulin (Physics), Dr. T. Imai (Physics), Dr. J.E. Greedan(Chemistry) and Dr. H.A. Dabkowska(Brockhouse Institute for Materials Research) at McMaster, Dr. J. Kycia(Physics) at the University of Waterloo, Dr. Y.J. Uemura(Physics) at Columbia University and Dr. F. Ning(Physics) at Zhejiang.

Table of Contents

List of Figures

List of Tables

Chapter 1

Introduction

The first chapter of this thesis lays the ground work for understanding the context in which the niobate materials are to be examined. The background for the concepts behind magnetism and legitimization of the techniques described in chapter 2 are contained within. The 3^{rd} chapter contains results from muon spin rotation (μSR) experiments as well as some preliminary neutron scattering data on cobalt niobate ($CoNb_2O_6$). The 4^{th} chapter is a detailed publication on the synthesis of our attempt to create the spin-1 analogue, nickel niobate ($NiNb_2O_6$), which resulted in the discovery of a new polymorph of the material. The initial characterization of this polymorph is described in chapter 5, while further neutron scattering experiments and μSR experiments are covered in chapter 6.

The flow of the theory parts of this chapter are derived from several sources, specifically textbooks [1, 2, 3, 4, 5, 6, 7, 8], course notes [9, 10, 11, 12, 13, 14, 15, 16] and theses [17, 18].

1.1 Quantum Mechanical Nature of Magnetism

Chemical bonding, electricity and magnetism are highly interrelated subjects, all of which form the crux of this thesis as will be evidenced in the techniques presented in chapter 2.

The reason that electricity and magnetism are intertwined is due to the fact that magnetism is a result of the motion of electric charges. The interactions between the electrons and the nuclei of atoms can be broken into two angular momentum components, one representing the orbital angular momentum (m_l) and one representing the spin angular momentum (m_s) where electrons are canonically either spin up ($m_s = \frac{1}{2}$) or spin down ($m_s = -\frac{1}{2}$). The orbital angular momentum portion refers to the localization of the electrons to a particular type of orbitals, where the shape of a specific set of orbitals is nominally represented by the letters s ($l = 0$), p ($l = 1$), d ($l = 2$) and f ($l = 3$), originally standing for the sharp, principal, diffuse and fundamental orbitals, based on original chemical classification using optical spectroscopy [19]. The orbital angular momentum, can therefore take a value of m_l={-l, -l+1,...,0,...,l-1,l}. The shapes of these orbitals are defined using spherical harmonics and represent the probability of an electron to be in a certain position in real-space.

The total spin quantum number in an atomic system (S) can be represented by equation 1.1 where $n_\uparrow$ represents the number of electrons in the spin up state and $n_\downarrow$ represents the number of electrons in the spin down state. Similarly, the total orbital quantum number (L) can be represented by equation 1.2.

$$S = \frac{1}{2}(n_{\uparrow} - n_{\downarrow}) \text{ [3, 8]} \tag{1.1}$$

$$L = \sum_{l} m_l \text{ [3, 8]} \tag{1.2}$$

The total quantum number of a system (J) is found by following Hund's rules, which incorporate the Pauli exclusion principle, Coulomb repulsion and spin-orbit coupling. Hund's first rule states that a system desires the maximum value of S consistent with the exclusion principle, which requires that a system distribute charges so that they are aligned where possible and only a single spin up or down occupies a given orbital. Hund's second rule requires that for the maximum value of S, the configuration with the largest L is selected. This means that the electrons, being similarly charged, are located as far away from each other as possible. Hund's third rule relates how S and L are coupled to determine J. If a system has its orbitals less than half filled, $J = |\text{L - S}|$. If the system has its orbitals more than half full, then $J = L + S$ [3, 6].

The original theory of valence bonding in materials was first derived as an equation, from quantum mechanical principles, by Heitler and London in 1927, describing how two hydrogen atoms interact (σ-orbital bonding) [20]. In this regime the two atomic orbitals, u_A and u_B along with their respective positions, $\vec{r}_1$ and $\vec{r}_2$ can be described by equation 1.3.

$$\Psi(\vec{r}_1, \vec{r}_2) = \frac{1}{\sqrt{2}}(u_A(\vec{r}_1)u_B(\vec{r}_2) + u_A(\vec{r}_2)u_B(\vec{r}_1)) \text{ [3, 21]} \tag{1.3}$$

This equation was one of the first descriptions of an exchange interaction. The physical meaning of this exchange was that there existed a probability that the electrons of atom one could be at the position of $\vec{r}_2$, and vice versa. Hence it is an "exchange interaction". This exchange causes a reduction in energy for the total system, which leads to the chemical bonding between two atoms.

Instead of considering the wave function relating to electron location, denoted by $\Psi(\vec{r}_1, \vec{r}_2)$ in equation 1.3, for magnetism the more important component is the quantum mechanical spin wave function, $\chi(\vec{S}_1, \vec{S}_2)$, and the respective spin states, $\vec{S}_1$ and $\vec{S}_2$. The total quantum mechanical (QM) wave function is based on these orbitals and their spin components. In the above case the Heitler-London equation was symmetric. Since the two functions multiplied together are required, due to the Pauli Principle, to be anti-symmetric, we must change the sign between the terms to reflect this. We replace $\vec{r}_1$ and $\vec{r}_2$ with the discrete spin up and spin down states, $\vec{S}_1 = \frac{1}{2}$ and $\vec{S}_2 = -\frac{1}{2}$ representing our m_s components and u_A and u_B with, canonically, α and β where $\alpha(\frac{1}{2}) = \beta(-\frac{1}{2}) = 1$ and $\alpha(-\frac{1}{2}) = \beta(\frac{1}{2}) = 0$. The result of this replacement is shown in equation 1.4.

$$\chi(\vec{S}_1, \vec{S}_2) = \frac{1}{\sqrt{2}}(\alpha(\vec{S}_1)\beta(\vec{S}_2) - \alpha(\vec{S}_2)\beta(\vec{S}_1)) \tag{1.4}$$

These two equation, 1.3 and 1.4, lead to a spin-singlet state. The negative sign in 1.4 implies antiparallel spins and a symmetric orbital wave function, leading to antiferromagnetism in a single atom basis system and, from the Pauli principle, a homopolar chemical bond. In systems that can be described

as two atom basis magnetic gases this same set of equations gives rise to diamagnetic behaviour.

A second class of materials, where Coulomb repulsion of the electrons is dominant, leads to the spin-triplet state, where the positive and negative signs in equations 1.3 and 1.4 are swapped, leading to parallel spins and an anti-symmetric wave function. In single-atom basis systems this gives rise to a ferromagnetic exchange interaction. In systems that can be described as a two atom basis magnetic gas, this gives rise to paramagnetism.

Without an applied magnetic field, in a paramagnetic regime, normally electron spins are randomly oriented, so we see no net magnetization in the bulk of a material. If we, however, apply a magnetic field then the spins will experience a magnetic torque which will align them, leading to net magnetization of a sample. The net magnetic moment can be characterized by an orbital component, typically denoted μ_l and a spin component, μ_s which are represented by equations 1.5 and 1.6. In these equations μ_B is the Bohr Magneton, $g_l(=1)$ and g_s(nominally $\sim$2) are the orbital and spin Landé g-factors.

$$\vec{\mu_l} = -g_l \mu_B \vec{L} \tag{1.5}$$

$$\vec{\mu_s} = -g_s \mu_B \vec{S} \tag{1.6}$$

The total moment, $\vec{\mu_j}$, is the sum of these two components. This can be written in the same fashion as in equations 1.5 and 1.6 and g_j itself can be factored using those equations written as a separate equation, 1.8. This

factorization assumes that $g_s = 2$, which is an excellent approximation [22]. The negative sign arises from the fact that if we consider the electron in a classical sense: assuming that the spin angular momentum comes from the mass of the electron rotating around an axis, a current will be set up in the opposite direction of the rotation due to the negative charge of the electron. This means that the the magnetic moment will be antialigned to the particles spin. In the case of a positron, having a positive charge, we would find that the magnetic moment would be aligned in the direction of the spin.

$$\vec{\mu_j} = -g_j \mu_B \vec{J} \tag{1.7}$$

$$g_j = \frac{3}{2} + \frac{1}{2}\frac{S(S+1) - L(L+1)}{J(J+1)} \text{ [6]} \tag{1.8}$$

1.2 Magnetic Susceptibility

The magnetic character of a material is typically assessed by applying a field and measuring the response of the material. This is known as the magnetic susceptibility, χ. This is typically defined as follows: Take a quantum-mechanical system at zero temperature and calculate the change in the ground state energy, E_0, when a field is applied. The magnetization density is given by 1.9 where V is the volume of the sample. The susceptibility is then defined as in equation 1.10.

$$M(H) = -\frac{1}{V}\frac{\partial E_0(H)}{\partial H} \text{ [3]} \tag{1.9}$$

$$\chi = \frac{\partial M}{\partial H} \text{ [3]} \tag{1.10}$$

At non-zero temperatures, E_0 needs to be replaced by the equivalent free energy of the system.

Equation 1.4 was used to describe various types of magnetic responses: diamagnetism and paramagnetism. Typically when we have a negative value for χ we get diamagnets, where the spin anti-aligns with the field, and a positive value leads to paramagnets, where the spins are randomly oriented in zero field, but can gain a non-zero average in an applied field. The response is built up of several components depending of how the orbitals are filled [3, 6].

For electrons in a totally full atomic orbital, the sample consists of atomic ions where the shells are filled, so the wave function in the ground state has zero angular and zero spin momentum, or where $L = S = 0$. In this case there is no contribution of the ground state energy to the first order term of the Hamiltonian describing the magnetic response, and we get a small second-order contribution known as Larmor diamagnetism.

In the case of electrons in partially filled orbitals, there are two component. The first is known as Van Vleck paramagnetism. It arises due to field-induced electronic transitions and is the dominant term for a non-degenerate ground state ($J = 0$). The relatively large separation of electronic states makes this contribution small, and typically it only plays a role in atoms that are one electron short of being half-filled. It is on the same order as Larmor diamagnetism, and in most cases these two contributions are small and opposite and

generally cancel each other out. Calculating the Van Vleck contribution requires us to expand the equation for the free energy terms based on increasing powers of the applied field, as in equation 1.11. In this equation, $E_n^{(0)}$ is the energy of level n with no applied field, $E_n^{(1)}$ is the first order Zeeman term which is linear with field and $E_n^{(2)}$ is the second order Zeeman term, which is quadratic with field. It is typically not necessary to take the expansion further than second order [23].

$$E_n = E_n^{(0)} + HE_n^{(1)} + H^2E_n^{(2)} + \dots \text{ [24]} \tag{1.11}$$

Considering the Van Vleck effects, it the Van Vleck equation, equation 1.12, can be derived [24].

$$\frac{M}{H} = \chi = \frac{N_A \sum_n \left(\frac{E_n^{(1)2}}{kT} - 2E_n^{(2)}\right) e^{\frac{-E_n^{(0)}}{kT}}}{\sum_n e^{\frac{-E_n^{(0)}}{kT}}} \text{ [24]} \tag{1.12}$$

If $J \neq 0$ the response from partially filled orbitals is known as Curie paramagnetism. This is generally the dominant response in a paramagnetic material. It is characterized by the magnetic moments aligning with the field. This is the response of the component that relates to equation 1.7. This is also the only component of susceptibility that is not typically constant in temperature [6].

If we assume that a system is a metal and can have free conduction electrons, we have two additional cases. From the spin contributions of the electrons we get a response known as Pauli paramagnetism. This is representative of the free electrons in a Fermi sea polarizing along an applied external mag-

netic field [6]. Additionally, from the orbital motion of the electrons, we get a diamagnetic response that is typically one-third of the magnitude of Pauli paramagnetic response, known as Landau diamagnetism [3]. This is the result of a weak field opposite of the applied field that forms when the trajectory of a free electron is curved due to the Lorentz force.

1.3 Constrained Magnetism

Early work on magnetism constrained to lower than three dimensions was a theoretical pursuit for the first half of the 20^{th} century. With the development of quantum mechanical theory, thought was given about magnetism as a quantum effect, with non-integer spins explaining what had previously only been a classical system described phenomenologically. The first attempt to create a lower dimension quantum mechanical system was attributed to Ernst Ising in 1925 [25]. This was an attempt to provide an explanation for Weiss' molecular field theory of cooperative behaviour in magnets using the machinery of quantum and statistical mechanics [26]. This work was subsequently followed by development of the Bethe ansatz in 1931 which allowed a quantum mechanical ground state solution of the 1D Heisenberg case [27].

For the next forty to fifty years this area of research remained a theoretical pursuit. Although Bethe was confident that he could easily extend his model to the 3D case, which he was obviously unable to, theorists continued to develop further models. Onsager was able to extend the exact solution for the Ising case from 1D to 2D [28]. Additionally, cases were made to tie the 1D Heisenberg model to the classical 2D model by Lieb [29], Schultz [30] and

Baxter [31]. The development of Mermin-Wagner theory showed that low-dimension magnets would have the absence of long range order in a model with continuous symmetry at finite temperature [32]. This particular development included the case of the ground state in some circumstances as well [33]. An interesting exception to this was shown by Kosterlitz and Thouless in 1973 showing a metastable 2D XY transition was possible [34].

It was only in the 1970's when scientists realized that the 1D and 2D models that had been developed could be expressed in existing materials, or those that could be synthesized by crystal growers. Magnets with restricted dimensionality can exist as bulk crystals where there is an exchange interaction in one or two dimensions that is significantly larger than in the other directions or direction, leading to a quasi-1D or quasi-2D situation. The advantage of these systems is that experiments that investigate thermal and dynamic properties can be done, in contrast to the theoretical states such as 2D surface states or 2D electron gases in quantum wells which are much more difficult to experiment on [35].

The links between theory and experiment became much more apparent in the 1980's due to the revelation of the spinon nature of the excitation of the spin-$\frac{1}{2}$ antiferromagnetic chain by Faddeev and Takhatajan [36] and the development of Haldane chains, showing the difference between spin-$\frac{1}{2}$ and spin-1 chain excitation spectra [37], with the latter now being named after Haldane. The next period of development came when these theories were applied to the area of high-T_c superconductivity research, where strong

magnetic fields, possible in low dimensional magnetic materials [35], are a possible pairing mechanism [38].

Most compounds that have been synthesized rely on atoms with particular ionic states, such as Co^{2+} which realizes the spin-$\frac{1}{2}$ state as described below, or Ni^{2+} which realizes spin-1. In the research in this thesis we use the spin-1 state of nickel in $NiNb_2O_6$. Atoms such as Co^{2+}, although in a spin-$\frac{3}{2}$ state, because of spin-orbit coupling have an energy difference that essentially create a barrier. The energy gap between the ground Kramers doublet ($m_l = \pm 1$, $m_s = \pm 3/2$) and the first excited state ($m_l = \pm 1$, $m_s = \pm 1/2$) is assumed to exceed the exchange splitting, so at low temperatures we can consider the cobalt atoms as effectively pseudospin-$\frac{1}{2}$ [39]. This is the case for $CoNb_2O_6$ when we are concerned with 1D magnetism in the low-lying doublet. An example of this splitting is given in figure 1.1.

1.4 Ising Model

Starting from the assumptions in the previous section, mainly that atomic spins can be in the up or down states, $\vec{S_1}$ and $\vec{S_2}$, or with a +1 (up) or -1 (down) magnetic spin, we can then model an atomic lattice, or regular atomic spacing, of a material by tiling magnetic moments that are constrained to be only up or down. In such a system the simplest operation is that of one spin acting upon its closest neighbour as an exchange interaction as described in the previous section. At each lattice site, k, we assume that there is a discrete variable, σ_k which is set to either a spin up or spin down state. For any two adjacent sites, i and j, for example, we can compute their exchange

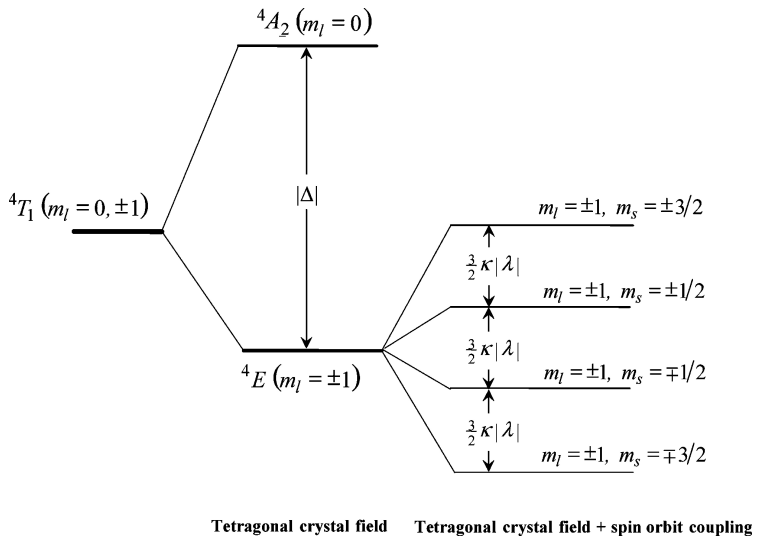

Figure 1.1: Splitting of the ground cubic $^4\mathrm{T}_1(3\mathrm{d}^7)$ term of a Co(II) ion by a tetragonal crystal field and spin-orbit coupling (Reprinted with permission from **A Highly Anisotropic Cobalt(II)-Based Single-Chain Magnet: Exploration of Spin Canting in an Antiferromagnetic Array** Andrei V. Palii et al. Journal of the American Chemical Society 2008 130 (44), 14729-14738 DOI: 10.1021/ja8050052. Copyright 2008 American Chemical Society) [39].

interaction, labelled J_{ij}. Additionally, any site can have a second interaction with an external magnetic field, typically denoted h. We can write this as a Hamiltonian, shown in equation 1.13 where the first summation is over pairs of adjacent spins, counting each pair only once, and the second summation is the effect of the external field on the site and where μ represents the magnetic moment.

$$H(\sigma) = -\sum_{<i,j>} J_{ij}\sigma_i\sigma_j - \mu\sum_k h\sigma_k \text{ [5]} \tag{1.13}$$

The probability of a given configuration of spins is given by a Boltzman distribution, 1.14, where $\beta = \dfrac{1}{k_b T}$ and k_b is the Boltzman constant. This rep-

resents the probability of a state with a spin configuration σ being occupied. The partition function, equation 1.15, representing the summation of all possible microstates of the thermodynamic system, is the normalization constant for equation 1.14 and can be determined by standard methods [5, 16, 4].

$$P_\beta(\sigma) = \frac{e^{-\beta H(\sigma)}}{Z_\beta} \text{ [5, 40]} \tag{1.14}$$

$$Z_\beta = \sum_\sigma e^{-\beta H(\sigma)} \text{ [5, 40]} \tag{1.15}$$

Because the magnetic moment of the electron is anti-parallel to its spin, you would expect that the second term would have a positive sign in front of it in equation 1.13, but it has been conventionally defined the other way [41]. This was shown generally in equation 1.7. Both sign conventions have become used in literature. Keeping this defined sign convention, in the case where $J_{ij} > 0$ we obtain the ferromagnetic case. In this situation the spins desire to be aligned together, so the probability defined in 1.14 will be heavily favouring states with aligned spins. For $J_{ij} = 0$ the solution is trivial as this implies that the spins are non-interacting (there is no exchange interaction) and in this case the probability for any state to exist is equal. For $J_{ij} < 0$ the interaction is antiferromagnetic and 1.14 will favour states where the interacting neighbours are anti-aligned.

Given the sign convention, regarding the second term and assuming that the field is applied longitudinally compared to the spins, if $h > 0$ then the k^{th} site would be preferentially spin up and if $h < 0$ then the k^{th} site would be

preferentially spin down. In the case that $h = 0$ the external field would not influence the spin site. The case of a transverse field is different, and will be treated after an introduction to the Heisenberg model.

1.5 Heisenberg Model

In the previous section it was shown that the lowest energy state of an Ising system occurs when all the spins in a system are aligned or antialigned. We can generalize the spins from $\sigma_j = \pm 1$ to Pauli spin matrices (σ^x, σ^y and σ^z), allowing each spin to be treated more accurately in a quantum mechanical sense. The Pauli spin matrices for spin $s = \frac{1}{2}$ are defined as in equations 1.16, 1.17 and 1.18 [42].

$$\sigma^x = \begin{pmatrix} 0 & 1 \\ 1 & 0 \end{pmatrix} \tag{1.16}$$

$$\sigma^y = \begin{pmatrix} 0 & -1 \\ i & 0 \end{pmatrix} \tag{1.17}$$

$$\sigma^z = \begin{pmatrix} 1 & 0 \\ 0 & -1 \end{pmatrix} \tag{1.18}$$

Using this we can take equation 1.13 and generalize it to the Heisenberg model as shown in equation 1.19 where we substitute the Ising coupling constant, J, for the orientation dependant equivalents J_x, J_y and J_z, factor out the negative sign and multiply by $\frac{1}{2}$ due to the definition of the Pauli spin

operators. The external field h is assumed transverse and so is only operated on by the σ^z operator.

$$\hat{H} = -\frac{1}{2}\sum_{j=1}^{N}(J_x\sigma_j^x\sigma_{j+1}^x + J_y\sigma_j^y\sigma_{j+1}^y + J_z\sigma_j^z\sigma_{j+1}^z + h\sigma_j^z) \tag{1.19}$$

The physics of this model are similarily dependent to the Ising model. In the previous section it was demonstrated that in the case where the interaction $J_{ij} > 0$ we had a ferromagnetic system in the single spin case. In the Heisenberg model if the coupling constant J is positive, we also always get a ferromagnetic state. In the case of $J < 0$ the ground state is antiferromagnetic in two and three dimensions which correlates to the Hubbard model. In the case of one dimension, it depends on the spin of the system. Above we assumed that this was a spin-$\frac{1}{2}$ case, which would result in quasi-long range order. In the case of an integer spin only short range order can be present.

1.5.1 Transverse Field Ising Model in 1 Dimension

A simplified version of the Heisenberg Model is the Transverse Field Ising Model (TFIM), where we assume a strong, anisotropic spin system with J_1, or nearest neighbour, antiferromagnetic interactions [29]. As with the Ising model with nearest neighbour interactions [25], this model also shows no phase transition occurring at finite temperature [43]. At zero temperature there is antiferromagnetic long range order, but this disappears when the transverse field exceeds a critical strength, giving a quantum critical point and a subsequent phase transition. This model is important because it has been shown

that it can be used to study magnetic ordering in materials with singlet crystal field ground states [44]. In this model we assume that the transverse field is applied in the x-direction and that the interactions are only in the z-direction. In this system, we can determine that the interactions in the Hamiltonian that occur are due to a number of spins flipping states owing to the applied field. The interaction term that describes spins along z can be taken straight from equation 1.13, and is the first term of equation 1.20. In equation 1.20 gJ_z represents the tunnelling energy required to be exceeded to allow a spin flip and J_z represents the short range particle-particle interaction [45]. The second term, which is representative of the field interaction, is where the spin operator is applied in the x direction and scales in probability with the number of flips, as the energy barrier increases as a function of J^n [45]. Because of this, any term other than the first can be safely ignored. Doing these substitutions, we can rewrite equation 1.19 as equation 1.20.

$$\hat{H} = -J_z \sum_{j=1}^{N} \sigma_j^z \sigma_{j+1}^z - gJ_z \sum_{j=1}^{N} \sigma_j^x \text{ [45]} \tag{1.20}$$

Equally, we could choose the y-direction to make a Transverse Field Ising Chain (TFIC), but these are mathematically equivalent and x is chosen canonically. If the field were along the z-direction we would have the longitudinal version of the system mentioned previously.

The Ising model is a representation where we assume that the tunnelling parameter goes to zero and the free-spin system has the first J_z term going to zero. The effect the free-spin term creates is to order the spins along x,

while the tunnelling term tends to destroy order by spin-flips [43], with the order parameter, M_x expressed as $M_x = \langle 0|s_i^x|0\rangle$ where $|0\rangle$ is the ground state. As the tunnelling energy goes from zero to infinity the system goes from completely ordered to disordered. This happens because if we let $g \to \infty$ we can ignore the $\langle j, j+1\rangle$ term, or solve equation 1.21.

$$\hat{H}_{g\to\infty} = -\sum_{j=1}^{N} \sigma_j^x \text{ [43]} \tag{1.21}$$

In this case all terms commute, so the ground state is the simultaneous ground state of each individual term. This state preserves the symmetry such that a unitary operator, $\mathbf{S}$, acting on the ground state can simply returns the original ground state, or $\mathbf{S}\,|gs\rangle = |gs\rangle$ [45].

Now if we take the opposite case where we let $g \to 0$ then we have equation 1.22.

$$\hat{H}_{g\to 0} = -\sum_{j=1}^{N} \sigma_j^z \sigma_{j+1}^z \text{ [45]} \tag{1.22}$$

In this case we get the ground states shown in equation 1.23, as well as any linear combination. In this case the ground states are not symmetric, since $\mathbf{S}\,|\pm\rangle = |\mp\rangle$ and from this it appears that symmetry is broken by the ground state.

$$|+\rangle \equiv |\uparrow\uparrow\cdots\uparrow\rangle\,, |-\rangle \equiv |\downarrow\downarrow\cdots\downarrow\rangle \tag{1.23}$$

However, much like when we consider the superposition of these states, we arrive at a state $|A_{\pm}\rangle \equiv \frac{1}{\sqrt{2}}(|+\rangle \pm |-\rangle)$ which are symmetric, or where $\mathbf{S}|A_{\pm}\rangle = |A_{\pm}\rangle$. In fact, for $g \neq 0, |+\rangle$ and $|-\rangle$ are not eigenstates, and $|A\rangle$ is the ground state [45]. The problem here is that to change between the two states of $|+\rangle$ and $|-\rangle$ we need to flip all N spins. Based on the perturbing Hamiltonian, $\Delta\hat{H} = -gJ\sum_{j=1}^{N}\sigma_j^x$ we get a tunnelling amplitude of $T \sim g^N \langle -|\sigma_1^x\sigma_2^x \cdots \sigma_N^x|+\rangle$ [46] which goes to zero for small g and for $N \to \infty$, meaning it isn't possible to tunnel between these states. Additionally, each state $|A\rangle$ is a macroscopically distinct quantum state. Because of quantum decoherence, the concept of a macroscopic quantum state is not physically realizable for this system [45]. Any possible perturbation to this system would constitute a measurement of the state of a single spin, and this would give a measurement the state of the whole chain. Finally, if we consider applying a very small symmetry-breaking perturbation such as an initial field, this time in the z-direction, the perturbing Hamiltonian, $\Delta\hat{H} = -gJ\sum_{j=1}^{N}\sigma_j^z$ would split the degeneracy between the $|+\rangle$ and $|-\rangle$ states. For example, for $h > 0$ $|+\rangle$ would be the ground state [45]. If we were then to turn off this perturbation, for a finite system ($N < \infty$) the system would be in an excited state of the $h = 0$ Hamiltonian since $|+\rangle$ will no longer be a stationary state, and there is a possible tunnelling amplitude into the $|-\rangle$ state. However, if before we turn down the perturbation to zero, we take the thermodynamic limit and then turn off the perturbation we will be able to remain in the initial state. This means that we can expect spontaneous symmetry breaking in the $N \to \infty$ limit, where $|+\rangle$ and $|-\rangle$ can be considered approximate eigenstates for the system, where that approximation gets better as the size of the system grows. This

is a $\mathbb{Z}_2$-symmetric system which spontaneously breaks $\mathbb{Z}_2$ symmetry, which is the definition of a ferromagnet [45]. A $\mathbb{Z}_2$ symmetry is representative of a physical system where we can have a pair of states that differ only by a negation operator, for example $\phi(x)$ and $-\phi(x)$ where their energies are equal: $\mathrm{E}(\phi(x)) = \mathrm{E}(-\phi(x))$. This implies an invariance when the system is rotated by π radians [45].

At the extremes of $g = 0$ and $g \to \infty$ we have a unique symmetric ground state and two symmetry-breaking ground states. It would be unphysical for this situation to continuously vary between these two states, so we need to consider the intermediate cases where $g \gg 1$ and $g \ll 1$ and see what happens when they converge.

1.5.2 $g \gg 1$

For the system in the state $g \gg 1$ we are in an excited state in the paramagnetic phase. This phase can be typified by considering a single spin flip in the chain. Given $\hat{H} = \hat{H}_\infty = -gJ\sum_{j=1}^{N}\sigma_j^x$, this spin flip would cost $2gJ$ energy above the ground state. There are N possible states with this configuration, which we can represent as:

$$|n\rangle \equiv |\rightarrow \cdots \rightarrow \leftarrow \rightarrow \cdots\rangle$$

$$\left(\hat{H}_\infty - E_0\right)|n\rangle = 2gJ\,|n\rangle \;\; [45] \tag{1.24}$$

We can now use perturbation theory to explore what happens to the system by employing a spin-flip operator, σ_j^z. For $\sigma_j^z\sigma_{j+1}^z \left|{\rightarrow_j}{\leftarrow_{j+1}}\right\rangle = \left|{\leftarrow_j}{\rightarrow_{j+1}}\right\rangle$ meaning $\langle n \pm 1| \sum_j = 1^N \sigma_j^z \sigma_{j+1}^z |n\rangle = 1$ which is equivalent to the ferromagnetic term hopping by one spin flip from the j^{th} site to the $j + 1^{th}$ site to the right. From this we can derive an effective hopping term as in equation 1.25 [45].

$$\hat{H}_{eff} \left|n\right\rangle = -J \left(\left|n+1\right\rangle + \left|n-1\right\rangle\right) + \left(E_0 + 2gJ\right) \left|n\right\rangle \text{ [45]} \tag{1.25}$$

If we assume periodic boundary conditions we can solve this using a Fourier transform, resulting in:

$$\left|n\right\rangle \equiv \frac{1}{\sqrt{N}} \sum_{j=1}^{N} e^{-ikx_j} \left|k\right\rangle \text{ [45]}$$

where $x_j = ja$ and $k = \dfrac{2\pi m}{Na}$ for $m = 1 \ldots N$. This generates the following momentum states:

$$\left(H - E_0\right) \left|k\right\rangle = \left(-2J \cos ka + 2gJ\right) \left|k\right\rangle \text{ [45]} \tag{1.26}$$

which results in a dispersion of spinon particles that can be described by:

$$\epsilon\left(k\right) = 2J\left(g - \cos ka\right)$$

which in the case where $k \rightarrow 0$ gives:

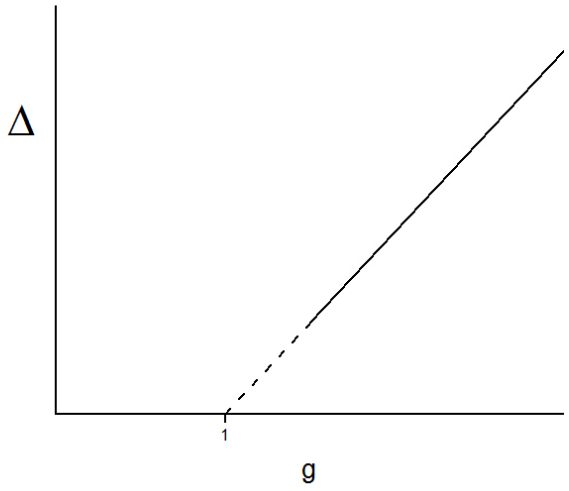

Figure 1.2: A plot of Δ versus g for the Transverse Field Ising Model derivation case where $g \gg 1$

$$\epsilon(k) \simeq \Delta + J(ka)^2, \Delta = 2J(g-1) \text{ [45]}$$

where Δ represents a potential energy gap. If we plot this energy gap against the value of g, we find that we get a gapless point as we approach $g = 1$ as seen in figure 1.2.

1.5.3 $g \ll 1$

For the case where $g \ll 1$, we can start by considering the case where the system is ferromagnetically ordered, the case we called $|+\rangle$ previously (Although we could equally use $|-\rangle$). This is one of the two eigenstates of equation **??**. The ground state energy here is $E_0 = -JN$. We can excite the system by flipping one spin so our system now looks like:

$$|\cdots\uparrow\uparrow\uparrow\cdot\downarrow\cdot\uparrow\uparrow\uparrow\cdots\rangle$$

In this interaction, we are making two bonds unhappy, giving an energy cost of $2J + 2J = 4J$. However, once we have this, we can flip neighbouring spins with no cost. The reason is that each spin flip costs $2J$ in energy, but once we have paid that cost the domain wall can propagate freely, since any single spin flip leaves the same number of perturbed domain walls [16]. Any domain wall must be created in a pair. A system equivalent to the above could be any of the following (or any system that only has one pair of domain walls):

$$|\cdots\uparrow\uparrow\uparrow\cdot\downarrow\downarrow\cdot\uparrow\uparrow\cdots\rangle\,;|\cdots\uparrow\uparrow\cdot\downarrow\downarrow\downarrow\cdot\uparrow\uparrow\cdots\rangle \text{ [16]}$$

The creation of a pair of domain walls is therefore the elementary excitation within this system.

For $g = 0$ a domain wall is localised in that it exists at a fixed position for a particular energy eigenstate, just like spinons were in the case where $g = \infty$. Because of this we can add a paramagnetic term as a perturbation to the system, where a spin flip creates a domain wall around $|j\rangle$ which leaves excitations at $|j+1\rangle$ and $|j-1\rangle$. Similar to equation 1.26 we get:

$$\left(\hat{H}_{eff} - E_0\right)|j\rangle = -gJ\left(|j+1\rangle + |j-1\rangle\right) + 2J\,|j\rangle \text{ [45]} \tag{1.27}$$

This gives us an energy dispersion of:

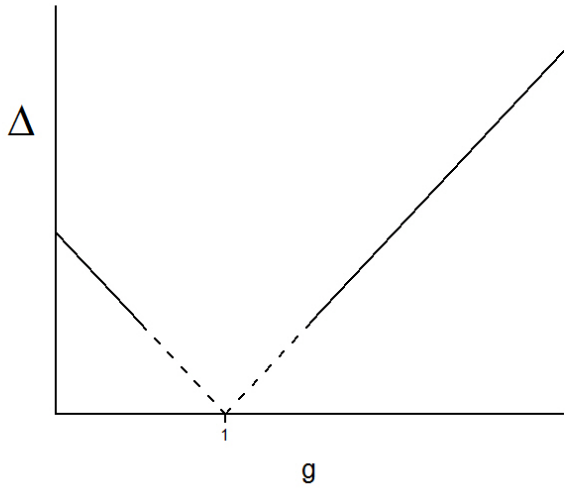

Figure 1.3: A plot of Δ versus g for the Transverse Field Ising Model derivation for both the $g \gg 1$ and $g \ll 1$ cases

$$\epsilon_{wall}(k) = 2J(1 - g\cos ka) \quad [45]$$

which gives us an energy gap:

$$\Delta = 2J(1 - g\cos ka) \quad [45]$$

We can overlay this with figure 1.2 which shows us that we can expect the phase transition to occur at $g = 1$, as seen in figure 1.3.

1.6 Cobalt Niobate

Cobalt niobate was a material that was first analysed for its magnetic and crystallographic properties in the late 1970's [47, 48], with more recent sus-

ceptibility investigations to better map out its magnetic phase space done in the late 1990's [49, 50].

More recent theoretical and experimental work has shown that this system exhibits a physical realization [51] of the E_8 mathematical symmetry group [52] and has generated significant additional interest in this material as a model of the spin-$\frac{1}{2}$ quasi-1D Ising system. Systems like these create important ties between theoretical models and real-world systems. The internal structure of materials allows for the "simulation" of toy model systems in the real world due to lattice and magnetic constraints that cause some interactions to be much more energetically favourable, essentially eliminating other considerations. In the case of cobalt niobate, the atoms are aligned in one dimensional ferromagnetic chains, where the chains are only weakly antiferromagnetically interacting [51]. The neutron scattering work by Coldea has shown a distinct quantum phase transition from an antiferromagnetic state to a quantum paramagnet [53], via the application of a strong transverse magnetic field. Coldea observed that the application of the transverse field caused a change in state of the system observed via neutron scattering from a pair of kinks in the ordered state to one that is paramagnetic [51]. Additionally, NMR work showed the finite-temperature effects of quantum criticality for the first time [54]. NMR measurements observed that the ^{93}Nb longitudinal relaxation rate, $\frac{1}{T_1}$, could identify the various regions of magnetic ordering at near zero K, changed using an applied transverse field, and specifically showed that at the field associated with the quantum phase transition in $CoNb_2O_6$ that a power law behaviour of $\frac{1}{T_1} \sim T^{0.75}$, as predicted by quantum critical scaling, was present.

Previous work done in my Masters thesis showed that the material had highly dynamic spins on the μSR time scale, and this work as well as heat capacity measurements showed that the material has a thermal relaxation time constant that increased exponentially at low temperature to be on the order of days, likely owing to weak spin-lattice coupling [17]. In this work I further explore the phase space with μSR as well as some measurements utilizing time-of-flight neutron scattering. This work is described in chapter 3.

1.7 Nickel Niobate

Regarding the topic of nickel niobate, from a physics point of view very little work has been done. Chemically, it was first described in literature by Goldschmidt in an overview of niobate materials in 1960. In this article he showed the phase diagram, which listed several possible structures for formation, each in a different space group: columbite (P_{bcn}), ixiolite($P2/c$) and tri-rutile($P4_2/mnm$). Based on the work of Coldea on cobalt niobate, it was desired to place an atom that would have an integer spin, as opposed to a half-integer spin and so the obvious choice was to use nickel in the +2 state.

Single-crystal nickel niobate in the columbite structure was claimed to have been grown by Prabhakaran [55] in their report on the growths of niobates, so using their starting work as a springboard we attempted to replicate their results and hopefully generate the same chain of spin-1 spins that exist as spin-$\frac{1}{2}$ spins in cobalt niobate. The results of the growth attempts are detailed in chapter 4. There were few characterization details and no images given by

Prabhakaran and we were unable to reproduce their growth using the published method.

We synthesized the columbite phase as well as a previously unreported polymorph, which we call the pseudo-trirutile phase, or β-$NiNb_2O_6$. When we analyzed this material with single-crystal x-ray diffraction, we were able to determine the space group as $P4_2/n$. The original group that measured this structure classified it as a simple rutile structure, space group $P4_2/mnm$, but with a unit cell where the volume is $\frac{1}{3}$ that of a tri-rutile, because $c_{trirutile} = \frac{1}{3}c_{rutile}$. We believe that they did so in error, as the data does fit well to that group and the only difference is that in the trirutile system one of the oxygens is at a symmetric Wyckoff position, while we found it to actually be in a general position by a small amount. This was unique in that other compounds in the AB_2O_6 family actually do form in the trirutile space group.

We compared the position of the niobium atoms to those of the tantalum atoms in nickel tantalate ($NiTa_2O_6$) in chapter 5. This is a good comparison because the Shannon (ionic) radii for Nb^{5+} and Ta^{5+} are identical, 0.64Å. The measurements done comparing these materials using SQUID magnetometry data shows that the difference in atomic positions that causes a change in space group and a small distortion in the structure is actually of little importance. The space group for the tantalum compound is $P4_2/mnm$, in contrast with the space group that we determined for the nickel compound, $P4_2/n$. The difference in the positioning of the niobium atoms, compared to the tantalum atoms, may be due to the second-order Jahn-Teller effect [56]. Many d^0 ions in the 4d and 5d series show highly distorted octahedral environments, typically

not simple tetragonal or trigonal distortions [57]. It is not theoretically clear why this effect would be stronger in Nb^{5+} and Ta^{5+} [56].

A full characterization of the magnetic structure of the new material was performed using neutron diffraction techniques. Initial powder diffraction was inconclusive with regards to the possible magnetic arrangement of atoms, so single crystal scattering was done to break the ambiguity. We determined that the material attempts to anti-align all spins, but experiences both intraplanar and interplanar frustration. Regarding the columbite material, we were able to synthesize some small crystals and do some characterization using μSR. The μSR results show that the β polymorph has a critical exponent that is slightly below what would be expected in a true 3D spin system, which is likely due to the frustrated moments. The columbite polymorph shows a much lower critical exponent, on the order of what would be expected for a 1D spin system, although both these measurements are meant as guides to future work, as the number of data points immediately adjacent to T_c is insufficient to make a case for proven low dimensionality. The neutron diffraction and μSR results on nickel niobate are presented in chapter 6.

1.8 Summary

This chapter has developed the theoretical machinery behind the investigations and methods that were used in the remainder of the thesis and outlined the bulk of the experiments performed. The results of the transverse field Ising model describe the cobalt niobate system, and the effects of energy gap explain the effective spin-$\frac{1}{2}$ nature. The theoretical underpinnings of constrained and

frustrated magnetism are evidenced in the β-nickel niobate system in particular, as we see interchain and intrachain frustration leading to the magnetic structure we determine. Our data also seems to show that the spin-1 columbite nickel niobate shows some of the same characteristics as the cobalt niobate, but the limited data taken does not allow for a more conclusive statement.

Chapter 2

Experimental Techniques and Methods

This chapter details the theory behind and the uses for the different experimental techniques performed in this thesis. The intent is not to give a comprehensive overview of every technique, but rather to put the experiments into an appropriate context. The importance of synthesis and characterization of materials relies on understanding the methods of creating those materials as well as examining their properties: magnetic, thermal and transport typically being those of greatest interest to condensed matter physics. Typically, this journey is begun with characterization using powder x-ray diffraction to determine the crystal structure, followed by SQUID magnetization and specific heat measurements to determine if there are interesting properties. Using Laue x-ray diffraction we can determine orientation, and using single crystal x-ray scattering we can determine the atomic positions, while powder diffraction or single crystal scattering can give us lattice constants and structure. We can then examine the magnetic structure and response in more detail using the machinery of muon spin rotation and both powder and single crystal neutron scattering.

2.1 Materials Chemistry

A significant portion of the work done for this thesis is sample preparation and synthesis. The core of sample preparation, from the perspective of a physicist, comes from two sides. First, synthesis of materials is done in the hopes that systems will have interesting properties from a physical point of view. With respect to this thesis, that means that the desired materials have magnetic phase transitions. A key requirement for magnetism to exist is that there needs to exist the possibility for unpaired electrons, while the total electronic structure is charge-neutral. This condition allows for a quantum mechanical exchange interaction to take place in the physical system, which is the key to magnetism occurring. Understanding this leads to the second point, namely that although we desire a system with certain properties, it has to be physically realizable; by that it is meant that chemistry allows for the system to exist. The first cardinal rule of material synthesis is that all materials must be charge neutral, or that the number of electrons donated by cations equals the number of electrons received by anions. Whether a material is a cation or an anion in a compound is related to the relative electronegativity in a material. Given a series of chemicals it is relatively easy to determine which materials would be an anion and which would be a cation. In this thesis oxide materials are used, and in every case the oxygen atom exists in a O^{2-} oxidation state, meaning it is the anion and is receiving electrons to create the bonds with the cations: cobalt, nickel and niobium. To solve charge balance, the potential oxidation states of the materials need to be known, and can be looked up on most periodic tables. Typically there are oxidation state values that are likely or predominant in nature, allowable and forbidden. Although, for example,

we synthesized $CoNb_2O_6$ [47] which has Co^{2+}, Nb^{5+} and O^{2-}, but this same combination under different synthesis conditions can form $Co_4Nb_2O_9$ [58] with the same oxidation states, or it can form $CoNbO_4$ [59] if cobalt is oxidized to its other permissible state of Co^{3+}.

To determine the feasibility of forming materials, in addition to charge balancing the size of the ions needs to be taken into account. This is done based on Shannon Radii, which are the assumed radii that an ion would have in an ionic solid if they were solid objects. The first measurements were done by Landè using ionic solids that had extreme differences in ionic radii, such as LiI and RbI. He assumed that the iodine atom was so large in comparison to the cations that they would contact each other, and the cations would simply fit in the gaps. He was able to determine 8 radii using this method [60]. This was followed by experiments by Wasastjerna [61] and Goldschmidt [62] used electric polarizability through measurements of the refractive index to determine the radii of various ions. Linus Pauling then did the same using the effective nuclear charge to create proportionate distances between the anions and the cations [63, 64]. Shannon followed up these with a review of available crystallographic data, and was able to split the radii into categories based on their oxidation state, as well as whether they existed in a high-spin or low-spin state in the cases of chromium, manganese, iron, cobalt and nickel. He created two sets of tables: one based on Pauling's determination of a O^{2-} radii as 140 pm [65] and one based on an ionic radius of 126 pm, determined from the data set alone. This created two tables: one of 'effective' ionic radii, and one of 'crystal' ionic radii [66]. Of note, in space groups that are not cubic, ionic volumes are elliptical, not spherical, which can have physical effects on the

compound. What has been recently discovered is that although the ionic radii are not constant, the ionic volumes appear to be constant between materials. This makes logical sense if you treat an ionic solid as packed ellipsoids with a finite amount of charge [67, 68].

Using this basic knowledge of chemistry we have a starting point for determining if it is possible to synthesize desired materials.

2.2 Crystallography

When we talk about solids we can broadly separate them into two categories - Crystalline solids and amorphous solids. An amorphous solid is simply one that is characterized by atomic disorder. The formula units of the material are all self-consistent, but there is no alignment or preferred orientation. Whereas in crystalline solids this alignment tends to lead to interesting physics, and condensed matter physics often relies upon exact crystallographic repetition to connect theories and models to real world systems.

A perfect crystal would be an idealized system where we have a single grain or alignment, of all the formula units. In our idealized case all atoms are arranged in a periodic array in three dimensions, where all the atomic positions and distances are equal and exactly known. In reality, when we talk about single crystals we are ignoring microscopic things such as trace impurities, interstitial vacancies or voids in the material, incorrect site occupancy (where one atom sits on a site that should be occupied by another), stacking faults within a crystal as well as a host of other potential issues. These, however, typically are ignorable because their quantities make up only a miniscule frac-

tion of the crystal. Any time we can state that we have an infinite array of discrete points that look identical from any other point we have a Bravais lattice [3]. This can be represented as a vector $\vec{R}$ as shown in equation 2.1. This means that any two atoms occupying identical Wyckoff positions are related to each other by a constant transformation and that the local environment around each atom can be considered identical. In a real system edge effects and surface states do matter, but in the idealized environment we assume an infinite lattice by appropriate choice of boundary conditions. This patterning is referred to as long range crystallographic order [69].

$$\vec{R} = u\vec{a} + v\vec{b} + w\vec{c} \text{ where } \{u, v, w \in \mathbb{Z}\} \text{ [3]} \tag{2.1}$$

Type	Axis Symmetry	Angle Symmetry	Crystal Symmetry
Simple Monoclinic (P)	a ≠ b ≠ c	$\alpha = \gamma = 90^o, b \neq 90^o$	Monoclinic Single 2-Fold
Base Centred Monoclinic (C)			
Triclinic (P)	a ≠ b ≠ c	$\alpha \neq \beta \neq \gamma \neq 90^o$	Triclinic, Identity
Simple Tetragonal (P)	a = b ≠ c	$\alpha = \beta = \gamma = 90^o$	Tetragonal Single 4-Fold
Body Centred Tetragonal (I)			
Rhombohedral (R)	a = b = c	$\alpha = \beta$ $90^o, \gamma \neq 90^o$	Trigonal, single 3-fold
Hexagonal	a = b ≠ c	$\alpha = \beta = 90^o, \gamma = 120^o$	Hexagonal, single 6-fold
Primitive Orthorhombic (P)	a ≠ b ≠ c	$\alpha = \beta = \gamma = 90^o$	Orthorhombic Three 2-Fold rotation or roto-inversion axes
Body-Centred Orthorhombic (I)			
Base-Centred Orthorhombic (C)			
Face-Centred Orthorhombic (F)			
Simple Cubic (P)	a = b = c	$\alpha = \beta = \gamma = 90^o$	Cubic Four 3-fold axes
Body-Centred Cubic (I)			
Face-Centred Cubic (F)			

Table 2.1: A list of the axial, angular and crystal symmetries for each of the 14 Bravais lattices [70], illustrated in Figure 2.1.

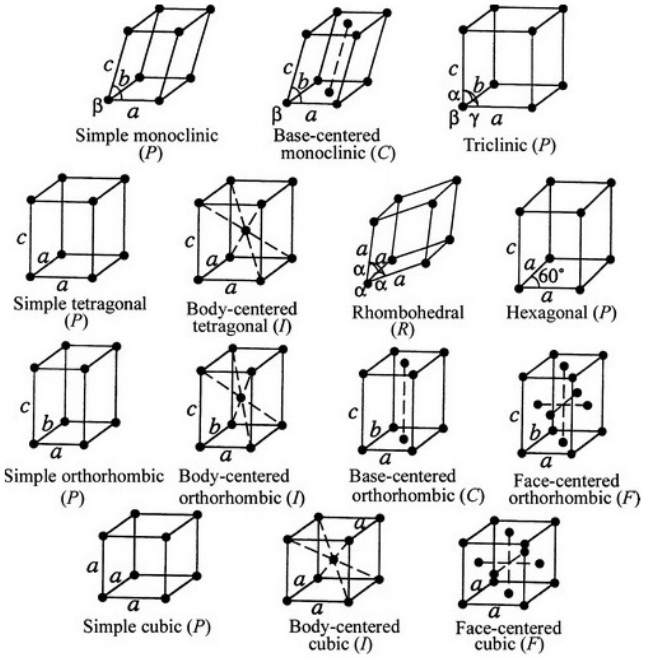

Figure 2.1: The fourteen Bravais lattices. From: "X-Ray Diffraction Crystallography: Introduction, Examples and Solved Problems, Geometry of Crystals, 2011, 25, Y. Waseda, E. Matsubara and K. Shinoda, (©Springer-Verlag Berlin Heidelberg 2011) With permission of Springer" [71]

In equation 2.1, $\vec{a}$, $\vec{b}$, and $\vec{c}$ represent three mutually orthogonal vectors. Within a unit cell created on a Bravais lattice an atom can occupy a corner of the cell (simple), inside the body of the cell (body-centred), on the face of the cell (face-centred), on the base of the cell(base-centred) or in the case of a hexagonal system inside the cell (rhombohedrally-centred). The lattices are shown in figure 2.1. A table of the conditions and the type of lattices is given in table 2.1.

The lattice itself can be deconvolved into a set of parallel and evenly spaced planes. A given family of planes are characterized by Miller indices which are

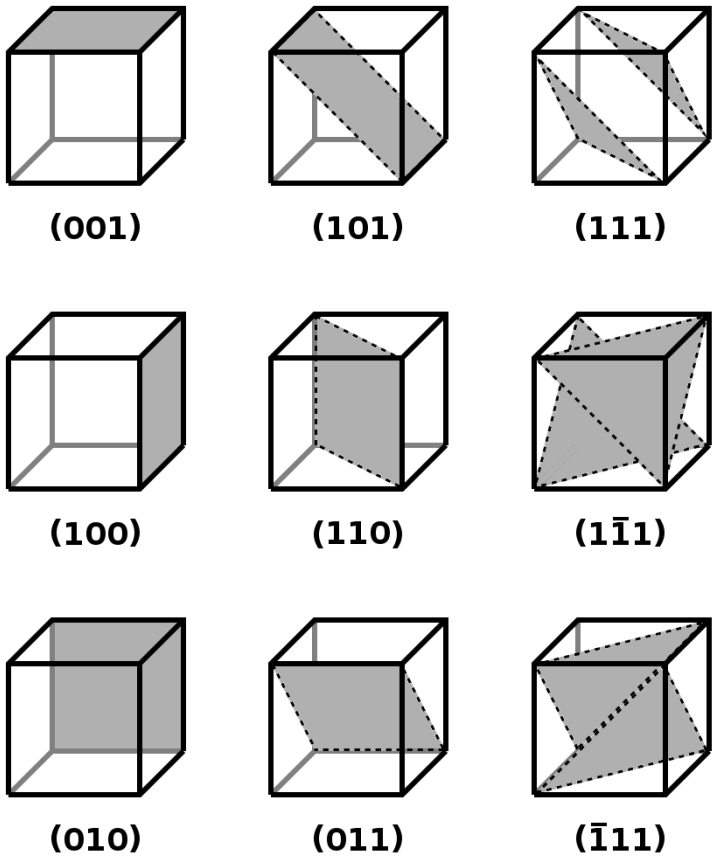

Figure 2.2: A sample of basic Miller Indices (Adapted from [72])

typically denoted by $[h, k, l]$. Each integer represents an intercept within the unit cell of $\frac{1}{h}$, $\frac{1}{k}$ and $\frac{1}{l}$. These indices are directly related to the unit cell as follows: given a set of Miller indices $[h, k, l]$ and axes with lengths (a, b, c) give intercepts for the plane within the unit cell of $\frac{a}{h}$, $\frac{b}{k}$ and $\frac{c}{l}$. An example of the basic Miller indices are shown in figure 2.2.

2.3 Diffraction Theory

Typical interatomic distances in a solid are on the order of an angstrom, or 10^{-10} m. To satisfy the diffraction conditions a wavelength on this order of

distance is required, which, using photons, is the realm of x-rays, as determined by equation 2.2 [3].

$$h\omega = \frac{hc}{\lambda} \simeq \frac{hc}{10^{-8}\text{ cm}} \simeq 12.3 \times 10^3 \text{ ev} \quad [3] \tag{2.2}$$

In 1913, Bragg and Bragg noticed that in well-ordered crystalline solids, when x-rays were shone on them, peaks of scattered radiation could be observed at certain angles, and that this was not true in liquids. These are now known as Bragg peaks. This was attributed to collimated x-rays interacting with the electrons and specularly reflecting. Assuming that the atomic planes were spaced a distance d apart, Bragg derived the condition for specular reflection, equation 2.3.

$$n\lambda = 2d\sin\theta \ [3] \tag{2.3}$$

If we take a non-polarized x-ray, where the electromagnetic field is oscillating in all directions randomly, perpendicular to the direction of propagation and make it incident with an electron, to first order the interaction takes place entirely with the electric field of the electron; to first order we neglect the magnetic and nuclear interactions. From Maxwell's electromagnetic theory, the electron scatters electric waves perpendicular to the electric field, as given by equation 2.4 where I_0 and I_f are the initial and final intensity, $\vec{k_0}$ and $\vec{k_s}$ are the initial and scattering wave vectors, R_0 is the distance from the scattering event to the observation and 2θ is the angle between the incoming and outgoing momentum vectors. This represents Thomson's model of a spheri-

cal wave scattered elastically by a free electron, similar to Rayleigh scattering and visible light. The scattering vector, $\vec{Q}$, is the difference between the two scattering wave vectors.

$$I_f\left(\vec{k_s}\right) = I_0\left[\frac{e_e^4}{R_0^2 m_e^2 c^4}\right]\frac{1+\cos^2 2\theta}{2}\ [73] \tag{2.4}$$

When considering this type of scattering event, it is assumed that the frequency of vibration of the electron is much smaller than that of the incident radiation, ignoring the anomalous case where they are comparable. Additionally, the mass factor in the denominator of the first term motivates neglecting the nuclear contribution to scattering. The second term in this equation is known as the polarization factor, because the outgoing wave becomes partially polarized [73].

If we now consider scattering between two particles by an incoming wave with wave vector $\vec{k_0}$ and scattered wave vector $\vec{k_f}$ we will end up that a path difference, given by the dot product $\left(\vec{k_0} - \vec{k_f}\right)\cdot\vec{r}$ where $\vec{r}$ is the vector between the two scattering centres.

Using the generic wave equation, $\psi = Ae^{\left(i\vec{k}\cdot\vec{x}\right)}$ and using the first particle as the origin for our system, we can write the equation of the first wave as $\psi_1\left(\vec{x}\right) = e^{\left(i\vec{k_s}\cdot\vec{x}\right)}$ and the second wave, with a scattering vector $\vec{Q}$ and a distance between the two centres $\vec{r}$ as $\psi_2\left(\vec{x}\right) = e^{\left(i\vec{k_s}\cdot\vec{x}\right)}\cdot e^{\left(i\vec{Q}\cdot\vec{r}\right)}$. The total scattering is then given by summing the two waves, as in equation 2.5, where $F\left(\vec{Q}\right)$ is the phase factor.

$$\psi_1(\vec{x}) + \psi_2(\vec{x}) = e^{\left(i\vec{k_s}\cdot\vec{x}\right)} \cdot \left(1 + e^{\left(i\vec{Q}\cdot\vec{r}\right)}\right) = F\left(\vec{Q}\right) \cdot e^{\left(i\vec{k_s}\cdot\vec{x}\right)} \text{ [3, 74]} \tag{2.5}$$

Expanding the case to scattering produced by a series of atoms, we can get coherent phase differences between the interatomic vectors which will describe the relative positions of the atoms. In a molecule or an aggregate of atoms, this is the effect of internal interference. External interference is the effect that we see between molecules or aggregates of atoms. Internal interference typically gives rise to the relative intensity of scattering at a given angle θ to all other angles while external interference gives the positions in θ-space where the maxima occur. The scattering phenomenon corresponds to the internal order of a sample, or the correlation between the positions of different atoms. To do this we can add the phase shifts of all particles. We can do this by taking equation 2.5 and summing over all particles in the crystal, as shown in equation 2.6 where $\rho(\vec{r})$ is the electron density function.

$$F\left(\vec{Q}\right) = \sum_j \rho_{\vec{r_j}} e^{\left(i\vec{Q}\cdot\vec{r_j}\right)} \text{ [3, 74]} \tag{2.6}$$

The Fourier transform of $F\left(\vec{Q}\right)$ is a representation of the electron density, which is directly related to the atomic distibution [73, 74]. However, the measurements that we obtain from scattering are the intensity. The intensity is given in equation 2.7.

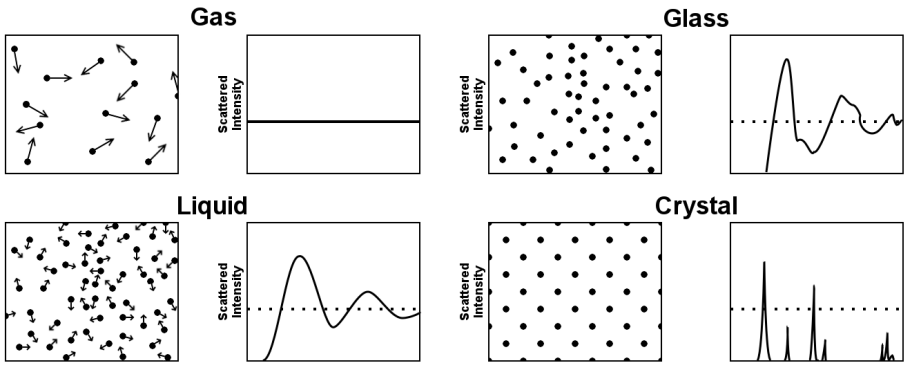

Figure 2.3: A cartoon showing the distribution of atoms and expected scattering profiles of a gas, a liquid, an amorphous solid and a crystalline solid. These cartoons neglect any background contribution and assume a monochromatic beam of x-rays. Adapted from [73].

$$|F\left(\vec{Q}\right)|^2 = |\sum_j e^{\left(i\vec{Q}\cdot\vec{r_j}\right)}|^2 = \sum_{j,k} e^{\left[i\vec{Q}\cdot(\vec{r_j}-\vec{r_k})\right]} \text{ [3, 74]} \tag{2.7}$$

One of the problems here is that although we are now dealing with a real value, we have lost all the phase information that was contained before squaring. This means that all the information we have about the atoms is relative to a common origin, so we cannot directly obtain the atomic positions from the intensity [74].

In a crystalline case, where we have repeated unit cells, this gives rise to diffraction. The difference between expected scattering intensity due to gases, liquids, amorphous glass solids and crystalline solids are shown in figure 2.3. This is explored further in a few paragraphs. Additionally, for an ordered solid we can replace our values of $\vec{r_j}$ with the values $\vec{R}$ from equation 2.1.

In a system with multiple species of particles, each type of particle will scatter slightly differently. To account for this, we can modify 2.6 as equation

2.8. In this equation f_j is known as the x-ray atomic scattering factor while in neutron scattering it is known as the scattering length, where the square of this value gives the neutron cross-sectional area [74].

$$F\left(\vec{Q}\right) = \sum_j f_j e^{\left(i\vec{Q}\cdot\vec{r_j}\right)} \text{ [3, 73, 74]} \tag{2.8}$$

Because x-rays scatter off of the electrons, and specifically the electron cloud, this changes how diffraction will occur. Considering an atom with Z electrons (where Z is the atomic number) we would expect that the scattering intensity would increase Z times. This is, however, only true in the case of backscattering in the incident direction because the distance between the electrons of an atom are on the order of the wavelength of the x-ray radiation, causing partial destructive interference. Mathematically, this is shown by equation 2.9b. Here we refer to the x-ray case specifically, denoting it as $f\left(\vec{Q}\right)$. The intensity decreases as θ increases. To describe the ratio between the amplitude of a scattered electron in an atom and that of a single electron we use the atomic scattering factor. Because the speed of the electrons in an atom is so much larger than the variation of the electric vector of the wave, the incident x-ray only sees an average electron cloud, characterized by the density of charge, $\rho(r)$. This is shown in equation 2.9a. The equation for the x-ray atomic scattering function will not be an analytical function. However, the value for $\rho_{el}\left(\vec{r}\right)$ can be computed using quantum mechanics, so numerical fitting is done for most atoms and ions and are available in the International Tables of Crystallography [74].

$$f\left(\vec{Q}\right) = \int \rho_{el}\left(\vec{r}\right) e^{\left(i\vec{Q}\cdot\vec{r}\right)} d\vec{r} \tag{2.9a}$$

$$f\left(\vec{Q}=0\right) = \int \rho_{el}\left(\vec{r}\right) d\vec{r} = \mathrm{Z}\ [74] \tag{2.9b}$$

Returning to the case of an ordered crystal and diffraction, the geometric relationships give rise to specific phase differences, which is evident by through the sharpening of the intensity in fourth panel of figure 2.3. The co-operative effects of the external interference of the incident waves sample the lattice, effectively like a 3D diffraction grid. The peaks that are detected from the scattering can be described in terms of the reciprocal of the atomic lattice.

Within the structure of the lattice, an atom can be defined at a position relative to a common origin by use of a vector. This vector is defined in equation 2.1. The vector $\vec{R}$ represents a position in real space and is specifying a relationship between an arbitrary origin and positioning of an atom within a unit cell. We can also refer to the plane spacing using the miller indexes defined above in section 2.2. The equation for the plane spacing is given in equation 2.10a, where the conversion between the real space vectors ($\vec{a}$, $\vec{b}$, and $\vec{c}$) and their reciprocal space counterparts ($\vec{a^*}$, $\vec{b^*}$, and $\vec{c^*}$) can be accomplished simply because of their relationship through the Fourier transform that was shown above. The direct conversion for $\vec{a}$ to $\vec{a^*}$ is given in equation 2.10b, while the remainder can be solved simply by changing the basis.

$$\vec{d_{hkl}} = h\vec{a^*} + k\vec{b^*} + l\vec{c^*}\ [73] \tag{2.10a}$$

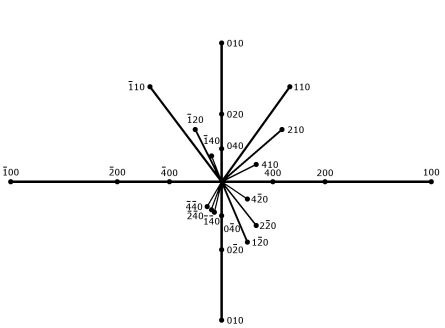

(a) p

lane.]A plot of $\vec{d}_{hkl}$ vectors in real space, representing the $\vec{Q}$ from the origin to the face of the [hkl] plane. Adapted from [75]

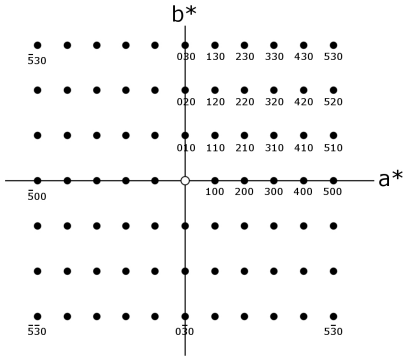

(b) A plot of reciprocal space, which maps the $\vec{d}_{hkl}$ from figure 2.4a. Adapted from [75]

Figure 2.4: A comparison of $\vec{d}_{hkl}$ in real space and the Bragg peaks they correspond to in reciprocal space.

$$\vec{a^*} = 2\pi \cdot \frac{\vec{b} \times \vec{c}}{\vec{a} \cdot \left(\vec{b} \times \vec{c}\right)} \text{ [3]} \tag{2.10b}$$

Each of the $\vec{d}$ vectors exists in real space as shown in figure 2.4a and maps into reciprocal space as mapped in figure 2.4b. The vector here represents the spacing between atomic layers, where those layers are spaced as shown in figure 2.2.

At given angles of 2θ, based on the spacing represented by the $\vec{d}_{hkl}$ vector we will get an increase in peak intensity due to the scattering.

As we defined before, the vector difference between $\vec{k}_0$ and $\vec{k}_s$ is the scattering vector, $\vec{Q}$. For this scattering to be detected $\vec{d}^*$ must lie on the surface of a sphere of radius $\frac{2\pi}{\lambda}$, mathematically, because both wave vectors $\vec{k}_0$ and $\vec{k}_s$ have the same magnitude. This means that for a given $\vec{d}^*$ to be detected, it

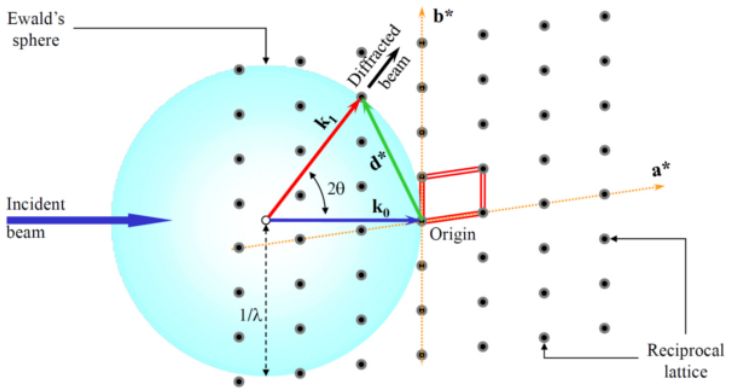

Figure 2.5: The visualization of diffraction using the Ewalds sphere with radius $\frac{1}{\lambda}$ and the two-dimensional reciprocal lattice with unit vectors $\mathbf{a}^*$ and $\mathbf{b}^*$. The origin of the reciprocal lattice is located on the surface of the sphere at the end of $\mathbf{k}_0$. Diffraction can only be observed when a reciprocal lattice point, other than the origin, intersects with the surface of the Ewalds sphere [e.g., the point $(\bar{1}3)$]. The incident and the diffracted beam wavevectors, $\mathbf{k}_0$ and $\mathbf{k}_1$, respectively, have common origin in the center of the Ewalds sphere. The two wavevectors are identical in length, which is the radius of the sphere. The unit cell of the reciprocal lattice is shown using *double lines*. "Fundamentals of Powder Diffraction and Structural Characterization of Materials, Fundamentals of Diffraction, 2009, 145, V.K. Pecharsky and P.Y. Zavalij, (©Springer Science+Business Media, LLC 2009) With permission of Springer" [76]

must be equal to $\vec{Q}$. Given that reciprocal space is a lattice, as shown in figure 2.4b, we can superimpose a sphere using the scattering vector as its radius. This sphere is known as the Ewald sphere, based on his original studies (he termed it the sphere of reflection [77]). This is shown in figure 2.5.

The lattice points of the reciprocal lattice are the values of momentum transfer where the Bragg diffraction condition, equation 2.3, is satisfied. For diffraction to occur the scattering vector must be equal to a reciprocal lattice vector. Geometrically, this means that if the origin of reciprocal space is placed

at the tip of $\vec{k}_0$ then diffraction will occur only for reciprocal lattice points that lie on the surface of the Ewald sphere [78].

2.4 Optical Floating Zone Synthesis

An optical floating zone image furnace is a crucibleless method for crystal growth using halogen or xenon arc lamps as a source of infrared radiation to melt a ceramic solid into a liquid which can, under ideal conditions, be crystallized into a single grain crystal. The system uses typically either two or four elliptically machined mirrors, where the infrared source is placed at one focus and the melt point is located at the second focus, common to all the mirrors. The growth occurs inside a quartz tube which allows for the isolation of materials from the external environment and also allows for a desired atmosphere to be introduced. Although air can be used, there are cases where different atmospheres, typically oxygen for an chemically oxidizing atmosphere and either a 90% argon, 10% hydrogen gas mixture or carbon monoxide for a chemically reducing atmosphere can be used instead to assist in the chemical reaction desired to fully react a material. This allows us to increase the potential number of materials that can be grown with this technique.

A congruently melting material is one where, in a binary compound for example, all members of the compound can co-exist with a liquid of the same composition as in figure 2.6a. In this figure the intermediate compound, AB_2, also melts congruently because there is a point where at some temperature, at

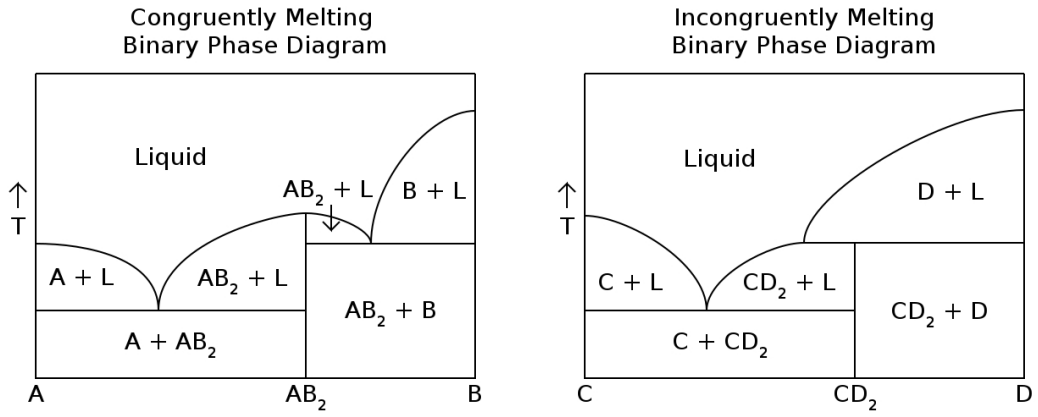

(a) A congruently melting phase diagram made up of chemicals A and B, both of which melt congruently.

(b) An incongruently melting sample made up of chemicals C and D, both of which melt congruently.

Figure 2.6: A comparison of the binary phase diagrams of a congruently and incongruently melting sample.

the top of the AB_2 phase boundary line it coexists with a liquid of the same composition.

In an incongruently melting material there exists a temperature at which one of the solid phases transforms into another solid phase and a liquid phase, both of which are a different chemical composition than the original material, as seen in figure 2.6b. In this figure the intermediate compound, CD_2, is incongruently melting because at the top of the CD_2 phase boundary the material melts to D plus a liquid that is not the same composition (It would have an excess of chemical C since D has precipitated as a solid).

Both congruently and incongruently melting materials can be grown by the optical floating zone method. Commonly the optical floating zone is characterized as a system which uses a travelling solvent floating zone (TSFZ). This type of crystal growth is characterized by having two liquid-solid interfaces and

is crucibleless. The solvent here is either one of the constituent materials or, commonly in the case for incongruent materials, a flux material that changes the liquid phase to allow for proper formation of the final material without precipitating out one component preferentially. In this case it is important that the flux material not be likely to incorporate itself into the resultant crystal. At the melting interface the solvent melts the material in the charge, which in our case is typically a stoichiometric rod of pre-reacted resultant material as a ceramic, described below. The two constituent materials are then mixed in the molten zone and at the second liquid-solid interface the material nucleates. This nucleation is strongly preferential to the resultant material due primarily to thermodynamic considerations, which rejects the flux material allowing it to remain in the zone [79]. In many cases this means that the resulting single crystal can have a higher purity than the original materials used, since any impurities tend to remain in the flux. Ideally, the concentrations of the constituent materials should remain constant in the liquid portion of the zone, so a uniform feeding rate is ideal.

A normal growth is done by first chemically preparating the desired final phase of the material as a ceramic powder. Constituent materials will be sintered at a low temperature, between 150 and 700 degrees Celsius (depending on the material) to remove water and impurities. The materials will then be weighed and mixed in a stoichiometric ratio. The exception to this is when it a material is desired to be intentionally off-stoichiometry, or if it is known that one of the constituents has a low vapour pressure as some of that element will be lost in the growth so additional material is needed to account for this loss. The materials are then mixed mechanically and then pre-reacted. The purpose

Figure 2.7: A post-sintered, pre-reacted ceramic powder after ball milling.

of the pre-reaction is to attempt to form, as a ceramic, the desired material product. This reaction is done at approximately two thirds of the melting point of the materials in a crucible in a standard box furnace, or in a tube furnace if a specific atmosphere is needed to allow for a reduction or oxidation reaction to occur. Materials are heated or cooled at the allowable rates for the furnace, and dwell times are typically multiples of 8 or 12 hours. Generally the materials are removed after a heating, dwell and cooling cycle and reground into a powder. An example of material at this stage is given in figure 2.7. At this point the materials can be analyzed by powder x-ray diffraction, described in section 2.5, to determine the completeness of the reaction. A rule of thumb is that the ratio of intensity of the largest peak of the precursor material should be less than 5% of the intensity of the largest peak of the desired material. If this is not the case the material is put through a subsequent cycle in the furnace.

Once fully reacted, the material is well ground, typically mechanically and via an automated grinder using zirconia pellets and is then formed into rods. To do this the material is packed into forms; in the case of this thesis latex balloons were used. Rods are typically between 8 and 13 cm in length and are between 7 and 8 mm in diameter. The packing needs to be done firmly and with uniform pressure for an optimal growth to occur. Variations in the density and in the radius of the rod will be reflected in the final product since melt temperature is a function of the amount of material in the zone, as the incident thermal energy is essentially fixed. Alternatively, incident radiation can be increased and decreased but this comes at a loss of replicability. These rods are then vacuum packed to remove as much air as possible from the ground ceramic and then subjected to 50-60 MPa of hydrostatic pressure for 15 to 20 minutes to press the material into the rod shape. A hydrostatic press is shown in figure 2.8.

The rod will then be removed from the balloon carefully. An example of this is in the lower panel of figure 2.9. This will then be carefully weighed and placed into a ceramic boat, typically lined with a non-reactive oxide, and put through another thermal cycle in the furnace to sinter, or harden, the rod. This can be seen for a pair of rods in the upper panel of figure 2.9. When this cycle is completed the rod should be quite sturdy and around 60-80% of the expected density of the single crystal.

Typically two ceramic rods are mounted in the optical floating zone furnace, one to be used as seed material and one as feed material. The seed can also be a previously grown crystal or, in the case of rare or expensive materials, a

Figure 2.8: A hydrostatic press.

Figure 2.9: An example of rods before being sintered (below) and after being sintered (above).

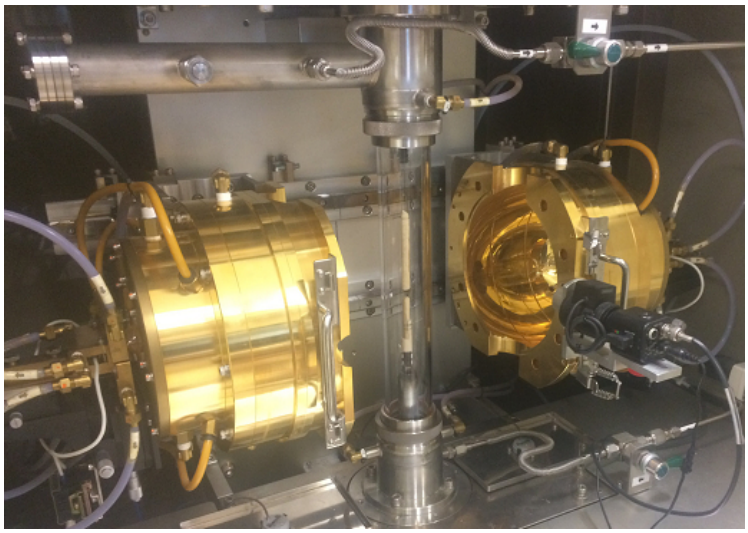

Figure 2.10: A ceramic seed and feed mounted inside a two-mirror OFZ system. One of the two light bulbs at the focii of the polished, gold mirror is visible.

ceramic of similar composition and space group. For example, a ceramic rod of holmium titanate ($Ho_2Ti_2O_7$) can be grown on a seed of dysprosium titanate ($Dy_2Ti_2O_7$) relatively easily due to the fact that they have very similar lattice constants. Aside from the shape and density of the material, the alignment of the rods in the furnace is critical to the quality and stability of the zone. Being off-centre can pull the material away or have the zone located in a position that is not the focus to all the incident radiation. This can reduce the effective temperature of the zone drastically. Figure 2.10 shows a mounted seed and feed rod inside the sealed quartz chamber within the elliptical mirrors of this two-mirror OFZ system. Also visible is one of the light bulbs that supplied the infrared radiation used to melt the material at one of the focii of one of the ellipsoidal mirrors.

During an optical floating zone crystal growth, the operator has the ability to control four parameters: the rate of growth, the incident energy, the rotation rate of the sample and the gas pressure and flow.

The rate of growth generally determines the stability of the crystallization front of the material and is controlled by changing the rate at which the material is pulled from the zone (the growth rate) and the rate at which material is fed into the zone (the feed rate). This is done either by physically raising or lowering the rods or by physically raising or lowering the lamp/mirror assembly. Of the lamp/mirror assembly, the upper rod and the lower rod, at least two of the three must be adjustable. Congruently melting materials can generally be grown at speeds significantly faster than incongruently melting ones as there is no need to wait for flux reactions in the diffusion layer of the material to occur. The exception is materials with a low vapour pressure. If it is possible for these to be grown they must be grown quickly; As the material is melted some will evaporate. A cold finger can be used to try to collect this material, but typically some will end up on the surface of the quartz tube, causing a layer of material to be deposited on the quartz tube that will make the glass opaque to the infrared, causing a subsequent decrease in energy delivered to the liquid zone.

The second parameter, the incident energy, is simply the flux of infrared radiation that is output by the lamps. The amount of energy can be turned up or down similar in concept to a dimmer switch on a light. There is a direct correlation between the wattage supplied to the element, the emission of infrared radiation and the temperature in the liquid zone. Determining

an exact value for a temperature within the zone is, however, a very difficult proposition. Instead, certain values of input power are known to correspond to melting temperature of various materials and so a melt temperature can be inferred approximately.

The third parameter that can be controlled is the rotation rate. The nature of the growth necessitates rotation to assist with diffusion of both constituents and, most importantly thermal energy. Thermal currents are created via forced Margioni convection. Modelling has shown that the convective cells are less symmetric than would be expected, are elliptical in nature with less material exchange between the cells than would be expected [80]. In incongruently melting materials this is especially important as it leads to material segregation. The rotation rate also determines the thickness of the diffusion layer and the shape of the crystallization front. The thickness of the diffusion layer is important because it sets the rate limit for transport to the crystallization interface which in turn sets the limit for the growth rate, which is the point at which defects will increase significantly.

The fourth controllable parameter is gas pressure. Typically, gas composition is unalterable during the growth. Inert gases, especially those with higher molecular weights, can be used to reduce the diffusion of vapours from the liquid zone. Increasing the gas pressure decreases sample temperature due to an increased thermal exchange with the atmosphere because of the corresponding increase in gas density. Effectively increasing pressure necessitates an increase in incident energy to obtain the same temperature. Additionally, an increase in pressure can lead to the formation of gas bubbles within the zone. These

occur either due to gases trapped in the porous ceramic being unable to escape or, in the case of reactions involving reduction or off-stoichiometric growth, the evolution of oxygen gas in the melt through decomposition.

Once a crystal has been grown to the desired length, the liquid zone must be terminated. This is done by reducing the incident energy to lower the temperature while continuing to draw material out of the zone. Because the thermal gradient of the system is on the order of hundreds of degrees Celsius per cm, it is impossible to avoid thermal shock in the system. To mitigate this as much as possible, the disconnect is done at as high a temperature as is feasible and, once completed, the material is left in the hot zone, which is cooled slowly; typically at a rate of 3% to 5% power per hour, which is roughly equivalent to between 75 and 125 degrees Celsius an hour. Figure 2.11 shows a side-by-side image of a crystal as observed while being grown (left) and after being grown (right). In the left panel the ceramic is above the molten zone and the crystal as grown is below the molten zone. Defined edges of the liquid-solid interface are clearly visible. In the right panel the resultant crystal is shown. The unmelted portion of the feed rod was raised out of the picture during the cooling phase.

Since a significant thermal stress has been applied, a post-annealing at a low temperature, usually around 800 degrees Celsius, is advisable to reduce any internal thermal stresses. The difference between pre- and post-annealed samples and the relaxation of thermal stress can be seen using polarized light. The exception to this cooling rule is when there is reason to quench a material, typically done to force a phase transition. An example of an as-grown crystal

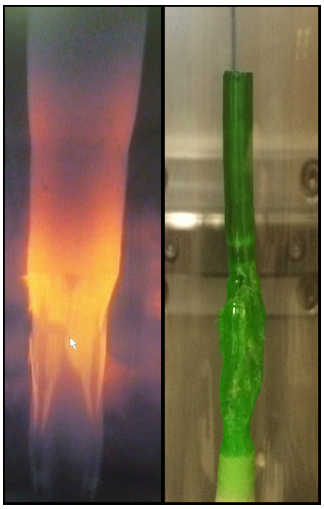

Figure 2.11: The left panel is an image from the mounted camera looking at the molten zone. The right panel shows a crystal after being grown.

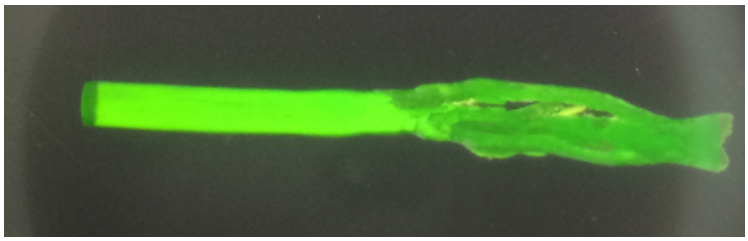

Figure 2.12: A photograph of an as-grown crystal under polarized light. As lit there is no evidence of any internal stress remaining in the crystal. Examples of stress can be seen in the portion of the crystal that was grown poorly (right side of the crystal, dark), compared to the ideal single crystal (left side, light and uniform in colour).

under polarized light is given in figure 2.12. In this image the left hand side of the crystal is an ideal, unstressed single crystal. The right hand portion actually grew so poorly that gaps are visible. The dark, uneven colouring on the right side is indicative of the crystal stress. Additionally, the left tip of the crystal is dark. This is because the crystal grew with a concave crystallization front, so there is a void at the tip which causes the dark colour.

The primary benefit to growths utilizing the optical floating zone technique is the purity of the end product. This method is crucibleless, so there is a significantly decreased chance of contamination or inadvertent chemical reactions. Additionally, the ability to homogeneously grow both congruently and incongruently melting materials is a significant benefit to this technique. The ability to form incongruently melting materials is enhanced using this method because the large thermal gradient reduces the chance of supercooling occurring in the liquid and allows for faster growth of the materials. The homogeneity is typically because there is only a small volume of liquid at any time. A drawback to this is that it can help to drive systems into off-stoichiometric or stuffed states more easily, due to enhancement of the steady-state reaction, compared to other methods with larger volumes of material to grow from [81, 82].

Limitations of the optical floating zone set-up include the maximum obtainable temperature. At present, standard halogen lamps allow materials up to approximately 2500 degrees Celsius to be grown, while Xenon lamps are effective up to approximately 2800 degrees. Above this, a modified style of optical floating zone system, the laser diode floating zone, has been used to melt higher melting temperature materials, however these systems are not yet in common use. The small volume of the liquid zone means that the stability of the growth is marginal, and small changes in power, gas flow, or external influences such as vibration can cause drastic changes or failure of the growth. Getting a definite temperature of the melt is generally impossible, as there is no way to get a direct measure, especially of the core/crystallization front of the material where that would be most useful, due to the inaccessibility of the points of interest. Additionally, although the large thermal gradient is helpful

for the purposes of incongruent crystal growth, it also subjects the system to large thermal stresses during the growth.

As a crystal grows it tends to have fewer grains, causing energy that is caught up in grain boundaries to be released, and therefore it becomes better able to conduct phonons. If no adjustments are made the temperature of the zone compared to the incident energy increases and the thermal gradient changes. Because of these stresses, a ceramic after-heater can be installed. It is also the reason that post-annealing should be done in most cases. Finally, because of how the growth occurs, there are practical sample diameter and length limits which preclude the growth of large boules and typically optical floating zone machines are used exclusively for the generation of research materials. Commercially, for important single crystal growth a Czochralski or Bridgeman methods of crystal growth are more typical due to this quantity consideration.

2.5 Powder X-ray Diffraction

Powder x-ray diffraction is typically one of the first things that is done before proceeding with the synthesis of a material, and then is generally done at every step along production. This is initially to ensure that the starting material is the expected material and doesn't have any significant impurities. During production it is done to ensure that the material and phase being synthesized are been formed and that it is as pure as possible within our limit of detection.

In a powder measurement a single wavelength of x-rays is selected. This is done by use of monochromators, collimators and absorbing materials. When

Element	$K_{\alpha 1}$	$K_{\alpha 2}$	K_{α} line	K_{β}
Co	1.789010 Å	1.792900 Å	1.790307 Å	1.620830 Å
Cu	1.540598 Å	1.544426 Å	1.541874 Å	1.392250 Å
Mo	0.709319 Å	0.713609 Å	0.710749 Å	0.632305 Å

Table 2.2: X-ray Wavelengths for Selected Anode Materials [85].

x-rays are generated they typically produce a continuum of energies starting with a lower short wavelength cut-off limited by the initial energy input into the system, with no limit to the long wavelength tail. There is a large maximum before the tail with several sharp peaks. The peaks correspond to specific electronic excitations, where the peaks corresponding to 1s-orbital excitations are known as K edges. These occur at the lowest wavelengths, are less susceptible to absorption and are generally generated in higher quantities due to the higher transition probability. 2s and 2p excitations generate L edges, 3s, 3p and 3f generate M edges and so on [83]. Of the K edges, which are typically used in powder x-ray diffraction, the first three peaks are known as $K_{\alpha 1}$, $K_{\alpha 2}$ and K_{β}. Typically the strength of $K_{\alpha 1}$ is double that of $K_{\alpha 2}$ and five times that of K_{β}. The $K_{\alpha 1}$ and $K_{\alpha 2}$ peaks are usually so proximate that they are either hard to filter from each other or turn into a single peak, at which point they are generalized as the K_{α} line. Typical anode materials for the generation of x-rays are copper, cobalt and molybdenum depending on the constituents of target material. In some cases the radiation is actually absorbed by the structures being investigated, as typically happens with copper radiation and biological samples, so generally anode material selection is dependent on the material. Table 2.2 gives typical values for $K_{\alpha 1}$, $K_{\alpha 2}$, the K_{α} line and K_{β} [84].

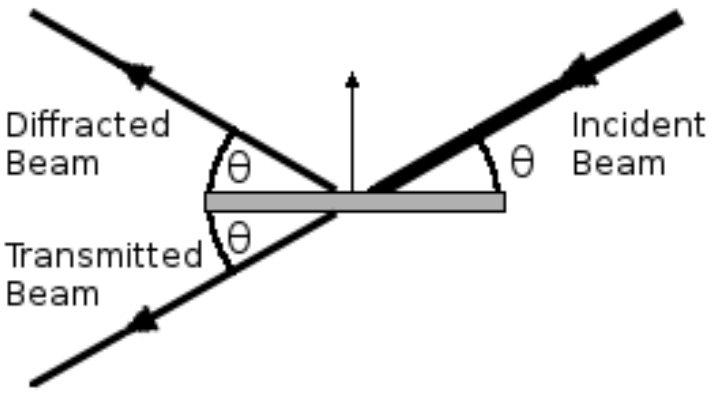

Figure 2.13: A cartoon of the Debye-Scherrer geometry

For powder x-ray diffraction, a Debye-Scherrer geometry is typically used, as shown in figure 2.13. The x-rays are set at an incident angle, θ to the sample, and the detector is placed at a mirrored angle so that the total angle between the source and the detector is 2θ.

A sample used for powder XRD is typically a polycrystalline or ceramic sample, or a single crystal, that has been ground very finely mechanically. This will leave the basic structure intact, but it will also generate a random orientation in every direction. The reason this is done is to reduce the problem of a three-dimensional space into two dimensions. Crushing the crystal destroys the orientation dependence and diffraction would cause a ring of scattering instead of a point of scattering in reciprocal space. These are known as Debye-Scherrer rings. We then observe the system over only one trace of space. This trace, which is a measure of the intensity of scattering against a given value of 2θ, creates a unique fingerprint based on the structure of the material. An example of this type of input was shown in the right panels of the cartoon labeled figure 2.3 for systems with increasingly broken symmetry.

Often when initial patterns are done, especially when quality control is important, a small amount of finely ground silicon powder can be added to the sample. This is because silicon, in the diamond-structure phase, produces a small number of very sharp peaks which are easily identified. In this arrangement it is in a diamond lattice, which is two interpenetrating FCC lattices. Because both atoms are silicon, some of the interference wipes out a significant number of peaks, which explains why this is used. The addition of the silicon powder allows an experimenter to correct 2θ values for instrument error by scaling or shifting a pattern as necessary in plotting or calibration such as DiffracPlus EVA from Bruker by use of a known standard.

The sample itself is generally mounted on a pure slab of single crystal semiconductor grade silicon. This is because this substrate will generate essentially zero-background. A comparison of powder diffraction holders shows that in most metrics this is the optimal method [86]. The sample is adhered to the silicon holder by use of petroleum jelly dissolved in toluene. This mixture is applied to the crystal and the toluene is allowed to evaporate off. This leaves the surface 'sticky'. In addition, petroleum jelly is unlikely to cause a significant background signal, or at least only a small one that would be removed with a simple background subtracting in software, due to its 'liquid-like' and amorphous nature.

It is important to note that the chemical formula matters very little, other than localizing the atoms for diffraction. As an example, figure 2.14 shows three different polymorphs of silicon dioxide. The plot shows the diffraction for crisobalite (space group 9, C1c1), α-quartz (space group 136, $P3_221$) and

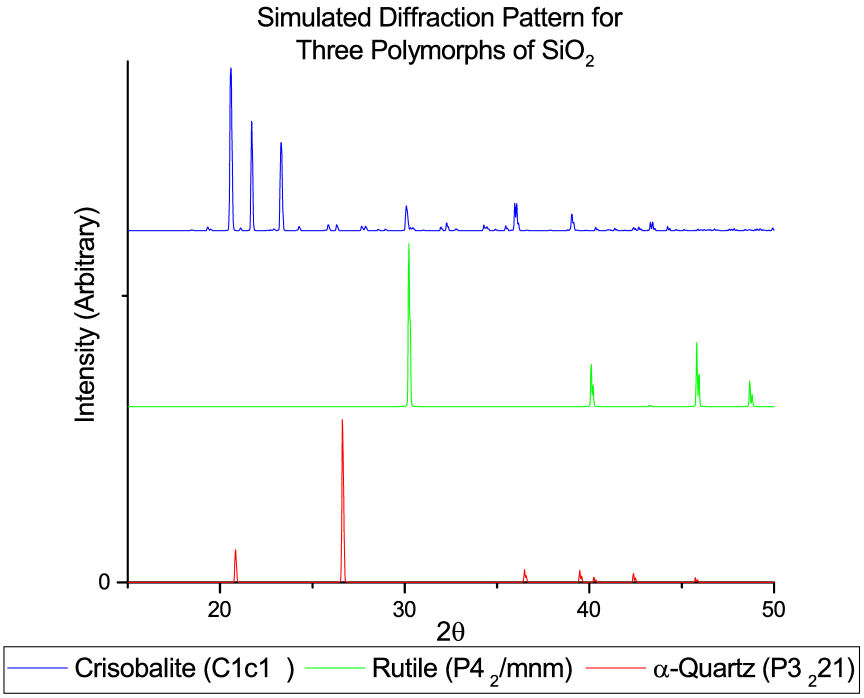

Figure 2.14: X-ray diffraction patterns for three polymorphs of SiO_2. The patterns were simulated using the FullProf Software suite [87] from different crystallographic information files from the inorganic crystal structures database. (Crisobalite [88], α-quartz [89], rutile [90])

rutile (space group 136, $P4_2/mnm$). The difference here is not chemical, but structural, hence we get different patterns for the same element. These structures are shown in figure 2.15. Using databases such as the Inorganic Crystal Structure Database we can look up reference patterns for previously made materials to determine what material we have. Additionally, it is possible to do peak searches to attempt to identify an unknown compound. We can also perform Rietveld refinements using software such as the EdPCR module of FullProf to determine accurate lattice parameters which can assist in assessing quality of a sample as well.

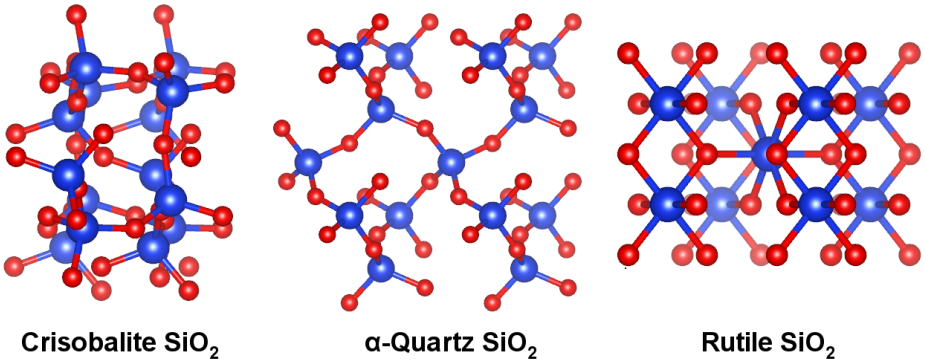

Figure 2.15: Crystal structures of the Crisobalite, α-Quartz and Rutile polymorphs of SiO_2, generated by VESTA. The blue atoms represent silicon and the red atoms represent oxygen. The patterns were generated using VESTA Software [91] from different crystallographic information files from the inorganic crystal structures database. (Crisobalite [88], α-quartz [89], rutile [90])

2.6 Laue Diffraction

Laue diffraction is a sub-type of scattering, which for the purpose of this thesis was done with x-rays, that allows capture of the entirety of reciprocal space in real time. The primary use for Laue diffraction is for the purpose of alignment. Although material identification can be done, it is typically easier and more accurate to do this with powder scattering. Refinement of lattice parameters could be accomplished as well, but again this is far easier with single crystal scattering. For powder x-ray diffraction a single wavelength is used, which allows for the higher level of precision.

For alignment, however, speed is a huge factor and aligning a material within one to three degrees is easily accomplished with a Laue setup. Additionally, the Laue diffractometer is the fastest way to tell if there are multiple crystal grains or growth orientations as the patterns will change abruptly.

Twinning of a crystal can also be seen as twinned Laue patterns. A Laue diffractometer only operates on the surface of the crystal.

A typical Laue x-ray is generated using some form of high-energy rotating anode and cathode. In a normal x-ray setup, filters are applied to the generated x-rays to remove all x-rays except for a specific wavelength. In the case of a copper anode, typically the strong Cu K-α_1 emission. The choice of anode for x-ray scattering depends on the chemical system being probed. In the case of a Laue system, a normalized white beam of x-rays would be preferable. This beam is approximated by filtering out the strongest peaks, such as the Cu K-α_1 and Cu K-α_2 lines. The exiting beam of filtered x-rays is then collimated and made incident on a sample. The x-rays will be subject to Bragg scattering.

Laue diffraction can be done in two different geometries: transmission and reflection. In the transmission setup a white x-ray beam is shone upon a relatively thin piece of single crystal. The beams diffracted by this crystal are captured on a film or 2D multiwire area detector situated behind the crystal. In this case the entire bulk of the crystal is illuminated, with the limitation that increasing the thickness of the crystal will backscatter more and more of the x-rays and give a diminishing signal. As the x-rays diffract each of the maxima will correspond to a given reflection normal to an hkl plane. The diffraction patterns give peaks along the intersection of a plane cut through the Ewald sphere, which will give an elliptical pattern around the F_{000} peak, which is transmission directly through the crystal [92]. Normally this information is discarded for x-ray scattering, since any information is obscured by the beam itself. The exponential term in F_{000} is one, as shown in equation 2.9b, which

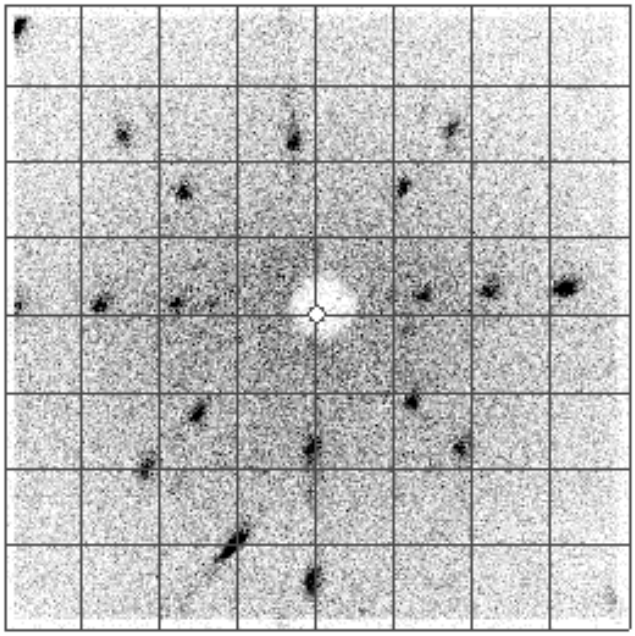

Figure 2.16: A sample Laue transmission diffraction pattern of a cobalt niobate single crystal along [021].

leaves this value equal to the number of electrons in the unit cell (or in the case of 2.9b the atom in question, although this is easily generalized from the derivation above to a unit cell). All other peaks average to zero, which means that the value of F_{000} represents the maximum amplitude for the electron density map, effectively scaling the result [93]. A sample of a transmission image is shown in figure 2.16.

Transmission Laue diffraction is generally considered an obsolete technique, compared to back-scatter Laue [92]. Back-scatter Laue is done using back-scattered x-rays with a 2D multiwire detector located behind the collimated x-ray output. Previously, Guinier cameras would be used to capture the images on films, however the use of a multi-wire detector is faster, in that there are no developing times, and more importantly changes of orientation can be done

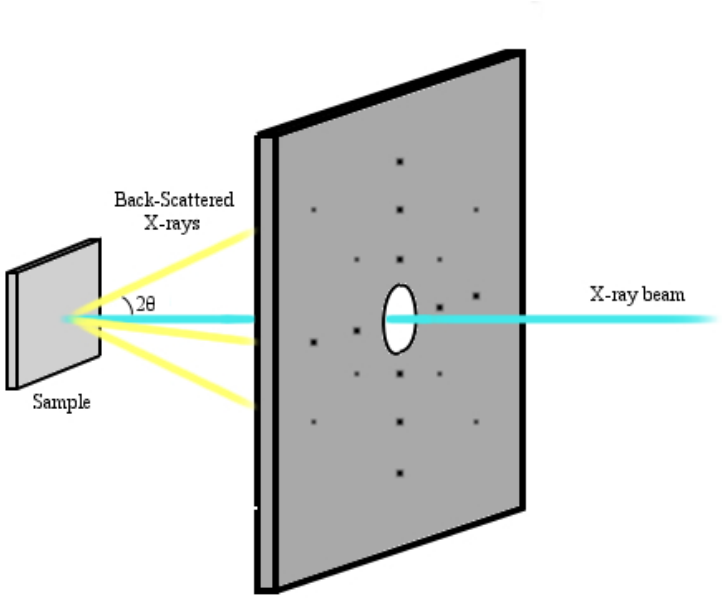

Figure 2.17: A schematic of how Laue backscatter in the reflection geometry works. Adapted from [94].

in real time. Using a back-scatter setup means that there will be a hole where the x-ray collimator is located where the x-ray beam emerges. A larger or smaller volume of reciprocal space can be probed by moving the sample away from or towards the source and detector, respectively. The geometry is shown in figure 2.17.

This technique is only useful for materials that are single crystalline, or nearly so. If you were to load a polycrystalline sample, the diffraction would cause Debye-Scherrer rings (described in section 2.5), instead of Bragg spots to be seen.

The sample is typically mounted on a goniometer, which allows for independent motion of the crystal in three linear dimensions for centering and scanning the length of larger crystals, as well as three rotational dimensions for the ac-

tual alignment. Typically Laue software is setup to use the detected points to match a reciprocal space position to the projections of an Ewald sphere computed using the space group and lattice parameters for the material. By matching these points the position in reciprocal space can be determined and a crystal may be aligned along a specific crystallographic direction.

The reason that this method is so powerful for alignment is that an experimenter can see reciprocal space, and move reciprocal space to align the crystal in real time. Using software, an Ewald sphere with projected Bragg spots can be created based on the known lattice parameters and space group, from which selected points can be fitted for and adjustments can be made with a goniometer. As stated above, a Laue setup will allow precision alignment of a crystal to within 1 to 3°. This is usually sufficient for cutting a crystal, since machining a crystal can really only be done to within the same margin of accuracy. For improved alignment more luminous sources of x-rays or additional techniques like neutron scattering can be done, but pre-aligning within a few degrees in this case is very helpful. The single crystal neutron work done on both $CoNb_2O_6$ and $NiNb_2O_6$ were both first aligned using a Laue, x-ray setup and then re-aligned with neutron scattering. Especially in the case of $NiNb_2O_6$, this pre-alignment with Laue diffraction was important as the peaks of the $NiNb_2O_6$ measured had a FHWM of less than 0.7°. For reference, the silicon standard used for instrument calibration is $\sim$1° FWHM, which gave a nice, if incidental, measure of the quality of the crystal. Peak broadening occurs due to things like dislocations, stacking faults, twinning, microstresses, grain boundaries and chemical heterogeneties [95]. Typically it is assumed that the surface is what is being imaged, since unlike transmission

Laue the beam does not pass through the crystal, and we are looking at the back-scattered, as opposed to the transmitted rays. In reality, some of the bulk will be probed, although the technique is not nominally assumed to be a bulk probe. Probing the bulk is better left to a weaker-interacting probe such as neutrons. In the back-scattering setup the transmitted beam is not being imaged, although that information is lost due to the hole in the detector.

An example of a Laue backscatter image can be seen in figure 5.3 from chapter 5. The instrument used was a MWL110 back-scatter Laue detector from multiwire labs with NorthStar 7 software for visualization and fitting.

2.7 Single Crystal X-Ray Diffraction

All of the mathematical machinery from section 2.3, 2.5 and 2.6 is a starting point for single crystal diffraction. In Laue diffraction, we see the entirety of reciprocal space for a given orientation because we are using a beam of white x-rays. In powder diffraction we see Bragg spots diffracted off in every valid direction, which on an area detector would create rings. Based on the geometry for Bragg-Brentano collection, we get a two dimensional representation cut along 2θ. In the case of single crystal x-ray, we are only illuminating only the Bragg peaks in reciprocal space where reflections at a given [h k l] are satisfied, or where planes satisfy the relation given in equation 2.10a for a given λ.

When performing single crystal x-ray scattering a CCD detector (typically) will capture an image of the diffraction based on a particular orientation of the crystal. The crystal can then be rotated along multiple axes to rotate reciprocal space, with the idea being to capture many Bragg peaks. Because

Lattice	Reflection Condition
Simple	none
Body-Centred	$h+k+l=2n$
Face-Centred	h,k,l all even or odd
Base-Centred (A)	$k+l=2n$
Base-Centred (B)	$h+l=2n$
Base-Centred (C)	$h+k=2n$
Hexagonal	$-h+k+l=3n$
Rhombohedral	$h-k+l=2n$

Table 2.3: A table of expected extinctions due to the structure factor for different types of Bravais lattices [96].

Screw Axis	Reflection Condition	Reflections Involved
2_1	$h,k,\text{or}l=2n$	
$4_2, 6_3$	$l=2n$	$h00$ for axis —— $\hat{a}$
$3_1, 3_2, 6_2, 6_4$	$l=3n$	$0k0$ for axis —— $\hat{b}$
$4_1, 4_3$	$l=4n$	$00l$ for axis —— $\hat{c}$
$6_1, 6_5$	$l=6n$	

Table 2.4: A table of expected extinctions due to the existence of screw axes [96].

we know the rotation we can start to build up the stereoscopic picture of reciprocal space. Unlike a Laue scan, we know the wavelength of the light so we can make the connection to the d-spacing as well. Ideally, what we can then do is take this data and index the reciprocal cell of the lattice based on known peaks and expected extinction peaks. If we are unsure of the space group, the extinction peaks will help to narrow that down, as the structure factor disallows certain reflections for certain crystal structures. The structure factors for each of the types of Bravais lattice can be computed to determine which peaks are expected to be extinct due to the structure of the crystal. These are summarized in tables 2.3, 2.4, and 2.5.

Glide Plane	Reflection Condition	Reflections Involved
a	$h = 2n$	
b	$k = 2n$	$0kl$ for plane $\perp \hat{a}$
c	$l = 2n$	$h0l$ for plane $\perp \hat{b}$
n	$h+k, k+l,$ or $h+l = 2n$	$hk0$ for plane $\perp \hat{c}$
d	$h+k, k+l,$ or $h+l = 4n$	

Table 2.5: A table of expected extinctions due to the existence of glide planes [96]. Note that the list for d-glides is not comprehensive.

The results of the scans can then easily be assessed by computer software to extract peaks, strengths and locations in reciprocal space, and using analysis software this can then be used to refine both the structure of the crystal, meaning the space group, the lattice parameters and the atomic positions, as well as the occupancy factors of those positions. This is data that cannot be obtained as easily from other x-ray scattering techniques. Programs like the EdPCR module of FullProf are able to take data sets from powder and single crystal x-ray and neutron scattering and all the types together to perform a refinement, utilizing the strength of each technique.

2.8 Neutron Scattering

Neutron Scattering is similar in application to x-ray scattering, but with additional advantages. The wavelength of neutrons can be on the order of interatomic spacing, which means that neutrons can be used as an atomic probe in the same manner described for x-rays. Since they are massive particles, especially when compared to photons, their kinetic energy is important, and fortunately, is comparable with that of atoms within a solid. Neutrons interact in different ways than x-rays and electrons do. X-rays and electrons have

Charge	0
Mass	$m_n = 939.565 \frac{Mev}{c^2}$
Spin	$I_n = \frac{1}{2}$
Magnetic Moment	$\mu_{n(magnetic\ moment)} = -1.913\ \mu_{n(Nuclear\ Bohr\ Magneton)} \frac{MHz}{T}$
Mean Lifetime	$\tau_n = 881.5s$ (free neutron)

Table 2.6: Table of Neutron Properties (extracted from [103]).

purely electromagnetic interactions with the electron cloud around an atom. Neutrons are scattered off of the nuclei of atoms, and because they have a nuclear magnetic moment they can scatter from unpaired electrons, from which we can see magnetic and dipole-dipole interactions [97].

2.8.1 Neutron Interaction with Matter

Because x-rays and electrons interact with the electrons within a solid, their penetration depth is typically limited to on the order of ones to hundreds of microns. The depth decreases with increasing atomic number, owing to an increasing density of electrons, with predictable variations across a row of the periodic table. Neutrons, however, penetrate on the order of millimetres to metres, excepting a few elements that strongly absorb neutrons such as boron, cadmium, samarium and gadolinium. With neutrons there is no systemic dependence on the atomic number of a material with respect to its penetration depth. These depths are plotted in figure 2.18. This means that unlike electrons and x-rays, neutrons are probing the bulk properties of the material [98]. That being said, it is possible to do surface measurements using neutrons (neutron reflectometry) [99]. The neutron is a baryon with properties given in table 2.6.

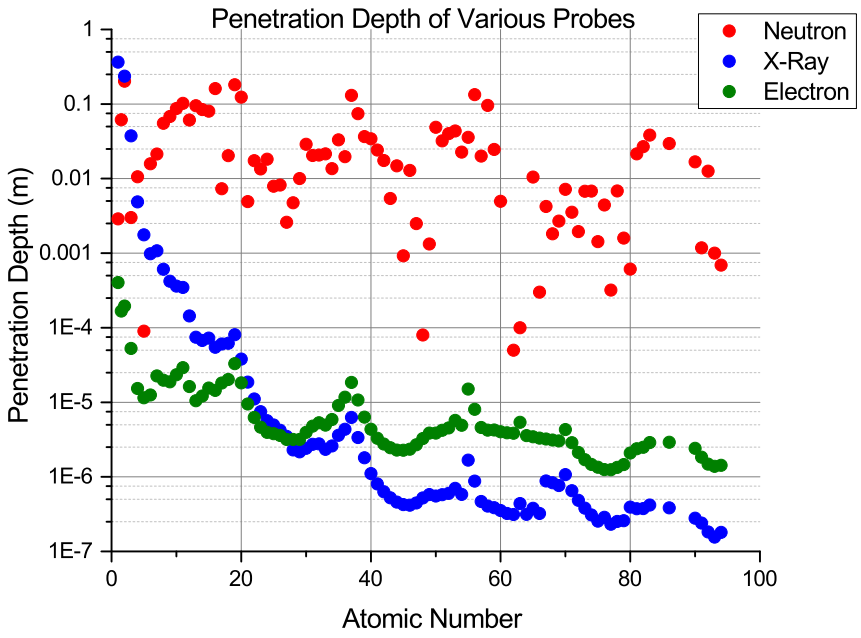

Figure 2.18: The penetration depth of beams of thermal neutrons (λ = 1.8 nm) [100], x-rays (Cu-K_α 8.041 keV, $\lambda = 1.54$Å) [100, 101] and electrons (200 keV, $\lambda = 2.74$ pm) [101, 102] on a log scale based on atomic number.

Neutron scattering can probe a material in several ways. Neutron diffraction is done in the same manner as described in sections 2.5 and 2.7 with the neutron replacing the photon. The geometry is the same but some of the differences, owing to the different interactions, are described below. Additionally, with x-rays we were only really looking at the elastic interactions. Inelastic x-ray scattering is possible [104], but is a new, emerging technique when contrasted to inelastic neutron scattering. Nuclear inelastic scattering allows us to examine the excitations of solids such as phonons (lattice vibrations) and crystal field transitions. Finally, both of these techniques can also be leveraged to include magnetic information such as the magnetic structure (analogous to

the atomic structure and elastic scattering) and the magnetic interactions such as magnons or spin waves (complimentary to the atomic vibrations). Additionally, neutron beams can be polarized to give information regarding vector magnetization as well [105].

Neutrons follow the same rules of scattering for elastic diffraction as was shown in figure 2.5 and in section 2.7. The exception is that the momentum vectors, k_0 and k_1 are now subtended by a scattering vector $\vec{Q}$ which does not have the same 'elastic' requirements of the previous vector $\vec{d}_{hkl}$ because unlike the large majority of photons as defined in x-ray scattering, a neutron can gain and lose energy, so that momentum of the neutron can be gained or lost from or to the lattice. When the vector $\vec{Q}$ meets the same conditions as $\vec{d}_{hkl}$, insofar as there is no energy transferred, this is known as elastic scattering. This type of scattering gives us information about the atomic positions. Otherwise, if energy is gained or lost, this is known as inelastic scattering. This is identical to the terminology used to describe collision models in classical mechanics [106].

To define this more mathematically, we can start with the concept of the neutron scattering cross section (σ, or the total number of neutrons scattered per second) divided by the total number of neutrons incident per cm^2 per second, where the divided term is known as Φ. The quantity of interest is generally $\frac{d\sigma}{d\Omega}$, where Ω represents the solid angle. Given a nucleus at a position $\vec{R}_i$, we get an equivalent incident wave of $e^{i\vec{k}_0 \cdot \vec{R}_i}$. A neutron incident on a nuclei with wave vector $\vec{k_0}$ with λ_0 will be scattered into a new state with wave vector $\vec{k_1}$ with λ_1. The neutron wavelength is typically expressed as in equation 2.11, for energy in meV [107].

$$\lambda = \sqrt{\frac{h^2}{2mE}} = \frac{9.04}{\sqrt{E}}\text{Å [107]} \tag{2.11}$$

The probability of this transition, from $|\vec{k_0}\lambda_0\rangle$ to $|\vec{k_1}\lambda_1\rangle$ is given by Fermi's golden rule, equation 2.12.

$$\sum_{\vec{k_1}} W_{\vec{k_0},\lambda_0\rightarrow\vec{k_1},\lambda_0} = \frac{2\pi}{\hbar}\rho_{\vec{k_1}} |\, \langle \vec{k_1}\lambda_1|\hat{V}\left(\vec{Q}\right)|\vec{k_0}\lambda_0\rangle\,|^2 \text{ [108]} \tag{2.12}$$

In this equation W represents the transition rate, ρ is the density of states and V is the operator representing the interaction potential between a nucleus and the neutron and $\vec{Q} = \vec{k}_1 - \vec{k}_0$ represents the scattering (transfer) vector.

The observed quantity in a neutron scattering experiment is the double differential cross section [108], which can be derived using the Born approximation plus converting the wave functions into an exponential representation, and results in equation 2.13. This cross section represent the number of neutrons scattered per second into solid angle $d\Omega$ with an energy between E and E'.

$$\begin{aligned}\frac{\partial^2\sigma}{\partial\Omega\partial E'} &= \frac{1}{2\pi\hbar}\frac{k_j}{k_i}\sum_{i,j} b_i b_j \int \langle e^{i\left(\vec{k}_0-\vec{k}_1\right)\cdot\left(\vec{R}_i-\vec{R}_j\right)}\rangle e^{i\omega t}dt \\ &= \frac{1}{2\pi\hbar}\frac{k_j}{k_i}\sum_{i,j} b_i b_j \int \langle e^{i\vec{Q}\cdot\left(\vec{R}_i-\vec{R}_j\right)}\rangle e^{i\omega t}dt \text{ [108, 109]}\end{aligned} \tag{2.13}$$

In equation 2.13 the vectors $\vec{R}_i$ and $\vec{R}_j$ are actually quantum mechanical position operators representing the nucleus at $t = 0$, but we can think of them in classical terms for simplicity [98]. Additionally, the terms b_i and b_j were

introduced. These represent the scattering length. The scattering lengths depend on the nuclear isotope, the spin relative to the neutron and the nuclear eigenstate. Generally there is no correlation to the nuclear spin state and its position in a sample. When we evaluate this for the two cases where $i = j$ and $i \neq j$ we arrive at equation 2.14 [109].

$$\begin{aligned}\frac{\partial^2\sigma}{\partial\Omega\partial E'} = &\frac{1}{2\pi\hbar}\frac{k_j}{k_i}\langle b\rangle^2 \sum_{i,j}^{i\neq j}\int \langle e^{i\vec{Q}\cdot\left(\vec{R}_i-\vec{R}_j\right)}\rangle e^{i\omega t}dt \\ &+ \frac{1}{2\pi\hbar}\frac{k_j}{k_i}\langle b^2\rangle \sum_{i}^{i=j}\int \langle e^{i\vec{Q}\cdot\left(\vec{R}_i-\vec{R}_j\right)}\rangle e^{i\omega t}dt \text{ [108, 109]}\end{aligned} \tag{2.14}$$

Mathematically, the coherent scattering cross section will be the scattering that would exist if every element had the same scattering length. Incoherent scattering arises from two of the effects listed in the previous paragraph. The first is that nuclei can have different spin states, so the interaction with the neutron will change depending on which state the nucleus is in. Additionally, different nuclei can have different isotopes, which can also have different spin states. There is, strictly speaking, no correlation between two atomic positions and their spin state or isotopic composition, which again allows us to treat the system using thermodynamic averages, as in the second term of 2.14. Based on that assumption, we can define $\langle b\rangle^2$ and $\langle b^2\rangle$ as in equations 2.15a and 2.15b, where we are looking over 4π steradians.

$$\overline{b_i \cdot b_j} = \langle b\rangle^2 \qquad \text{for } i \neq j \tag{2.15a}$$

$$\overline{b_i \cdot b_j} = \langle b^2 \rangle \qquad \text{for } i = j \text{ [109]} \tag{2.15b}$$

From this assumption, a value for both the coherent and incoherent scattering cross sections can be derived [108] as $\sigma_{coh} = 4\pi\langle b\rangle^2$ and $\sigma_{inc} = 4\pi\left(\langle b^2\rangle - \langle b\rangle^2\right)$. We can therefore rewrite 2.14 as 2.16.

$$\begin{aligned}\frac{\partial^2\sigma}{\partial\Omega\partial E'} &= \frac{1}{8\pi^2\hbar}\frac{k_j}{k_i}\sigma_{coh}\sum_{i,j}^{i\neq j}\int\langle e^{i\vec{Q}\cdot\left(\vec{R}_i-\vec{R}_j\right)}\rangle e^{i\omega t}dt \\ &+ \frac{1}{8\pi^2\hbar}\frac{k_j}{k_i}\sigma_{inc}\sum_{i}^{i=j}\int\langle e^{i\vec{Q}\cdot\left(\vec{R}_i-\vec{R}_j\right)}\rangle e^{i\omega t}dt \\ &= \left(\frac{\partial^2\sigma}{\partial\Omega\partial E'}\right)_{coh} + \left(\frac{\partial^2\sigma}{\partial\Omega\partial E'}\right)_{inc} \text{ [108, 109]}\end{aligned} \tag{2.16}$$

Interpreting this is a physical sense, the coherent scattering is what this system would give if every nuclei was uniform, or had a scattering length equal to $\langle b\rangle$. The incoherent scattering arises from the random distribution of deviations of scattering lengths from the mean. Mathematically this is simply the variance of a random variable.

The cross section is often written in terms of the time-dependent pair-correlation function, G($\vec{R}$,t) and the scattering function, S($\vec{Q}$,ω). The pair-correlation function describes the position of the nuclei in both time and space. An ensemble of N nuclei is described as in equation 2.17.

$$G\left(\vec{R},t\right) = \frac{1}{N}\sum_{i,j}^{N}\langle\delta\{\vec{R}+\vec{R}_i\left(0\right)-\vec{R}_j\left(t\right)\}\rangle \text{ [109]} \tag{2.17}$$

The space Fourier transform of equation 2.17 gives the intermediate scattering function, equation 2.18

$$\begin{aligned} I\left(\vec{Q},t\right) &= \int_{-\infty}^{\infty} G\left(\vec{R},t\right) e^{-i\vec{Q}\cdot\vec{R}} d\vec{R} \\ &= \frac{1}{N}\sum_{i,j}\langle e^{i\vec{Q}\cdot\left[\vec{R}_i(0)-\vec{R}_j(t)\right]}\rangle \text{ [109]} \end{aligned} \tag{2.18}$$

A time Fourier transform of equation 2.18 gives the scattering function, or the dynamic structure factor, which gives the information on the sample state as a function of energy and momentum. This is given in equation 2.19.

$$S\left(\vec{Q},\omega\right) = \frac{1}{2\pi\hbar}\int_{-\infty}^{\infty} I\left(\vec{Q},t\right) e^{-i\omega t} dt \text{ [109]} \tag{2.19}$$

Both the intermediate and dynamic scattering function can be broken into coherent and incoherent components as well, which means we can rewrite equation 2.16 as 2.20.

$$\frac{\partial^2\sigma}{\partial\Omega\partial E'} = \frac{\sigma_{coh}}{4\pi\hbar}\frac{k_j}{k_i} N S_{coh}\left(\vec{Q},\omega\right) + \frac{\sigma_{inc}}{4\pi\hbar}\frac{k_j}{k_i} N S_{coh}\left(\vec{Q},\omega\right) \text{ [109]} \tag{2.20}$$

Elastic, coherent scattering specifically tells us about the equilibrium state of the structure of the material, while inelastic, coherent scattering tells us about the collective motion of the atoms in the lattice; mainly phonons or vibrational waves. Elastic, incoherent scattering is generally not a useful mea-

sure. Because it is uniform in all directions it is generally considered background noise in an experiment. Finally, inelastic, incoherent scattering tells us about the interactions of a neutron with the same atom at different positions at different times, which can give information about atomic diffusion [98, 109].

2.8.2 Magnetic Neutron Scattering

The math defining scattering processes for non-magnetic systems, although slightly different in derivation from x-ray scattering, is essentially the same. The real difference is, as mentioned above, that the neutrons interact with the nucleus instead of with the electron cloud. However, as noted above and in table 2.6, the neutron has a magnetic moment.

Magnetic neutron scattering arises primarily due to the dipole-dipole interaction of the neutron with the magnetic dipole moment of the unpaired electons around a nucleus. We can safely neglect other magnetic scattering factors as they cause an effect that is at least two orders of magnitude smaller [110].

Because the nuclear and magnetic interactions experienced by the neutron are on the same order of magnitude, so too are the corresponding Bragg reflections [98]. This means that the scattering needs to be separated out. Most materials go through magnetic transitions at different temperatures than they go through structural transition, which is a useful way to distinguish between the two types of peaks. Scans above and below a magnetic transition with no structural transition in between them can be used to determine which peaks are magnetic Bragg peaks, and which peaks have additional intensity from magnetic scattering. This is because the structural peaks will vary only by a

slight amount over a typical temperature range as the thermal, vibrational contribution captured in the Debye-Waller term is generally a much smaller effect than the onset of magnetic ordering and the consequential scattering [111]. By subtracting the pre-existing peak prior to the transition we get a very good approximation to the portion of elastic scattering related strictly to the magnetism.

Also, unlike the nuclear scattering case, for magnetic scattering the interaction, due to the fact that it is primarily a dipolar shape, is anisotropic in nature. Therefore the strength of the interaction between the neutron and a magnetic scattering centre depends on the relative orientation of the magnetic moments of the nucleus and the neutron. Because it is dipolar, the neutron only sees the component of the nuclear magnetic moment that is perpendicular to the scattering vector. Because of this anisotropic nature, in single crystals the magnetic and nuclear peaks can be easily separated. This can be done either by changing the orientation or by applying a magnetic field parallel to $\vec{Q}$ [112]. Finally, observing the $\vec{Q}$-dependence of a signal can also tell you whether or not the observed feature is magnetic, as at higher $\vec{Q}$ the magnetic scattering is suppressed off due to the evolution of the magnetic form factor.

Deriving equation 2.14 gave us the scattering function for the nuclear component of any detected signal. We can do a similar derivation from Fermi's golden rule (equation 2.12), but substituting in the electromagnetic potential based on the Zeeman interaction for our $\hat{V}\left(\vec{Q}\right)$ [113] with the one given in equation 2.21, where μ_N is the nuclear magneton, γ_N is the neutron gyromagnetic ratio, $\hat{p}$ is the electron momentum operator, $\hat{s}$ is the electron spin

operator, $\hat{\sigma_n} = 2\hat{s_n}$ is the Pauli spin operator and $\vec{R}$ is the the distance vector measured by the electron and $\hat{R}$ is a unit vector equal to $\frac{\vec{R}}{|\vec{R}|}$.

$$\hat{V}_{mag}\left(\vec{r}\right) = \frac{\mu_0}{2\pi}\gamma_N\mu_n\mu_B\hat{\sigma_n}\cdot\left[\nabla\times\left(\frac{\hat{s}\times R}{|R|^2}\right)+\frac{1}{\hbar}\frac{\hat{p}\times\hat{R}}{|R|^2}\right] \text{ [114]} \tag{2.21}$$

In 2.21 the first term is representative of the field created by the magnetic moment associated with the electron spin angular momentum. The second term is the magnetic moment due to the orbital angular momentum of electronic charges [114]. This substitution gives us equation 2.22 where r_0 is the classical radius of an electron $\left(\frac{\mu_0 e^2}{4\pi m_e}\right)$, α and β are the indexes representing the basis vectors (typically $\hat{x}, \hat{y}, and \hat{z}$), $\delta_{\alpha\beta}$ is the Kronecker delta and $\hat{Q}_\alpha$ represents the operator for the α-component of the time-evolved Fourier transform of the magnetic moments in the system [115].

$$\left(\frac{\partial^2\sigma}{\partial\Omega\partial E'}\right)_{inc} = \frac{1}{\hbar}\frac{k_j}{k_i}\left(\gamma_N r_0 g/2\right)^2|F\left(\vec{Q}\right)|^2 e^{-2W}\sum_{\alpha\beta}\left(\delta_{\alpha\beta}-\hat{Q}_\alpha\hat{Q}_\beta\right)S^{\alpha\beta}\left(\vec{Q},\omega\right) \text{ [115]} \tag{2.22}$$

From this we can see directly that due to the $\sum_{\alpha\beta}\left(\delta_{\alpha\beta}-\hat{Q}_\alpha\hat{Q}_\beta\right)$ term the magnetic cross section is insensitive to any magnetic moments that are not perpendicular to $\vec{Q}$ [115]. Additionally, we can extract a dynamic scattering function, which can be easily added as an additional component to 2.20. The magnetic dynamic scattering function is in equation 2.23.

$$S^{\alpha\beta}\left(\vec{Q},\omega\right) = \frac{1}{2\pi}\sum_{\vec{R}_i,\vec{R}_j} e^{-i\vec{Q}\cdot\left(\vec{R}_i-\vec{R}_j\right)} \int_{-\infty}^{\infty} \langle S^{\alpha}_{\vec{R}_i}(0)\, S^{\beta}_{\vec{R}_j}(t)\rangle e^{-i\omega t} dt \text{ [115]} \quad (2.23)$$

Additionally, because the derivation now depends on the operator described in equation 2.21, a consequence is that as we go to higher values of $\vec{Q}$ the magnetic signal will die off in amplitude because the form factor reduces.

2.8.3 Production of Neutrons

Neutrons are produced in two possible ways: through fission and by spallation. Both of these methods are used in facilities to create sources of neutrons.

Fission takes place in fissile nuclei, which are almost always ^{235}U or ^{239}Pu, when they capture a stray neutron which splits the nucleus into two nearly-equal parts as well as approximately 2 to 3 neutrons of 2 MeV energy, on average, for each fission event. These parts carry on the order of 160 to 170 MeV of kinetic energy. A cartoon of the fission process demonstrates this in figure 2.19. The excess neutrons 'evaporate' from the nuclei of the daughter products. The total energy released from a single fission reaction is approximately 190 MeV, where the remaining 20 to 30 MeV comes from beta decay, gamma wavelength photons and neutrinos. All of the components other than energy lost to neutrinos heats the reactor fuel as well as the surroundings [116]. Most of the neutrons that are emitted do so 'promptly', meaning in a time scale of femtoseconds after the initial decay. Crucially, approximately one in 200 appear a few seconds after the initial decay and are critical to maintaining

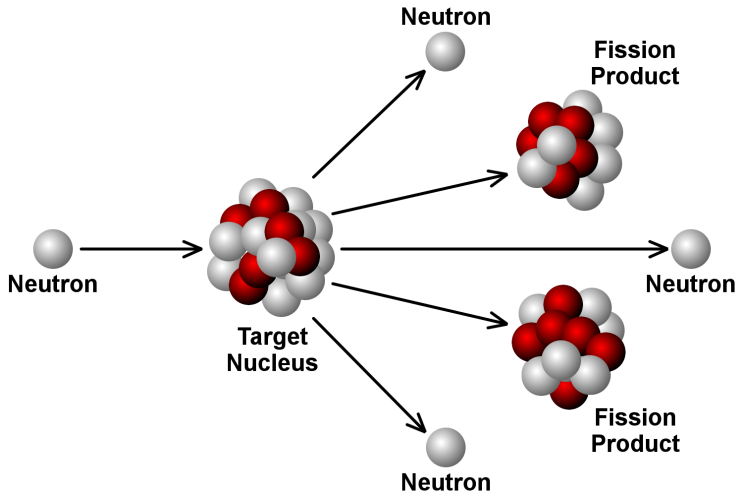

Figure 2.19: A cartoon showing the process of fission. Adapted from [117].

reactor control. From the 2-3 neutrons that are produced, one of the neutrons will continue on to start another fission reaction. Half of the time one of the neutrons will be absorbed either by control rods or some other parasitic process within the reactor. This leaves, on average, one extra neutron from which we can perform useful science, in the context of a fission reactor that is designed for this purpose. These neutrons that emerge are typically "slow" neutrons because they will have collided multiple times before exiting the fuel and surrounding moderator [111]. Because of the way that this process works, and because one reaction breeds the next one in a stoichastic-like process, we get a steady, continuous stream of neutrons from this type of design [117].

Spallation sources rely on a particle accelerator. Spallation refers to a complex sequence of multiple collisions when particles with energies on the order of GeV such as protons, neutrons or pions collide with heavy nuclei. In this scenario a single input particle will produce a yield of neutrons an order of magnitude larger than a single neutron in a fission reactor will. This

allows for spallation sources to be potentially much more luminous a source. The particles that start the collision are accelerated and then collide with a thick target made of dense material such as uranium, tungsten, tantalum or mercury [117]. The particles collide and leave the target nuclei in a highly energetic state, but don't transfer all of their energy in a single collision. It is more likely that they will collide with and excite multiple nuclei. These excited nuclei typically shed the excess energy by evaporating mostly neutrons until enough energy is lost that that decay channel is no longer energetically favourable. They then lose the remaining energy through beta and gamma emission, similar to the fission process described above. The majority of the 20-30 neutrons that emerge are produced by the evaporation channel and have average energies of 2 MeV. This is demonstrated in a cartoon in figure 2.20. A few percent emerge from classical collisions with nuclear particles and are at a much higher energy, typically a Maxwell-like distribution centred on the order of hundreds of MeV. These high-energy neutrons require that spallation sources have much thicker shielding than a fission reactor. Most spallation sources run by using pulses of particles dumped from accelerator storage rings with neutron pulses that have a FWHM of less than 1 μs and are pulsed at frequencies between 10 and 60 Hz [111].

Neutrons that are created come in three 'flavours' based on their energy: hot, thermal and cold. The ranges are identified in table 2.7.

Based on the numbers from table 2.7 regardless of the type of reactor used, the primary reactions coming out are far too energetic to be useful for neutron scattering, so the neutrons require moderation. In slow-neutron facilities,

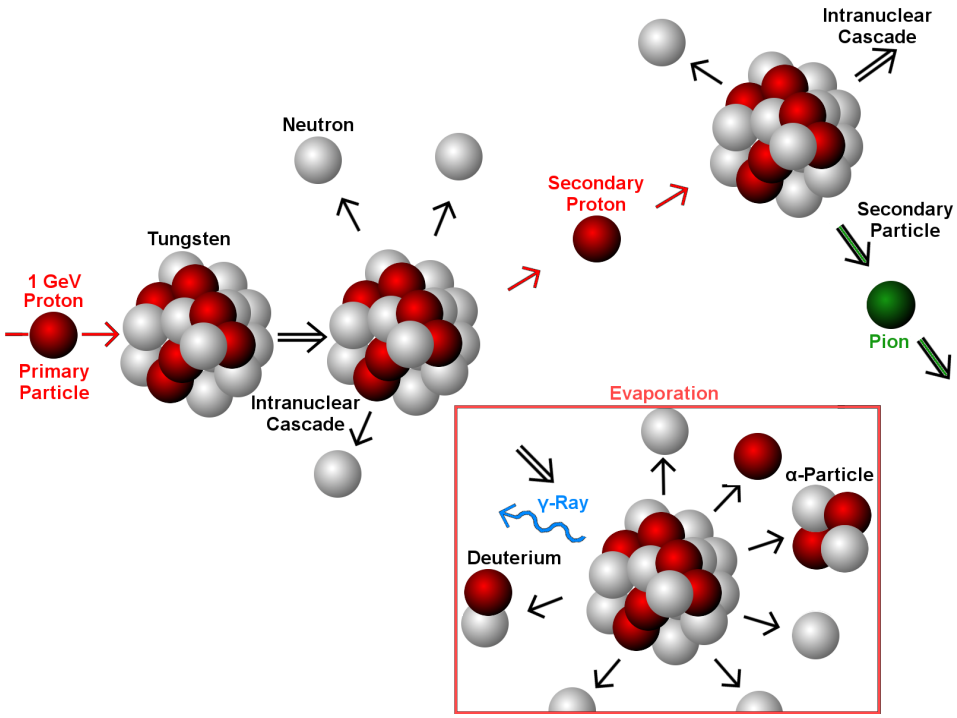

Figure 2.20: A cartoon of the spallation process. Adapted from [117, 118].

Type	Energy (meV)	Temperature (K)	Wavelength (nm)
Cold	0.1 to 10	1 to 120	0.4 to 3
Thermal	5 to 100	60 to 1000	0.1 to 0.4
Hot	100 to 500	1000 to 6000	0.04 to 0.1

Table 2.7: A characterization of neutrons based on the energy that they emerge with or are moderated to [109].

moderators are arranged around the source to slow the neutrons down even further. Typically, for reactor sources, the moderator is a cubic metre volume of beryllium or deuterated water (D_2O). The best materials are those that have light nuclei, which slow down neutrons most effectively, but also with a very low neutron absorption cross section, so that the total number of neutrons is reduced as little as possible by the moderating material. The moderator also gives a chance for neutrons that leak out to be reflected back

to the core before thermalizing, which then have a subsequent opportunity to cause a fission reaction, reducing the fuel usage and amount required to maintain a steady-state reaction. The neutrons collide with moderator atoms and lose momentum until they are thermalized with the moderating material [119]. This creates 'thermal' neutrons.

Cold neutrons are those that have energies that are far less than room temperature provides. This is done by way of a moderator for fast neutrons from a spallation source or thermal neutrons from either type of source that is maintained at a cryogenic temperature. This works the same as the conventional moderator, but gives a lower energy point at which the neutrons would be thermalized with their environment. Typically this moderator is liquid hydrogen (H_2) or deuterium (D_2), or potentially methane (CH_4) for spallation sources [117], at 20 to 30 Kelvin. This increases the intensity of emitted low-energy neutrons [111].

Similar to cold neutrons, hot neutrons follow the same process. The difference is that instead of liquid hydrogen or deuterium the neutrons enter a block of graphite maintained around 2,300 Kelvin, which is heated by the incoming neutrons as well as gamma radiation from the reactor [111]. The only current source of hot neutrons is the ILL in France [117].

Summarizing production by comparing reactors and spallation sources, they each have advantages [117]:

- With respect to energy per neutron, when created at a pulsed spallation source the average energy is around 20 MeV, while at a reactor it is closer to 180 MeV.

- At a spallation source the neutron spectrum is slowed down, which preserves the pulse-like structure. At a reactor we have a stoichastically driven Maxwellian distribution of energies.

- Spallation sources give constant $\frac{\delta\lambda}{\lambda}$ at high neutron energy which gives excellent resolution at large $\vec{Q}$ and E values. In a reactor the resolution can be more easily tailored to experimental requirements, excepting for hot neutrons where monochromators and choppers are typically less effective.

- At a spallation source there is typically a large number of hot neutrons as described above, which similar to the small $\frac{\delta\lambda}{\lambda}$ is better for large values of $\vec{Q}$ and E. A reactor, by contrast, has a large flux of cold neutrons which is better in the case of measuring slow dynamics or large objects.

- A spallation source is inherently low background, due to the pulsed nature, which leads to a high signal to noise ratio. A reactor, however, because it operates continuously can create a pulse rate for time-of-flight instrumentations tailored to different spectrometers, so that each can set its own "pulse" frequency.

- single-pulse style experiments are obviously significantly easier at a pulsed facility, while neutron polarization measurements are significantly simpler at a reactor source.

By considering these factors an experimenter can decide where to go and what spectrometer to use based on the desired results for the type of experiment

and it is why both reactor and spallation sources are both still in development and operation.

2.9 SQUID Magnetometry

A magnetometer is an instrument that measures the magnetic response function of a material. The basis of a SQUID (Superconducing QUantum Interference Device) is a Josephson junction, which is two superconductors separated by an insulating barrier. This effect was predicted by Josephson in 1962 [120] and first observed in 1963 by Anderson and Roswell [121]. The Josephson effect can be expressed simply as the fact that the electrical current density through a weak electric contact between two superconductors depends on the phase difference, $\Delta\phi$, of the two superconducting wave functions. The time derivative of $\Delta\phi$ is correlated with the voltage across this weak contact. In a superconducting ring with one weak contact, $\Delta\phi$, is additionally influenced by the magnetic flux, Φ, through this ring. Therefore, such a structure can be used to convert magnetic flux into an electrical voltage [122]. This allows measurement down to the order of one one-thousandth of a flux quantum, 2.07×10^{-7} G-cm^2 [123].

The SQUID itself is considered the most sensitive device for measuring magnetic fields. The SQUID, however, does not measure the sample in a MPMS. Instead a magnetic sample is moved through a detection coil made of and connected to the SQUID by superconducting wires. The coils are located outside of the sample holder and at the centre of the superconducting magnet that applied the external field. As the sample moves through the coils, owing

to Faraday's laws, an electric current is driven through the detection coils and into the superconducting wires. This closed superconducting loop and the SQUID are inductively coupled. Therefore, any change in flux in the coil creates a current in the loop proportional to the change in flux. The SQUID itself functions as a highly sensitive current-to-voltage detector, so the output of the SQUID's voltage is directly proportional to the magnetic moment of the sample.

The actual SQUID itself can be constructed in one of two ways: a DC- and an RF-SQUID setup. These two methods exploit either the DC or the AC Josephson effect, respectively. In the DC-SQUID there are two Josephson junctions in parallel in a superconducting loop. In the absence of a field a current is split through both branches equally. As a field is applied a screening current is generated to cancel the field, parallel to the current in one branch and antiparallel in the other. When the field causes the current to increase past the critical current in the junction a voltage can be detected. If the field is further increased to more than half the magnetic flux quanta(Φ_0), the system will energetically prefer to allow that within the superconducting loop, at which point the screening current will flip. The sign of this will flip every $\frac{\Phi_0}{2}$ [121]. The change in flux, $\Delta\Phi$ can be estimated as a function of the voltage change, ΔV [124].

The RF-SQUID is comprised of only a single loop and is based on the AC Josephson effect. THE RF-SQUID is coupled inductively to a resonant tank circuit. When the field applied to the SQUID is changed the effective inductance of the tank circuit also changes, which causes a corresponding

change to the resonant frequency of the circuit. The frequency changes can be easily detected and measured, and are a periodic function of the applied magnetic flux, the period being Φ_0 [125]. The measurements in this thesis were done using an RF-SQUID.

For this system to function the sensor needs to be shielded from external fields, which include the superconducting magnet that drives the system. To do so it is shielded by a superconducting shield making use of the Meissner effect. The field itself does not have to be non-zero, but it does have to have very little variation. Inside the shield, the ambient field is the one that was trapped from the last time the system went superconducting.

The detection coil is a simple second-order gradiometer. It is made by creating a single clockwise turn, two counter-clockwise turns and another clockwise turn. Based on this configuration, if you have a uniform field it is expected that any fluctuation in the background field will be equal on both the two clockwise and two counter-clockwise coils which will balance. This is an important design feature as it almost entirely eliminates any background field fluctuations that would otherwise be recorded.

Over long periods of time, large persistent currents can build up. To avoid this having an effect on the system the MPMS heats a small portion of the detection coil whenever the magnetic field is being changed [126].

To generate the large external fields a superconducting magnet made of a large number of turns in a solenoid is used. The important part of this magnet is that it is a closed loop, which means that the magnet can be operated in persistent mode: once the magnet is charged the leads are disconnected and

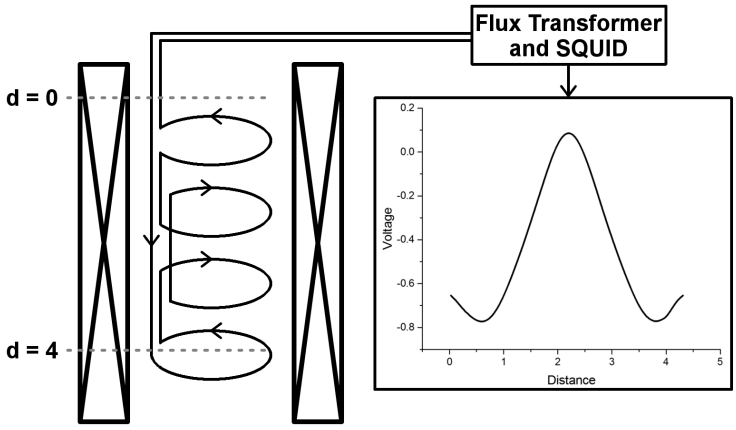

Figure 2.21: A cartoon of an MPMS. 'd' represents the distance travelled by a sample through the coils. The signal plotted is a typical response of the SQUID as a magnetic material is moved from d = 0 cm to d = 4 cm through the pick-up coils. Adapted from [127]

cooled so that the field is as stable as possible and not subject to a driven electric field from an external power source which could be susceptible to "dirty" input power. It is possible for residual field to exist in the wires of the superconducting solenoid once it is closed, creating a non-homogeneous field, especially when going from a high field to a low field. To remove this trapped flux the field can be oscillated from the high value to the negative field, reducing in step each size (such that the third step would be positive and a fraction of the orignal field size) in a process known as degaussing. This reduced the trapped field. To eliminate the trapped field the superconducting magnet would have to be either quenched or warmed up to a point at which the material in the magnet is in a paramagnetic state.

A cartoon of the system with the sample, the second order gradiometer, the SQUID and superconducting magnet and a sample response is shown in figure 2.21. The reason for lobes on the left and right of the main peak is due

to the first and last coils that are counter-wound. The size of these negative lobes is half that of the main peak for obvious reasons when we expect a linear response.

$$\mathrm{B} = \mathrm{H} + 4\pi\mathrm{M}\ [1] \tag{2.24}$$

The output of the MPMS is a plot of the magnetic moment, M, recorded in emu (electromagnetic units) against the variable of interest, usually applied magnetic field in either Oersted, or the temperature in Kelvin. The measurements are done in CGS units, magnetically the basis for which are found in equation 2.24. In this frame B is the net local field, H is the static field applied by the superconducting magnet, and M is the field that changes the local field(B) within the coils when the sample is moved through it. Therefore, from Faraday's law, the current induced in the superconducting loop connected to the SQUID is directly proportional to the total magnetic moment of the sample. The magnetic susceptibility, χ, scales the moment by the magnetic field. The equation for temperature-dependent susceptibility is given in equation 2.25a. For field field-dependent susceptibility, converted to Bohr magnetons per atom, it is in equation 2.25b. In these equations M is the molar mass of the material, m is the mass of the material and μ_B is the Bohr Magneton ($9.274 \times 10^{-24} \frac{\mathrm{J}}{\mathrm{T}}$)

$$\chi_\rho \left[\frac{\mathrm{emu}}{\mathrm{mol}}\right] = \frac{\mathrm{M}\,[\mathrm{emu}] \cdot M\,[\mathrm{g/mol}]}{\mathrm{H}\,[\mathrm{Oe}] \cdot m\,[\mathrm{g}]} \tag{2.25a}$$

$$\chi_{\mathrm{mol}} \left[\frac{\mu_B}{\mathrm{atom}}\right] = \frac{\mathrm{M}\,[\mathrm{emu}] \cdot M\,[\mathrm{g/mol}]}{5585\,[\mathrm{emu \cdot atom}/\mu_B \cdot \mathrm{mol}] \cdot m\,[\mathrm{g}]} \tag{2.25b}$$

$$1\frac{\mu_B}{\text{atom}} = 5585\frac{\text{emu}}{\text{mol}}\ [18] \tag{2.25c}$$

2.10 Heat Capacity

The specific heat of a material, c, is an intensive variable of a material that relates the heat per unit mass supplied to the material as a result of an absolute temperature change of the system itself. The mathematical expression for this is given in equation 2.26a. Heat capacity, denoted typically as C, is the amount of heat needed, dQ to raise the temperature of the material by a unit of temperature, dT in a constrained system, or is the specific heat multiplied by the number of atoms in the system. Typical constraints are constant pressure or constant volume within the system. Heat capacity goes to zero as temperature goes to zero. This means at low temperatures a very small amount of heat will change the system by a large amount. Typically heat capacity measurements are done at constant pressure, as maintaining constant volume is experimentally difficult. The equation governing heat capacity is given in equation 2.26b. Heat capacity is an extensive variable, since it does depend on the size of the system.

$$c_x = \frac{1}{n}\left[\frac{dQ}{dT}\right]_x ; x \in p, V \tag{2.26a}$$

$$C_x = \left[\frac{dQ}{dT}\right]_x ; x \in p, V\ [4] \tag{2.26b}$$

Specific heat as a function of constant pressure is always larger than specific heat as a function of constant volume because c_V does not take thermal expansion into consideration.

At high temperatures c_V of a crystal is almost entirely due to the contribution of phonons, which is well approximated by the Dulong-Petit law, $c_V = 3\frac{R}{m}$ where R is the ideal gas constant [128]. The Debye model gives a slightly more detailed result that at high temperatures approximates this, validating the early model. At low temperature other effects start becoming important and the Dulong-Petit model breaks down. In equation **??** c_{ph} represents the phonon heat capacity,

One such effect is that the electronic contribution starts to become important. This was derived by Sommerfeld when he applied Fermi-Dirac statistics to free electrons in metals. He determined that there is a linear dependence of temperature for the electronic specific heat, which when compared to the phonon contribution can be considered to have little impact until very low temperatures, since the electronic dependence is linear, while the phonon contribnution is cubic. The electron contribution is given in equation 2.27, where γ is the Sommerfeld coefficient, which is a material-dependent co-efficient of the order of $\frac{\mathrm{mJ}}{\mathrm{mol}\cdot\mathrm{K}}$. N_A is Avogadro's constant, E_F is the Fermi Energy and k_B is the Boltzmann constant.

$$c_e\left(T\right) = \frac{\pi^2}{2}\frac{N_A}{E_F}k_B^2 T = \gamma \cdot T \text{ [3]} \tag{2.27}$$

Thus for a metal, we can usually approximate the specific heat as a sum of these two terms, as in equation 2.28. Typically values are plotted $\frac{c}{T}$ versus T^2, where θ_D is the Debye Temperature, the highest temperature at which you can have a single normal vibration through the crystal lattice.

$$c\,(T) = \gamma \cdot T + \frac{1944r}{\theta_D^3} \cdot T^3 \text{ [129]} \tag{2.28}$$

From the above, it can be seen that specific heat, at least in the case of conductors, is entirely monotonic, but this is not the case when we get to a phase boundary. Given that we usually, for example, hold temperature and pressure constant, the Gibbs free energy, $G = H - TS$ must not change under these conditions. However, the Ehrenfest theorem states that an ith order phase transition is characterized by a discontinuity of the ith derivative of G, with all other derivatives being continuous [130]. In practicality this implies a first or second order phase transition although higher derivatives are possible [129], and due to this a second order transition is sometimes referred to as an nth order transition [12].

A first order transition is characterized by a discontinuity in the first derivative of the Gibbs free energy, being the entropy, $S = -\frac{\partial G}{\partial T}_T$, and the volume, $V = -\frac{\partial G}{\partial p}_T$, while the heat capacity, $c_p = T\frac{\partial S}{\partial T}_p$, goes to infinity. As the temperature approaches the transition point there is no evidence that this discontinuity is going to occur. Such first order phase transitions are commonly seen as melting, vapourization or sublimation and are characterized as having a latent heat capacity component at the transition temperature, meaning that

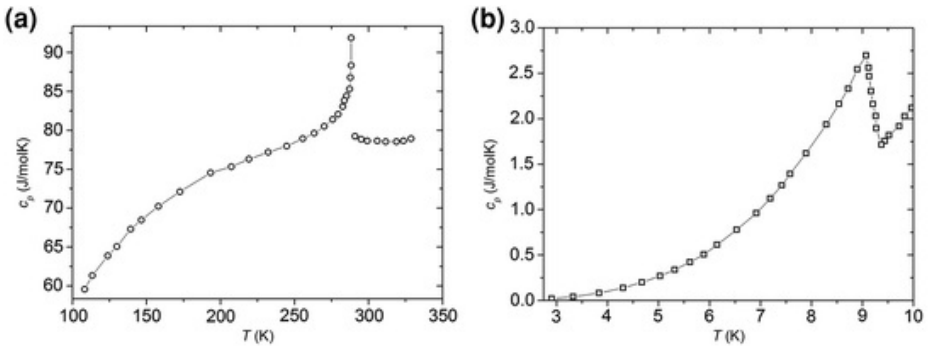

Figure 2.22: Examples of: **a** first-order phase-transition in SbSI from Ref. [63], **b** second-order phase-transition in Nb from Ref. [64]. "Thermal Properties of Solids at Room and Cryogenic Temperatures, Heat Capacity, 2014, 15, G. Ventura and M. Perfetti, (©Springer Science+Business Media Dordrecht 2014) With permission of Springer" [129]. (Note, figure references in caption refer to the original references per copyright requirements.)

the addition of heat does not change the temperature of the material, hence c_p going to infinity.

A second order phase transition exists when the entropy, volume, temperature, pressure and Gibbs free energy all remain constant, but the specific heat, the coefficient of volume expansion, β, and the isothermal compressibility, ζ_T, show changes. This implies that the first derivative of G must be continuous while the second derivative is not. The definitions of these two variables are: $\beta = \frac{1}{V}\left(\frac{\partial V}{\partial T}\right)_p$ and $\zeta_T = -\frac{1}{V}\left(\frac{\partial V}{\partial p}\right)_T$ [74, 129]. The second order transition arises from either a divergence or a discontinuity in the second order derivatives listed above. If all derivatives change in this manner, producing infinite changes in C_p, β and ξ_T, then the second order transition will exhibit an λ-anomaly [129]. Figure 2.22 gives an example of a first order (panel a) and a second order (panel b) transition as seen through specific heat measurements. The second order transition is one where a λ-anomaly is not present.

There is one other kind of transition, a λ anomaly. In solids, this is usual seen in order-disorder transition, the onset of molecular rotation and the ordering of axes of molecular rotations. This can be due to either cooperative interactions (strong interactions between particles) or non-cooperative interactions (particles changing energy states independently). Of importance to this thesis are the cooperative interactions that result from magnetic spin alignment [129].

The reason for this is the fact that if a material has atoms that can be temporarily or permanently magnetized, we need to add a MdH term to our heat capacity, as in equation 2.29.

$$dQ = T \cdot dS = dE + p \cdot dV + M \cdot dH \text{ [129]} \tag{2.29}$$

Normally $p \cdot dV$ can be neglected as it is generally orders of magnitude smaller than the magnetism term, so we can write equivalent Maxwell relations for the specific heat at constant field and magnetizations as equations 2.30a and 2.30b.

$$C_H = \left(\frac{dQ}{dT}\right)_H = T\left(\frac{dS}{dT}\right)_H \tag{2.30a}$$

$$C_M = \left(\frac{dQ}{dT}\right)_M = T\left(\frac{dS}{dT}\right)_M \text{ [129]} \tag{2.30b}$$

All magnetic behaviours except for diamagnetism and Pauli paramagnetism influence specific heat. This is because those two types of magnetism are temperature independent by their nature, so they cannot contribute [131].

A magnetic peak can be suppressed due to the application of a strong field. In the case where the applied field starts to exceed the strength of the ferromagnetic or antiferromagnetic interactions between the atoms we can get a metamagnetic transition [132].

Specific heat is measured by taking a, preferably small, single crystal sample in an isothermal heat bath and adding a small amount of thermal power. Under adiabatic conditions, it is expected that the sample heating can be described by equation 2.31a. The importance of the small sample size is so that there can be the largest change for the smallest amount of thermal power input and that this will allow for the fastest relaxation. Since heat capacity is proportional to mass, its key difference from specific heat, less sample will take less time to heat and to thermalize with the bath. Given power applied from time t_0 to time t, we input an amount of heat Q into the system. The relationship to the heat capacity is given in equation 2.31b. Therefore, if we measure $T - T_0$, the temperature change from the peak at the input power back to thermalization with the external bath as heat is transferred out, and if we know the heat, Q, that we have input into the system as well as the amount of time it takes to thermalize (which is an exponential decay based on Newton's laws of cooling) then we can determine $C_S(T)$ [129]. This is the principle by which most devices that measure heat capacity, including the ExaLab, operate.

$$P(t)\,dt = C_S(T)\,dT \tag{2.31a}$$

$$\int_{t_0}^{t} P(t)\,dt = Q = \int_{T_0}^{T} C_S(T)\,dT \text{ [129]} \tag{2.31b}$$

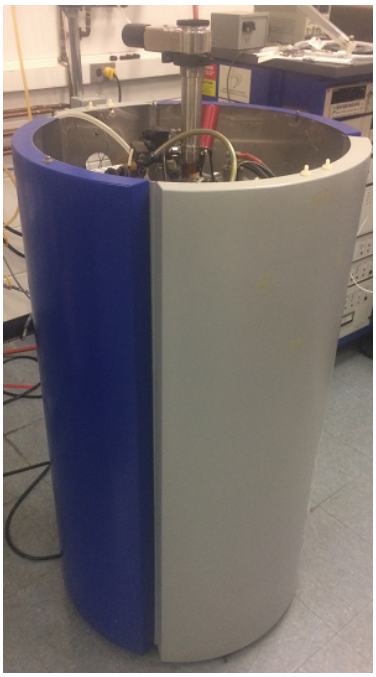

Figure 2.23: The ExaLab dewer. The loading port for the sample holder and sample is visible on the top of the dewer.

Determining this change is known as calorimetry, invented by Joseph Black in the 18$^{\text{th}}$ century [133]. A calorimeter is any device which measures heat and the rate of heat exchange. The most common, and most accurate type of measurement comes from doing adiabatic calorimetry pioneered by Nernst in the early 20$^{\text{th}}$ century [134]. Its power comes from the simplicity of the measurement, based on the definition of heat capacity: The rate of change of heat with temperature change as that change goes to zero, summed up in equation 2.32.

$$C_p = \lim_{\Delta T \to 0} \left(\frac{\Delta Q}{\Delta T} \right)_p \text{ [129]} \tag{2.32}$$

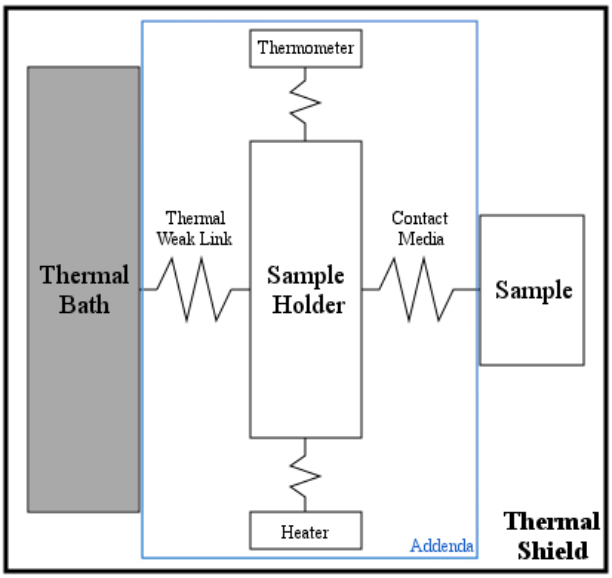

Figure 2.24: A cartoon of thermal linking in a mounting system for calorimetry. Adapted from [129]. Note that there can also be a sample thermometer and a sample heater wired directly to the sample in some systems. They are not shown here.

Of the types of specific heat measurements done, the one that is representative of this work is Heat Pulse Calorimetry. The type that the ExaLab performs is not strictly adiabatic, as the sample is connected to the thermal bath by a weak link. An image of the ExaLab system is shown in figure 2.23. The sample is placed on a thermally well-conducting substrate, a plate of single crystal sapphire, mounted with Apiezon N grease. Both of these have heat capacities, however they are known and this addenda can be subtracted. A cartoon of how this set-up works is given in figure 2.24. The resistance icons on the figure 2.24 refer to different thermal resistances of the thermal links between components of the system.

The way heat pulse calorimetry works is as follows: The sample sits in a heat bath, and a known pulse of heat, ΔQ, is applied by an electric heater

The temperature rises, and then decays back to the temperature of the thermal bath to its original temperature exponentially following Newton's laws of cooling with a time constant of $\tau = R_T C$, where R_T is the thermal resistance of the link between the sample and the heat bath and C is the total heat capacity of the sample plus the addenda. In this case several measurements are taken of the time, so ΔT can also take the size of intermediate steps back to the original temperature. This curve can be fit to an exponential, or in the case where there is a large difference between the spin-spin and spin-lattice contributions an associated exponential [17].

2.11 Muon Spin Rotation and Relaxation

μSR is a generic term that typically encompasses multiple measurement techniques involving muons to measure internal properties and generally is considered to stand for muon spin relaxation, rotation and resonance. The first two are the important portions for this thesis.

2.11.1 Production of Muons

μSR uses muons, an unstable elementary particle, generated in such a fashion as to be spin-polarized to measure internal magnetic fields within matter by means of the spin precession of muons implanted into an experimental sample. The reason that muons are useful is first that they can be generated in this spin-polarized fashion: the most common decay channel for pions, or π-mesons, is to decay into a neutrino and an anti-muon(μ^+) as in equation 2.33. Due to the nature of neutrinos, which can only exist with a specific handedness, any

generated anti-muons violate parity because they uniformly have the opposite handedness due to conservation of angular momentum. Additionally, the decay of a pion into a neutrino and an anti-muon is a two-body process, so when a pion decays at rest due to conservation of momentum the energy of the emitted muon is also known, shown in equation 2.34.

$$\pi^+ \rightarrow \overline{\mu}^+ + \nu_m \qquad\qquad \pi^+ \rightarrow \mu^+ + \overline{\nu}_m \text{ [135]} \tag{2.33}$$

$$\begin{gathered} \sqrt{m_\pi^2 c^4 + p_\pi^2 c^2} = \sqrt{m_\mu^2 c^4 + p_\mu^2 c^2} + \sqrt{m_\nu^2 c^4 + p_\nu^2 c^2} \\ p_\pi = 0, p_\nu = -p_\mu, m_\nu \simeq 0 \\ \therefore m_\pi = 139.57 \frac{MeV}{c^2} \text{ [135]} \end{gathered} \tag{2.34}$$

The muon energy can then be determined, using equation 2.35.

$$E_k = \sqrt{m/_\mu^2 c^4 + p_\mu^2 c^2} - m_\mu c^2 = 4.119 \frac{MeV}{c^2} \text{ [135]} \tag{2.35}$$

The muon decays by emitting a positron preferentially in the direction of its spin. Muons themselves can be detected by a thin muon counter entering the sample space, at which point they precess in the local, internal magnetic field. The muon then decays in a three body process; in the case of an anti-muon into a neutrino, an anti-neutrino and a positron. The direction of decay of the positron is preferentially in the direction of the muon spin. This is shown in figure 2.25. The decay into a positron is captured by a positron detector, and knowing the time at which the muon entered the sample space, the time at

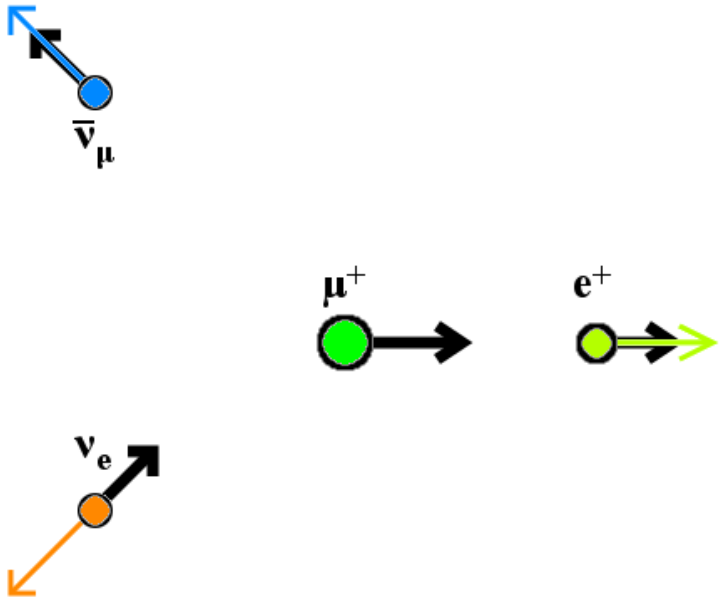

Figure 2.25: Cartoon of a muon decay into a positron, electron neutrino and muon antineutrino. Adapted from [137].

Charge	± 1
Mass	$m_\mu = 0.1126, m_p = 206.7684(6), m_e = 105.65849(4)\frac{\text{MeV}}{\text{c}^2}$
Spin	$I_\mu = \frac{1}{2}$
Gyromagnetic Ratio	$\frac{\gamma_\mu}{2\pi} = 135.53875(6)\frac{\text{MHz}}{\text{T}}$
Mean Lifetime	$\tau_{\mu^+} = 2.19703(4)\mu s$
Surface Muon Energy	$E_{\mu^+} = 4.12\text{MeV}$
Surface Muon Momentum	$p_{\mu^+} = 29.8\text{MeVc}$

Table 2.8: Table of Muon Properties [138, 139].

which the positron is detected and the detector upon which the positron was detected you can build an ensemble of counts that can determine the internal field. A significant difference between using μSR compared to both the x-ray and neutron techniques discussed in this chapter is that muons do not use scattering processes to determine information about the system [136].

The muon is a lepton with properties given in table 2.8.

To produce intense muon beams, the simplest method is to use the decay written as equation 2.33.

In the laboratory, pions can be created by causing high energy (> 500 MeV) protons to collide, preferably with a low-Z material (low atomic number) such as carbon or beryllium. This proton-proton collision results in a pion, a proton and a neutron per equation 2.36.

$$p + p, n \rightarrow \pi^{+} + n + p, n \tag{2.36}$$

In this equation a high energy proton collides with the second particle, either a proton or a neutron, and the proton making the collision decays into a neutron, bouncing back the second particle at a lower energy and emitting a pion along the same momentum vector [140].

2.11.2 μSR Theory

When muons are incident on a sample, they come to rest typically through Coulomb scattering. This is because the initial energy of the muon is on the order of a few MeV, which is huge compared to the electrons it collides with, which are typically at a few eV if in the valence shell or a few hundred keV if in the inner shells of heavy elements [140]. In the range of 0.1 to 500 MeV, the stopping power is dependent on the Bethe-Bloch equation [141], equation 2.37, where the stopping power, -$\frac{dE}{dx}$ tells us that the necessary material density to stop muons is approximately 150 $\frac{mg}{cm^2}$ which equates to a penetration

between 0.1 and 1 mm for an average sample used in condensed matter physics experiments [137].

$$-\frac{dE}{dx} = Kz^2\frac{Z}{A}\frac{1}{\beta}\left[\frac{1}{2}\ln\frac{2m_e c^2\beta^2\gamma^2 T_{max}}{I^2} - \beta^2 - \frac{\delta}{2}\right] \text{ [141]} \tag{2.37}$$

During this process muons leave a wake of electrons and ions behind them. However, once the muon energy is below the ionization threshold they can generally still travel a long distance from the area that they have disturbed by the time they thermalize with their environment, so in most circumstances the perturbations that they have made to the system can be ignored.

Typically, muons end up at interstitial sites in crystals. The spin dynamics in this case depends highly on whether the muon sits at a coherent or incoherent spin state. Within the materials we get coherent spin states when the muon localizes at an interstitial site in a magnetically ordered environment where it can experience hyperfine and dipolar couplings, in the case of most condensed matter systems. Incoherent spin environments occur when the magnetic moments of the local electrons fluctuate rapidly on the time-scale of the muon spin dynamics. In a condensed matter sense, this is a paramagnetic state. In metals with free elctrons we have the Fermi liquid characterized by Pauli paramagnetism. In this case the electron charge screening and spin dependent scattering in the electron liquid prevents the formation of a bound state for the muon. At high magnetic fields a Knight shift can be observed for metals. Additionally, a disordered state would be seen above the magnetic ordering temperature of a material and is a second example of an incoherent spin environment [140].

In most materials, there exists a number of distinct stopping sites for muons to stop at, each with a different probability of stopping. These can exist potentially due to distinct interstitial sites due to crystal symmetries, or due to sites with different electronic configurations, such as in intrinsic semiconductors. This generally leads to inequivalent sites with different dipolar fields. We account for this by measuring the asymmetry of each site.

An asymmetry is generated by comparing the time and direction that a muon was incident on a sample, done by detecting the muon entering through a thin muon counter scintillator in the case of a continuous muon source or based on the time a pulse was generated in a pulsed muon source, and the time that its radioactive decay product, a positron, as well as the detector it was counted in. By building up a profile of thousands to millions of these interactions we can determine information about the internal magnetic field.

Because the decay is a three-body process, and because neither neutrinos nor antineutrinos are easily detectable, there is a level of uncertainty as to the direction that the positron is emitted from the muon decay. The positron is therefore only preferentially emitted in the direction of that the muon was pointed [142]. This can be seen in the following derivation [138, 143].

$$d^2W = W(\theta,\epsilon)\, d\epsilon\; d(\cos\theta)$$
$$= \frac{G^2 m_\mu^5}{192\cdot\pi^3} \times (3-2\epsilon)\,\epsilon^2 \left[a + \frac{(2\epsilon-1)}{3-2\epsilon}\cos\theta\right]\; d\epsilon\; d(\cos\theta)$$

Integrating over $\cos\theta$

$$dW(\epsilon) = W(\epsilon)\;\; d\epsilon = \frac{2\,(3-2\epsilon)\,\epsilon^2}{\tau_\mu}\;\; [138,\, 143]$$

where	W			is the decay distribution of the positron
	τ_μ	=	$\frac{192\cdot\pi^3}{G^2 m_\mu^5}$	Average muon lifetime (2.19698 μs)
	G_μ	=	1.16637×10^{-5} GeV^{-2}	Fermi electroweak coupling constant
	m_μ	=	105.658 MeV	Muon rest mass
	A(ϵ)	=	$\frac{2\epsilon-1}{3-2\epsilon}\times$ P	Asymmetry factor for a given polarization
	ϵ	=	$\frac{E}{E_{max}}$	
	E_{max}	=	52.83 MeV	Maximum energy of a decay positron
	θ			Angle between the muon spin and the direction of positron emission

The result is shown diagrammatically in figure 2.26. In this figure, the probability of positron emission when a muon decays with its spin in the direction represented by the arrow. The red circle is an average over all positron emissions at all energies, while the blue cardioid represents the scenario of positrons emitted at the maximum energy, which is the likely case and what is selected for in μSR. The angular distribution of positrons can be rewritten from the above derivation more simply as in equation 2.38 [144].

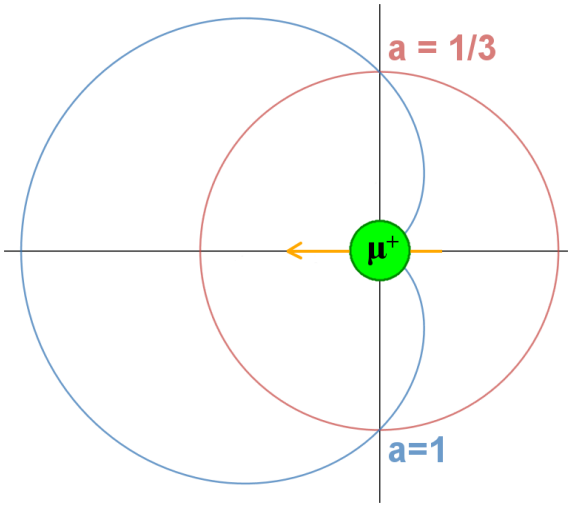

Figure 2.26: A cartoon of the decay probability of a muon based on its direction of spin, or polarization vector $P(t)$. The red circle represents positrons at all energies. The blue cardioid represents the positrons emitted at maximum energy, which is what is expected in the decay process. Adapted from [144].

$$W(E,\theta) = 1 + a(E)\cos\theta \text{ [144]} \tag{2.38}$$

By doing a large count, we will get, on average, a robust measurement of the muon decay captured into scintillators positioned around the sample. In the case of a continuous source, the system is electronically gated so that a single muon is assumed to be in the system at any given time. A timeout window is given to watch for the decays, typically on the order of 5 to 6 muon lifetimes. Because this is a radioactive process, after 5 lifetimes 99.3% of muons will have decayed. In the case of 6 lifetimes it is 99.8%. Additionally, the system maintains a watch for any extra decays due to additional muons that have arrived 'early' from the continuous source or created by other sources muons. In a pulsed source all muons are counted and all decays are recorded since

they all have an identical 'start' time and one or two extra muons is, at worst, a rounding error because of the large number of incident muons and will be lost as noise.

In a system which we described above as having a coherent spin state for the muon to observe what we will get is the muons thermalizing to rest in relatively identical processes as described above and then sitting at one of the interstitial sites. The muon will then begin to precess in the local field. This means that there will be a frequency at which the muons move in one rotation to the next so that the vector that it decays upon will be pointed in the same direction. In either the case of a continuous or pulsed source, because of the defined timing we can be confident in the initial polarization vector of the muon, $P(0)$, and from that we can try to determine $P(\mathrm{t})$. The polarization function is site-dependent, since it is related directly to the strength of the local field. For the j^{th} site we have a polarization function $P_j(\mathrm{t})$. We can determine this polarization function by recording the number of decay positrons, $N_j(\mathrm{t})$, by recording the time of their decay compared to the time the muon counter was triggered or the time when the pulse was generated via equation 2.39 [17]. We can then rewrite the polarization function as equation 2.40 [17].

$$N_j(t) = N_i^0 e^{-t/\tau_\mu}\left[1 + A_j^0 P_j(t)\right] + B_i^0 \text{ [138]} \tag{2.39}$$

where N_i^0 is a normalization constant

A_i^0 is the maximum precession amplitude, or the intrinsic asymmetry of the positron detector

$P_j(t)$ is the time evolution of the muon spin polarization function (equation 2.40)

$$P_j(t) = \cos(\omega_\mu t + \theta_i) \text{ [138]} \tag{2.40}$$

where θ_j is the initial phase of the muon spin polarization vector.

The initial phase θ_j is due to stray fields in flight from the point where the muon scintillator is triggered to the point of deposition in a sample. This phase is dependent on the size of the applied field between the thin muon window and the sample, and in most cases be constant. During thermalization muons lose their kinetic energy through electrostatic interactions with the material. This does not generally change the muon polarization vector/the spin of the muon [145]. The signal to noise ratio of a μSR experiment is typically proportional to $A_j^0\sqrt{N_j^0}$ [146].

It is important to note that equation 2.39 is applicable to each scintillator, and that the values of A^0 and B^0 are dependent on the construction and alignment of each of the scintillators relative to the sample. For the case of an opposing counter, equation 2.39 should have an amplitude that mirrors the middle term, in that $\left[1 + A_j^0 P_j(t)\right]$ will correspond to $\left[1 - A_{\bar{j}}^0 P_{\bar{j}}(t)\right]$.

If we take a pair of counters, forward (N_F) and backwards (N_B), we can determine a total asymmetry of the counts for the pairs.

$$N_F(t) = N_F^0 e^{(-t/\tau_\mu)} [1 + A_F(t) P_z(t)] \tag{2.41}$$

$$N_B(t) = N_B^0 e^{(-t/\tau_\mu)} [1 - A_B(t) P_z(t)] \tag{2.42}$$

$$A_F(0) P_z(t) = \frac{\alpha N_F(t) - N_B(t)}{\alpha\beta N_F(t) + N_B(t)} \text{ [147]} \tag{2.43}$$

$$\text{where} \quad \alpha = \frac{N_B^0}{N_F^0}$$
$$\beta = \frac{A_B}{A_F}$$

Equation 2.43 has two special parameters, α and β. These are correction factors. α corrects for the difference in solid angle that each of the detectors are exposed to. This is especially important in forward-backward pairs, since the forward counter will typically have a large hole in the centre to allow the muons to be incident on them. Additionally, α also relates the detection efficiency of the two counters, as well as parameters relating to beam intensity and delivery. Typically, α is fit by applying a weak field transverse to the detectors in the range of 20 to 100 gauss. When this asymmetry is fit to the known field alpha is simply a fitting parameter and can then be applied to other data.

β is the "asymmetry ratio", and is related to construction and efficiency differences between the two counters. Typically, this value is assumed to be 1 and not fit in normal circumstances [147].

As mentioned above, we can have multiple, inequivalent sites that muons can sit at. This turns out to be a mathematically simple thing to do, since we can treat each precessing component independently. Each inequivalent site

should have a different local magnetic environment, and a certain percentage of muons will end up near each, in a ratio that is proportional to the sites electronegativity and multiplicity. The full asymmetry can be written as in equation 2.44, where each term of the summation is simply another inequivalent site.

$$\begin{aligned} A(t) &= \sum_{j=1}^{N} A_j(t) \\ &= \sum_{j=1}^{N} A_j(0) P_j(t) \ \ [148] \end{aligned} \tag{2.44}$$

The easiest way to determine the number of sites is to perform a Fourier transform on the asymmetry data. Any peaks correspond to an oscillatory signal which should form one of the components, where the field is directly related to frequency of oscillation, or the peak value in the Fourier transform based on the muon's gyromagnetic ratio.

Equation 2.40 assumes that the field is aligned along the initial direction of muon spin. This is a bit of a simplification. The value of $P_j(t)$ can be modified as follows for the general case. We start with the definition of the derivative as given in equation 2.45. The assumption is that $\vec{B}$ in this case is a static field, meaning that over the observation window, which we defined earlier as 5 to 6 muon lifetimes, the field is constant, or $\frac{\vec{B}(t)}{d\vec{B}(t)/dt} \ll \tau_\mu$. If we assume that $\vec{B}(0) = B_z$ and $\vec{P}(0) \parallel \hat{z}$ then we can derive equation 2.46, where $\omega_L \equiv \gamma_\mu B$ is the Larmor precession frequency. This is shown schematically in figure 2.27.

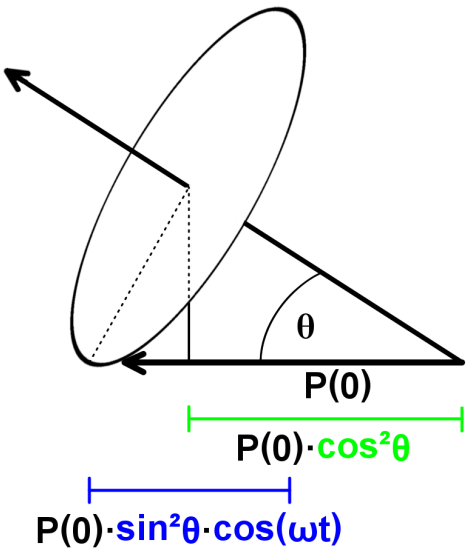

Figure 2.27: A cartoon of muon precession around an internal magnetic field. Adapted from [149]

In the case where there is a field distribution, we can extend equation 2.46 as 2.47 by integrating the field distribution, $p\left(\vec{B}\right)$, with our original equation.

$$\frac{d\vec{P}}{dt} = \gamma_\mu \left(\vec{P} \times \vec{B}\left(t\right)\right) \tag{2.45}$$

$$\begin{aligned} \vec{P}_{\vec{B}}\left(t\right) &= \cos^2\theta + \sin^2\cos\left(\omega_L t\right) \\ &= \frac{B_z^2}{B^2} + \frac{\left(B_x^2 + B_y^2\right)}{B^2}\cos\left(\gamma_\mu B t\right) \end{aligned} \tag{2.46}$$

$$\begin{aligned} \vec{P}_{\vec{B}}\left(t\right) &= \int p\left(\vec{B}\right)\vec{P}_{\vec{B}}\left(t\right)d^3\vec{B} \\ &= \int p\left(\vec{B}\right)\left[\frac{B_z^2}{B^2} + \frac{\left(B_x^2 + B_y^2\right)}{B^2}\cos\left(\gamma_\mu B t\right)\right]d^3\vec{B}\ [138,\ 148] \end{aligned} \tag{2.47}$$

In the case of a randomly ordered magnetic sample, we can substitute $p\left(\vec{B}\right)$ for the unit solid angle, $\frac{1}{4\pi}$ and integrate over $\cos\theta$ and the z-axis(ϕ)

as in equation 2.48, where we get the final result, with a $\frac{1}{3}$ component that is static and a $\frac{2}{3}$ component that oscillates with the field. This corresponds to the moments aligned (the longitudinal component) and non-aligned (the transverse component) with the field, respectively. This is because one third of the magnetic moment lies along the field and will not precess, hence a static portion.

$$\vec{P}(t) = \frac{1}{4\pi}\int \cos^2\theta + \sin^2\theta \cos\left(\gamma_\mu |\vec{B}| t\right) d\phi\, d(\cos\theta) = \frac{1}{3} + \frac{2}{3}\cos\left(\gamma_\mu |\vec{B}| t\right) \text{ [149]} \tag{2.48}$$

There is no special reason why both of these components necessarily need to relax at the same rate. Given that the nature of relaxation is exponential, we can take equation 2.48 and combine it with equation 2.44 to come up with a sample asymmetry for a magnetic powder, equation 2.49.

$$A(t) = A_0\left[\frac{1}{3}e^{-\lambda_L t} + \frac{2}{3}e^{-\lambda_T t}\cos\left(\gamma_\mu |\vec{B}| t\right)\right] \text{ [149]} \tag{2.49}$$

2.11.3 μSR Types and Analysis

Although there are numerous techniques that can be performed using the data that is obtained by muon spin rotation, relaxation and resonance, the ones of importance that will be discussed are zero/longitudinal field and transverse/weak transverse field. Each of these techniques is looking for something different. To separate these two things, the only experimental parameter that

needs to change is the initial muon polarization vector compared to the applied field. In the case of the longitudinal geometry, we want $\vec{P}_0 \parallel \hat{z}$, or that the initial muon polarization is transverse to the static component of the local field, $\vec{B}_0$. To observe longitudinal relaxation we will be looking at the positron detectors along $\hat{z}$. For a transverse measurement, the complimentary condition is necessary, mainly that $\vec{P}_0 \perp \vec{B}_0$. To observe this signal we normally say that $\vec{P}_0 \parallel \hat{x}$ which necessitates looking at positron detectors in the yz plane.

In the case of longitudinal fields, longitudinal relaxation is due to the recovery of a thermodynamic equilibrium (T_1 or *spin-lattice* relaxation) which requires a thermodynamic reservoir, in this case the lattice, to dissipate any excess energy stored by the spins in the out-of-equilibrium initial muon polarization [140]. Longitudinal relaxation of the signal can only be due to time-dependent interactions, such as those introduced by things such as thermally populated excitations like phonons or magnons, or externally applied RF-fields. A special case exists for muons that they can measure the zero field relaxation of materials. For μSR there is no special experimental parameters to do this. This compares with nuclear quadrupole resonance (NQR) which can also measure this, but requires a nucleus with a spin larger than spin-$\frac{1}{2}$ and a strong quadrupolar interaction, or with nuclear magnetic resonance (NMR) with special conditions and a field cycling system. Neither technique has the simplicity or universality that μSR has for these specific measurements. For relatively weak and random magnetic fields this makes μSR a very powerful technique. The mathematic machinery for this type of measurement is detailed below and based on the work of Kubo and Toyabe [150, 151].

For transversely applied magnetic fields, the relaxation is due to a dephasing of the precessions (T_2^* or *spin-spin* relaxation). In this case no external thermodynamic reservoir is needed [140]. Transverse relaxation generally has a T_1 like component due to time dependent interaction, which can be separated from the time independent interactions; the static component [140].

The following sections explain the basics of each technique.

2.11.3.1 Zero Field (ZF) and Longitudinal Field (LF) μSR

For zero and longitudinal field μSR we are interested in the relaxation of a signal with either no field applied or a field applied along the direction of initial muon polarization; a longitudinal field. In this scenario we can have two distinct types of sample: one that has static magnetism on the lifetime of the muon and one where the magnetism is dynamically fluctuating.

We can generally make the assumption that a system of interest for condensed matter physics is comprised of concentrated dipole moments [149], and like the case of nuclear dipoles, our probability distribution, $p(\vec{B})$, can be modelled as a Gaussian distribution (equation 2.50) [138]. For dilute systems, we can better model the system as a Lorentzian distribution (equation 2.51) [148]. From the point of view of the asymmetry and data analysis, these two distributions are essentially identical with the exception of the fastest portion of the front end of the signal, where a Gaussian will turn over and flatten as it approaches zero while a Lorentzian will keep an exponential shape to zero.

$$p^G(B_i) = \frac{\gamma_\mu}{\sqrt{2\pi}\Delta} e^{-\gamma_\mu^2 B_i^2/2\Delta^2} \tag{2.50}$$

$$p^L(B_i) = \frac{\gamma_\mu}{\pi} \frac{a}{a^2 + \gamma_\mu^2 B_i^2} \text{ [138, 148]} \tag{2.51}$$

where
γ_μ is the muon gyromagnetic ratio
$\gamma_\mu B = \omega$, the precession frequency
Δ/ω is the FWHM of the Gaussian distribution
$a = \Lambda\gamma_\mu$
Λ is the FWHM of the Lorentzian distribution
$i \in \{x, y, z\}$

Equations 2.50 and 2.51 can then be applied as was done in 2.47 and integrated to give us the form of the muon polarization vector in the Gaussian (equation 2.56) and Lorentzian (equation 2.57) cases. These equations are known as the zero field Kubo-Toyabe equations [150, 151, 152]. The rate of depolarization for the non-static $\frac{2}{3}$ component is equal to $1/\Delta$ for the Gaussian form and at a rate of $1/a$ in the Lorentzian form.

$$P_z^G(t) = \frac{1}{3} + \frac{2}{3}\left(1 - \Delta^2 t^2\right) e^{-\frac{\Delta^2 t^2}{2}} \tag{2.52}$$

$$P_z^L(t) = \frac{1}{3} + \frac{2}{3}(1 - at)\, e^{-at} \text{ [138, 148]} \tag{2.53}$$

If we apply a longitudinal field, assumed along the $\hat{z}$ direction, we should create a situation where the Kubo-Toyabe functions recover to a flattened

asymmetry of $\frac{A_0}{3}$. In this case for both the Gaussian and Lorenztian function we are adding an applied longitudinal field, B_{ext}, to equations 2.50 and 2.51 to get equations 2.54 and 2.55.

$$p^G\left(B_z\right) = \frac{\gamma_\mu}{\sqrt{2\pi}\Delta} e^{-\gamma_\mu^2 \left(B_z - B_{ext}\right)^2 / 2\Delta^2} \tag{2.54}$$

$$p^L\left(B_z\right) = \frac{\gamma_\mu}{\pi} \frac{a}{a^2 + \gamma_\mu^2 \left(B_z - B_{ext}\right)^2} \text{ [138, 148]} \tag{2.55}$$

The solution can be integrated to give analytical solutions for the muon polarization function, which are shown in equations 2.56 and 2.57 [138]. Due to the fact that the value Δ/ω_{LF} in the Gaussian case and a/ω_{LF} in the Lorentzian case tend to zero, any term other than the leading 1 in the relaxation rate also tends to zero. In these equations j_0 and j_1 are spherical Bessel functions of the first kind.

$$P_{LF}^G\left(t\right) = 1 - \frac{2\Delta^2}{\omega_{LF}^2}\left[1 - e^{-\frac{\Delta^2 t^2}{2}} \cos\left(\omega_{LF} t\right)\right] + \frac{2\Delta^4}{\omega_{LF}^3} \int_{\tau=0}^{t} e^{-\frac{\Delta^2 \tau^2}{2}} \sin\left(\omega_{LF}\tau\right) d\tau \tag{2.56}$$

$$\begin{aligned} P_{LF}^L\left(t\right) = 1 &- \frac{a}{\omega_{LF}} j_1\left(\omega_{LF} t\right) e^{-at} - \frac{a^2}{\omega_{LF}}\left[j_0\left(\omega_{LF} t\right) e^{-at} - 1\right] \\ &- \left[1 + \frac{a^2}{\omega_{LF}}\right] a \int_{\tau=0}^{t} j_o\left(\omega_{LF}\tau\right) e^{-a\tau} d\tau \text{ [138, 148]} \end{aligned} \tag{2.57}$$

In the case of dynamic magnetism, where the magnetic moments are fluctuating at a rate that is within the lifetime of the muon, we assume Brownian mo-

Collisions	Probability
None	$e^{-\nu t} P^G_{Static}(t)$
One	$\nu \int_{\tau=0}^{t} P^G_{Static}(\tau)\, P^G_{Static}(t-\tau)\, d\tau$
2	$\nu^2 \int_{\tau_1=0}^{t} \int_{\tau_2=0}^{\tau_1} P^G_{Static}(\tau_2)\, P^G_{Static}(\tau_1-\tau_2)\, P^G_{Static}(t-\tau_1)\, d\tau_1 d\tau_2$

Table 2.9: A table of probabilities of the number of collisions and subsequent collisions in a time interval t assuming Brownian motion [138].

tion is occurring and can use the strong collision approximation (SCA) [138]. For the SCA model, it is assumed that each step occurs at a rate of $\omega_0 t$, where ω is the same $\gamma_\mu B$ from the static magnetism derivations. The relaxation time (T_1) is defined as the time it takes for a phase deviation of one radian. The relaxation rate ($1/T_1$) is proportional to $\omega_0^2 \tau = \frac{\omega_0^2}{\nu}$ where ν is the fluctuation rate. Larger fluctuation rates give rise to a better averaging of randomness of the local field, which leads to a smaller relaxation rate [138].

The SCA assumes the probability of collisions ($\rho(t)$) is equal to $1 - e^{-\nu t}$. If the assumption that the system has a Gaussian distribution with no field applied, we can determine the probability of collisions as is done in table 2.9. The table can be extended further by chaining additional derivatives as subsequent collisions. Summing all the probabilities together gives a convolution integral which can be solved by performing a Laplacian transformation [151, 153].

In the slow collision limit, where $\nu/\Delta \ll 1$, the solution to the convolution integral gives equation 2.58 [138, 152]. In this limit the $1/3$ tail is not a constant, but slowly decays. In the fast limit, where $\nu/\Delta \gtrsim 5$, the solution gives equation 2.59. [138, 152] In this case the $1/3$ tail is typically absent and only an exponential decay remains.

$$G^{G}_{Dynamic(slow)} = \frac{1}{3}e^{-\frac{2}{3}\nu t} \tag{2.58}$$

$$G^{G}_{Dynamic(fast)} = e^{-\frac{2\Delta^2 t}{\nu}} \text{ [138]} \tag{2.59}$$

For a fast-relaxing dilute system, we can still use the Lorentzian distribution to model, however the collisions are still assumed to be Gaussian in nature due to the use of the SCA. Therefore, the only real change is to the exponent, which is seen in equation 2.60 [138].

$$G^{L}_{Dynamic} = e^{-\sqrt{\frac{4a^2 t}{\nu}}} \text{ [138]} \tag{2.60}$$

With local fields that are static, it would be expect to observe a decoupling or separation of longitudinal fields as the spins depolarize compared to the zero-field value. This specific case requires the condition that $\omega_{LF} \gg \Delta$. In the case of fast, dynamic local fields there is little difference between observations at zero field and with field applied and that there is only a small dependence [138].

2.11.3.2 Transverse Field (TF) μSR

The asymmetry signal from transverse field μSR gives us information about the relaxation processes that do not require energy loss, spin-spin or T_2 relaxation processes. This is useful for determining field distribution in inhomogeneous samples such as in superconductors and is useful in determining local mag-

netic susceptibility. The weak transverse field variant is useful in determining volume fraction.

We can model the distribution of internal fields either with a Gaussian or Lorentzian lineshape as discussed in the previous section on zero and longitudinal field μSR. The field distribution within a material leads to a dephasing of the muon spins similar to what occurs in NMR, we causes the muons to depolarize [154].

The mathematical form of the lineshape in the case of a static field distribution can be taken from the decaying portion described by the zero-field Kubo-Toyabe functions, 2.52 and 2.53. They aren't a part of the set of Kubo-Toyabe equations but the derivation of the envelope is similar. Those polarization functions are given for the Gaussian form as equation 2.61 and for the Lorentzian form as equation 2.62. In these cases the damping factors are given by Δ_x and $\sqrt{a}$, respectively.

$$P_x^G(t) = e^{-\frac{\Delta_x^2 t^2}{2}} \tag{2.61}$$

$$P_x^G(t) = e^{-at} \text{ [138, 148]} \tag{2.62}$$

With dynamic fields we have a similar case to the zero and longitudinal field cases where we can either have a quickly or slowly fluctuating field. The slowest fields we can approximate using the static case above. A quickly fluctuating field is defined whenever we have the case $\tau_c \Delta_z \ll 1$, where τ_c is the correlation time, or the inverse fluctuation rate. We can express this function

as in equation , which can be re-written by creating the term $\lambda = \Delta_x^2 \tau_c$ is now our dynamic damping factor which we can directly relate to T_2 as shown.

$$P_x(t) = e^{-\Delta_x^2 \tau_c t} \tag{2.63}$$

$$P_x(t) = e^{-\lambda t} = -\frac{t}{T_2} \text{ [138, 148]} \tag{2.64}$$

There also exists a middle range where neither description of the internal field distribution and fluctuation rate is particularly ideal. For these scenarios the Abragam lineshape, equation 2.65, can be used. Extracting accurate fluctuation rates in this regime of slowly oscillating transverse fields is difficult, so performing longitudinal or zero field measurements are typically more advantageous.

$$P_x(t) = e^{-\Delta_x^2 \tau_c^2 \left[e^{(t/\tau_c)} - 1 + (t/\tau_c)\right]} \text{ [138]} \tag{2.65}$$

Within each of these potential envelopes we will get a signal that precesses in the form of one (or potentially multiple) cosines. The general form of the asymmetry can be written as the multiplication of the envelope of the function and this cosine term, and is given in equation 2.66.

$$A(t) = P_x(t) \cos(\omega_{local} t) \text{ [148]} \tag{2.66}$$

Using equation 2.44 we can then build up our full asymmetry of the signal. Each of the asymmetry components will represent a different, distinct local field at a muon stopping site.

By contrast, in software we do the deconvolution of these signals to determine the information about the sample that we desire in exactly this way: by modelling the asymmetry signal with various functions and performing least-squares best fits. The software used in this thesis was musrfit [155].

2.11.3.3 weak Transverse Field (wTF) μSR

A special case of transverse field measurements is the use of a weak transverse field in a longitudinal setup. The first reason that this is done is to perform a calibration of the value of the α parameter. A known, small field can be applied to a paramagnetic sample and the transverse field response should be a non-relaxing, non-precessing state, excluding precession caused by the small external field. Knowing the small external field this can be easily fit to give a value of α that is accurate for the current sample, mounting, detectors, scintillators and properties of the muons being delivered based on their generation and the management of the beam pipe.

The second reason to use a weak transverse field is in a state that is partially magnetically ordered. In this case we would get a decaying, precessing signal. Assuming that the field strength from the magnetic order is much larger the muons in an ordered area will decouple. In the non-ordered area they would precess as above so by fitting the two components and determin-

ing what fraction of the asymmetry is in each we can determine the ordered volume fraction of the sample.

2.12 Conclusion

This chapter was a summary of the various techniques used to create and evaluate the samples described in chapter 1. These techniques formed a very powerful way to analyze what was happening structurally and magnetically to each system under a range of temperatures and magnetic fields to try and better understand the underlying physics. These techniques were used extensively in the following chapters.

Chapter 3

μSR and Neutron Scattering of Cobalt Niobate

3.1 Overview and Fit

The work in this chapter is the conclusion of my previous masters thesis, and an attempt to answer some of the unresolved questions. Specifically the focus was examining the very-long relaxation time. This was begun with a review of all the previous fits used for the cobalt niobate data that was reported in the previous thesis and briefly discussed below in section 3.2. The impetus for the review was partially that some of the fitting led to a stretched exponential fit, and that is relatively unsatisfying since it is phenomenologically-based. It was noted that some of the fits were potentially over-constrained, and this was partially software-limited previously. The second part of the drive to review the data was that the MuSRfit software was released. This software is based on the data analysis package ROOT created at CERN, and is an evolutionary step forward from msrFIT, which was used in the previous thesis. Several key features such as a larger number of variable allowed, allowing for more

extensive global fits, as well as an upgrade to the MINUIT2 fitting function allows for a better resolution and better fitting of the data. Additionally, adding in customized functions is something made far more accessible.

In addition to this review, complimentary data was taken using the cold neutron chopper spectrometer (CNCS) located at Oak Ridge National Laboratories. CNCS is a high-resolution, multi-chopper inelastic spectrometer used for time of flight measurements, allowing direct access to the dynamic structure factor, $S(Q,\omega)$. Of interest to this experiment, CNCS is suited to measurements of collective excitations, such as phonons and spin waves, and measurements of low-dimensional systems. The original idea was to observe a low-Q Bragg peak and monitor the evolution of the signal over time to help explore the anomalous measurements in transverse field from the previous thesis work. This required the use of a dilution refrigerator, and owing to the large fields required to reach the known quantum phase transition in cobalt niobate, a magnetic insert that was capable of generating a homogeneous 5 T Field. Unfortunately, this particular combination of two pieces of equipment cut down the range of low-Q that could be observed. The experiment was then modified to observe similar measurements to previous work reported by Coldea [51] with enhanced resolution. We did add to this a temporal component at low temperatures to determine if the signal from the neutron scattering was changing as well. The data here showed no time evolution, meaning that whatever process was observed with μSR is static on the neutron timescale (10^{-8} s to 10^{-13} s)) but dynamic on the muon timescale (10^{-4} s to 10^{-11} s)).

3.2 Previous Thesis Work

The following are short summaries of the work presented in the previous thesis [17], highlighting the important facts or conclusions.

3.2.1 Specific Heat Measurements

Measurements were made both at McMaster and with collaborators at the University of Waterloo to determine the specific heat of cobalt niobate. The expected peak in heat capacity at the transition at 2.9 K was seen, as well as smoothing of the peak followed by an increase in the temperature at which that peak occurred with increasing field. Aside from this, the most significant discovery was that at the lowest temperatures probed there was a significant decoupling of the spin-lattice (T_1) and spin-spin (T_2*) relaxation times, where the latter time became exponentially longer, until they were such a long time that the system could not hold sufficient liquid helium to make further measurements. The results are to be published shortly, but the low temperature data is shown in figure 3.1.

3.2.2 Zero and Longitudinal Field μSR

Longitudinal field sweeps, including a sweep made at zero field, were made in fields up to 2 T, with the majority in the range of 20 to 500 G. The temperature range for these sweeps was between 700 mK to 50 K using both the dilution refrigerator and the LAMPF spectrometer. Performing μSR at higher fields requires more specialized spectrometers, so most of the work was performed in general purpose, low temperature, low field spectrometers. The primary goal of

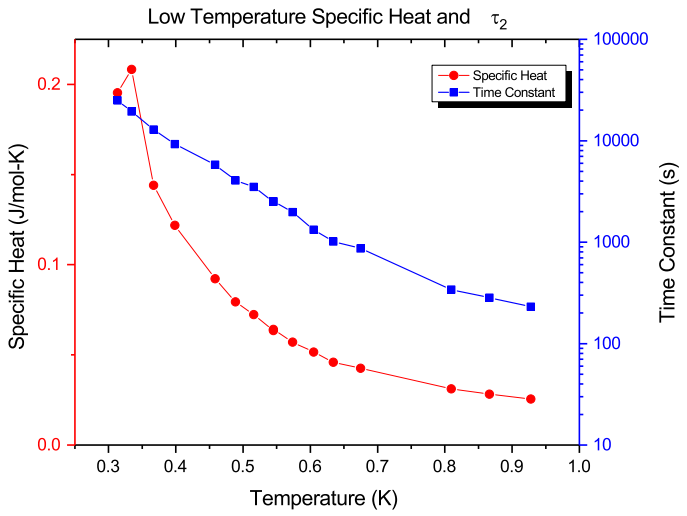

Figure 3.1: The lowest temperature data showing an exceptionally long time constant in cobalt niobate. Note that the scale is semi-log. From [17].

this investigation was to validate and explore using μSR the area where phase changes had been previously reported (at 1.9 K and 2.9 K) in temperature and field [49, 156, 157]. The crystals used in this experiment were aligned so that the field was applied along the crystallographic b-axis.

The data was previously fit to a stretched exponential model. In this model it was easy to capture the phase transition, as both the relaxation rate and the exponent would expect to have strong changes in their features between a magnetic and non-magnetic phase. The power of the exponential sharply decreased at the 2.9 K transition, verifying that transition. Throughout all the measurements, both with and without a field, it was noted that there were no oscillations, which showed no evidence of static order on the lifetime of the muon, as the signal is fully decoupled. The power of the exponent increases as the system is further decoupled with higher temperature. This is expected

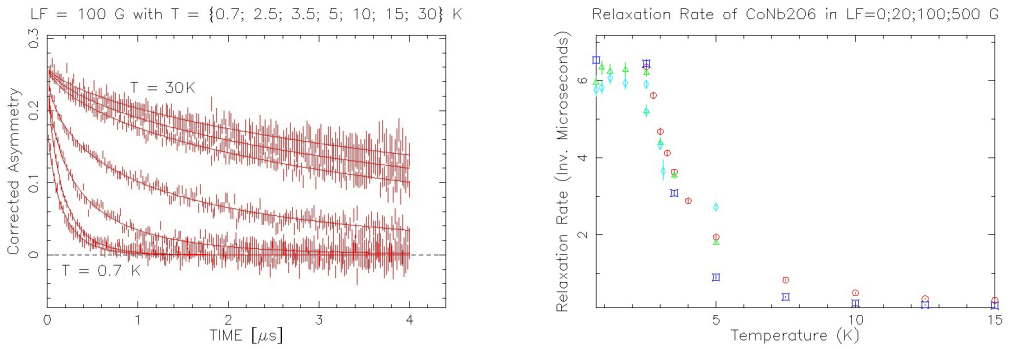

(a) (b)

Figure 3.2: A plot of muon asymmetry (left panel) and muon relaxation rates (right panel) versus temperature for cobalt niobate. In the left panel we see no signs of oscillation, indicating dynamic spin fluctuations. In the right panel, we see a sharp decrease of the relaxation rate at the 2.9 K phase transition indicating a change from an ordered to a paramagnetic state with the increase in temperature. From [17].

as eventually the signal should show no evidence of any change in asymmetry at the highest temperatures over time. This is shown in figure 3.2a.

Similarly, the relaxation rate both with applied field and in zero field showed very flat behaviour across the first phase transition at 1.9 K, and then a corresponding exponential decrease sharply at the upper transition. The relaxation rate tended to zero above the transition with an increase in temperature, again not unsurprising for a material in the paramagnetic regime. This leaves us with a system that, on the timescale that the muon can observe, is acting dynamically. This is shown in figure 3.2b.

3.2.3 Transverse Field μSR

The transverse field measurements were used primarily to confirm information

about the long relaxation time in this system. The reported data was between two different runs at 50 mK with a 5 kG external field applied separated by 14 hours in time (Run 5121 had been cooled for 8 hours, run 5126 had been cooled for 22 hours). Comparing the data in these two runs, a shift in peak frequency located at the expected silver precession frequency as well as other individual peaks was noted. Further, the Fourier transform of the signal showed that several sharp peaks merged into a single, broad feature. This change with 14 further hours of cooling, shown ahead in figure 3.8, seemed to confirm some of the information gathered from heat capacity measurements that were taken and are discussed in 3.2.1 and led to the neutron scattering experiments.

3.3 Updated μSR Analysis

Because of the development of muSRFit and muSRFFT, replacing msrFIT and msrFFT the original data was revisited, and a few subsequent measurements of additional data points in the longitudinal and zero field regimes were integrated into the previous data set. The big difference is that the statistical treatment of the data was performed with higher precision and the MINUIT2 function built into ROOT, instead of the MINUIT function which msrFIT relied upon.

msrFIT was actually more persistent software, in that it would search further in parameter space to find a more likely global minimum for a given fit. For muSRFit the software looked a smaller section of parameter space and was therefore much more likely to establish itself at a local minima, meaning that additional care was needed to ensure that an optimal fit would be arrived at; this meant initial conditions for the fit are much more important in this

software. To account for this individual fits were performed on the data, as well as a global fit of all runs, which was used to establish constraints on global parameters. These were then used to fit the local parameters in a second global fit of all runs with the global parameters set to be fixed.

3.3.1 Zero and Longitudinal Field μSR

Re-analyzing the zero field Fourier transforms, the majority of the spectral weight is located in the central peak, which is expected based on the plot. As temperature is increased the peak in the Fourier transform sharpens, which makes sense given the change in relaxation. However, even using a strong model to apodize the Fourier transform, the data shows an underlying broadening, which can be accounted for by using a second signal. These signals can be modelled as decaying exponentials in the form of equation 3.1, instead of as a stretched exponential, indicating that there are two unique muon stopping sites. This is a more conventional analysis, and is representative of a simpler dynamic system.

$$A(t) = A_1 e^{-\lambda_1 t} + A_2 e^{-\lambda_2 t} \tag{3.1}$$

The data was taken in two different temperature regimes, one with the dilution refrigerator (from mK to 4 K) and one in a conventional cryostat (From 2 K to 50 K). Aside from different total asymmetries and values for the α-parameter the data sets can be fit together nicely. The difference in these two values is due to cryostat design as well as beam delivery properties, as

they were taken on the same sample and not simultaneously. Because they were not taking simultaneously different beam properties would be expected based on the tune of the cyclotron, which would result in small changes to α. In contrast to previous fits (figure 3.2b), using this fit allows the direct observation of both known magnetic transitions, at 1.9 and 2.9 K, shown in figure 3.3.

In the faster fluctuating component, at low temperatures we see a relatively constant value, followed by a sudden peak and die-off around the first transition point, 1.9 K. In the slower relaxing component, we see a relatively flat plot, with a similar enhancement at the second transition point, around 2.9 K.

This function was used to fit data up to 20 K, however between 8 and 10 K the data can also be fit to a single exponential. At this point the asymmetry of the slower component dominated the fast-relaxing front end and the value and error bars on the fast-relaxing component become so large that the fit being accurate is improbable. The fit was performed again, forcing this component to totally die off and for the asymmetry to be absorbed at this cross over. With this done we get a relaxation plot, figure 3.3. There is a small mismatch between the two signals; this is likely due to a simple difference in thermometry, as a small shift in temperature corrects this error.

The longitudinal field data was also refit to the form of equation 3.1. On the LAMPF spectrometer, the magnet was restricted to a maximum of 1.85 kG during the time of measurement, but complimentary, overlapping rates were taken at 500 G. The relaxation rates show agreement below and above the higher transition. A data set taken at 100 G was compared to one taken at

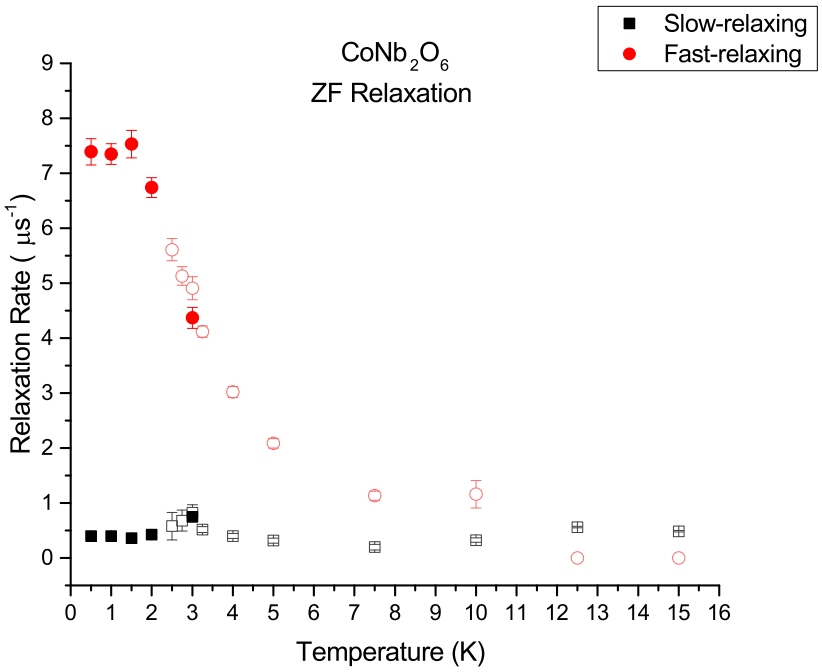

Figure 3.3: The zero-field relaxation of cobalt niobate. The hollow symbols are data from LAMPF spectrometer, while the solid symbols are data from the dilution refrigerator/PANDORA spectrometer.

the maximum field, shown in figure 3.4a. Although there is more scatter in the data at 1.85 kG, the trend generally shows that up to the maximum field the relaxation rates are essentially invariant. In both cases, both values of λ are small values for relaxation determined by μSR and independent of field, which is an indicator of dynamic relaxation [158]. There does exist a difference, notably below the upper transition temperature (which is accessible to the LAMPF setup), but the data taken in the dilution refrigerator continues this trend, shown in figure 3.4b. The data from the DR should be taken as more reliable as the DR was not at its measurement limit, where that wasn't the

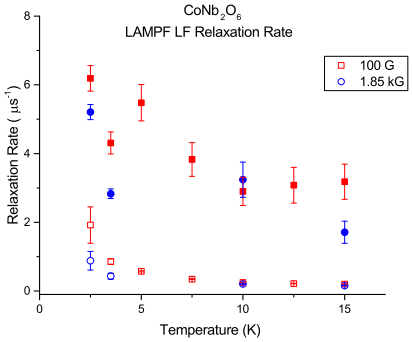

(a) The relaxation rates of cobalt niobate at 100 G and 1.85 kG as a function of temperature. The solid circles are the lower relaxation rate and the muted circles are the higher relaxation rate. These rates are shown as a sample for 100 G in figure 3.5.

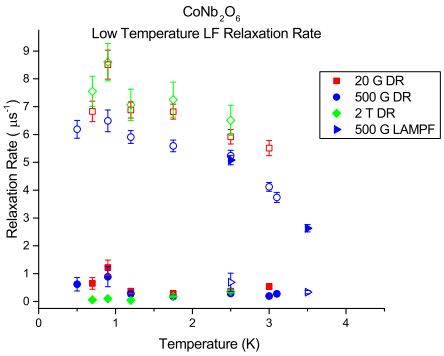

(b) The relaxation rates of cobalt niobate measured at low temperature in the dilution refrigerator. The points for 500 G that were also measured on the LAMPF spectrometer are shown as well.

Figure 3.4: Plots of the relaxation rate as a function of temperature and field for $CoNb_2O_6$.

case with the conventional LAMPF cryostat, although the 500 G data lines up quite well across the boundary.

At the transition temperature, the asymmetries, shown in figure 3.5, do show a trade off where the slower relaxation signal takes over a dominant contribution to the total asymmetry. This is a typical response for longitudinal fields as the signal will continue to depolarize until the asymmetry is totally flat with a zero relaxation rate at high enough temperatures.

3.3.2 Transverse Field μSR

A set of higher temperature data was taken using the HELIOS cryostat. This system has a much smaller distance between the samples and the detectors,

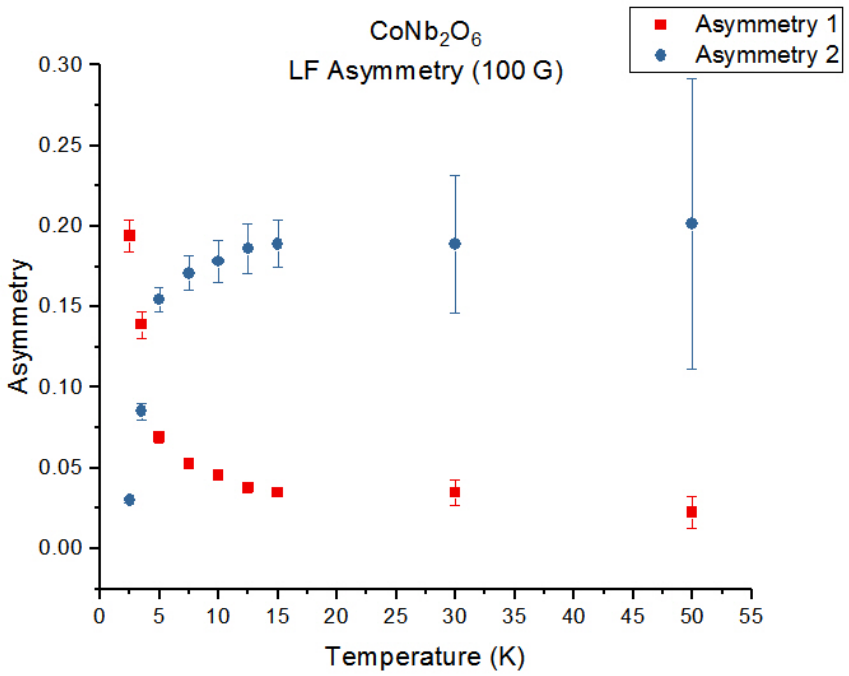

Figure 3.5: The asymmetry of a sample longitudinal field measurement of cobalt niobate at 100 G. The crossover is approximately at the critical temperature. The red points representative of the component of the higher relaxation rate, the blue points of the lower relaxation rate. The total asymmetry was determined and remained fixed. The trade-off shows that the first asymmetry component is more important below the magnetic transitions, while the second is dominant above.

allowing higher fields to be easily applied. This is still a conventional cryostat, which does not use He^{3+}, so temperatures below ~2.4 K are not achievable, and fall to the same potential errors as referred to above with respect to the LAMPF spectrometer, compared to the dilution refrigerator. In a 1 T field the fourier transform shows three separate peaks. From low temperature (50 mK) measurements in the dilution refrigerator, it was seen that increasing the field strength separated an increasing number of components in the Fourier transform: Below 2 kG two components were resolvable, between 2 and 5 kG

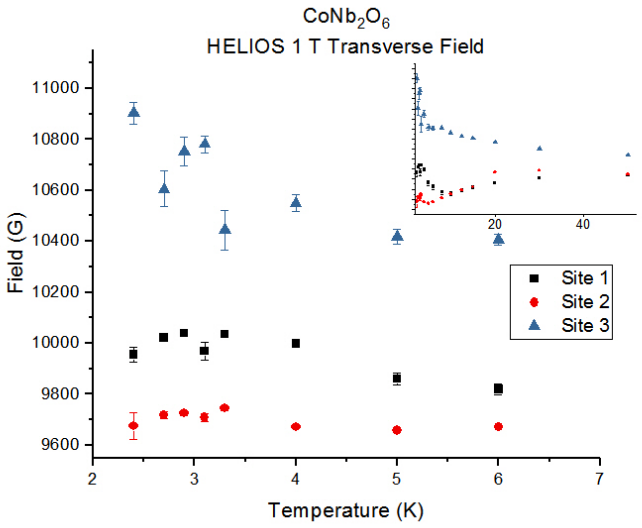

Figure 3.6: A plot of the evolution with temperature of the internal fields at three inequivalent muon sites in cobalt niobate in a 1 T transverse field.

three components were resolvable, and above that, up to 2 T, four components were resolvable. Therefore, the HELIOS data was fit to three components, shown in figure in figure 3.6.

Within HELIOS the sample is mounted in a veto cup, and had essentially no background, excepting a double layer of mylar and a double layer of silver painted aluminium tape. Both of these were thin enough that in this field they can be neglected. Going to a field higher than 1 T in HELIOS was not possible owing to the very strong magnetic interaction between the cobalt moments and the field; above a 1 T transverse field the sample in an attempt to align the moments could not be held in place and the aligned, tiled single crystal plates pulled themselves out of the mount and into the veto cup.

Approaching the transition from below, there is a dip in the lower two fields and an increase in the higher field, indicating that a transition is oc-

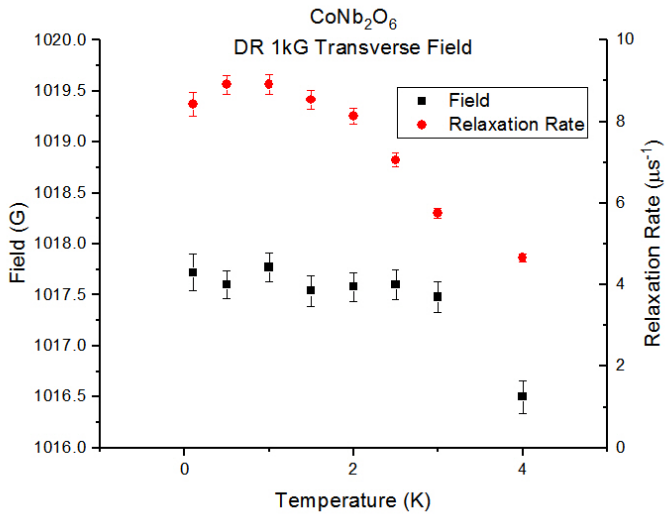

Figure 3.7: The evolution of the internal field and relaxation rate of cobalt niobate at 50 mK as observed in the dilution refrigerator.

curring. Above 8 K all three components begin to get closer to each other and merge, which also occurs in the Fourier transform. Additionally, the fields start to normalize to the applied field, which is what would be expected for a paramagnet.

Looking at the data from the DR, however, at 1 kG the non-silver field shows very flat behaviour, with a potential kink at the upper 2.9 K transition. A similar trend with a decreasing relaxation rate is also shown, both in figure 3.7.

The other major finding was that the sample continued to relax over time. Measurements were made in the dilution refrigerator at 50 mK for a period of a full day. The measurements were initially made using an increasing field over time, with the exception of two fields at the end. The first was a point fill in the data set at 7.5 kG. This gave a result that did not mesh with the

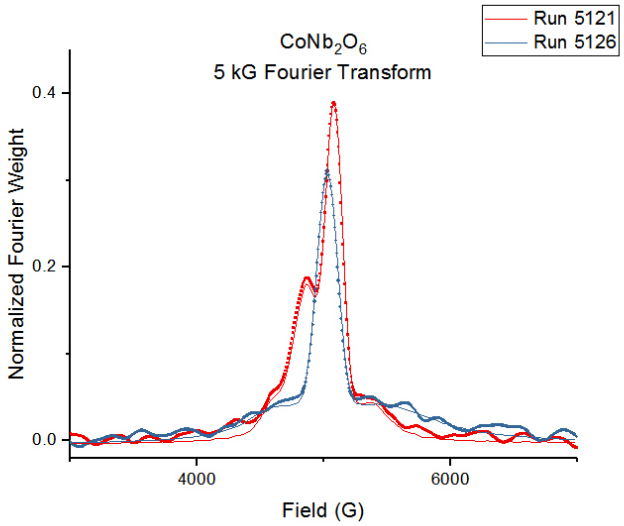

Figure 3.8: A Fourier transform of two datasets measured at 5kG in 50 mK. The runs are separated temporally by 14 hours, and at the time of the first run (5121) the sample had been cooled for 8 hours.

other data; the signal was less well resolved and the Fourier transform was less sharp. To investigate this an identical point at the nearest lower field was taken, being 5 kG. The results of the Fourier transforms of these two runs are shown in figure 3.8.

What is immediately evident is that they are very different. The side lobe that had emerged at a slightly lower field than the main silver peak had essentially disappeared or merged with the lowest field, and had broadened out into a more Gaussian shape, indicating that there was now a more continuum-like distribution of internal fields. This broadening was also evident around the upper field, but less-remarkably so. Additionally, there was a shift in the centre of the peak indicating that the silver is potentially being affected by the bulk magnetism of the sample and the spectral weight is correspondingly reduced, again a sign of a more continual distribution of internal fields.

This data seemed to compliment the heat capacity measurements made in the previous thesis work discussed above, where there are two components that are coming to thermal equilibrium, and where the time constant of the T_2 interaction was exceptionally long. This led to the investigation using time-of-flight neutrons.

It should be noted that the other parameter that did change was that the sample was subjected to a 3 T field. When the sample was removed the alignment had not changed, so that should not have been a factor given the same field. Additionally, the higher field could have set some moments and given a field-induced effect, but nothing that would indicate this was seen in prior SQUID magnetometry effects.

3.4 Neutron Scattering

The first portion of the measurements that we wanted to perform using neutron scattering was to replicate some of the results reported by Coldea [51]. To do this we used the cold neutron chopper spectrometer (CNCS) at Oak Ridge National Laboratory (ORNL).

Coldea reported the change of state from a magnetically ordered to a quantum paramagnetic state at 40 mK, with a crossover just above 5.5 T. His first set of measurements at zero-field cooling through the upper magnetic phase transition showed a broad continuum of scattering near T_N splitting into a Zeeman-ladder structure (figure 3.9b) which enhanced with a decrease in temperature, where the kinks at the minimum integrated over energy corresponded to quasi-particle excitations representative of symmetry in the E_8 Lie group

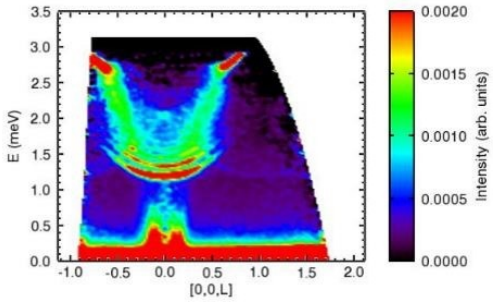

(a) An image of data taken at 75 mK in zero field integrated over all H and K.

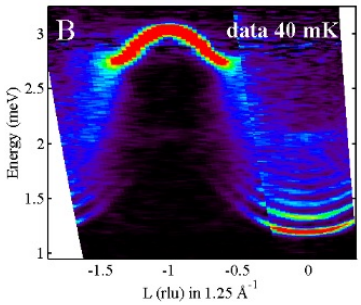

(b) .

An image of data showing the Zeeman ladder at 40 mK in zero field from "**Quantum Criticality in an Ising Chain: Experimental Evidence for Emergent E8 Symmetry** Coldea, R. et al. Science 2010 327(5962), 177–180 DOI: 10.1126/science.1180085 [51]. Reprinted with permission from AAAS.

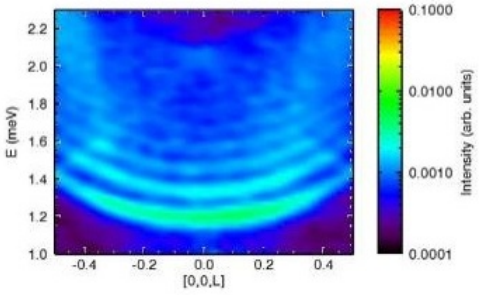

(c) An image of the data we took at CNCS showing the Zeeman ladder integrated over all H and K at 75 mK in zero field. Although it is washed out by integration in 3.9d, we can see potentially 8 quasiparticle excitation bands.

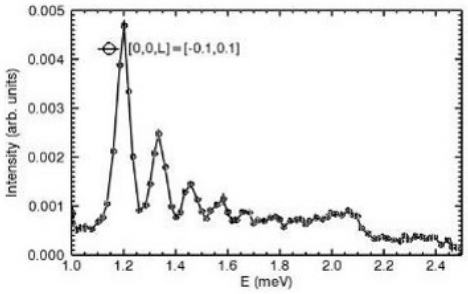

(d) A cut of data along L integrated from -0.1 to 0.1, over all H and K showing the quasiparticle excitations from the Zeeman ladder at 75 mK in zero field.

Figure 3.9: A series of cuts of neutron data of $CoNb_2O_6$ in zero field at 75 mK. The neutron incident energy was 3.315 meV for all CNCS data.

predicted by Zamolodchikov [52]. The measurements that we took (figure 3.9a) match the results of Coldea favourably (figure 3.9b), and the higher resolution measurements performed on CNCS show additional quasiparticle excitations. A comparison of these results can be seen in figure 3.9.

At higher fields (4.5 and 5 T) Coldea showed that the second excitation of the first quasi-particle created a continuum that washed out any higher order particles, so the focus of the experiment after verifying that we could reproduce his data was to investigate the change of the spectra over time based on the known long relaxation time and the transverse field neutron data.

Measurements were performed in zero field, as well as at 1 and 2 T with a specific order of sweeps. A sweep of angles was done in 4^o steps over the range of the detector. At the conclusion of one sweep the initial angle was incremented by 2^o, then -1^o, then 2^o covering the full range of the detector in 1^o steps. The idea is integration of each of the 4^o sweeps would show an evolution over time similar to that shown in the Fourier transforms in figure 3.8. The theory was that the largest change should occur at the start, as, typically, the expression of relaxation time with respect to heat capacity was shown to be exponential in nature. The results showed that this wasn't the case. Each run took 45 minutes, meaning that between the end of the first run and the start of the third 90 minutes had elapsed, with corresponding scans offset by 3^o being approximately 135 minutes apart. No difference was evident and all the data sets can be easily integrated with no visible anomalies. From this it seems that time is not the key factor when it comes to the change of the excitations. It is possible that there is a required initial cooling time before

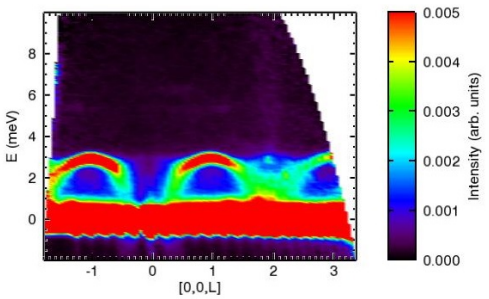

(a) An image of data taken at 100 mK in zero field taken in 4^o steps immediately after the temperature was set.

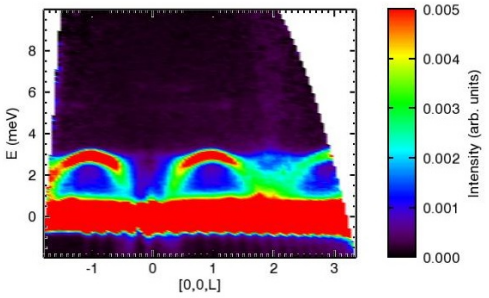

(b) An image of data taken at 100 mK in zero field taken in 4^o steps starting approximately 135 minutes after the temperature was set for the data taken in figure 3.10a, offset by $+3^o$.

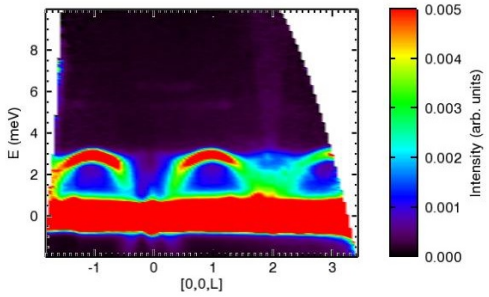

(c) An integration of all data taken at 100 mK. The improved image quality is because the data integration only had 1^o steps between scans, vice the 4^o in figures 3.10a and 3.10b.

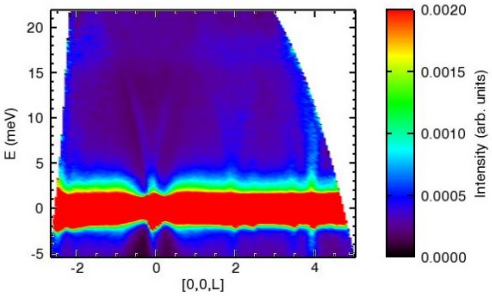

(d) A scan of data, using an E_i of 25.23 meV to show a larger range of $\vec{Q}$ at 270 K.

Figure 3.10: A series of cuts of neutron data of $CoNb_2O_6$ in zero field at 100 mK for the first three panels and 270 K for the final panel. The neutron incident energy was 5 meV for the first three panels and 25.23 meV for the final panel.

the change is evident, but, more likely, this is probably an effect of field, or a field-induced shift in the internal magnetic ordering. This is a significant difference from the ideas that were generated from the μSR results or shown with magnetometry measurements sweeping through similar and higher fields.

In the analysis, it is evident that we have magnon-like bands when we integrate over all H and K at odd integers of L, shown in figure 3.10c. In addition, there is a weak phonon-like feature at [002] with a peak at approximately 3 meV, and potentially an enhancement at other even or zero features. Using the high temperature data, figure 3.10d shows that these are destroyed with an increase in temperature, allowing the identification as a magnon. Additionally, coming out of the even values of L a phonon mode is evident. This is identified due to the enhancement in the strength. This figure is taken at and E_i of 25.23 meV instead of 12 meV at 270 K. The 12 meV plot show the same thing, but the higher E_i shows further into $\vec{Q}$-space, allowing us to see the [00-2] and [004] peak. The [004] peak, which is higher in $\vec{Q}$, also shows a stronger response; another sign of phonons. Finally, in the 25.23 meV picture, between 20 and 25 meV we see a band of scattering. In 50 meV data (not shown) this wide band wipes out the phonons, and no scattering above that band is obvious, although the data quality is insufficient to rule out excitations at a higher energy.

Additionally, the data obtained by Coldea shows what happens at zero field as well as at fields close to the quantum critical point. Our continued examination looked at the evolution of the magnons as a field was applied from zero field up to 4.5 T, the case of the data reported by Coldea. The evolution is certainly interesting. Our data also shows a significantly larger range than that reported by Coldea, as he focused on a much narrower range of HKL-space. Between zero field and 1 T (figure 3.9a and figures 3.11a to 3.11d) the destruction of the Zeeman ladder occurs in a way that can be described as messy. It appears that there are field-induced effects that cause the signal to

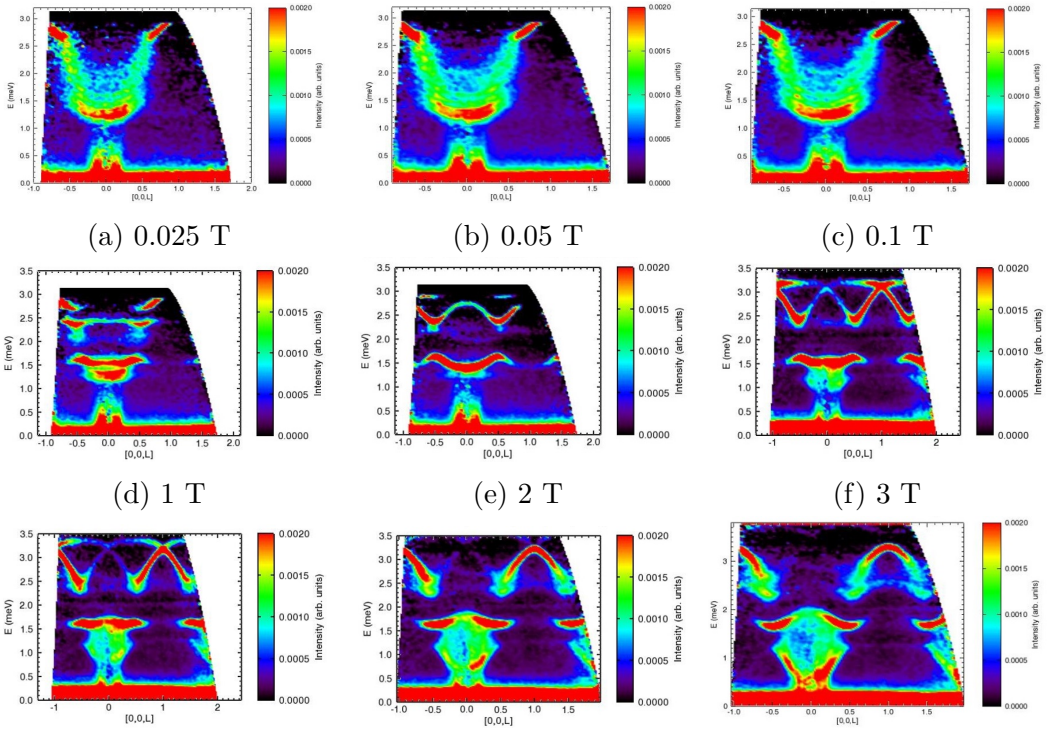

(a) 0.025 T (b) 0.05 T (c) 0.1 T

(d) 1 T (e) 2 T (f) 3 T

(g) 3.5 T (h) 4 T (i) 4.5 T

Figure 3.11: A series of cuts of neutron data of $CoNb_2O_6$ at 90 mK from 0.025 T to 4.5 T. The neutron incident energy was 4.4 meV and the data was integrated over all H and K. The panel at 4.5 T (3.11i) was measured at 150 mK.

be blurred, as well as the emergence of a band-like structure starts to occur. At 2 T (figure 3.11e) the signal is quite sharp and two disconnect bands, one centered around 1.5 meV with a maxima at values of $\frac{2L+1}{2}$ and one centered around 2.5 meV with maxima at integer values of L. Additionally, we start to see the formation of a flat band just below 3 meV.

At 3 T (figure 3.11f) the lower band appears essentially unchanged, while the upper oscillating signal has strengthened in relative intensity and connected to the 'flat' band seen in the 2 T data, which is starting to show weak oscillation of its own.

At 3.5 T (figure 3.11g) it can be seen that instead of two different bands, the signal is actually two overlayed magnons which begin at positions of $\frac{2L+1}{2}$ and terminate at positions of $\frac{2L+5}{2}$.

At 4 T (figure 3.11h) we see that the bands that are $\pm\frac{1}{2}$ of even values of L disappear and at 4.5 T (figure 3.11i) we start to see the lower band, which has been relatively unchanged, begin to increase in amplitude with respect to energy, as well as the addition of a third band between the previously observed two band that oscillates identically to the upper band/in counterpoint to the lower band with a reduced amplitude. Note that the data taken at 4.5 T was done at 150 mK vice 90 mK due to warming of the system caused by the application of the magnetic field interacting with the spins in the sample. The system used takes a very long time to cool below 250 mK and the temperature was stable in this field on the length of time that the experimental run was performed. Based on the evolution it is suspected that this small amount of heating has little to no impact on the neutron spectra.

To further explore these features, a corresponding set of measurements was taken at 5.5 K, above the two magnetic transitions reported for $CoNb_2O_6$. These results are equally interesting, and further suggest that there are field-induced effects at play.

Starting in zero-field, we see some remnant of the same structure that existed below the magnetic transition, thought it is not nearly as sharp. Taking a scan similar to figure 3.9d we see essentially diffuse scattering in figure 3.12i, meaning that any definitive quasiparticles or the entire Zeeman ladder are wiped out. Scanning up to 1T (figures 3.12a to 3.12c) we see the destruction

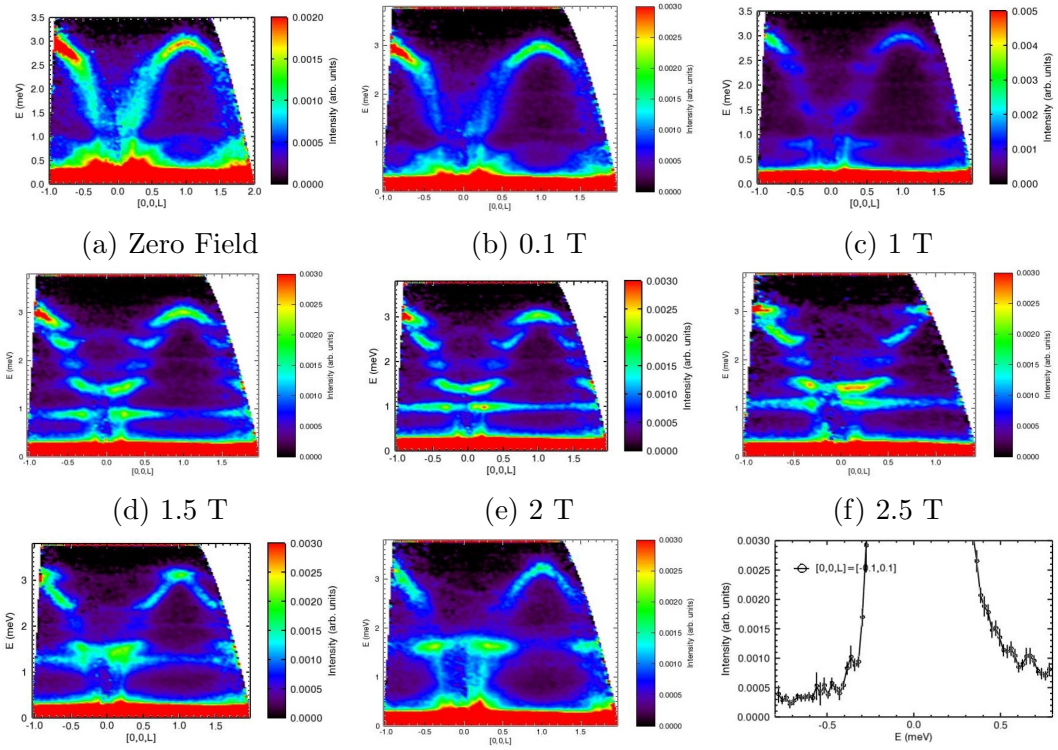

(a) Zero Field (b) 0.1 T (c) 1 T

(d) 1.5 T (e) 2 T (f) 2.5 T

(g) 3 T (h) 4 T (i) 4.5 T

Figure 3.12: A series of cuts of neutron data of $CoNb_2O_6$ at 5.5 K from zero field to 4 T. The neutron incident energy was 4.4 meV and the data was integrated over all H and K. The bottom right panel is an integration over all H and K and L from -0.1 to 0.1 (3.12i) as a comparison to the 90 mK value shown in figure 3.9d.

of the structure and the wipeout of intensity. At 1 T, however, some of the similar oscillations that we saw in the lower temperature data seem to be emerging. At 1.5 T (figure 3.12d) we see a significant increase in strength, as well as the appearance of a large number of signals or bands, compared to the lower temperature data. The bands seem to become enhanced up to 2 T (figure 3.12e), then unlike the higher field data, at 2.5 T (figure 3.12f) they start to become less sharp or get destroyed.

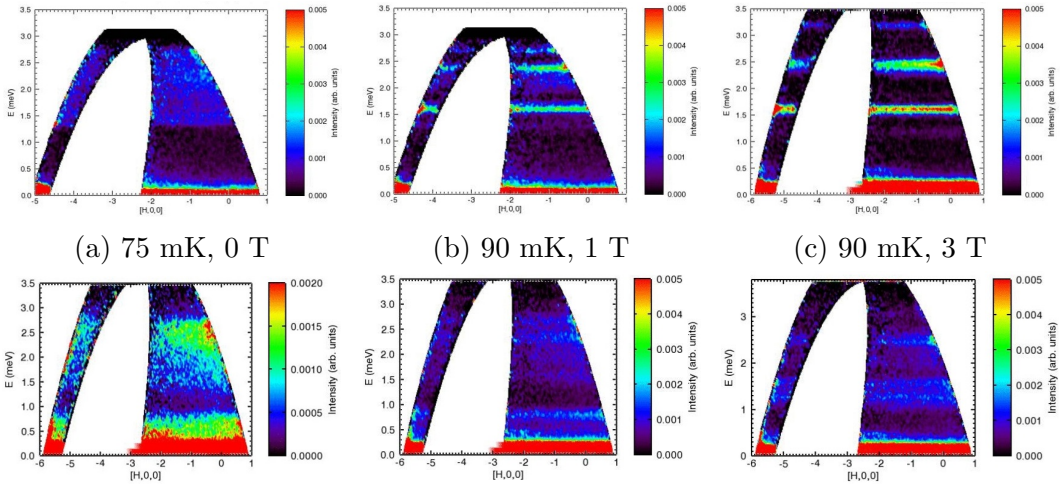

(a) 75 mK, 0 T (b) 90 mK, 1 T (c) 90 mK, 3 T

(d) 5.5K, 0T (e) 5.5 K, 1 T (f) 5.5 K, 3 T

Figure 3.13: A series of cuts of neutron data of $CoNb_2O_6$ at 75/90 mK and 5.5 K at field of 0, 1 and 3 T. The neutron incident energy was 3.315 meV for panels 3.13a and 3.13b and 4.4 meV for all the remainder, and the data was integrated over all K and in L over a range from 0.4 to 0.6. The data shows how the dimensionality of the bands is evolving with temperature and field.

At 3 T and 4 T (figures 3.12g and 3.12h) a reduction in the number of bands is evident, as well as a more defined structure. This inspires the belief that there are numerous, competing interactions that we are seeing in this material as it approached the quantum critical point.

Additionally, we can take a look at a cut integrated over all K and around the maximum at L (0.4 to 0.6) to get an idea of the dimensionality of the system, shown in figure 3.13. In the case of no applied field, we seee relatively diffuse scattering across the bands over all H, with the highest intensity near H = 0 (figures 3.13a and 3.13d). At 1 T the scattering has evolved into bands that stretch across all H, with stronger intensity noted in the lower temperature data. The intensity varies only slightly with an increase in H (figures 3.13b and 3.13e). At 3 T, we see that the bands change in energy

(figures 3.13c and 3.13f), which correlated with the respective change in the E vs. L plots (figure 3.11f and 3.12g) cut between L = 0.4 and 0.6. The uniform strength throughout all of H in this integration indicated that we are dealing with reduced dimensionality both below and above the zero field T_N.

3.5 Conclusions

The re-analysis of the μSR data as well as the neutron scattering data seems to increase the number of mysteries surrounding cobalt niobate. The heat capacity and μSR data both show strong evidence that the large difference in the coupling time constant of the spin-lattice and spin-spin components causes an interesting interplay, and that a very long period of time, on the order of 10^4 to 10^5 seconds at 300 to 400 mK, may be required before the ground state of this material is actually achieved. Due to this we do see an evolution in the signal on the time scale of μSR measurements (10^{-4} s to 10^{-11} s)). The re-analysis did 'clean up' some of the theory surrounding the μSR interpretation. By removing the stretched exponential and being able to fit the material to more conventional fitting functions, we are more certain in the physics behind the material.

It appears that the application of magnetic field may play a much larger role in the evolution of this material than was originally believed, based on the μSR data. The neutron data shows that on the time scale of neutron interactions (10^{-8} s to 10^{-13} s)) there appears to be very little change in the measurements. This may imply that there is some form of field-induced ordering in the material at low temperatures and fields in the ordered phase as

well as approaching the quantum critical point from below, which would be an interesting future avenue for exploration.

Given an applied field, we find that there are a very large number of features that are emerging. Since this material has been shown to be quasi-1D in nature, the appearance and evolution of spin-wave-like features, even at zero field, is inherently interesting. Although the system is quasi-1D, in the sense that it is composed of ferromagnetic 1D chains that are weakly coupled antiferromagnetically, the strength of the neutron response seems oddly strong and is likely tied to the transversely applied field.

In any case, these investigations certainly show that significant future experimental work as well as theoretical computation will be required if a full explanation of the features that have been observed are to be reconciled with what has been seen and proposed for cobalt niobate to this point. At present, because there isn't a theory that covers the evolution of the structures seen in the neutron data determining why they are happening and fitting to a theory is not yet possible.

Chapter 4

Synthesis of Nickel Niobate

4.1 Overview and Fit

Following the work on cobalt niobate ($CoNb_2O_6$), it was decided to attempt to recreate this system with nickel replacing the cobalt atoms. From literature [55] it was known that the isomorph of the cobalt material could be synthesized with nickel, although there was very little other data reported on its structure. Given the recent interest in cobalt niobate, it was thought that replacing the effective spin-$\frac{1}{2}$ with a spin-1 particle could give similarly interesting quasi-1D physics due to the same chained nature with a transverse field applied.

We began by investigating the phase diagram for NiO and Nb_2O_5, which seemed to indicate that this would be similar to the synthesis of cobalt niobate using CoO and Nb_2O_5. We attempted to use the same technique as was used for growing high quality crystals of $CoNb_2O_6$. The results were not what was expected. After a significant amount of analysis using x-ray diffraction and magnetometry we were able to determine that the structure of the crystal as-grown was not a columbite structure, but something different. Because of

this we performed single crystal diffraction on a small, unique crystal that was found in the core of one of the growths. A literature search found that this material had not been reported, although a publication from the 1950's from a chemistry synthesis group reported something similar. Likely this was the same material, however it was misclassified. This was likely due to the assumption that it belonged to the same space group as other AB_2O_6 materials. The difference between our classification and that of the one that may have been done previously is a slight deviation in the position of one of the Oxygen Wyckoff positions, which they reported at a symmetric site, while we found it to be at a general site. We were able to fit to their space group, but found that a different space group fit significantly better. Our precision and ability to make this conclusive determination is likely a due to improved instrument resolution in the intervening 60 years since this material was classified. The single crystal data was able to fit into that space group, however a better fit was found by changing to a different space group, one that had never been reported for AB_2O_6 compounds. This was the start to a change in scope of the thesis: from a direct comparison of two materials material having spin-$\frac{1}{2}$ or spin-1 particles arranged in chains in a columbite structure to the characterization and classification of an unreported compound (as the only other reported synthesis was by the aforementioned chemistry group).

Eventually we were able, through a significant amount of effort involving over and underdoping, change of growth condition and change of growth atmosphere to create small crystals in the columbite phase. The following chapter, an article written for publication in the journal 'Crystals', gives an explanation of the steps we took, the materials we created and the powder x-ray classifica-

tion of the new polymorph of nickel niobate in the two forms, black and green, that we found. Additionally a comparison to columbite nickel niobate and its synthesis is presented.

4.2 Front Matter

The title for this paper is "Oxide Self-Flux in Optical Floating Zone Crystal Growth of Nickel Niobate ($NiNb_2O_6$)" and it has been submitted to the journal *Crystals* and is also available from the MDPI preprint server [159].

The authors of this article are, in order, Timothy J.S. Munsie (McMaster University), Anna Millington (McMaster University), Dr. Graeme M. Luke (McMaster University, the Brockhouse Institute for Materials Research and the Canadian Institute for Advanced Research), and Dr. Hanna A. Dabkowska (McMaster University and the Brockhouse Institute for Materials Research).

The relative contributions of each co-author is written as part of the submitted article below in section 4.10.

This paper is reproduced with permission.

4.3 Abstract

Growing crystals of nickel niobate ($NiNb_2O_6$), we noticed that changing growth conditions allowed our material to enter different areas of the phase diagram. We also found that excess material accumulated within and above the liquid zone. Analysis showed that this was an excess of NiO. Changing the ratio of the constituent oxides - an excess of $\sim$4% of either NiO or Nb_2O_5 gave us the

opportunity to investigate changes in zone stability, melting temperature and quality of the resulting crystal. We found that a small excess of nickel oxide decreases the melting temperature significantly, and created the best pseudo-rutile $NiNb_2O_6$ crystal studied ($P4_2/n$, space group 86), while higher amounts of niobium oxide allowed us to stabilize the $NiNb_2O_6$ columbite phase (Pbcn, space group 60). This research reinforces the idea that self-flux as a travelling solvent can significantly impact crystal growth parameters and quality.

4.4 Introduction

The optical floating zone (OFZ) crystal growth method creates an opportunity to grow crystals of congruently and incongruently melting oxides [160]. Whereas to obtain crystals of congruently melting materials the grower has to well understand the interplay between melting temperatures, pulling speeds and growth atmospheres, the growth of incongruently melting oxides is much more demanding. Understanding of the applicable phase diagram allows for finding the appropriate "flux", which not only helps to grow the proper phase but also to stabilize it in post growth heat treatment.

Cobalt niobate ($CoNb_2O_6$), which has previously been grown and studied by our group [54], has been identified as a material with a quantum critical point [51, 156, 161, 162], a topic that has been of significant interest recently in the physics community [163, 164, 165, 166, 167, 46, 168, 169, 170]. QCPs are the boundaries of phase transitions that are not driven by temperature changes. Cobalt niobate consists of ferromagnetic spin-$\frac{1}{2}$ chains along the b-axis, with neighbouring chains weakly coupled antiferromagnetically due to

isolation by non-magnetic niobium atoms [48]. This gives rise to an effective 1D Ising system. Testing the physical realization of the 1D Ising system is useful in the determination of how well the theoretical model matches nature.

Following the previous research done on the transverse field Ising spin model, we decided to extend our investigation of this system to the spin-1 analogue, nickel niobate ($NiNb_2O_6$). Both cobalt niobate and nickel niobate have previously been reported to form the columbite structure [47, 171, 172], space group 60 (Pbcn), and reports on successful growths via the optical floating zone have been presented in [55], although no experimental details were given. The $NiNb_2O_6$ material has not been well explored due to the complicated phase diagram [173] and having high quality crystals of it would allow us to compare and contrast a potential spin–1 magnetic system against a similar spin–$\frac{1}{2}$ system. Specifically this would let us examine the regime under which the spin–$\frac{1}{2}$ system undergoes a quantum phase transition, which is not likely in a spin-1 system. Some results on single crystals of columbite $NiNb_2O_6$ grown via flux methods are available for heat capacity and magnetometry [174, 175].

In this paper, we report the growth of small single crystals of nickel niobate, up to a size of ∼5 mm x 3 mm x 1 mm. We did not succeed in obtaining one single crystalline boule, which was the case with $CoNb_2O_6$ [54], but after 16 growths, generally forming an external, polycrystalline shell of columbite-structure nickel niobate and various internal phases, we can report creating good quality single crystals of both the columbite and pseudo-rutile phases of $NiNb_2O_6$. The latter phase was a previously unreported polymorph of nickel niobate (β-$NiNb_2O_6$) [176]. This particular structure was of additional interest

due to the fact the space group that it was in, $P4_2/n$ (space group 86), has not been reported before in the family of AB_2O_6 materials [177].

We have recently reported the basic structure and magnetic response data for β-$NiNb_2O_6$ [176] in space group 86 and here we report the methodology behind the synthesis of the material and various attempts made in an effort to stabilize β-$NiNb_2O_6$ as well as the columbite phase of $NiNb_2O_6$ via the optical floating zone growth technique. This paper details the effects of changing the growth atmosphere, the growth speed and the material initial stoichiometry on the resultant grown boule.

4.5 Results

The first two growth attempts were done in a Crystal Systems optical floating zone image furnace near the maximum power settings of the system (4 x 300 W lamps). Remaining growths were performed in a NEC OFZ image furnace with higher wattage (2 x 1 kW) lamps.

Initially, the growths were done in reducing conditions, required to stabilize the $NiNb_2O_6$ phase [173], using a commercially mixed gas of 90% argon and 10% hydrogen in an attempt to obtain the columbite structure. At the beginning the growths were done with a significant number of manual adjustments. Gas pressure was modified throughout the growth in an attempt to reach more stable conditions. After growth 4, all growths except 13, which was performed in air, were done in a 100% oxygen gas (O_2) environment at 200 kPa overpressure up to growth 8, 40 kPa overpressure for growth 9 and with no overpressure for all remaining growths.

On the NEC system we were able to stabilize the growth at the rate of about 4 mm/hr. Although ultimately the zone spontaneously lost stability and began to widen to the point that the growth was unsustainable. A subsequent attempt at a slightly increased speed was also unstable, leading to the conclusion that this material grows best at 3 mm/hr in the reducing atmosphere.

Because the material is not congruently melting, evidenced by the residual material left at the end of the growth, we decided to pre-melt it in an oxygen environment, as we wanted to densify the rod and make it uniform. Based on the stability exhibited during the pre-melt we continued growing in oxygen for future attempts. Growth of the pre-melted boule at a speed slower than 3 mm/hr, consistent with successful speeds used for growth of cobalt niobate, was unsuccessful.

The following growth was done at 10 mm/hr, which resulted in a boule of material with one dominant orientation. This was then grown at the most stable observed speed, which was about 5 mm/hr. Post-analysis showed that the tip was overheated and that a concave crystallization front was formed. Based on this we decided to reduce the oxygen overpressure for the next growths as stated above.

With 1.4% extra nickel oxide (NiO) added via a flux pellet, we again pre-melted the rod. This resulted in a crystal with a facet. Within the boule there was a mixture of polycrystalline columbite, a black phase consisting of a mixture of columbite and the pseudo-rutile phase, as well as a few green single crystals, approximately 5 mm x 3 mm x 1 mm, that were pure ex-

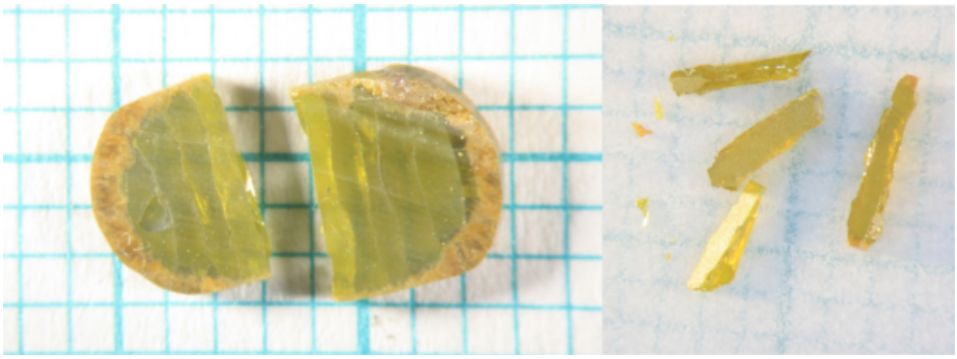

Figure 4.1: As grown crystal from growth 10, using a nickel oxide flux. The outer core is yellow, polycrystalline columbite. The green crystals in the centre are β-$NiNb_2O_6$, in single crystalline form as verified by both Laue and single-crystal x-ray scattering. The right hand panel shows the crystals separated after applying light, mechanical pressure with a scalpel between the ceramic and crystal portions, as well as along the fractures within the crystal itself. Lattice parameters for this sample found via x-ray scattering are a = 6.6893(3) Åand c = 9.0956(11) Å. Full refinement details have been published in reference [176].

amples of β-$NiNb_2O_6$. A slice of this material is shown in figure 4.1. The powder x-ray pattern is shown in figure 4.6 with the reference pattern for the tri-rutile($P4_2/mnm$) $NiNb_2O_6$ pattern from reference [172]. The boule was quenched according to the phase diagram [173] to stabilize the as grown phase.

Attempts made with higher concentrations of nickel oxide were unsuccessful at producing more of the green crystals, as can be seen in figure 4.2. We did, however, manage to stabilize black crystals, which were crystallographically identified as the same material but with a niobium deficiency. At the highest concentration, the additional material drove the resultant crystal back into the columbite area of the phase diagram. Both an amber and black columbite niobate (growth 16) are shown in figure 4.4.

Figure 4.2: The result of growth 11 with 1.4% excess nickel oxide from stoichiometric. (**a**) The boule cut down the growth axis. There is a mixture of niobium-deficient β-$NiNb_2O_6$ (black) as well as polycrystalline columbite (yellow). (**b**) The as-grown boule.

The growth of the material with an excess of niobium oxide produced boules of both the black β-$NiNb_2O_6$ (growth 15) and the black columbite (growth 14), seen in figure 4.3 with the primary difference being the growth speed. A powder x-ray comparison can be seen in figure 4.6 for growth 15 and in figure 4.5 for growth 14. In figure 4.5 the pattern is compared with one of the yellow polycrystalline pieces from the surface (in this case, from growth 12) as well as with the expected pattern for the columbite form from the database [47]. The obtained crystals were quenched, and this may be the reason for mechanical fracturing into plates. For β-$NiNb_2O_6$, the faces of the plates were perpendicular to the growth direction and oriented along [110]. These can be seen in figure 4.3.

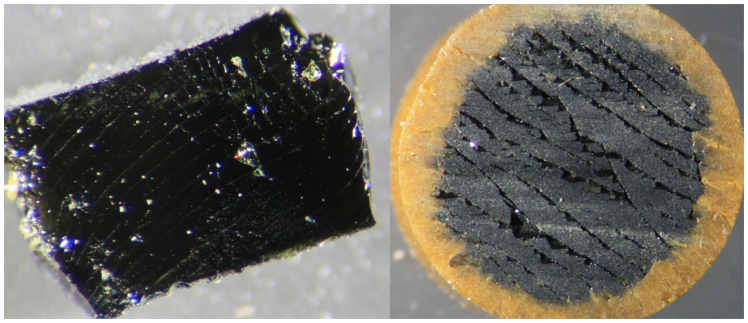

Figure 4.3: The result from growth 14 with 4% excess niobium oxide. (**a**) A cleaved plate of columbite $NiNb_2O_6$. The face shown is [110]. (**b**) A cross section cut of the material. Likely, the cracks formed on cooling due to a change in lattice parameters through a phase transition. A scalpel inserted into these cracks easily separated the grains.

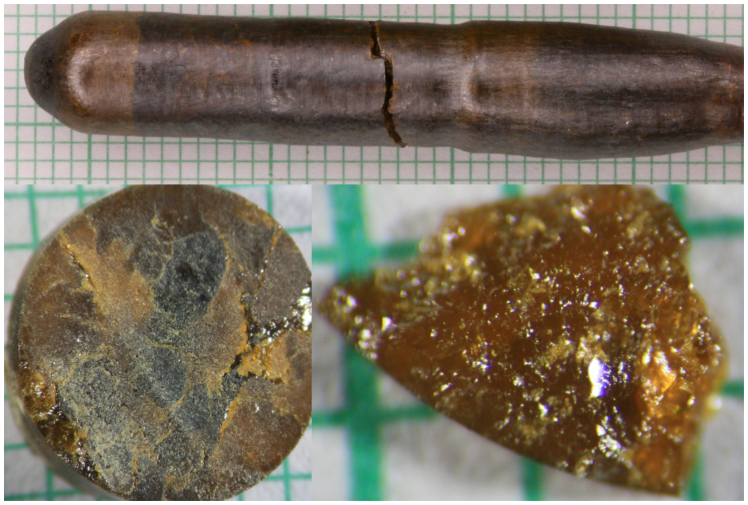

Figure 4.4: The result from growth 16 with 4% excess nickel oxide from stoichiometric. (**a**) The as grown boule, which cracked on removal from the image furnace. The dark, outer shell seemed to indicate that we had gotten closer to stabilizing the black phase. (**b**) A slice from inside the crystal, which shows definite mixture of phases despite the external picture. (**c**) A separated piece of columbite niobate crystal. Black pieces were also easily separated mechanically.

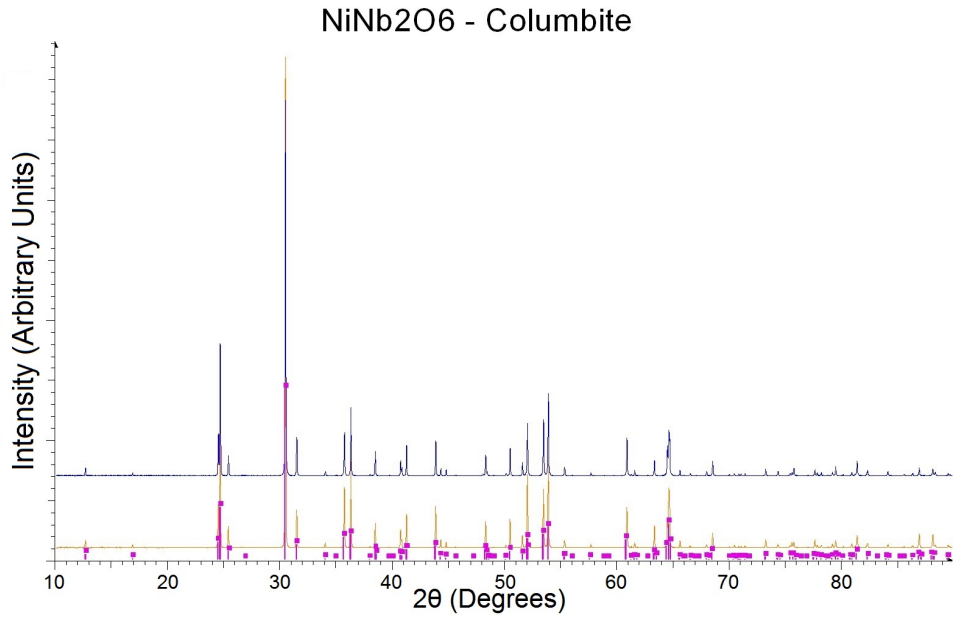

Figure 4.5: Powder x-ray diffraction from the black columbite phase single crystal (Top line, blue - Growth 14), the yellow polycrystalline niobate (bottom line, yellow - From growth 12, but essentially identical to all other growths) and a reference powder database (pattern 01-076-2354; a = 14.032 Å, b = 5.687 Å, c = 5.033 Å [172], magenta, peak intensity scaled arbitrarily.)

4.6 Discussion

β-$NiNb_2O_6$ was most stable when grown at higher speeds and with an excess of niobium oxide present as a flux. At slower speeds the system does form this phase, and the outcome is polycrystalline material, or small single crystals (mixed black and dark green) no larger than 1 mm x 1 mm x 1 mm. Additionally, there is almost always an outer shell of yellow polycrystalline columbite. The thickness of the shell depended on the atmosphere in which it is grown. Increasing the oxygen content as well as an excess of niobium oxide tended to make the outer shell thinner.

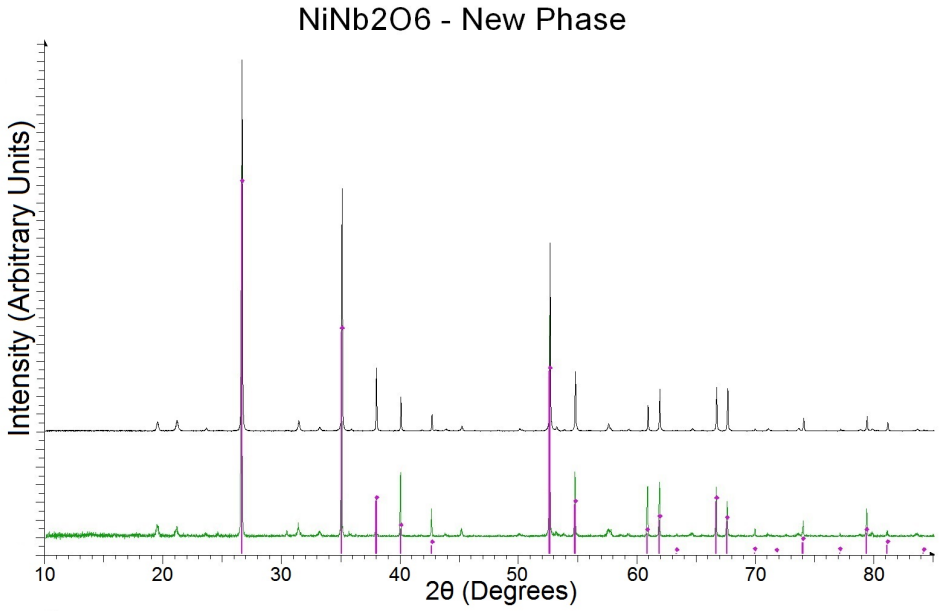

Figure 4.6: Powder x-ray diffraction from the black β-$NiNb_2O_6$ single crystal (Top line, black - Growth 15), the green single crystal (Bottom line, green - Growth 10), and a reference database orthorhombic cell, reported as tetragonal (pattern 01-076-2355; a = 4.71 Å, c = 3.038 Å, space group 136 [172] with scaled lattice parameters, magenta, peak intensity scaled arbitrarily)

Attempts to stabilize the material as a single crystal by growing slower does not visually create the same material. Based on x-ray analysis, we get a niobium deficient version, with vacancies on the niobium sites. Under a stereoscope, the material appears black and opaque, but thin pieces under light are transparent and dark green in colour. A SQUID magnetometry assessment of the black and the green material shows that the magnetic response does not change with slight deficiencies of niobium. A portion of these SQUID analyses appears in reference [176]. This is not an unsurprising result as niobium is not the magnetic species in this system, and a change like this would only lead to a small reduction in the nickel moment size due to the gain of a small percentage of extra electrons for charge balancing.

Using excess nickel oxide flux, we were able to significantly lower the growth temperature (by roughly 200 degrees). This allows us to avoid quenching and stabilized the columbite phase. Additionally, it allowed for more stable growth. This is to be expected as viscosity is inversely proportional to temperature. The nickel niobate in the columbite structure that were grown still had a thin layer of yellow polycrystalline material on the outside. The black internal material was identical to the polycrystalline shell, confirmed via powder XRD. With a lower temperature we obtained an external layer of polycrystalline material that could only be seen under magnification using the stereoscope; in essence we had eliminated the shell. The grown material was a mosaic of single crystals, both amber coloured and black, that were small (1-3 mm across).

4.7 Materials and Methods

The materials were prepared using 5N-purity niobium(V) oxide (Nb_2O_5) and 4N-purity nickel(II) oxide (NiO). Each of these materials was separately placed in a ceramic crucible and heated to 725 K in air for 12 hours with a ramp rate of 100 K per hour to remove any moisture. Weighting and hand-mixing of the oxides either stoichiometrically or with various excesses of NiO or Nb_2O_5 was performed. The oxides were pre-reacted in ceramic crucibles at 1475 K for 48 hours with a ramp rate of 100 K per hour and were subjected to intermediate grinding.

The obtained materials were checked for complete reaction using a PANalytical X'Pert powder X-ray diffractometer on a low-background silicon disk. The patterns were checked against the standards for nickel oxides, niobium

oxides and other nickel-niobium oxide compounds, such as $Ni_4Nb_2O_9$ and the obtained materials were reground and re-heated if necessary.

Once the powder was successfully synthesized, the materials were shaped into rods and placed in a hydrostatic press under a pressure of 50 MPa for 15 minutes. The rods were removed from their forms, placed in a ceramic boat and then fired at 1475 K for 48 hours. Both seed and feed rods were made in this manner. The rods were approximately 6 to 7mm in diameter and 8 to 11 cm in length.

The seed rod as hung on nickel wire in the OFZ furnaces. For the growth using a flux, a 5mm thick NiO flux pellet was used.

The materials were heated in the OFZ furnace initially at a ramp rate of approximately 1.5% power per minute and, in all cases, the seed and the feed rotating at approximately 6 rpm in the same direction. Once melting was evident, the rods were connected via a liquid bridge and counter-rotation was started. After a period of 1 to 2 minutes to stabilize, the growths were begun. Rotation was done in a counter-rotating fashion and speeds between 10 and 40 RPM were attempted, with 10 RPM on the top rod and 30 RPM on the bottom rod being the most successful.

During the growth, significant changes were only made at the beginning of the growth unless otherwise needed. Initial increases in rotation speeds were done in 5 minute intervals, and in steps of no more than 5 rpm. Temperature adjustments were made as necessary, depending on the growth speed. As an example, an experiment done with between 5 and 7 mm/hr growth speed

required a delay of approximately 15 minutes to see changes unless exceptional circumstances required a manual adjustment.

When a growth was terminated, the rod separation was conducted by reducing lamp power at a rate of 1% per minute until the liquid zone was terminated. At this point the upper rod rotation and movement were stopped, the lower rotation speed was reduced in 5 rpm steps and 10 second intervals to 6 rpm, the seed speed was set to zero and the cooling rate was set to 3% power per hour down to 25% lamp power, and 5% power per hour below that. For growths that were quenched, the procedure was modified to cool at 1% lamp power per minute down to the appropriate lamp power.

Material assessment by powder XRD was performed. Pieces of crystal were either cut or mechanically separated, and then ground into a fine powder for x-ray diffraction. Separated crystals were analyzed using a Laue diffractometer to determine growth direction. The original classification of β-$NiNb_2O_6$ was done using single crystal XRD and is reported in reference [176].

4.8 Conclusions

Through the processes described above, we have grown 5 mm x 3 mm x 1 mm sized crystals of pseudo-congruently melting (congruent composition different than stoichiometric composition) nickel niobate via the optical floating zone method. We found, separated and assessed a new phase in space group 86 ($P4_2/n$), confirmed by powder x-ray diffraction. We have explored how the growth conditions are affected in the nickel-rich and niobium-rich cases, and how those conditions change the polymorph that is stabilized. In the nickel

rich starting material we predominantly formed the columbite-structure (space group 60, Pbcn) of nickel niobate as the excess NiO allowed us to work at a lower temperature. In the niobium rich material the growth resulted in the β-$NiNb_2O_6$ polymorph, which required a higher temperature and a thermal quench after growth to get the best quality single crystals. We are presently examining and comparing the magnetic properties of these different polymorphs.

4.9 Acknowledgments

The authors would like to thank Dr. J.E. Greedan and Dr. A. Dabkowski for useful discussions on experimental direction. Research at McMaster is supported by a NSERC grant from the Government of Canada. TJSM would like to acknowledge support in the form of an OGS grant from the Ontario Provincial Government.

4.10 Contributions

"T.M., G.L and H.D. conceived and designed the experiments; T.M., A.M. and H.D. performed the crystal growths; T.M. performed the x-ray scattering; T.M. analyzed the data; T.M. wrote the paper with input from all authors."

4.11 Conflicts of Interest

"The authors declare no conflict of interest. The funding sponsors had no role in the design of the study; in the collection, analyses, or interpretation of data; in the writing of the manuscript, and in the decision to publish the

results".

The following abbreviations are used in this manuscript:

OFZ: Optical Floating Zone

QCP: Quantum Critical Point

NSERC: Natural Science and Engineering Research Council

OGS: Ontario Graduate Scholarship

rpm: revolutions per minute

XRD: X-Ray Diffraction

4.12 Additional Material

The following table, table 4.1 is supplementary for clarification of the specific growth conditions and not submitted as part of the paper.

Table 4.1: A partial summary of growth conditions in the NEC OFZ Image furnace, including gas type and pressure, growth speeds, rotation rates and starting composition. Feed rate was adjusted to keep the growth stable.

Growth	**Overpressure (kPa)**	**Gas**	**Growth Rate (mm/hr)**	**Upper (rpm)**	**Lower (rpm)**	**Composition**
3	200	Ar-H_2	3.0 to 4.5	10	30	On Stoichiometry
4	200	O_2	5.0 to 6.9	12	25	On Stoichiometry
5	200	O_2	24.0	15	20	On Stoichiometry
6	200	O_2	2.6 to 2.8;30	15	20	On Stoichiometry
7	200	O_2	10.0 to 15.3	15	30	On Stoichiometry
8	200	O_2	4.0	0	0	On Stoichiometry
9	40	O_2	21.5	10	30	On Stoichiometry
10	0	O_2	3.1 to 3.7	10	40	1.4% NiO Excess
11	0	O_2	25.5	10	30	1.4% NiO Excess
12	0	O_2	20.0 to 23.0	20	20	1.4% NiO Excess
13	0	Air	20.0 to 22.2	15	30	1.4% NiO Excess
14	0	O_2	8.3	7	25	4% Nb_2O_5 Excess
15	0	O_2	3.3	10	25	4% Nb_2O_5 Excess
16	0	O_2	3.3	7	20	4% NiO Excess

Chapter 5

Characterizations of the New Polymorph of Nickel Niobate

5.1 Overview and Fit

The contents of this chapter are an example of a 'next-step' of the work described in chapter 4. The contents of this chapter describe the analysis and initial characterizations of the new polymorph of nickel niobate; now that we had a new material it was necessary to determine the properties that it exhibits to see what interesting physics, if any, exists.

In chapter 4, the synthesis and the x-ray diffraction validating this was presented. This chapter has a small amount of material that is repetitive due to the nature of publishing a full story, and expands by applying different techniques to better understand the material we created.

A natural first step, once we had determined that we had a polymorph of the original material that did not match anything in the database was to determine the structure for ourselves. The easiest way was to perform an anal-

ysis of x-ray diffraction on a single crystal. Here we were able to determine the space group and the structure unambiguously. From this analysis we learned that, potentially, this material was synthesized previously, but based on x-ray techniques and luminosity available at the time it was likely misclassified. The results of the single crystal x-ray data were uploaded to the Inorganic Crystals Structural Database (ICSD), available as structure 429821.

Following this analysis, the new material was examined using SQUID magnetometry to identify if any magnetic phase transitions existed. When low temperature transitions were shown, specific heat was also measured to allow a hypothesis on the type of phase transition to be created.

5.2 Front Matter

The title for this paper is "Crystal growth and magnetic characterization of a tetragonal polymorph of $NiNb_2O_6$" as well as the Corrigendum to the article. These were published in the *Journal of Solid State Chemistry*, Volume 236 pages 19 to 23 in 2016. The Corrigendum was published in the *Journal of Solid State Chemistry*, Volume 239 page 282 in 2016.

The authors of both articles are, in order, Timothy Munsie (Department of Physics and Astronomy, McMaster University), Anna Millington (Department of Physics and Astronomy, McMaster University), Dr. Paul Dube (Brockhouse Institute for Materials Research), Dr. Hanna Dabkowska (Brockhouse Institute for Materials Research), Dr. Jim Britten (Department of Chemistry, McMaster University; and the Brockhouse Institute for Materials Research), Dr. Graeme Luke (Department of Physics and Astronomy, McMaster University;

the Brockhouse Institute for Materials Research; and the Canadian Institute for Advanced Research) and Dr. John Greedan (Department of Chemistry, McMaster University; and the Brockhouse Institute for Materials Research).

The relative contributions of each co-author is written as part of the submitted article below in section 5.12.

This paper is reproduced with permission.

5.3 Abstract

A previously unidentified polymorph of nickel niobate, $NiNb_2O_6$, was grown and stabilized in single crystalline form using an optical floating zone furnace. Key parameters of the growth procedure involved use of a slight excess of NiO (1.2% by mol), an O_2 atmosphere and a growth rate of 25 mm/hr. The resulting boule consisted of a polycrystalline exterior shell of the columbite structure - columbite is the thermodynamically stable form of $NiNb_2O_6$ under ambient conditions - and a core region consisting of transparent yellow-green single crystals up to 5 mm x 2 mm x 1 mm in dimension of the previously unidentified phase. The crystal structure, solved from single crystal x-ray diffraction data, is described in the $P4_2/n$ space group. Interestingly, this is not a subgroup of $P4_2/mnm$, the rutile space group. The Ni^{2+} ions form layers which are displaced such that interlayer magnetic frustration is anticipated. Magnetic susceptibility data shows a broad maximum at approximately 22 K and evidence for long range antiferromagnetic order at approximately 14 K, obtained by Fisher heat capacity analysis as well as heat capacity measure-

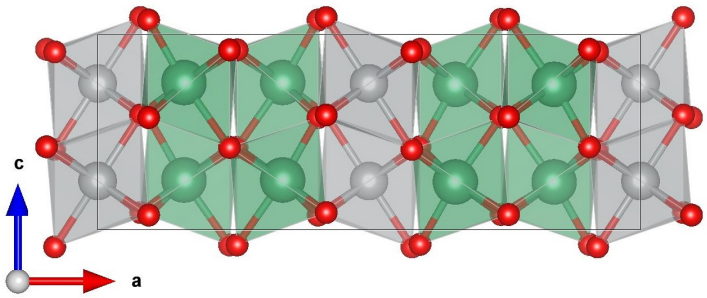

Figure 5.1: The unit cell for columbite nickel niobate. The chains of nickel and niobium octahedra can easily be seen. The red atoms are oxygen, the silver atoms are nickel and the green atoms are niobium.

ments. The susceptibility data for T > 25K are well fit by a square lattice S=1 model, consistent with the Ni sublattice topology.

5.4 Introduction

Metal niobates, ANb_2O_6 (A = Ni, Co, Fe) typically form a columbite phase(Pbcn) [55]. In this structure, figure 5.1, the oxygen atoms form corner-sharing octahedra around the A^{2+} and Nb^{5+} ions, creating isolated zig-zag chains of the A ions, which have recently been shown to exhibit interesting magnetic properties in the case of Co^{2+} [51, 171, 178]. For the case of $NiNb_2O_6$ it has been previously reported that, upon quenching from 1675 K, a disordered rutile polymorph ($P4_2/mnm$) can be recovered [172, 179].

The optical floating zone (OFZ) technique is highly suited to the growth of high purity single crystals, especially metal oxides [81]. The attempt to grow columbite nickel niobate was motivated by the desire to compare this material, where the nickel would be in a spin-1 state, to the cobalt version, where the spin is equivalent to spin-$\frac{1}{2}$. Additionally, a significant amount of work

has gone into engineering and synthesizing ANb_2O_6 nanopowders for applications to microwave resonators due to the wide range of magnetic transitions experienced by this family [180, 181, 182, 183].

5.5 Synthesis

Columbite $NiNb_2O_6$ powder was first synthesized using a solid state pre-reaction of a stoichiometric mixture of pre-annealed nickel(II) oxide (NiO) and niobium(V) oxide (Nb_2O_5). This mixture was subjected to hydrostatic pressure at 50 MPa for 15 minutes and then sintered below the melting point of the materials; at 1475 K for 48 hours with an intermediate grinding, reformation and pressing. The result was a sintered rod of 80 mm in length and 7 mm in diameter.

5.6 Crystal Growth

Crystal growth experiments were carried out by the optical floating zone (OFZ) technique [81] in a Canon optical floating zone image furnace. Initial attempts followed published reports on the growth of columbite $NiNb_2O_6$, using a mixture of 10% O_2 in Ar [55]. Several runs using a stoichiometric rod composition, the stated gas mixture at one atmosphere and at two atmospheres overpressure and a variety of growth rates in the range of 3 to 7 mm/hr failed to produce a crystal of the columbite phase. The results always consisted of a boule with a core/shell structure, with the shell being polycrystaline columbite

and the core consisting of small black crystals. Using pure O_2, again at the stated pressures, did not improve the result.

Our next step was to introduce a small excess of NiO (1.2 % by mol) into the starting rod. The decision was guided by previous reports where it was shown that excess NiO would drive the system into the columbite region of the phase diagram [184]. We found the optimal conditions had O_2 gas at a one atmosphere overpressure and a rapid growth rate of 25 mm/hr. The growth was terminated by a quench of the material from approximately 1675 K to room temperature over one hour. While a core/shell structure was still present, a portion of the core in this case consisted of transparent, yellow-green single crystals of dimension up to 5 mm x 2 mm x 1 mm. The crystals comprised about 20% of the volume of the grown boule. The Laue pattern in figure 5.3 confirms that these are indeed single crystals. Figure 5.2 shows a visual representation of the growth. The crystal begins with a black, single-crystalline phase. We determined this to be the same as the green crystals with some columbite inclusions. The system became stable and formed an external facet, visible in the upper panel of figure 5.2. The material had an outer core of columbite and had these crystals grown as shown in the second lower panel arranged perpendicular to the facet with 1-2 mm widths. Although externally no parameters were changed, the facet spontaneously stopped, which is marked by the third lower panel. Here we see some mix of the black and green crystals, with the emergence of a polycrystalline niobate core. Some inclusion of non-columbite material is still evident. By the time the growth was terminated, the tip was fully polycrystaline columbite.

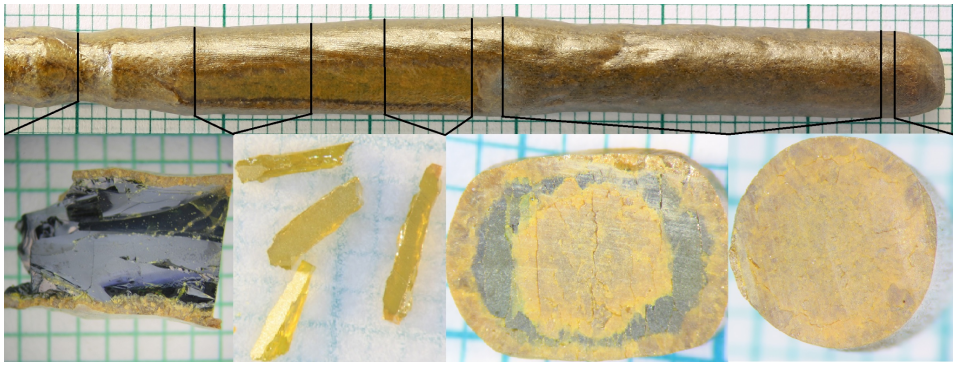

Figure 5.2: A sectioned, as-grown boule. The first portion of the crystal is the black $NiNb_2O_6$ crystal and extends until a facet is visible. Throughout the facet we get green single crystals that are easily separated from each other as shown in the second panel. At the termination of the facet some black phase re-emerges mixed with the green phase, as well as some columbite polycrystal. By the end the tip is entirely columbite polycrystal.

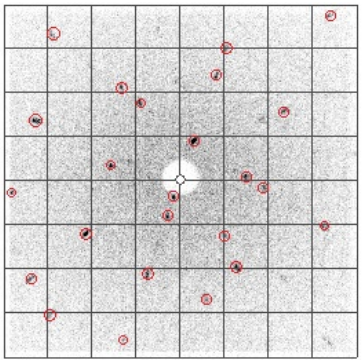

Figure 5.3: Laue diffraction pattern from one face of a nickel niobate crystal. The pattern was fit to a 24 point match indicating this face is aligned perpendicular to the a-axis. The red circles represent the points that were fit.

5.7 Structural Determination

We crushed some of the extracted single crystals into a fine powder and examined them using a PANalytical X'Pert powder x-ray diffractometer. The resulting diffraction pattern did not match the known structure for columbite $NiNb_2O_6$ nor a simulated pattern for the rutile phase [172]. Thus it was clear that we had stabilized an unreported polymorph of $NiNb_2O_6$.

A small piece of one single crystal was selected and single crystal x-ray diffraction was performed on the sample using a Bruker Smart Apex 2 diffractometer with a sealed tube molybdenum source and a TRIUMPH monochromator. ω- and ϕ-scans were used to obtain complete coverage of the diffraction pattern to 0.5 Å.

The data was refined using Olex2 [185] and the structure was solved using SHELXT [186]. We found that the structure belonged to space group 86 ($P4_2/n$) with lattice constants of a= 6.6893 (3)Å and c = 9.0956(11)Å. Using ADDSYM EXACT [187, 188], run from PLATON [189] before disorder modelling of the system confirmed the correct choice of space group. The determination of the space group and the lattice constants conclusively show that we have a new polymorph of $NiNb_2O_6$. The single crystals are merohedrally twinned 50/50 on a diagonal twinning mirror perpendicular to the a direction. By applying mirroring R1 dropped from 8% to 3.06%. Disorder refinement on the metal sites gave 98.8(2)% Nb:1.2% Ni on the Nb1 site and 97.5(4)%Ni: 2.5%Nb on the Ni1 site assuming fully occupied oxygen sites and charge balance. This operation dropped R1 to 2.96%. The results of this refinement are shown in tables 5.1 to 5.3. The crystal structure solution is available as a CIF from ICSD as CSD 429821.

For thoroughness, we compared this to the disordered rutile structure by ignoring the weak reflections and reducing the cell volume to $\frac{1}{6}$ by using the c-face diagonal as the a-axis and one third of the c-axis. Solution and refinement in the $P4_2/mnm$ space group gave the expected rutile structure with R1=8% and a large anisotropic displacement parameter for the mixed metal site.

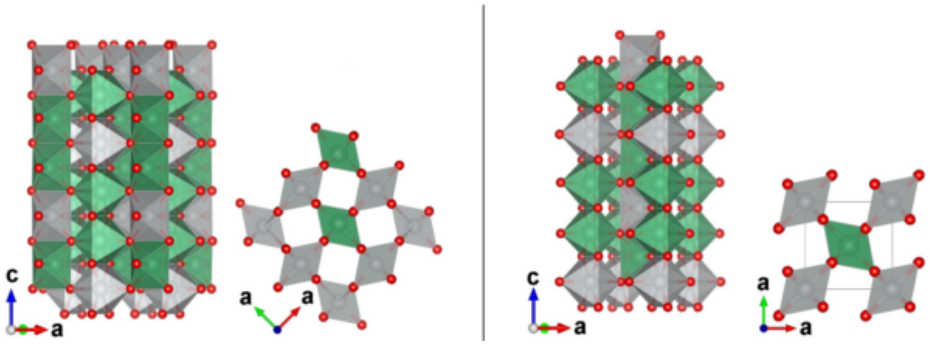

Figure 5.4: The left images show the solved structure of the as-grown polymorph of nickel niobate from space group 86. The right images show $NiTa_2O_6$ in the tri-rutile space group(136, $P4_2/mnm$) [190]. The red atoms are oxygen, the silver atoms are nickel and the green atoms are niobium on the left and tantalum on the right.

In comparison, assuming a trirutile structure, we again ignored the weak reflections and the cell volume was reduced to $\frac{1}{2}$ by using half the c-face diagonal as the a-axis. Solution and refinement in the $P4_2/mnm$ space group gave the expected structure with R1=13% and unacceptable anisotropic displacement parameters for the metal sites. This is further confirmation of the proposed larger cell and the $P4_2/n$ space group. We subsequently refined the powder data using EdPCR, a part of the FullPROF suite [87] which agreed well with the theoretical pattern based on the atomic arrangment found using single crystal scattering.

The structure of $NiNb_2O_6$-$P4_2/n$ differs only in subtle ways from that of tri-rutile, $P4_2/mnm$, although there is no strict symmetry relationship as $P4_2/n$ is not a subgroup of $P4_2/mnm$. This is illustrated in Figure 5.4 where $NiNb_2O_6$ is compared with the tri-rutile phase $NiTa_2O_6$. Both structures are based on infinite chains of edge-sharing octahedra that are linked by corner-sharing with site ordering of Ni/Nb and Ni/Ta and the a-plane projections are essentially

Table 5.1: Fractional Atomic Co-ordinates (x10^4) and equivalent isotropic displacement parameters (Å^2)x10^3 for $NiNb_2O_6$

Atom	**x**	**y**	**z**	**U(eq)**
Nb1	164.9(4)	5222.0(4)	6685.7(2)	6.99(6)
Ni1	5000	5000	5000	4.35(8)
Ni2	164.9(4)	5222.0(4)	6685.7(2)	6.99(6)
Nb2	5000	5000	5000	4.35(8)
O1	-1(3)	7044(2)	8275.1(17)	5.2(2)
O2	7(2)	6910(2)	4996.9(19)	4.88(18)
O3	3017(2)	5013(3)	6737.5(17)	5.3(2)

Table 5.2: Anisotropic displacement parameters (Å^2)x10^3 for $NiNb_2O_6$

Atom	$\mathbf{U_{11}}$	$\mathbf{U_{22}}$	$\mathbf{U_{33}}$	$\mathbf{U_{23}}$	$\mathbf{U_{13}}$	$\mathbf{U_{12}}$
Nb1	7.11(9)	8.47(10)	5.40(8)	-0.23(7)	-0.05(8)	-0.41(5)
Ni1	4.65(15)	4.01(14)	4.39(12)	0.21(17)	0.28(14)	0.07(7)
Ni2	7.11(9)	8.47(10)	5.40(8)	-0.23(7)	-0.05(8)	-0.41(5)
Nb2	4.65(15)	4.01(14)	4.39(12)	0.21(17)	0.28(14)	0.07(7)
O1	8.1(6)	2.6(5)	5.0(4)	-0.5(4)	-0.4(4)	0.0(4)
O2	7.9(5)	3.2(4)	3.5(3)	0.6(4)	-0.4(4)	-0.2(3)
O3	2.7(5)	8.1(6)	5.0(4)	-0.5(5)	-0.5(4)	0.5(4)

Table 5.3: Bond lengths for $NiNb_2O_6$

Atom	**Atom**	**Length (Å)**	**Atom**	**Atom**	**Length (Å)**
Nb1	O1	1.8942(16)	Ni1	O3	2.0633(16)
Nb1	O1	2.0931(16)	O1	Nb1	2.0931(16)
Nb1	O2	1.9092(16)	O1	Ni1	2.0812(16)
Nb1	O2	2.0950(16)	O1	Ni2	2.0931(16)
Nb1	O3	1.9135(17)	O1	Nb2	2.0812(16)
Nb1	O3	2.0608(16)	O2	Nb1	2.0950(16)
Ni1	O1	2.0812(16)	O2	Ni1	2.0672(14)
Ni1	O1	2.0812(16)	O2	Ni2	2.0950(16)
Ni1	O2	2.0672(14)	O2	Nb2	2.0672(14)
Ni1	O2	2.0672(14)	O3	Nb1	2.0607(16)
Ni1	O3	2.0633(16)	O3	Ni2	2.0607(16)

the same after accounting for the different unit cells. The a-axis for $NiNb_2O_6$ is $\sqrt{2a}$ in comparison to $NiTa_2O_6$ (a= 4.271 Å). However, the Nb^{5+} ion occupies a general site, 8e, while Ta^{5+} is found in 4e with 2mm symmetry. The result is a tilting of the Nb-O polyhedron that gives rise to the larger unit cell for $NiNb_2O_6$. This is remarkable as the accepted VI-fold radii for Nb^{5+} and Ta^{5+} are identical, 0.64 Å [66]. The observations above have implications for the expected magnetic properties, as the Ni sublattice will be essentially identical to that for $NiTa_2O_6$, i.e. body-centred tetragonal, a topology which is known to give rise to a type of interlayer geometric frustration [191, 192].

5.8 Magnetometry

The 4.63 mg sample of the yellow single crystal fragment was used for susceptibility measurements in a Quantum Design MPMS XL SQUID magnetometer. The data taken from 2 K to 300 K can be found in figures 5.5-5.6. From figure 5.5 a broad maximum at $\sim$ 22.5 K, typical for low dimensional magnetic materials. These results are very similar to those for the related tri-rutile phase $NaTa_2O_6$ [191] and, given that the Ni sublattices of this phase and $NiNb_2O_6$ are essentially identical, this is not surprising. Data for the tantalate material have been fitted to various short range models including a S = 1 square planar [193], a S = $\frac{1}{2}$ Ising [191] and a S = 1 Heisenberg chain [192].

The solid line in Figure 5.5 is a fit to the square lattice S = 1 model of Rushbrooke and Wood [194] which yields G = 2.29(7) and J/k_B = -5.26(3) K.

This fit is merely illustrative of the low dimensionality of the magnetism in $NiNb_2O_6$ and is hardly definitive. The issue of the best model for describing the

short range order will be dealt with in a companion paper. Note that a g-factor > 2 is expected for d^8 Ni^{2+} as the d-shell is greater than half-filled. In the inset to Figure 5.5 is shown a fit to the Curie-Weiss law, equation 5.1, over the range 50 K to 300 K. The extracted parameters are C = 1.406 emu/mole-K and θ = -37.0(9) K, indicating dominant antiferromagnetic exchange correlations. The derived $\mu_{eff} = 3.354(5)\mu_B$ corresponds for a S = 1 system to g = 2.372(4), in excellent agreement with that obtained using the square lattice model.

$$\chi(T) = \chi_0 + \frac{C}{(T - \theta)} \tag{5.1}$$

In addition, a Fisher heat capacity analysis was carried out to locate T_N [195] and this is shown in figure 5.6, superimpopsed on the low temperature susceptibility data, giving a value of $\sim$ 14 K. The ratio $\theta/T_N = 1.6$ is smaller than that for $NiTa_2O_6 = 25.5/10.3 = 2.47$ [191].

5.9 Heat Capacity

We performed heat capacity measurements on a 4.63 mg single crystal of nickel niobate in an Oxford Instruments MagLab EXA system over a temperature range of 2 to 50 K. This data is plotted up to 30 K in figure 5.7. A quantity of 100 μg of Apiezon N grease was used to secure the crystal to the sapphire substrate, for which the software automatically subtracted the contribution to the signal. The heat capacity shows a sharp anomaly between 14 and 14.5 K, indicative of an ordering transition.

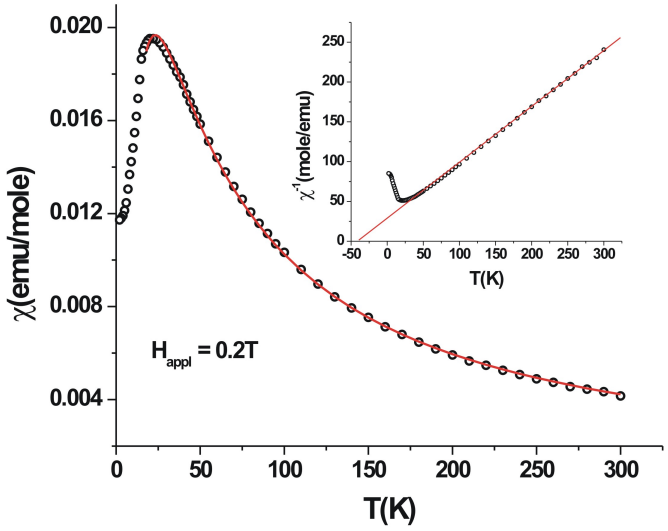

Figure 5.5: SQUID magnetometry measurements with a 2 kOe field applied along the c axis. The susceptibility curve is fit to a S=1 2D model. The inset shows the Curie-Weiss Fit to the inverse susceptibility.

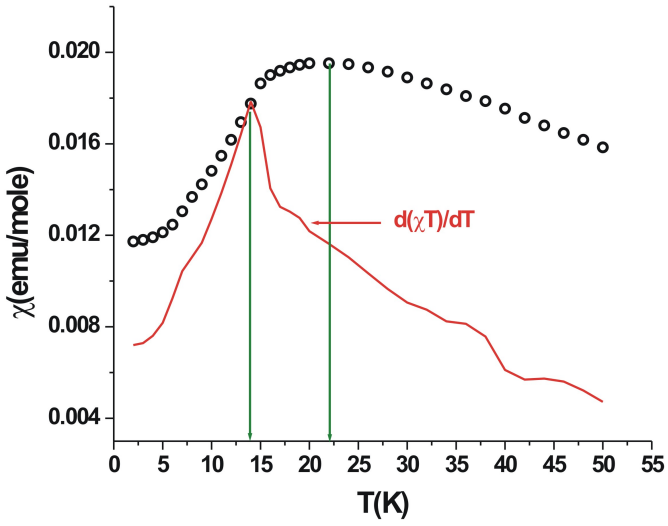

Figure 5.6: The red curve drawn on top of the susceptibility data is the Fisher Heat Capacity, $\frac{d(\chi \cdot T)}{dT}$. We see a definite peak in the heat capacity at between 14.5 K and 15 K, indicative of the phase transition. This is in contrast to the broad peak in the susceptibility data, which we see between 22 and 22.5 K.

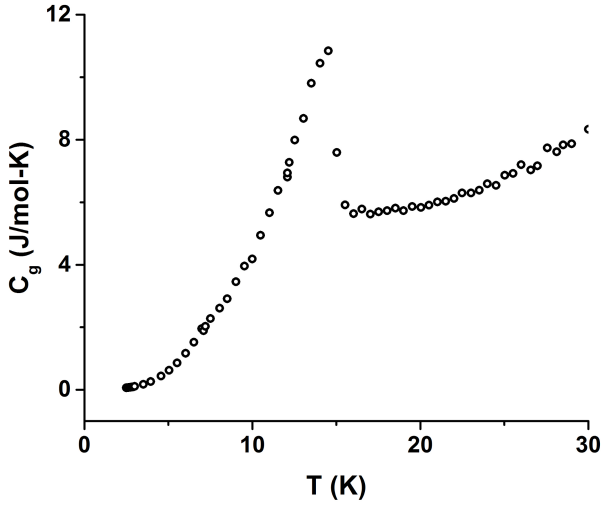

Figure 5.7: Heat Capacity of Nickel Niobate measured from 2 to 30 K. A peak is seen at 14 K.

5.10 Conclusion

A polymorph of $NiNb_2O_6$ not previously well characterized has been grown in the form of relatively large single crystals using the optical floating zone method. The structure of this phase is described in $P4_2/n$, a space group not previously reported for the family of AB_2O_6 materials. The structure is very closely related to that of tri-rutile, $P4_2/mnm$, but there does not exist a true group-subgroup relationship between the two space groups. The a-axis in $NiNb_2O_6$ is related to that for tri-rutile as $\sqrt{2a_{tr}}$ due to distortions in the Nb-O octahedron which are not present in the TaO octahedron in tri-rutile $NiTa_2O_6$, while the c-axes of the two materials are essentially identical. As suggested in the discussion of the structure solution, it is not impossible that this $P4_2/n$ form of $NiNb_2O_6$ is the same as that reported earlier, but described in a primitive rutile cell of one sixth the volume with random Nb/Ni site disorder. Thus,

given that tri-rutile is the stable form for $NiTa_2O_6$, it is not surprising that a rutile related phase would be found in the $NiNb_2O_6$ system. The difference in ground state energy between columbite and the $P4_2/n$ structures may be small. As the topology of the Ni sublattice is the same as that for tri-rutile, there is an expectation of low dimensional magnetism. This is confirmed by magnetometry and heat capacity measurements. The bulk susceptibility shows a broad maximum at ∼22 K but long range antiferromagnetic order sets in at ∼14 K as verified by heat capacity data. The magnetic susceptibility above ∼25 K is well fitted by a square lattice S = 1 model. Studies of the magnetic structure using both powder and single crystal neutron diffraction are underway along with an investigation of the spin dynamics via muon spin relaxation.

5.11 Acknowledgements

We would like to acknowledge assistance with the crystal growth by Ms. C. Marjerrison and useful discussions with Dr. A. Dabkowski. Partial funding for this research came from an Ontario Graduate Scholarship (OGS) award and National Science and Engineering Research Council (NSERC) grants. Instruments used were purchased using a grant from the Canadian Foundation for Innovation(CFI).

5.12 Contributions

TJSM, AM and HAD synthesized and grew the $NiNb_2O_6$ and prepared the samples for measurements. AM and JB performed the single crystal x-

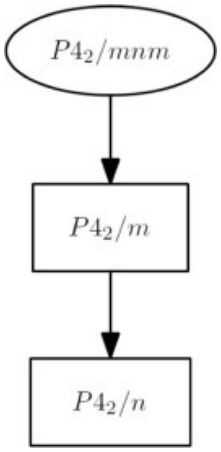

Figure C.1: A cartoon showing the relationships between space groups presented in the corrigendum.

ray and analysis. TJSM and JEG performed the powder x-ray and analysis. TJSM and PD performed the heat capacity measurements. TJSM performed the SQUID measurements. JEG, HAD and GML supervised the investigation. TJSM and AM wrote the paper with input from all authors.

5.13 Corrigendum

We have become aware of an error in this published manuscript. In it we stated that the space group of NiNb2O6, P42/n, is not a subgroup of the tri-rutile space group, P42/mnm. This is not correct. While the two space groups are not directly related, i.e. by a single step, they are connected via the intermediate symmetry P42/m, as shown below and which can be determined from a careful perusal of the International Tables for Crystallography (Vol. A) and of course the Bilbao Server. P42/m (#86) is a maximal non-isomorphic subgroup of P42/mnm (#186) and a minimal non-isomorphic supergroup of P42/n (#84). We thank Prof. J.M. Perez-Mato for guiding our understand-

ing of these relationships.Image 1The author would like to apologize for any inconvenience caused.

Chapter 6

Neutron Diffraction and Muon Spin Rotation in Nickel Niobate

6.1 Overview and Fit

In chapter 4 the synthesis and discovery of a new polymorph of nickel niobate was written, and in chapter 5 it was shown that the material exhibited a magnetic response. In chapter 5, development of material was typified as a three stage process.In this chapter the techniques of μSR and neutron scattering are used to examine the magnetism in the material, determine the magnetic structure and comment on the observed dynamics of the system.

Here, powder neutron scattering was done on a small sample owing partly to the limited amount of material available. The difference between the powder neutron scattering and data collected by x-ray is that the neutron scattering can see the magnetic interactions, as described in chapter 2. From this data we were able to determine that one of four spin structures was likely. The preliminary fits from susceptibility measurements as well as the known free

spin of Ni^{2+} ions suggested one set was more probable; this turned out to be incorrect and validates the continued study. To resolve the magnetic structure unambiguously, the method of choice was single crystal neutron scattering. This allowed us to focus on specific Bragg peaks, and additionally allowed us to characterize the critical transition as a power law with respect to temperature.

μSR was also conducted to examine the spin dynamics of the system. Antiferromagnetism shows up as the likely candidate for the type of magnetism based on the fits to the data measured. Additionally, as a small amount of powder of the columbite form was produced, a sister experiment allowed the comparison between the two different polymorphs, which showed that they have different magnetic responses, likely different classes of phase transition and different critical exponents.

Finally, the μSR results were briefly contrasted with those of cobalt niobate so that the differences between an effective spin-$\frac{1}{2}$ and a spin-1 particle on the magnetic site of am isomorphic columbite could be examined.

6.2 Front Matter

The title for this paper is "Neutron Diffraction and μSR Studies of Two Polymorphs of Nickel Niobate ($NiNb_2O_6$)" and it has been submitted in the journal *Physical Review B* and is available on the arXiv preprint server [196].

The authors of both articles are, in order, Timothy Munsie (Department of Physics and Astronomy, McMaster University), Murray Wilson (Department of Physics and Astronomy, McMaster University), Dr. Corey Thompson (De-

partment of Chemistry, Purdue University), Dr. Roxana Flacau (Canadian Neutron Beam Centre), Cui Ding (Department of Physics, Zhejiang University), Zhizhou Gong (Department of Physics, Columbia University), Shengli Guo (Department of Physics, Zhejiang University), Dr. Adam Aczel (Quantum Condensed Matter Division, Oak Ridge National Laboratory), Dr. Huibo Cai (Quantum Condensed Matter Division, Oak Ridge National Laboratory), Dr. Travis Williams (Quantum Condensed Matter Division, Oak Ridge National Laboratory), Dr. Hanna Dabkowska (Brockhouse Institute for Materials Research), Dr. Fanlong Ning (Department of Physics, Zhejiang University), Dr. John Greedan (Department of Chemistry, McMaster University; and the Brockhouse Institute for Materials Research) and Dr. Graeme Luke (Department of Physics and Astronomy, McMaster University; the Brockhouse Institute for Materials Research; and the Canadian Institute for Advanced Research).

The relative contributions of each co-author is as follows: TM and HD grew the sample of nickel niobate. TM prepared the sample for all experiments performed in this work. Initial characterization was performed by TM. Powder neutron measurements at Chalk River were performed by RF. Powder neutron data was analyzed by CT, TM and JG. Single crystal neutron scattering at Oak Ridge National Laboratory was performed by TM, HC, AA and TW. Single crystal data analysis was performed by TM, HC and AA. μSR measurements were performed by TM, MW, CD, ZG and SG. μSR data was analyzed by TM with input from MW and GL. The manuscript was written by TM and JG with input from the other authors. The project was conceived by TM, FN, JG and GL.

6.3 Abstract

Neutron diffraction and muon spin relaxation (μSR) studies are presented for the newly characterized polymorph of $NiNb_2O_6$ (β-$NiNb_2O_6$) with space group $P4_2/n$ and μSR data only for the previously known columbite structure polymorph with space group Pbcn. The magnetic structure of the $P4_2/n$ form was determined from neutron diffraction using both powder and single crystal data. Powder neutron diffraction determined an ordering wave vector $\vec{k} = (\frac{1}{2}, \frac{1}{2}, \frac{1}{2})$. Single crystal data confirmed the same $\vec{k}$-vector and showed that the correct magnetic structure consists of antiferromagnetically-coupled chains running along the a or b-axes in adjacent Ni^{2+} layers perpendicular to the c-axis, which is consistent with the expected exchange interaction hierarchy in this system. The refined magnetic structure is compared with the known magnetic structures of the closely related tri-rutile phases, $NiSb_2O_6$ and $NiTa_2O_6$. μSR data finds a transition temperature of $T_N \sim 15$ K for this system, while the columbite polymorph exhibits a lower $T_N = 5.7(3)$ K. Our μSR measurements also allowed us to estimate the critical exponent of the order parameter β for each polymorph. We found $\beta = 0.25(3)$ and 0.16(2) for the β and columbite polymorphs respectively. The single crystal neutron scattering data gives a value for the critical exponent $\beta = 0.28(3)$ for β-$NiNb_2O_6$, in agreement with the μSR value. While both systems have β values less than 0.3, which is indicative of reduced dimensionality, this effect appears to be much stronger for the columbite system. In other words, although both

systems appear to well-described by $S = 1$ spin chains, the interchain interactions in the β-polymorph are likely much larger owing to the higher critical exponent.

6.4 Introduction

Most transition metal niobates, ANb_2O_6, crystallize in the columbite space group (Pbcn, space group 60) [47, 171, 172], seen in Fig. 6.1a. In columbite, the zigzag edge-sharing chains of AO_6 octahedra are oriented parallel to the c-axis. These are separated by Nb-O edge-sharing chains in both the bc plane (shown) and by two such chains in the ac-plane (not shown) leading to dominant one dimensional magnetic interactions. The case of cobalt niobate ($CoNb_2O_6$) has been of strong, recent interest [156, 161, 51, 162, 54, 53, 197] since the cobalt ion has an effective spin of $\frac{1}{2}$ and exhibits a quantum phase transition in a modest applied field, with clear experimental signatures of quantum critical phenomena previously predicted for the transverse field Ising model [54].

Another columbite structure niobate that has been studied and is of special interest is $NiNb_2O_6$, where Ni^{2+} ($S = 1$) replaces Co^{2+} ($S_{eff} = \frac{1}{2}$). Short range ferromagnetic spin correlations develop in this material on cooling due to the dominant intrachain interactions, with long range antiferromagnetic order ultimately being achieved at $T_N = 5.7$ K due to finite interchain interactions [175, 174]. The magnetic structure of columbite $NiNb_2O_6$ was solved from powder neutron diffraction data [47], but the order parameter has not been reported.

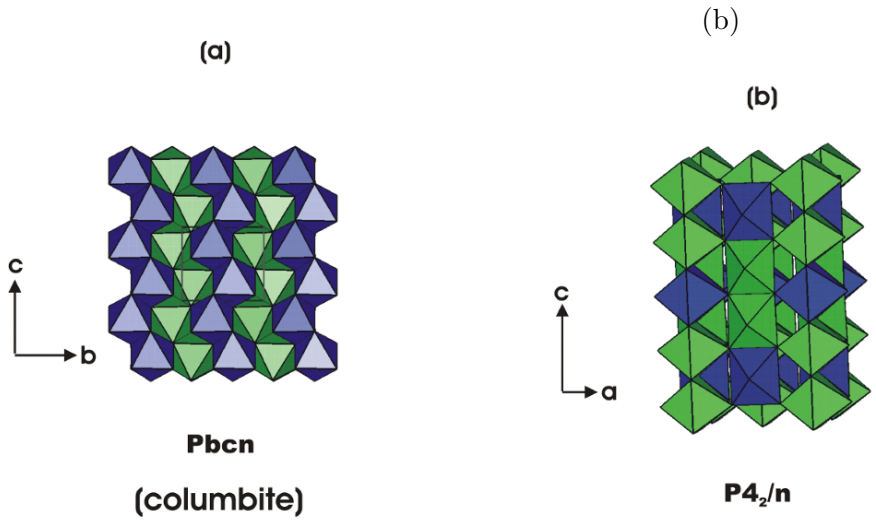

Figure 6.1: (Colour online)Two polymorphs of $NiNb_2O_6$. The blue (dark) octahedra contain nickel, the green (light) octahedra contain niobium. Images created with VESTA [91]. (a) A bc plane view of the columbite structure showing the zigzag chains of edge sharing Ni-O octahedra along c. Data from [47]. (b) An ac plane view of the $P4_2/n$ polymorph showing the absence of the edge-sharing Ni-O octahedra.

Initial attempts to synthesize $NiNb_2O_6$, following previously reported growth techniques [55], resulted in the formation of phases of both the expected columbite structure and a new polymorph crystallizing in $P4_2/n$ (space group 86), a space group not previously reported in members of the AB_2O_6 family [177]. Structural features of the new polymorph, β-$NiNb_2O_6$, are shown in Figs. 6.1b and 6.3a. Of note is the absence of edge-sharing NiO_6 octahedra as found in the columbite form, shown in Fig. (6.1a). Instead, the Ni^{2+} ions are seen to form a body-centred tetragonal (b.c.t.) lattice, which is identical to that found in the closely related phases $NiTa_2O_6$ and $NiSb_2O_6$ that crystallize in the tri-rutile (TR) structure, $P4_2/mnm$ (space group 136). $P4_2/mnm$ and $P4_2/n$ are related in a group-subgroup sense via the intermediate $P4_2/m$

symmetry [198]. The principle difference between the structures in the $P4_2/n$ group for nickel niobate and the more symmetric TR form ($P4_2/mnm$) is the position of the O^{2-} ions which results in a highly-distorted NbO_6 octahedron with six different Nb-O distances in the former. This is attributed to a second order Jahn-Teller distortion [57]. As a result of these distortions, the $P4_2/n$ unit cell has twice the volume of a TR cell with $a = \sqrt{2}a_{TR}$, $c = c_{TR}$.

Body-centred tetragonal sublattices are well-known to give rise to low dimensional antiferromagnetism; for example, K_2NiF_4 and many related materials exhibit strong two-dimensional spin correlations [199]. The cases of $NiTa_2O_6$ and $NiSb_2O_6$ are most relevant here. The bulk magnetic properties of these two systems are very similar to those of $NiNb_2O_6$, as summarized in Table 6.1. All three materials show a broad χ_{max} above 20K followed by long range order at significantly lower temperatures. Recent studies argue that $NiTa_2O_6$ and $NiSb_2O_6$ are best described as Heisenberg $S = 1$ linear chain antiferromagnets [202, 192]. Thus, the magnetic dimensionality is a strong function of the positions of the ligands with respect to the metal ions in the b.c.t. sublattice. This is illustrated in Fig. 6.2 for the K_2NiF_4, TR and the $P4_2/n$ structures. In K_2NiF_4 the strongest exchange pathway involves nearest-neighbour Ni–O–Ni 180° linkages resulting in two-dimensional magnetism. For the TR structure the dominant exchange is between next nearest neighbours involving a M–O–O–M 180° pathway along [1 1 0], which gives rise to the one-dimensional magnetism. Recent Density Functional Theory (DFT) calculations show that the exchange constant for this pathway is ∼40 times stronger than any other in the TR structure [204]. The ligand positions in $P4_2/n$ are very similar to those in TR structure, with the main difference being that one

B	$\mu_{eff}\,(\mu_B)$	$\theta_c\,(K)$	$T\,(\chi_{max})\,(K)$	$T_N\,(K)$	Ref.
Ta	4.10	-41	25.5	10.3	[200, 191]
Sb	3.00	-50	~ 30	2.5	[201, 202]
Nb	3.35	-37	22.5	14.0	[203]

Table 6.1: A summary of the bulk magnetic properties of NiB_2O_6 (B = Ta, Sb, Nb) family.

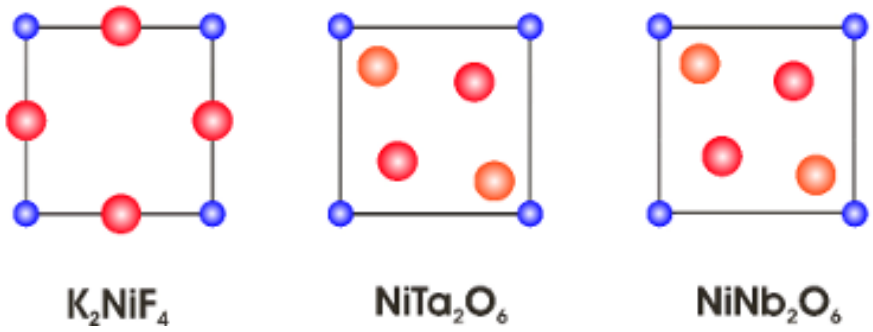

Figure 6.2: (Colour online) Ni (blue/small) and oxide ion (red and orange/large) positions in the K_2NiF_4, TR($NiTa_2O_6$ and $NiSb_2O_6$) and $NiNb_2O_6$ structures shown along a (001) square plane defined by the Ni ions. For K_2NiF_4 the oxide ions and the Ni ions are in the same plane. In $NiTa_2O_6$ and $NiNb_2O_6$ one set of O ions (red) are either exactly in the plane of the Ni ions (Ta) or only slightly out of the plane by 0.096Å (Nb), while the other set (orange) is either 1.55Å (Ta) or 1.57Å (Nb) from the plane.

set of O ions lies slightly out of the plane of the Ni ions, whereas in the TR structure these ions lie in the same plane. This is shown in Fig. 6.2.

The magnetic structures of the two TR phases are surprisingly different in spite of similar unit cell constants which differ by only 1-2%. For $NiTa_2O_6$, the magnetic structure is quite complex with $\vec{k} = [\frac{1}{4}, \frac{-1}{4}, \frac{1}{2}]$. The magnetic unit cell is orthorhombic with dimensions $a_M = \sqrt{2}a$, $b_M = 2\sqrt{2}a$ and $c_M = 2c$, V_M^{cell} = 8 V^{cell} [192, 204]. On the other hand, for $NiSb_2O_6$ the propagation vector is $\vec{k} = [\frac{1}{2}, 0, \frac{1}{2}]$ and the magnetic unit cell dimensions (also orthorhombic) are

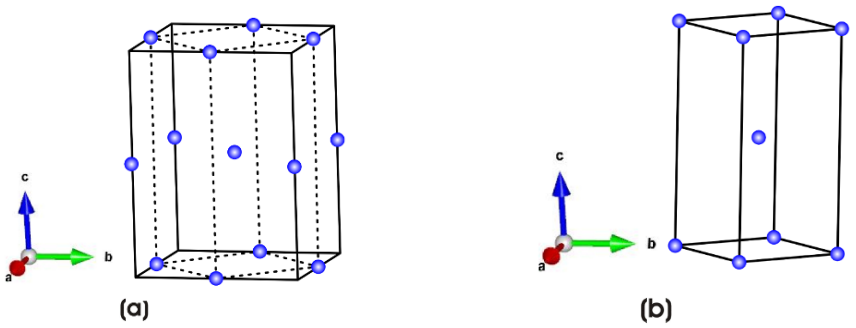

(a) (b)

Figure 6.3: A comparison of the nickel sites in (a) the β polymorph of nickel niobate and (b) the trirutile nickel tantalate. In Fig. 6.3a the cell of the same dimensions as the tantalate is outlined, demonstrating that for both materials the nickel sublattice has the same body-centred tetragonal symmetry.

a_M = a, b_M = 2b, c_M = 2c, V_M^{cell} = 4 V^{cell} [192]. Based on these findings, it is of particular interest to determine the magnetic structure for β-$NiNb_2O_6$.

We collected neutron diffraction data for β-$NiNb_2O_6$ on a powder sample at the Canadian Neutron Bean Centre and on a single crystal sample at Oak Ridge National Laboratory at selected temperatures between 4 and 20 K. Using μSR we studied both polymorphs of nickel niobate in their powder form with zero applied field as a function of temperature to measure their order parameters and to study spin dynamics.

6.5 Experimental Methods

A description of the growth of single crystal of both $NiNb_2O_6$ polymorphs has been reported [159].

Some single crystals of β-$NiNb_2O_6$ were separated and ground into a powder. Approximately 500 mg of sample was obtained. Powder neutron diffrac-

tion data were collected at the Canadian Neutron Beam Centre using the C2 diffractometer at 20 K and 3.5 K. Wavelengths of 1.33 Å and 2.37 Å were used. The sample was contained in a thin-walled vanadium can and cooled in a closed-cycle refrigerator.

The single crystal diffraction on the β-$NiNb_2O_6$ polymorph was done on a sample that was from the same crystal as the crushed powder. The crystal was oriented initially using Laue back-scattering x-ray diffraction and then realigned with neutrons in situ at the start of the experiment. The single crystal neutron diffraction experiment was performed at the HB3A four-circle diffractometer at the High Flux Isotope Reactor (HFIR) at Oak Ridge National Laboratory (ORNL) in the USA [205]. The sample was glued to the top of an aluminum rod and mounted in a closed-cycle helium-4 refrigerator with a temperature range of 4 to 450 K. The measurements used a monochromatic beam of neutrons with a wavelength of 1.546 Å selected from the (220) Bragg reflection of a bent silicon monochromator. The scattered intensity was measured using an area detector and the data were analyzed using the Graffiti software package [206] as well as the FullProf suite [87]. More specifically, we generated appropriate data for the nuclear refinement at 20 K by first fitting the rocking curves through the measured peak positions to Gaussians, and then the extracted integrated intensities were corrected by the appropriate Lorentz factors to obtain the experimental F^2 values. A similar procedure was used for the magnetic refinements, although the magnetic signal was first isolated by subtracting the high-temperature 20 K dataset from the corresponding low-temperature 4 K dataset.

Muon spin relaxation (μSR) [207, 138, 154] is a very sensitive technique that probes the internal magnetic field using the magnetic moment of the muon. These muons are implanted in a sample where they penetrate a few hundred μm, rapidly thermalize due to electrostatic interactions and finally settle at a Coulomb potential minimum in the material. Appropriate electronic vetoing removes any double counts due to cosmic ray muons or if multiple muons are generated and become incident on the sample within one observation window. A thin muon detector is placed at the entry to the sample chamber. The thin muon detector starts a clock registering the entry time of the muon. The muon will spontaneously decay into a positron and two neutrinos with a lifetime of 2.2 μs. In this decay, the positron is emitted preferentially in the direction of the muon spin at the time of decay. The positron will be detected in one of a number of scintilltors surrounding the sample and this will stop the clock and give a time from entry to decay. From the large ensemble of these events a histogram of positron counts in opposing detectors, N_A and N_B can be generated. Each positron counter will have an amplitude that fits the decay time of the muon with a signal representing the local field. By combining two opposing counters we can generate an asymmetry in the signal which is proportional to the spin polarization function: $A = \frac{N_A - N_B}{N_A + N_B}$. The LAMPF time-differential spectrometer with a helium-4 cryostat and a ultra low-background copper sample holder were used. This setup is capable of measuring in temperatures in the range of 2 to 300 K at fields from 0 to 4 kG applied longitudinally and allows for small transverse fields (up to $\sim$40 Gauss) to be applied using transverse Helmholtz coils. The time resolution for

the data bins was set to 0.2 ns and the data collection window was set to 11 μs plus a 125 ns background measurement for subtraction.

The samples used in the μSR measurements were originally single crystals, but were crushed into a fine powder to remove orientation dependence in the ordered sample; Therefore we expect $\frac{2}{3}$ of the signal to be oscillatory in nature, which arises from components of the local magnetic moment that are perpendicular to the initial muon polarization. The remaining $\frac{1}{3}$ of the signal, arising from components of the local magnetic moment that are parallel to the initial muon spin direction, will cause no precession [151]. With zero applied field, when a sample is in a paramagnetic state with no static magnetism we will see a nearly time independent asymmetry, with deviations caused by the nuclear magnetic moments. In an ordered state, we will see an oscillating asymmetry caused by precession at a frequency that is proportional to the magnetic field at the stopping site multiplied by the muon gyromagnetic ratio, $\sim$135.5 MHz/T. The powder was secured in thin-walled Mylar in the sample holder. All data was fit with the μSRfit data package [155].

6.6 Results and Discussion

6.6.1 Magnetic Structure of the β-$NiNb_2O_6$ polymorph

We refined the powder data at 20 K, well above $T_N \sim 15$ K, to check the sample quality and for any preferred orientation introduced by the grinding process. Our result shows good agreement with the single crystal model, al-

lowing for a shrinking of the cell dimensions due to cooling. This is shown in Figure 6.4 and Table 6.2.

a = 6.6851(4) Å		c = 9.0952(6) Å	
Atom	x	y	z	B(Å^2)
Ni	0.5	0.5	0.5	0.3(1)
Nb	-0.014(1)	0.4739(9)	0.6660(9)	0.5(1)
O1	0.005(3)	0.697(1)	0.832(2)	0.26(9)
O2	0.008(5)	0.695(1)	0.501(2)	0.26(9)
O3	0.292(1)	0.508(3)	0.683(2)	0.26(9)

R_{wp}	0.0461	R_{Bragg}	0.0857

Table 6.2: Cell constants, atomic positions, displacement factors and agreement indicies for the refinement of powder neutron diffraction data for $NiNb_2O_6$ in the $P4_2/n$ space group at 20 K.

Data were then collected at 3.5 K to determine the magnetic structure. Three magnetic reflections could be identified and indexed with $\vec{k} = (\frac{1}{2}, \frac{1}{2}, \frac{1}{2})$ as shown in Fig. 6.5.

Attempts to solve the magnetic structure were aided by representation analysis using the program SARAh [208]. For $P4_2/n$, $\vec{k} = \left(\frac{1}{2}, \frac{1}{2}, \frac{1}{2}\right)$ and Ni^{2+} at Wyckoff site 4e, there are four irreducible representations (IRs), Γ_1, Γ_3, Γ_5 and Γ_7, which provide potential basis vectors. The spin configurations consistent with these refinements are shown in Figure 6.6 based on the chemical unit cell.

Note that the models fall into two sets that are intricately related and cannot be distinguished by unpolarized neutron scattering. All the Ni ions are ordered in the Γ_1 and Γ_5 models, while for Γ_3 and Γ_7 only Ni ions in every other layer are ordered. The Γ_3 and Γ_7, taken separately, seems physically unreasonable as well; there is no experimental evidence that half of the spins

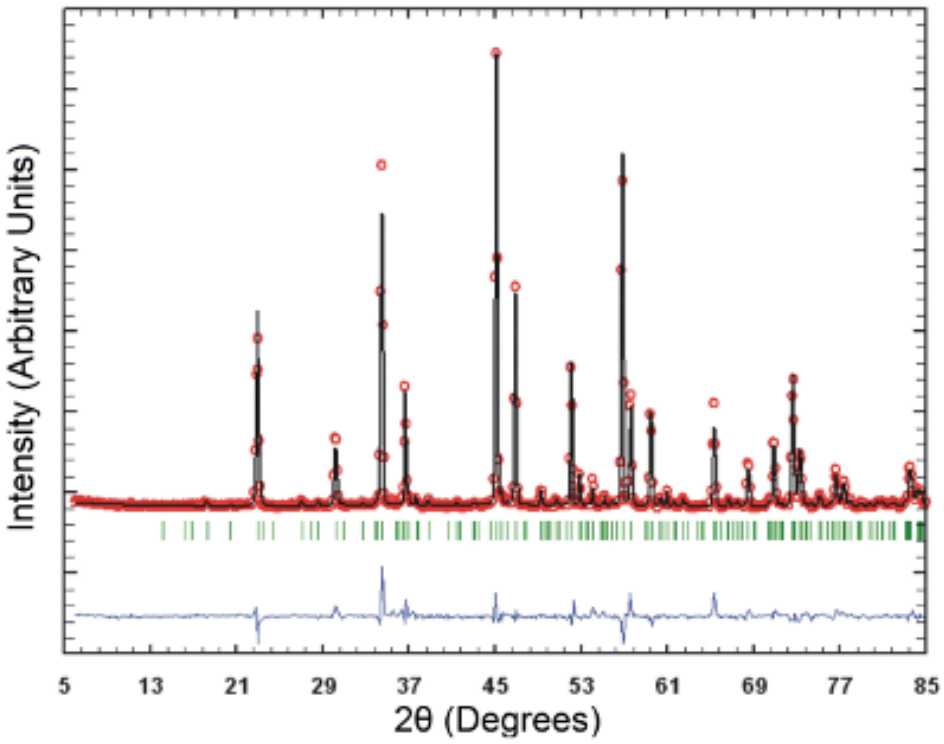

Figure 6.4: (Colour online) Rietveld refinement of neutron powder diffraction data at 20 K for β-$NiNb_2O_6$. The red circles are the data, the black line is the model, the blue line (below model) is the difference plot and the green tick marks locate the Bragg peaks. The wavelength is 1.33Å.

Atom	Γ_1	Γ_3	Γ_5	Γ_7
Ni1	$(\vec{v}_1, \vec{v}_2, \vec{v}_3)$	$(\vec{v}_1, \vec{v}_2, \vec{v}_3)$	$(\vec{v}_1, \vec{v}_2, \vec{v}_3)$	$(0, 0, 0)$
Ni2	$(-\vec{v}_1, -\vec{v}_2, \vec{v}_3)$	$(\vec{v}_1, \vec{v}_2, -\vec{v}_3)$	$(-\vec{v}_1, -\vec{v}_2, \vec{v}_3)$	$(0, 0, 0)$
Ni3	$(-\vec{v}_2, \vec{v}_1, \vec{v}_3)$	$(0, 0, 0)$	$(\vec{v}_2, -\vec{v}_1, -\vec{v}_3)$	$(\vec{v}_2, -\vec{v}_1, -\vec{v}_3)$
Ni4	$(\vec{v}_2, -\vec{v}_1, \vec{v}_3)$	$(0, 0, 0)$	$(-\vec{v}_2, \vec{v}_1, -\vec{v}_3)$	$(\vec{v}_2, -\vec{v}_1, \vec{v}_3)$

Table 6.3: A summary of the magnetic models from figure 6.6 based on their irreducible representations. $\vec{v}_1, \vec{v}_2,$ and $\vec{v}_3$ represent the ordered moment components along the a, b, and c crystallographic directions.

remain either paramagnetic or in a two-dimensional correlated state at 3.5 K. For example, there is no low temperature Curie-Weiss tail in the measured susceptibility [203] and the peak shape of the magnetic reflections, Fig. 6.5, shows

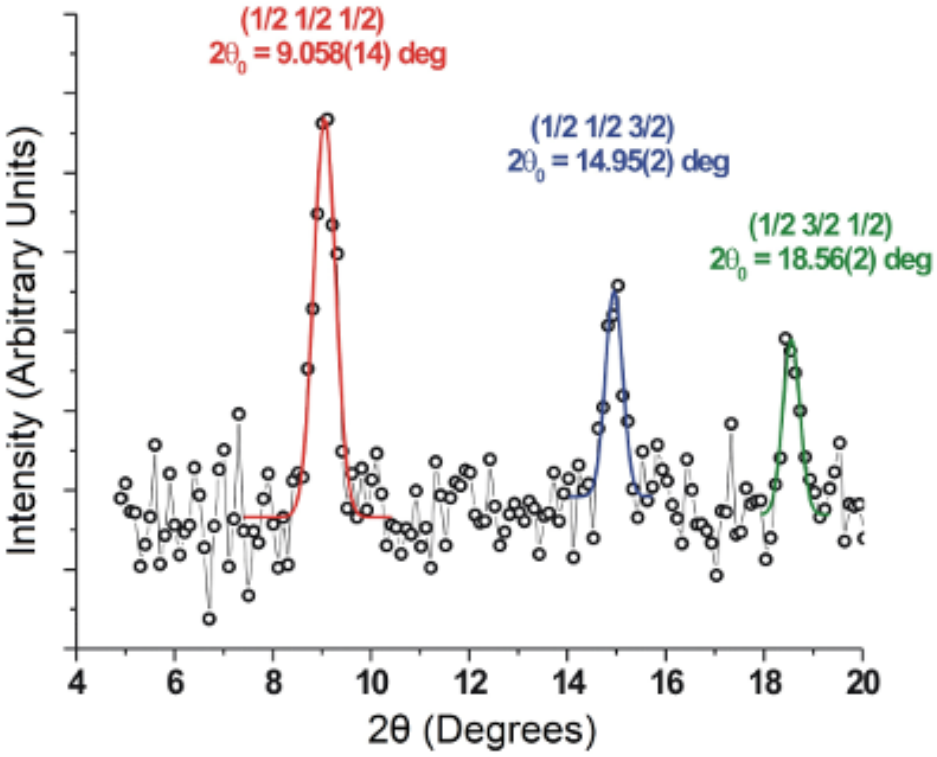

Figure 6.5: A difference plot (3.5 K - 20 K) showing three magnetic reflections indexed on $\vec{k} = (\frac{1}{2}, \frac{1}{2}, \frac{1}{2})$. The neutron wavelength is 1.33Å. The fits are to single Gaussians.

no Warren-like feature. Additionally, since Γ_3 and Γ_7 form a co-representation, they can be combined to form a new symmetry-allowed model. Refinements on the powder using each of these models gave equally probable values for every model due to the small number of magnetic peaks obtained from the powder neutron scattering. We therefore collected single crystal neutron diffraction data to determine the magnetic structure.

Two series of single crystal measurements were made. First, the intensity of the strongest magnetic peak, $\left(\frac{1}{2}, \frac{1}{2}, \frac{1}{2}\right)$ as determined from the powder neutron diffraction data, was measured from just above T_N to 4 K and the results are

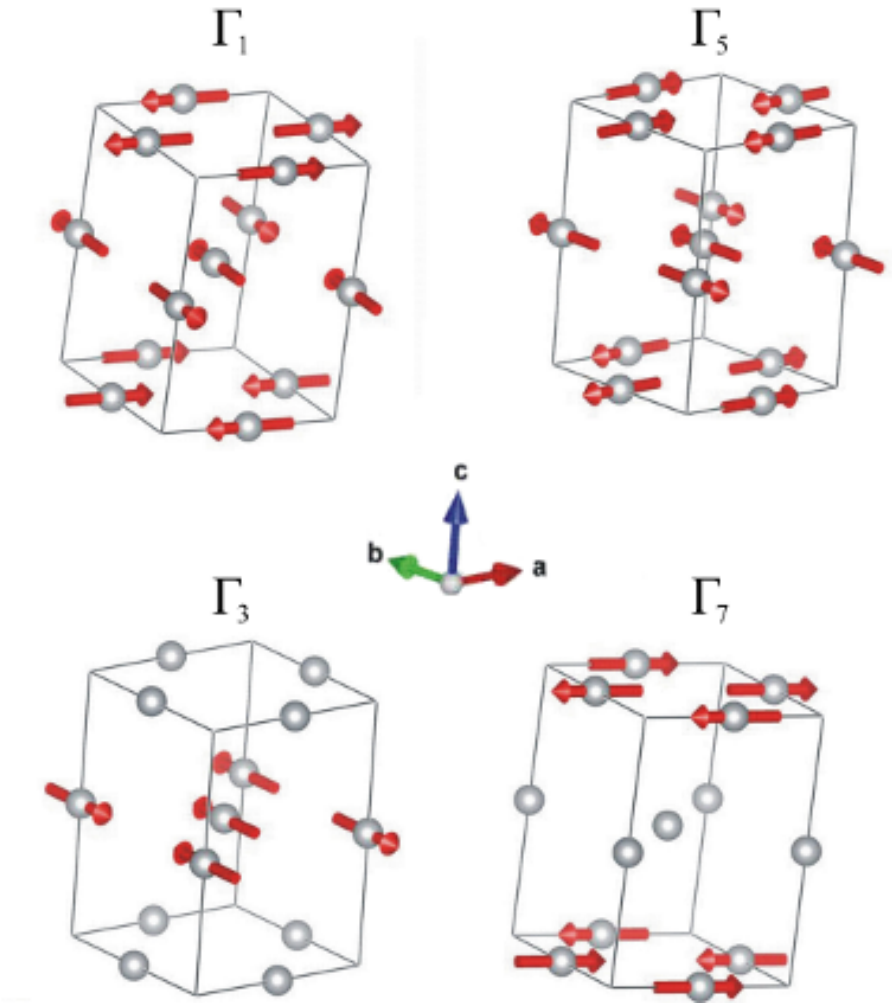

Figure 6.6: Four possible spin configurations for β-$NiNb_2O_6$ shown on the chemical unit cell. (Figure made using VESTA [91])

shown in Fig. 6.7. The data below the critical temperature were then fit to a power law given by the expression:

$$\frac{I}{I_0} = A\left|\frac{T - T_C}{T_C}\right|^{2\beta} \tag{6.1}$$

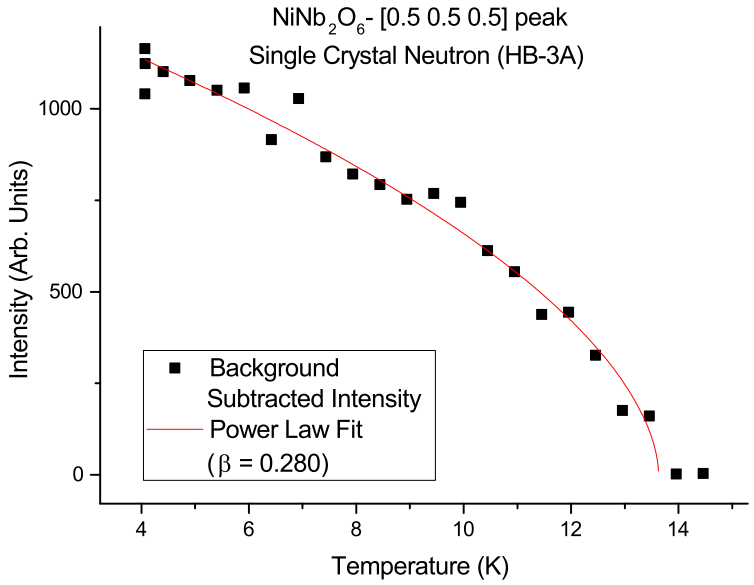

Figure 6.7: A plot of the T-dependence of the magnetic $\left(\frac{1}{2}, \frac{1}{2}, \frac{1}{2}\right)$ Bragg peak. A power law fit gives a value of the critical exponent $\beta = 0.28(3)$.

where $\frac{I}{I_0}$ is the normalized intensity, T is the temperature, T_C is the transition (critical) temperature and β is the magnetic critical exponent. The fitted values are $T_N = 13.6(2)$ K and $\beta = 0.28(3)$. Note that β is at 1σ of the expected value for the 3D Ising model (0.31), at 2σ of the 3D XY model (0.345) and within 3σ of the 3D Heisenberg model (0.36) [209]. Nonetheless, the range of data available is too narrow and of insufficient point density near T_C to determine an accurate value for β and this must be left to further study.

The second set of scans performed was a survey of both magnetic and structural peaks at a temperature below (4 K) and above (20 K) the transition temperature. We first performed a single crystal nuclear refinement with the 20 K data, and the resulting parameters agreed well with those from our powder diffraction measurement. Magnetic refinements were then performed

with a (4 K - 20 K) temperature difference dataset, which ensured that the magnetic scattering was isolated appropriately. We considered all candidate models discussed previously in the neutron powder diffraction section.

The values of the Ni^{2+} ordered moments are given in Table 6.4 for the Γ_1 and Γ_3 models, both of which belong to the I_c4_1/a magnetic space group, and the refinement quality is presented for these two cases in Fig. 6.8a and 6.8b. Neither of these models fit the data well and the Γ_3 model yielded a Ni^{2+} moment that is too large to be consistent with a simple spin-only $S = 1$ picture. We also tried to fit the data with $\Gamma_3 + \Gamma_7$ model, which belongs to the C_a2/c magnetic space group, discussed previously. This model clearly provides the best fit to the data as indicated by the lower χ^2 and R-factor of the three refinements attempted; the refinement result for the $\Gamma_3 + \Gamma_7$ model is displayed in Fig. 6.8c. The Ni moments were originally unconstrained in this refinement, resulting in nearly collinear moments pointing along the a-axis in adjacent ab-layers as shown in table 6.4. For the unconstrained fit, the R-factor was slightly worse, at 9.76 but the χ^2 value was slightly lower at 6.66. The lower χ^2 isn't unexpected comparing a relaxed system to a constrained system. Based on the small difference and the decreased R-factor the constrained model seems likely to be correct. In both the constrained and unconstrained models our fits assumed that there were two domains in a 1:1 ratio. The moments were then constrained to be collinear in adjacent layers and point exactly along the a-axis, which changed the goodness of fit negligibly. For this reason, the magnetic structure of the constrained refinement is considered to be the final solution; the ordered Ni^{2+} moment obtained in this case is shown in Table 6.4 and a schematic of the structure is presented in Fig. 6.9. The determined magnetic

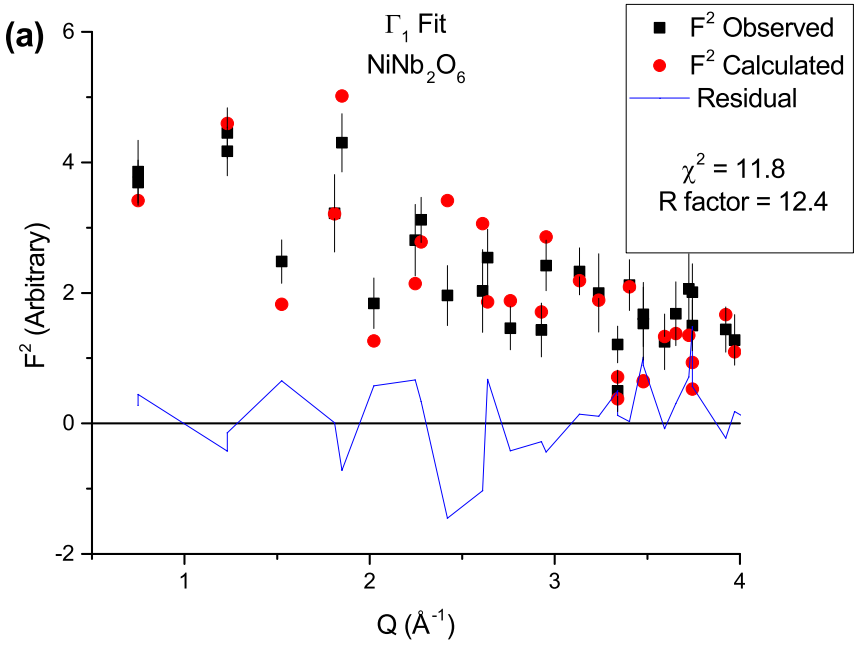
(a)
Γ1 Fit
NiNb2O6
F2 Observed
F2 Calculated
Residual
χ2 = 11.8
R factor = 12.4
F2 (Arbitrary)
Q (Å-1)
6
4
2
0
-2
1
2
3
4

(a)

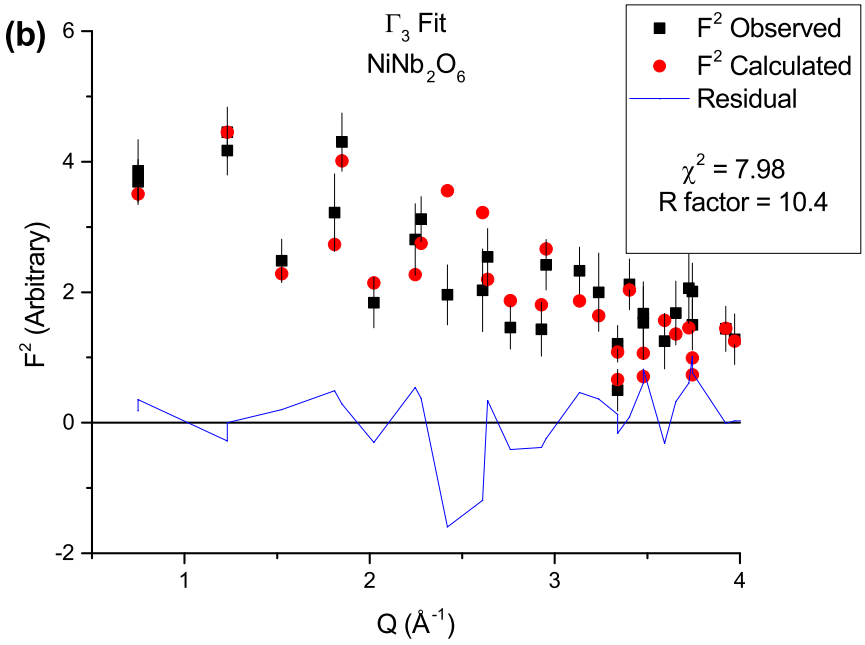
(b)
Γ3 Fit
NiNb2O6
F2 Observed
F2 Calculated
Residual
χ2 = 7.98
R factor = 10.4
F2 (Arbitrary)
Q (Å-1)
6
4
2
0
-2
1
2
3
4

(b)

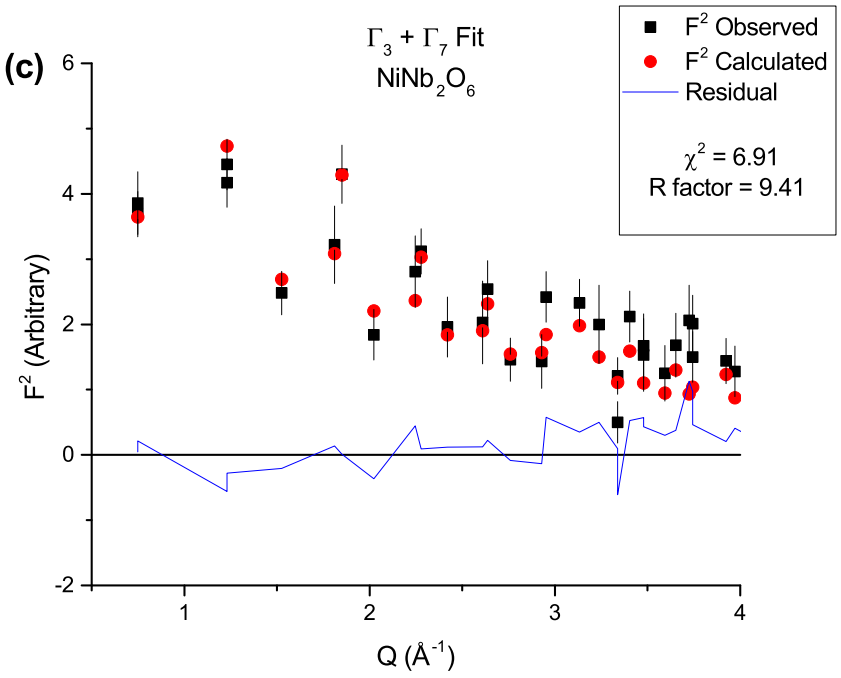

(c)

Figure 6.8: A comparison of fits of the actual data from single crystal neutron scattering on $NiNb_2O_6$ to the expected scattering given a different magnetic basis vectors. The calculated and observed values of F^2, the residuals, χ^2 and R-factor for (a) the Γ_1, (b) Γ_3, and (c) $\Gamma_3 + \Gamma_7$ models are shown.

structure for β-$NiNb_2O_6$ is consistent with the exchange interaction hierarchy expected from crystal structure considerations. As explained previously, the strongest exchange interaction likely corresponds to the in-plane 180° Ni–O–O–Ni pathway, which should be strongly antiferromagnetic. We note that this strong exchange pathway alternates along the a- and b-axes in adjacent ab-plane layers of Ni^{2+}. Furthermore, all other superexchange interactions are mediated by two or three ions with less favourable geometries for strong orbital overlap, and therefore one expects β-$NiNb_2O_6$ to be best described by

			$\Gamma_3 + \Gamma_7$		
			Unconstrained		
Moments	Γ_1	Γ_3	Site 1	Site 2	Constrained
μ_a	0.44(6)	2.15(3)	1.77(1)	1.31(1)	1.60(1)
μ_b	1.67(2)	0.41(3)	0.04(1)	0.14(1)	0
μ_c	0.16(3)	1.00(4)	0.23(1)	0	0
Total	1.73(5)	2.41(6)	1.78(5)	1.32(3)	1.60(1)

Table 6.4: The values of the refined moments from single crystal neutron diffraction data for various models. The ordered moments correspond to the vectors in table 6.3.

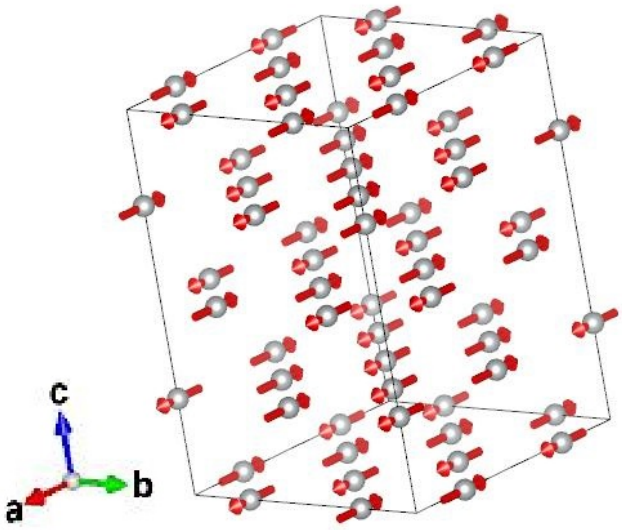

Figure 6.9: The full magnetic structure of $NiNb_2O_6$ in the $\Gamma_3 + \Gamma_7$ basis. (Figure made using VESTA [91])

a series of coupled antiferromagnetic Ni^{2+} chains [192] that ultimately achieve long-range order due to weak interchain interactions.

When comparing the magnetic structure for $NiNb_2O_6$ with those for $NiSb_2O_6$ [204] and $NiTa_2O_6$ [204] in Fig. 6.10, there are interesting similarities and differences. The magnetic structure of all three systems satisfies the dominant AF exchange interaction described above. More specifically, all three materials

consist of moments oriented along the [110] direction in the TR or TR-like cell that form AF-coupled chains running along the same direction, consistent with Fig. 6.2 and DFT calculations for $NiTa_2O_6$ [192]. Differences arise in the coupling of these AF chains to adjacent chains both within and between layers, which emphasizes the importance of the interchain interactions on determining the precise magnetic structure. In fact, the magnetic structures and the magnetic unit cells expressed in terms of the parent TR chemical cell are different for all three phases. For $NiSb_2O_6$ $a_M = 2a_{TR}$, $b_M = b_{TR}$ and $c_M = 2c_{TR}$ giving $V_M = 4V_{TR}$. For $NiTa_2O_6$ $a_M = 2^{\frac{1}{2}}a_{TR}$, bM = $2(2^{\frac{1}{2}})b_{TR}$ and $c_M = 2c_{TR}$, giving $V_M = 8V_{TR}$ while for $NiNb_2O_6$ $a_M = 2a_{TR}$, $b_M = 2b_{TR}$ and $c_M = 2c_{TR}$ also yielding $V_M = 8V_{TR}$. This is a remarkable result, given the close structural similarities among the three materials. The exact position of the ligands relative to the metal ions seems to serve as a very sensitive tuning parameter for the weak interchain interactions, which leads to the diverse magnetic ground states observed for this family of materials.

6.6.2 Zero Field μSR on the β-$NiNb_2O_6$ polymorph

Zero field μSR measurements of β-$NiNb_2O_6$ are presented in Fig. 6.11a. Asymmetry spectra at several temperatures with superimposed fits are shown. Each of the spectra are offset by a value of 0.05 per temperature step for clarity. At 2 K, it is evident that in the first 0.2 μs there is strong oscillation in the asymmetry, indicative of long range order in the material. A fast Fourier

* Images (a) and (b) reprinted from Journal of Magnetism and Magnetic Materials, 184, Ehrenberg, H; Wltschek, G; Rodriguez-Carvajal, J; and Vogt, T, Magnetic Structures of the Tri-Rutiles $NiTa_2O_6$ and $NiSb_2O_6$, 111–115, 1998, with permission from Elsevier

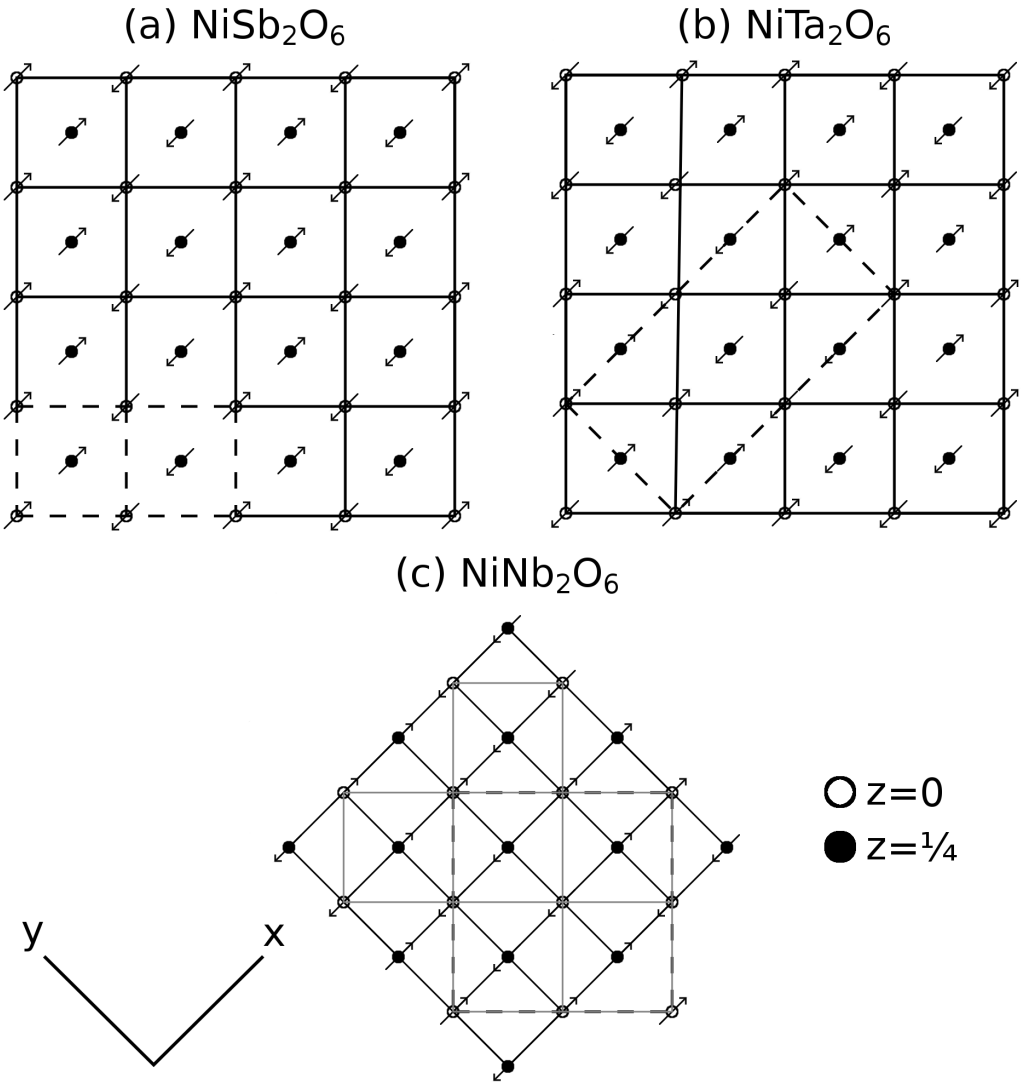

Figure 6.10: A comparison of the magnetic structures for (a) $NiSb_2O_6$ [204], (b) $NiTa_2O_6$ [204] and (c) β-$NiNb_2O_6$ projected along the c-axis and with two adjacent layers shown. In (c) the larger chemical cell is indicated by the darker solid lines and the smaller TR-like chemical cell by the lighter solid lines. In all three diagrams the dashed lines indicate the magnetic unit cell.*

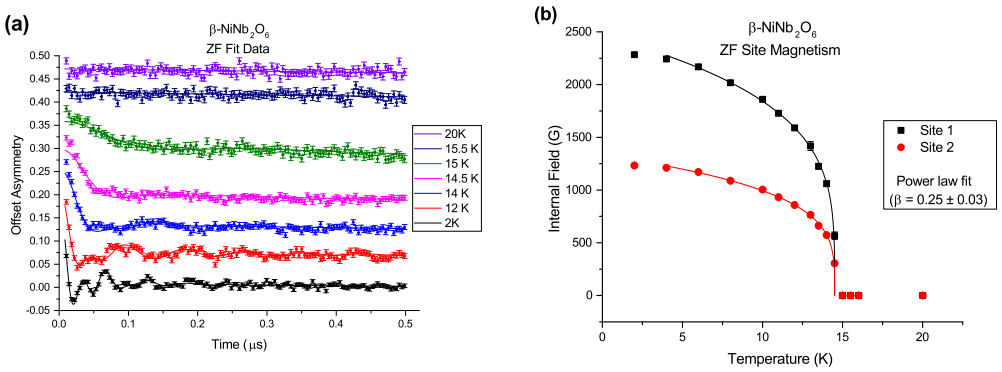

(a) (b)

Figure 6.11: Selected data and internal field fits from zero field μSR measurements performed on the β-$NiNb_2O_6$ polymorph. Panel (a) (Colour online) shows fits of μSR data from 2 to 20 K for β-$NiNb_2O_6$. Each asymmetry plot is offset by +0.05 for clarity. There is a distinct reduction in the local field with increasing temperature, followed by a transition to the paramagnetic state above 15 K. In panel (b), we plot the internal magnetic field strength at two different muon sites in β-$NiNb_2O_6$.

transform showed that there are likely two oscillating components, so the data was fit to the 3-component form given by the following expression:

$$\begin{aligned} A(t) =& A_1 \cos(\gamma_\mu B t + \phi)\, e^{-\lambda_1 t} + \\ & A_2 \cos(\gamma_\mu \delta B t + \phi)\, e^{-\frac{(\sigma_2 t)^2}{2}} + A_3 e^{-\lambda_3 t} \end{aligned} \tag{6.2}$$

Fitting this form, the value of α, the phase ϕ and the total asymmetry (A_1 + A_2 + A_3) were set to a constant determined by fitting a weak transverse field run. The scaling factor between the two fields (B) was fit globally and found to be 0.540(3). γ_μ is the muon gyromagnetic ratio. λ_n are the relaxation rates in μs^{-1} of the n^{th} term. The first two terms are relaxing, oscillating components

with an exponential (first term) and Gaussian (second term) envelope. The final term is a non-precessing component, which is fitting the long time tail of the signal, typical of relaxation due to fluctuations of the local field. Each individual asymmetry was fit as a free parameter.

The values of the local fields at the two muon stopping sites, as determined by fits to the data, are plotted in figure 6.11b. The extracted temperature dependence of the two local fields were fit simultaneously to a power law model, giving a value for the critical exponent $\beta = 0.25(2)$. This was fit using:

$$F = A \left| \frac{T - T_C}{T_C} \right|^{\beta} \tag{6.3}$$

where F is the internal field, T is the temperature, T_C is the transition (critical) temperature and β is the critical exponent for the order parameter. A value of $T_N = 14.5(3)$ K was determined from the fit, which agrees well with previous measurements [203]. The fit also yielded a value for the critical exponent $\beta = 0.25(3)$, which is lower than typical values for 3D universality classes. In this case all three classes are at least 3σ away from the fit value. This implies that reduced dimensionality is important in this material and is consistent with both previous DFT work [192] and the magnetic structure determined by neutron diffraction above.

6.6.3 Zero Field μSR on the columbite polymorph

Similar μSR measurements were performed on the crushed single crystal powder sample of the columbite polymorph of nickel niobate. The results from

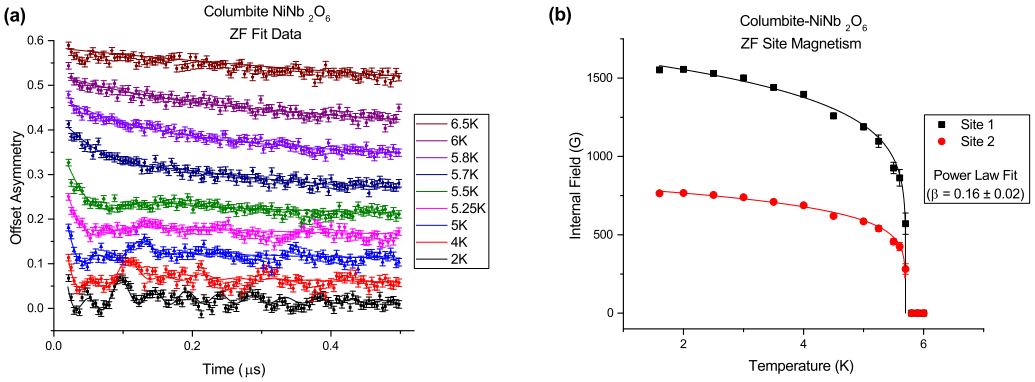

(a) (b)

Figure 6.12: Selected data and internal field fits from zero field μSR measurements performed on the columbite polymorph of $NiNb_2O_6$. In panel (a) (Colour online) we show fits of μSR data from 2 to 20 K for the columbite polymorph of $NiNb_2O_6$. Each asymmetry plot is offset by +0.05 for clarity. There is a distinct decrease in the local field with increasing temperature, followed by a transition to the paramagnetic state above 5.7 K. In panel (b) we plot the internal magnetic field strength at two different muon sites in the columbite polymorph of nickel niobate.

the temperature sweep with zero field applied are shown in figure 6.12. From a fast Fourier transform, it was again evident that there were two primary components. As in the case for the β-$NiNb_2O_6$ polymorph, there was also a relaxing tail. The function used to fit this data was:

$$\begin{aligned} A(t) =& A_1 \cos(\gamma_\mu B t + \phi) e^{-\lambda_1 t} + \\ & A_2 \cos(\gamma_\mu \delta B t + \phi) e^{-\lambda_2 t} + A_3 e^{-\lambda_3 t} \end{aligned} \tag{6.4}$$

The difference between this function and Eqn. 6.2 is that both oscillating components have exponential front ends. Here we found the ratio, δ to be 0.493(4).

In Fig. 6.12a, it is evident that there is a very slow decrease in the oscillation frequency with increasing temperature between 2 and 5 K. This trend is followed by a very large drop in frequency above 5 K, and the oscillations disappear completely between 5.25 and 6 K. Finally, by 10 K (not shown) there is only a very weak relaxation of the signal remaining.

Figure 6.12b plots the internal field strength against temperature. A power law fit was performed using Eqn. 6.3. A transition temperature of $T_N = 5.7(3)$ K was found from the fit, which is in good agreement with previous work[174, 175]. The fit also revealed a critical exponent $\beta = 0.16(2)$, which is even lower than the value found for the β-polymorph and therefore further away from typical 3D universality class exponents. This result emphasizes that columbite $NiNb_2O_6$ is a low-dimensional magnetic system and likely can be described by weakly-coupled $S = 1$ spin chains; therefore it is the true $S = 1$ cousin to the interesting $S_{eff} = \frac{1}{2}$ ferromagnetic Ising chain system $CoNb_2O_6$.

6.7 Conclusion

We have presented both neutron diffraction and μSR data on the β-polymorph of $NiNb_2O_6$ as well as μSR data on the columbite polymorph. Combined powder and single crystal neutron diffraction data allowed us to solve the magnetic structure unambiguously for β-$NiNb_2O_6$. We find a collinear arrangement of Ni^{2+} moments, which is consistent with a dominant in-plane AF exchange path that alternates along the a and b axes in adjacent Ni^{2+} layers. β-$NiNb_2O_6$ is best described as an $S = 1$ chain system with significant interchain interactions, ultimately leading to long-range magnetic order at $T_N = 15$ K. This

picture is supported by μSR measurements, which find a critical exponent for the order parameter $\beta = 0.25(3)$. μSR was also used to determine $\beta = 0.16(2)$ in the case of columbite polymorph. This exceptionally small value indicates that low dimensionality is an intrinsic property of the columbite polymorph, which is consistent with expectations for a weakly-coupled $S = 1$ chain system. Inelastic neutron scattering measurements will be indispensable for determining the coupling strength between the Ni^{2+} chains in these two polymorphs, and it will be extremely interesting to compare the inelastic neutron scattering spectrum of columbite $NiNb_2O_6$ to the cobalt analogue.

6.8 Acknowledgements

Partial funding for this research came from an Ontario Graduate Scholarship (OGS) award and Natural Science and Engineering Research Council (NSERC) Grants. Research at the High Flux Isotope Reactor at the Oak Ridge National Laboratory was sponsored by the Scientific User Facilities Division, Office of Basic Energy Sciences, US Department of Energy. Research at the Canadian Neutron Beam Centre was supported by the Canadian Nuclear Laboratories, Chalk River, Canada.

We would like to thank A.M. Hallas for assistance with the preliminary work as well as useful discussions throughout the data collection and writing process. We would like to thank the staff at TRIUMF National Laboratory, specifically Dr. G. Morris and Dr. B. Hitti for their assistance, guidance and

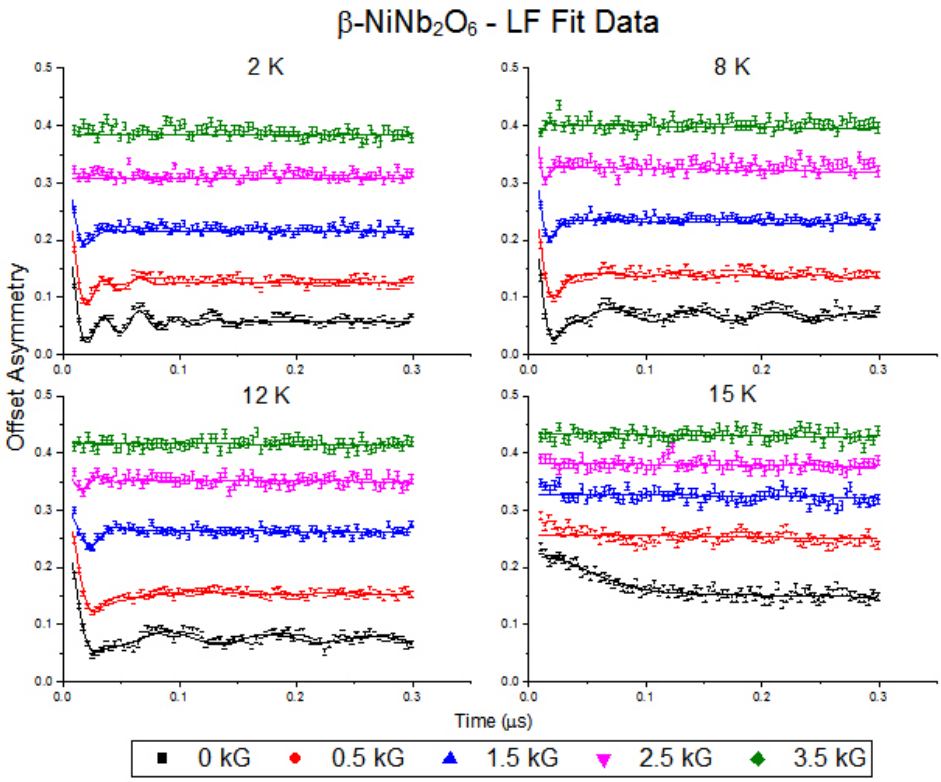

Figure SI.1: A series of plots of offset asymmetries and fits of data at 2 K(a), 8 K(b), 12 K(c) and 15 K(d) in fields applied longitudinally to the direction of initial muon polarization from 0 to 3.5 kG. The data is offset slightly from zero due to setup parameters of the recording electronics.

support throughout the μSR measurements.

6.9 Longitudinal Field Measurements in $NiNb_2O_6$

6.9.1 β-$NiNb_2O_6$ polymorph

In figure SI.1 the data from the fits of μSR runs with a field applied longitudinally to the original direction of muon spin is shown. In this case the external field adds to the field at the local site which is causing a decoupling of the magnetic signal, wiping out the oscillations.

The fitting function used in the zero field case, equation 6.2, was used again in the longitudinal field case. In the longitudinal field cases at 1.5 and 2.5 kG at the initial front end we see a dip and recovery of the asymmetry. This is typical of powdered systems with applied longitudinal field, where there is a loss of the front end of the asymmetry and the recovery of a $\frac{1}{3}$ tail representing orientations that were aligned along the field and initial muon polarization longitudinally.

Figure SI.2 shows the evolution of the asymmetry with the application of a longitudinal field, similar to figure SI.1 above. In this case the asymmetries are offset by 0.05 for each field (panels a, b and c) or temperature (panel d) step. Much like in the zero field case, and using the same fitting function as described in equation 6.4, the evolution of the spectra in the 2 and 5 K asymmetries proceeds in lockstep, with the oscillations dying off as a higher field is applied. The difference between the two polymorphs, other than the rapidity of onset of magnetism, is that the destruction of the magnetic phase requires a slightly higher field, which is not unsurprising when comparing the fields from figures 6.11b and 6.12b. In panel (c) of figure SI.2 the signal shows no sign of long range order. Another difference is that even at the highest field, there is a significant relaxing tail that remains in this polymorph. Panel (d) plots the asymmetry and the fit out to 5 μs. In this case as we approach and

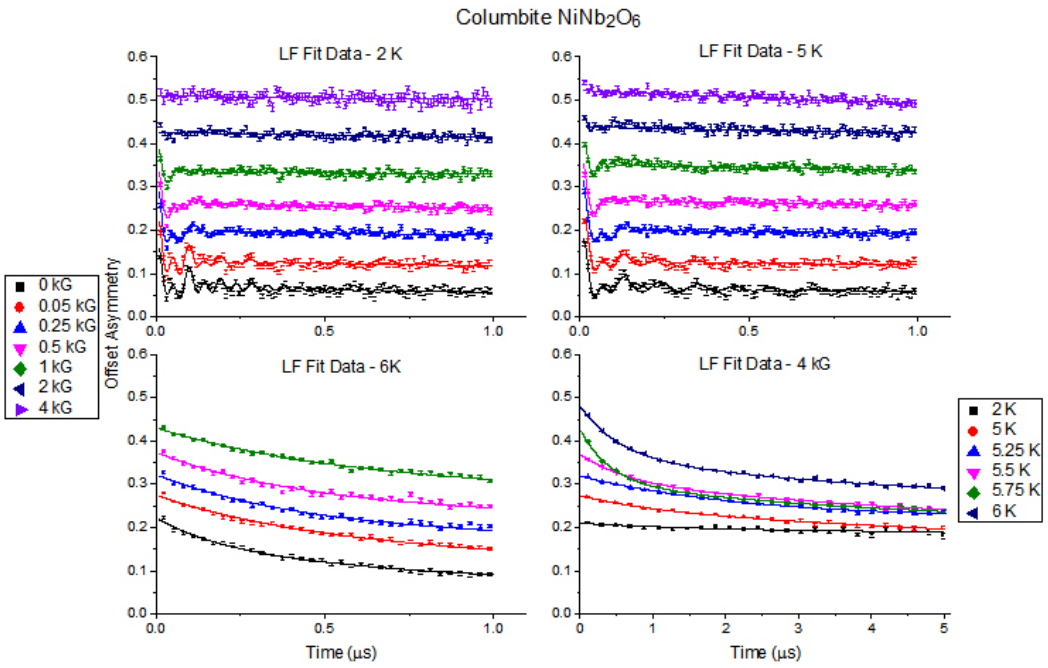

Figure SI.2: A series of plots of offset asymmetries and fits of data at 2 K(a), 5 K(b) and 6 K(c) in fields applied longitudinally to the direction of initial muon polarization from 0 to 4 kG per the left legend. Plot (d) shows the evolution of the asymmetry in a 4 kG longitudinal field from 2 to 6 K.

then break through the transition the flat asymmetry gains a strong front-end relaxation.

Both materials are ordered but the decoupling of the magnetic signal in cobalt niobate exists in zero field and wipes out with longitudinal field even faster than for the nickel analogue. This is shown by comparing figure 3.2a and equation 3.1 for cobalt niobate to figures SI.2 and equation 6.4 for the columbite polymorph of nickel niobate.

When comparing the longitudinal field data, again the fits for cobalt niobate are better behaved owing to, again, one fewer term in the fitting equation.

Otherwise similar trends based on the relaxation of the columbite cobalt and nickel niobates can be observed.

Chapter 7

Conclusion

7.1 Summary

This thesis focused primarily on the material nickel niobate, and specifically on the new polymorph that we created, β-$NiNb_2O_6$. The thesis highlights the complexity and a certain amount of random chance involved with material discovery and synthesis. Additionally, a small amount of the material that was initially desired, columbite nickel niobate, was created. We performed a μSR analysis to compliment work that has been previously published on this material [174, 175]. The thesis also concluded the investigation into cobalt niobate, with a more comprehensive and complete analysis of the μSR data as well as the presentation of the interesting features discovered in the neutron scattering data.

7.1.1 Cobalt Niobate

Between this work and the Masters thesis [17], the beginning of the story on this material has built up significantly. The μSR data in both zero and longitudinal field shows that the internal strength of the field is dynamic and strong. The strength of the cobalt ions is not at all surprising. The evolution of the μSR data over the range of transverse fields shows an enhancement in the number of resolvable, inequivalent muon stopping sites in the material, which is also expected as there are three inequivalent oxygen Wyckoff positions in the structure.

The more interesting results for cobalt niobate come from the neutron scattering data. The experiments performed were able to verify and enhance the detail of the experiments done by Coldea [51, 53], and fill in a blank area describing the evolution of the magnetic properties in this material.

The first important result that we see is that although heat capacity measurements showed a very long time constant at low temperatures, that the evolution of the magnetism to the ground state is not particularly visible on the neutron scattering timescale. This hints that the system may have interesting field-induced effects at low temperatures due to the interactions of the transverse field that have not been completely explored. The application of field we see a somewhat unexpected emergence of spin-wave like modes in the scattering data. The evolution of the structure of these modes is interesting itself, as is the fact that above the magnetic transitions, although changed, the underlying fundamental structure is still seen. Taking varying cuts of the neutron data for comparison, we can still make the claim that the material is

behaving in a low-dimensional manner similar to what Coldea showed, but this result leads to the potential for further questions, experiments and theoretical modelling of the data.

7.1.2 Nickel Niobate

With nickel niobate, a significant portion of the effort was put into the sample synthesis. It took nearly two years of dedicated work including an entire undergraduate thesis to come up with something that created small single crystals. Over four years the growing process was refined. Even after that, there is no single, simple recipe to making either polymorph of this material in a manner similar to that by which cobalt niobate is created.

However, the two polymorphs did give interesting results. We were able to determine that at low temperature both are magnetic, and neither behave quite the same as the cobalt compound. Preliminary work on the sample of the β-$NiNb_2O_6$ polymorph was interesting enough that we could state that reduced dimensionality was going to be a feature based on the fits and subsequent analysis, which allowed us the opportunity to further explore its magnetic structure. Comparing the columbite polymorph of nickel niobate to cobalt niobate shows that we have static magnetic order in the spin-1 case, which is different spin dynamics than was seen with the columbite cobalt niobate. A full characterization of the columbite version of nickel niobate using some previously published results as well as several of the techniques used to characterize β-nickel niobate would likely reveal more about the comparison between these two structures, and particularly how the spin-$\frac{1}{2}$ and spin-1 chains compare.

Through neutron scattering, a picture of the way that magnetism was constrained to lie in one dimension, aligned antiferromagnetically in a triangular lattice within the plane as well as in an interplanar fashion, shown in figure 6.9. This led to the understanding that the material is frustrated due to two competing antiferromagnetic interactions that are nearly equidistant and that are nearly equal in strength. The spins themselves apparently behave in an Ising-like fashion due to the fact that our fit magnetic moment exists solely along one crystallographic axis, but the magnetism orders in multiple dimensions. The μSR data showed a similar evolution to the magnetism, where the critical exponent with respect to temperature matched well between both neutron diffraction (in the β polymorph) and μSR and could be interpreted as a further indicator of magnetism being constrained by competing interactions and potentially causing reduced dimensionality in both the β polymorph and the columbite polymorph. The β polymorph has a critical exponent that is within $2\sigma\backslash 3\sigma$ of 3D ordering, although the magnetic analysis supports frustration and reduced dimensionality. The columbite polymorph has a critical exponent well below any 3D model, and based on its complimentary nature to cobalt niobate the μSR data supports the conclusion that this is a low dimensional system as well.

In both cases, the μSR also saw a more-static-like type of magnetic interaction compared to the dynamics shown via μSR in the columbite cobalt samples. This is an indicator that although we can find reduced dimensionality or constrained magnetism in both systems, that the mechanism causing the difference between an arrangement of effective spin-$\frac{1}{2}$ and spin-1 particles may have different underlying physics between the two models.

7.2 Future Work

In both systems, we are left with significant questions that remain to be answered. For the cobalt system the evolution of apparent spin waves is interesting and does not match with common theoretical models. Engaging a specialist in theory in better understanding this system will be a necessary component of future work. Because of the interesting physics that have been shown up to and above the quantum critical point, even as high as 5.5 K we could be seeing some emergent behaviour in the scattering data, and that possibility alone is exciting to explore.

Additionally, the heat capacity has not been measured down to the lowest temperatures, and in the previous thesis work the last data point observed could have been turning over. A further exploration of this is already ongoing with collaborators.

Although not totally disproved, the hypothesis that the long relaxation time is the driver for interesting low temperature physics may need to be re-examined in the context of field. Although it wasn't ever seen in susceptibility measurements, field-induced effects could be an avenue for future research in this material. In any case, all of the above are good reasons to help to better understand this compound, if not only because of the interesting physical comparisons to theory described in chapter 1.

For the nickel compounds, we have the start of a good characterization for the β-$NiNb_2O_6$ compound. The biggest outstanding question is why is there a difference in the total magnitude of the magnetic moment for the powder and the single crystal diffraction. A more careful examination as well as a

larger volume of crystals would help to better improve the understanding of this material.

Of larger potential excitement, is that crystals of the columbite form of this material are potentially now synthesizable based on the information of chapter 4. This will allow the future exploration of this material. The small amount of experimental work done so far show that we have a compound that seems to differ significantly compared to cobalt niobate, which means that the original intent behind this research, to compare the two different compounds directly, is a possible future goal.

Bibliography

[1] C. Kittel. *Introduction to Solid State Physics*. Wiley, 1996.

[2] C. Kittel and H. Kroemer. *Thermal Physics*. W. H. Freeman, 1980.

[3] N.W. Ashcroft and N.D. Mermin. *Solid State Physics*. HRW international editions. Holt, Rinehart and Winston, 1976.

[4] H.B. Callen. *Thermodynamics and an Introduction to Thermostatistics*. Wiley, 1985.

[5] M. Plischke and B. Bergersen. *Equilibrium Statistical Physics*. World Scientific, 2006.

[6] S. Blundell. *Magnetism in Condensed Matter*. Oxford Master Series in Condensed Matter Physics. Oxford University Press, 2001.

[7] J. Singleton. *Band Theory and Electronic Properties of Solids*. Oxford master series in condensed matter physics. Oxford University Press, 2001.

[8] D.J. Griffiths. *Introduction to Quantum Mechanics*. Pearson international edition. Pearson Prentice Hall, 2005.

[9] J. Patrick Clancy. Physics 729 Course Notes, September 2010.

[10] An Chang Shi. Physics 739 Course Notes, September 2010.

[11] Takashi Imai. Physics 730 Course Notes, January 2011.

[12] Erik Sorensen. Physics 750 Course Notes, January 2011.

[13] Jim Britten. Chemistry 730 Course Notes, November 2011.

[14] Jim Britten. Chemistry 736 Course Notes, January 2012.

[15] B. Gaulin, G. Luke, T. Imai, D. Venus, and T. Timusk. Physics 734 Course Notes, January 2013.

[16] Sung Sik Lee. Physics 753 Course Notes, September 2014.

[17] Timothy JS Munsie. Studies of the Low Temperature Behaviour of $CoNb_2O_6$, 2012.

[18] Eteri Svanidze. Search, Discovery, Synthesis and Characterization of Itinerant Magnets Composed of Non-magnetic Constituents, 2015.

[19] David J Rowe and John L Wood. *Fundamentals of nuclear models: Foundational models*. World Scientific Publishing Co Inc, 2010.

[20] W Heitler and F London. Interaction between neutral atoms and homopolar binding according to quantum mechanics. *Z. Physik*, 44:455, 1927.

[21] Philip Hofmann. *Solid State Physics: An Introduction*. Wiley-VCH, 2015.

[22] Klaus Hentschel. *Compendium of Quantum Physics*. Springer Berlin Heidelberg, Berlin, Heidelberg, 2009.

[23] William Stuart Tyree. Correlation of Structure and Magnetic Properties in Charge-transfer Salt Molecular Magnets Composed of Decamethylmetallocene Electron Donors and Organic Electron Acceptors, 2005.

[24] Kathryn Preuss. Paramagnetism - Lecture 5-3. online, 2015. http://www.chemistry.uoguelph.ca/educmat/chm710/files/5_3_Paramagnetism.pdf.

[25] Ernst Ising. Beitrag zur theorie des ferromagnetismus. *Zeitschrift für Physik A Hadrons and Nuclei*, 31(1):253–258, 1925.

[26] Pierre Weiss. L'hypothèse du champ moléculaire et la propriété ferromagnétique. *J. phys. theor. appl.*, 6(1):661–690, 1907.

[27] Hans Bethe. Zur theorie der metalle. *Zeitschrift für Physik*, 71(3-4):205–226, 1931.

[28] Lars Onsager. Crystal statistics. I. A two-dimensional model with an order-disorder transition. *Physical Review*, 65(3-4):117, 1944.

[29] Elliott Lieb, Theodore Schultz, and Daniel Mattis. Two soluble models of an antiferromagnetic chain. *Annals of Physics*, 16(3):407–466, 1961.

[30] Theodore D Schultz, Daniel C Mattis, and Elliott H Lieb. Two-dimensional Ising model as a soluble problem of many fermions. *Reviews of Modern Physics*, 36(3):856, 1964.

[31] RJ Baxter. One-dimensional anisotropic Heisenberg chain. *Physical Review Letters*, 26(14):834, 1971.

[32] N David Mermin and Herbert Wagner. Absence of ferromagnetism or antiferromagnetism in one-or two-dimensional isotropic Heisenberg models. *Physical Review Letters*, 17(22):1133, 1966.

[33] Sidney Coleman. There are no Goldstone bosons in two dimensions. *Communications in Mathematical Physics*, 31(4):259–264, 1973.

[34] John Michael Kosterlitz and David James Thouless. Ordering, metastability and phase transitions in two-dimensional systems. *Journal of Physics C: Solid State Physics*, 6(7):1181, 1973.

[35] Hans-Jürgen Mikeska and Alexei K Kolezhuk. One-dimensional magnetism. In *Quantum magnetism*, pages 1–83. Springer, 2004.

[36] LD Faddeev and LA Takhtajan. What is the spin of a spin wave? *Physics Letters A*, 85(6-7):375–377, 1981.

[37] F Duncan M Haldane. Continuum dynamics of the 1-D Heisenberg antiferromagnet: identification with the O(3) nonlinear sigma model. *Physics Letters A*, 93(9):464–468, 1983.

[38] N. Murai, T. Fukuda, T. Kobayashi, M. Nakajima, H. Uchiyama, D. Ishikawa, S. Tsutsui, H. Nakamura, M. Machida, S. Miyasaka, S. Tajima, and A. Q. R. Baron. Effect of magnetism on lattice dynamics in $SrFe_2As_2$ using high-resolution inelastic x-ray scattering. *Phys. Rev. B*, 93:020301, Jan 2016.

[39] Andrei V Palii, Oleg S Reu, Sergei M Ostrovsky, Sophia I Klokishner, Boris S Tsukerblat, Zhong-Ming Sun, Jiang-Gao Mao, Andrey V

Prosvirin, Han-Hua Zhao, and Kim R Dunbar. A highly anisotropic cobalt (II)-based single-chain magnet: Exploration of spin canting in an antiferromagnetic array. *Journal of the American Chemical Society*, 130(44):14729–14738, 2008.

[40] Barry A Cipra. An introduction to the ising model. *American Mathematical Monthly*, 94(10):937–959, 1987.

[41] Ralph Baierlein. *Thermal Physics*. Cambridge University Press, 1999.

[42] Jun John Sakurai, San-Fu Tuan, and Eugene D Commins. *Modern quantum mechanics, revised edition*. AAPT, 1995.

[43] Pierre Pfeuty. The one-dimensional Ising model with a transverse field. *ANNALS of Physics*, 57(1):79–90, 1970.

[44] Yung-Li Wang and Bernard R Cooper. Collective excitations and magnetic ordering in materials with singlet crystal-field ground state. *Physical Review*, 172(2):539, 1968.

[45] John McGreevy. Physics 239a Course Notes. Online, June 2016. http://physics.ucsd.edu/∼mcgreevy/s14/239a-lectures.pdf.

[46] Subir Sachdev. Quantum magnetism and criticality. *Nature Physics*, 4(3):173–185, 2008.

[47] H Weitzel. Kristallstrukturverfeinerung von Wolframiten und Columbiten. *Zeitschrift für Kristallographie-Crystalline Materials*, 144(1-6):238–258, 1976.

[48] W Scharf, H Weitzel, I Yaeger, I Maartense, and BM Wanklyn. Magnetic structures of $CoNb_2O_6$. *Journal of Magnetism and Magnetic Materials*, 13(1-2):121–124, 1979.

[49] C Heid, H Weitzel, P Burlet, M Bonnet, W Gonschorek, T Vogt, J Norwig, and H Fuess. Magnetic phase diagram of $CoNb_2O_6$: A neutron diffraction study. *Journal of magnetism and magnetic materials*, 151(1):123–131, 1995.

[50] C Heid, H Weitzel, P Burlet, M Winkelmann, H Ehrenberg, and H Fuess. Magnetic phase diagrams of $CoNb_2O_6$. *Physica B: Condensed Matter*, 234:574–575, 1997.

[51] R. Coldea, D. A. Tennant, E. M. Wheeler, E. Wawrzynska, D. Prabhakaran, M. Telling, K. Habicht, P. Smeibidl, and K. Kiefer. Quantum Criticality in an Ising Chain: Experimental Evidence for Emergent E8 Symmetry. *Science*, 327(5962):177–180, 2010.

[52] Aleksandr B Zamolodchikov. Integrals of motion and S-matrix of the (scaled) T= T_c Ising model with magnetic field. *International Journal of Modern Physics A*, 4(16):4235–4248, 1989.

[53] Ivelisse Cabrera, JD Thompson, R Coldea, D Prabhakaran, RI Bewley, T Guidi, JA Rodriguez-Rivera, and C Stock. Excitations in the quantum paramagnetic phase of the quasi-one-dimensional Ising magnet $CoNb_2O_6$ in a transverse field: Geometric frustration and quantum renormalization effects. *Physical Review B*, 90(1):014418, 2014.

[54] AW Kinross, M Fu, TJ Munsie, HA Dabkowska, GM Luke, Subir Sachdev, and T Imai. Evolution of quantum fluctuations near the quantum critical point of the transverse field ising chain system $CoNb_2O_6$. *Physical Review X*, 4(3):031008, 2014.

[55] D. Prabhakaran, F. R. Wondre, and A. T. Boothroyd. Preparation of large single crystals of ANb_2O_6 (A=Ni, Co, Fe, Mn) by the optical floating-zone method. *Journal of Crystal Growth*, 250:72–76, March 2003.

[56] J.E. Greedan. private communications, December 2016.

[57] P Shiv Halasyamani and Kenneth R Poeppelmeier. Noncentrosymmetric oxides. *Chemistry of Materials*, 10(10):2753–2769, 1998.

[58] R Castellanos, S Bernès, and M Vega-González. Redetermination of $Co_4Nb_2O_9$ by single-crystal X-ray methods. *Acta Crystallographica Section E: Structure Reports Online*, 62(5):i117–i119, 2006.

[59] U Lehmann and Hk Müller-Buschbaum. Einkristalle von $CoNbO_4$ mit $AlNbO_4$-Struktur. *Zeitschrift für anorganische und allgemeine Chemie*, 471(1):85–88, 1980.

[60] A Landé. Bemerkung über die Größe der Atome. *Zeitschrift für Physik A Hadrons and Nuclei*, 2(1):87–89, 1920.

[61] Jarl Axel Wasastjerna. *On the radii of ions*. Soc. Scientiarum Fennica, 1923.

[62] Victor Moritz Goldschmidt, Lars Thomassen, F Ulrich, Thomas Fredrik Weiby Barth, Gulbrand Oscar Johan Lunde, William Houlder Zachariasen, and D Holmsen. *Geochemische Verteilungsgesetze der Elemente*. I kommission hos J. Dybwad, 1925.

[63] Linus Pauling. The sizes of ions and the structure of ionic crystals. *Journal of the American Chemical Society*, 49(3):765–790, 1927.

[64] Linus Pauling. The principles determining the structure of complex ionic crystals. *Journal of the american chemical society*, 51(4):1010–1026, 1929.

[65] William B Jensen and William B Jensen. The origin of the ionic-radius ratio rules. *Journal of Chemical Education*, 87(6):587–588, 2010.

[66] R.T. Shannon. Revised effective ionic radii and systematic studies of interatomic distances in halides and chalcogenides. *Acta Crystallographica Section A: Crystal Physics, Diffraction, Theoretical and General Crystallography*, 32(5):751–767, 1976.

[67] Mario Birkholz. Crystal-field induced dipoles in heteropolar crystals I: concept. *Zeitschrift für Physik B Condensed Matter*, 96(3):325–332, 1995.

[68] Mario Birkholz. Crystal-field induced dipoles in heteropolar crystals II: Physical significance. *Zeitschrift für Physik B Condensed Matter*, 96(3):333–340, 1995.

[69] Jenö Sólyom. *Fundamentals of the Physics of Solids: Volume 1: Structure and Dynamics*, volume 1. Springer Science & Business Media, 2007.

[70] Theo Hahn and International Union of Crystallography. *International tables for crystallography: Brief teaching edition of volume A, Space-group symmetry*, volume 1. Kluwer Academic Pub, 1996.

[71] Yoshio Waseda, Eiichiro Matsubara, and Kozo Shinoda. *X-ray diffraction crystallography: introduction, examples and solved problems*. Springer Science & Business Media, 2011.

[72] Institute for Electronics and Telecommunications Engineers. AE04 - Materials and Processes; Q. 82 Solution - Miller Indices. PDF, 2016. http://iete-elan.ac.in/SolQP/soln/AE04_sol.pdf.

[73] M Martinez-Ripoli. Crystallography-Cristalografia. website, 2016. http://www.xtal.iqfr.csic.es/Cristalografia/index-en.html.

[74] Martin T Dove. *Structure and dynamics: an atomic view of materials*, volume 1. Oxford University Press, 2003.

[75] Edward Wilfrid Nuffield. *X-ray diffraction methods*. JS Wiley.; New York. NY; USA, 1966.

[76] Vitalij K Pecharsky and Peter Y Zavalij. *Fundamentals of powder diffraction and structural characterization of materials*, volume 69. Springer, 2009.

[77] PP Ewald. Introduction to the dynamical theory of X-ray diffraction. *Acta Crystallographica Section A: Crystal Physics, Diffraction, Theoretical and General Crystallography*, 25(1):103–108, 1969.

[78] Mario Birkholz. *Thin film analysis by X-ray scattering*. John Wiley & Sons, 2006.

[79] SM Koohpayeh. Single crystal growth by the traveling solvent technique: A review. *Progress in Crystal Growth and Characterization of Materials*, 2016.

[80] C.N. Baroud. Marangoni convection. In Dongqing Li, editor, *Encyclopedia of Microfluidics and Nanofluidics*, pages 1–8. Springer US, Boston, MA, 2013.

[81] H. Dabkowska and A. Dabkowski. Chapter 8 - Floating Zone Growth of Oxides and Metallic Alloys. In Peter Rudolph, editor, *Handbook of Crystal Growth (Second Edition)*, Handbook of Crystal Growth, pages 281 – 329. Elsevier, second edition edition, 2015.

[82] D Prabhakaran and AT Boothroyd. Crystal growth of spin-ice pyrochlores by the floating-zone method. *Journal of Crystal Growth*, 318(1):1053–1056, 2011.

[83] James E Penner-Hahn. *X-ray Absorption Spectroscopy*. John Wiley and Sons, Ltd, 2001.

[84] Bernard Dennis Cullity. *Elements of X-ray Diffraction*. Addison-Wesley Publishing House, 2001.

[85] G. Hölzer, M. Fritsch, M. Deutsch, J. Härtwig, and E. Förster. $K\alpha_{1,2}$ and $K\beta_{1,3}$ x-ray emission lines of the $3d$ transition metals. *Phys. Rev. A*, 56:4554–4568, Dec 1997.

[86] Joseph H Reibenspies and Nattamai Bhuvanesh. Selecting a Specimen Holder for X-ray Powder Diffraction. *Pharmaceutical Technology*, 37(6):38–42, 2014.

[87] Juan Rodríguez-Carvajal. Recent advances in magnetic structure determination by neutron powder diffraction. *Physica B: Condensed Matter*, 192(12):55 – 69, 1993.

[88] Kato, K and Nukui, A. Die Kristallstruktur des monoklinen Tief-Tridymits. *Acta Crystallographica Section B: Structural Crystallography and Crystal Chemistry*, 32(8):2486–2491, 1976.

[89] Baur, Werner H and Khan, Aijar A. Rutile-type compounds. IV. SiO_2, GeO_2 and a comparison with other rutile-type structures. *Acta Crystallographica Section B: Structural Crystallography and Crystal Chemistry*, 27(11):2133–2139, 1971.

[90] d'Amour, H and Denner, W and Schulz, Heinz. Structure determination of α-quartz up to 68 x 108 Pa. *Acta Crystallographica Section B: Structural Crystallography and Crystal Chemistry*, 35(3):550–555, 1979.

[91] Koichi Momma and Fujio Izumi. VESTA 3 for three-dimensional visualization of crystal, volumetric and morphology data. *Journal of Applied Crystallography*, 44(6):1272–1276, 2011.

[92] Bertram Eugene Warren. *X-ray Diffraction*. Courier Corporation, 1969.

[93] Gale Rhodes. *Crystallography made crystal clear: a guide for users of macromolecular models*. Academic press, 2010.

[94] D Lowney, T S Perova, M Nolan, P J McNally, R A Moore, H S Gamble, T Tuomi, R Rantamki, and A N Danilewsky. Investigation of strain induced effects in silicon wafers due to proximity rapid thermal processing using micro-Raman spectroscopy and synchrotron x-ray topography. *Semiconductor Science and Technology*, 17(10):1081, 2002.

[95] AK Singh. *Advanced x-ray techniques in research and industry*. IOS Press, 2005.

[96] John McGreevy. Crystallography Supplementary Subject - Lecture 7: Systematic Absences. Online, 2008. http://goodwin.chem.ox.ac.uk/goodwin/TEACHING_files/l7_handout.pdf.

[97] Peter Böni and Albert Furrer. *Introduction to Neutron Scattering*, pages 1–22. Springer Netherlands, Dordrecht, 1998.

[98] Roger Pynn. Neutron scattering: a primer. *Los Alamos Science*, 19:1–31, 1990.

[99] Jean Daillant and Alain Gibaud. *X-ray and neutron reflectivity: principles and applications*, volume 770. Springer, 2008.

[100] E. Prince. *International Tables for Crystallography,Volume C: Mathematical, Physical and Chemical Tables*. International Tables for Crystallography. Springer Netherlands, 2006.

[101] Meija, Juris and Coplen, Tyler B and Berglund, Michael and Brand, Willi A and De Bièvre, Paul and Gröning, Manfred and Holden, Norman E and Irrgeher, Johanna and Loss, Robert D and Walczyk, Thomas and others. Atomic weights of the elements 2013 (iupac technical report). *Pure and Applied Chemistry*, 88(3):265–291, 2016.

[102] Philip J Potts. *A handbook of silicate rock analysis*. Springer Science & Business Media, 2012.

[103] Peter J Mohr, David B Newell, and Barry N Taylor. CODATA recommended values of the fundamental physical constants: 2014. *Reviews of Modern Physics*, 88(3):035009, 2016.

[104] W Schülke. Inelastic X-ray scattering. *Nuclear Instruments and Methods in Physics Research Section A: Accelerators, Spectrometers, Detectors and Associated Equipment*, 280(2):338–348, 1989.

[105] B. Roessli and P. Bni. Polarized Neutron Scattering, 2000.

[106] Richard Wolfson and Jay Pasachoff. *Physics for Scientists and Engineers with Modern Physics*. Addison Wesley Publishing Company, 1999.

[107] Ewald Balcar and Stephen W Lovesey. *Theory of magnetic neutron and photon scattering*, volume 2. Clarendon Press, 1989.

[108] Gordon Leslie Squires. *Introduction to the theory of thermal neutron scattering*. Cambridge university press, 2012.

[109] Roger Pynn. Lecture 1: Introduction and Neutron Scattering "Theory", 2016. https://www.ncnr.nist.gov/summerschool/ss16/pdf/Lecture_1_Theory.pdf.

[110] Varley F Sears. *Neutron optics: an introduction to the theory of neutron optical phenomena and their applications*, volume 3. Oxford University Press, USA, 1989.

[111] John M Carpenter. Neutron Production, Moderation and Characterization. online, August 2004. http://www.neutron.anl.gov/NeutronProduction.pdf.

[112] Roger Pynn. Neutron ScatteringA Non-destructive Microscope for Seeing Inside Matter. In *Neutron Applications in Earth, Energy and Environmental Sciences*, pages 15–36. Springer, 2009.

[113] Léon Van Hove. Correlations in space and time and Born approximation scattering in systems of interacting particles. *Physical Review*, 95(1):249, 1954.

[114] Sara Haravifard. Neutron Scattering Measurements of Low-Dimensional Quantum Systems, 2009.

[115] James Patrick Ian Clancy. X-ray and Neutron Scattering Studies of Unconventional Spin-Peierls Systems, 2009.

[116] John M Carpenter and William B Yelon. Neutron Sources. *Methods in Experimental Physics*, 23:99–196, 1986.

[117] Roger Pynn. Lecture 2: Neutron Scattering Instrumentation and Facilities, 2016. https://www.ncnr.nist.gov/summerschool/ss16/pdf/Lecture_2_Facilities.pdf.

[118] IAEA Benchmark of Spallation Models. Online, 2015. https://www-nds.iaea.org/spallations/.

[119] J.R. LaMarsh. *Introduction to Nuclear Reactor Theory*. Addison Wesley, 1966.

[120] Brian David Josephson. Possible new effects in superconductive tunnelling. *Physics letters*, 1(7):251–253, 1962.

[121] Philip W Anderson and John M Rowell. Probable observation of the Josephson superconducting tunneling effect. *Physical Review Letters*, 10(6):230, 1963.

[122] SQUID Magnetometry. online, 2012. http://www.wmi.badw.de/methods/squid.htm.

[123] Mike McElfresh. Fundamentals of magnetism and magnetic measurements featuring Quantum Designs magnetic property measurement system. *Quantum Design*, 11578:132, 1994.

[124] John Clarke and Alex I Braginski. *The SQUID Handbook: Fundamentals and Technology of SQUIDs and SQUID Systems Vol. I*. Wiley, Weinheim, 2004.

[125] SN Erné, H-D Hahlbohm, and H Lübbig. Theory of rf-biased superconducting quantum interference device for nonhysteretic regime. *Journal of Applied Physics*, 47(12):5440–5442, 1976.

[126] Quantum Designs. *Magnetic Property Measurement System Hardware Reference Manual*.

[127] S Bedanta, O Petracic, M Aderholz, and W Kleemann. A sample holder design for high temperature measurements in superconducting quantum interference device magnetometers. *Review of scientific instruments*, 76(8):083910, 2005.

[128] K. Stowe. *An Introduction to Thermodynamics and Statistical Mechanics*. Cambridge University Press, 2007.

[129] Guglielmo Ventura and Mauro Perfetti. *Thermal properties of solids at room and cryogenic temperatures*. Springer, 2014.

[130] Paul Ehrenfest. Phase changes in the ordinary and extended sense classified according to the corresponding singularities of the thermodynamic potential. In *Proc Acad Sci Amsterdam*, volume 36, pages 153–157, 1933.

[131] Olivier Kahn. Molecular magnetism. *VCH Publishers, Inc.(USA), 1993,*, page 393, 1993.

[132] JP Sanchez, J-C Griveau, P Javorsky, E Colineau, R Eloirdi, P Boulet, J Rebizant, F Wastin, AB Shick, and R Caciuffo. Magnetic and electronic properties of $NpCo_2$: evidence for long-range magnetic order. *Physical Review B*, 87(13):134410, 2013.

[133] Joseph Black. *Lectures on the Elements of Chemistry: Delivered in the University of Edinburgh*, volume 1. Mathew Carey, 1807.

[134] W Nernst. Sitzungsbericht der K. *Preuss. Akad. Wiss*, 12:261, 1910.

[135] D.J. Griffiths. *Introduction to Electrodynamics*. Pearson Education, 2014.

[136] S.J. Blundell. Spin Polarized muons in condensed matter physics. *Contemporary Physics*, 40(175), 1999.

[137] Jess Brewer. Introduction to Muon Spin Rotation/Relaxation/Resonance. PDF, 2011. http://triumf.info/hosted/TSI/TSI11/lectures/L2-Brewer-Methods.pdf.

[138] Stephen L Lee, R Cywinski, and SH Kilcoyne. *Muon science: Muons in physics, chemistry and materials*, volume 51. CRC Press, 1999.

[139] Kanetada Nagamine. *Introductory muon science*. Cambridge University Press, 2003.

[140] Roberto DeRenzi. MuSR - PmWikiFisica, 2014. www.fis.unipr.it/ derenzi/dispense/pmwiki.php?n=MuSR.MuSR.

[141] DE Groom and SR Klein. Passage of particles through matter. *The European Physical Journal C-Particles and Fields*, 15(1-4):163–173, 2000.

[142] David Griffiths. Introduction to Particle Physics. *J. Wiley & Sons, Inc*, pages 22–28, 1987.

[143] Jacques Chappert and Robert I Grynszpan. *Muons and Pions in Materials Research: Lectures Delivered at the Spring School on Muon Spin Research, Aussois, France, May 1983*. North-Holland, 1984.

[144] Jeff Sonier. Muon Spin Rotation/Relaxation/Resonance (μSR), 2002. http://musr.ca/intro/musr/muSRBrochure.pdf.

[145] SFJ Cox. Implanted muon studies in condensed matter science. *Journal of Physics C: Solid State Physics*, 20(22):3187, 1987.

[146] Martin Tyssen Rovers. Spin Liquid Behavior in Geometrically Frustrated Chromium Oxides, 2001.

[147] D. R. Noakes, J. H. Brewer, D. R. Harshman, E. J. Ansaldo, and C. Y. Huang. Electron, muon, and nuclear spin dynamics in $smrh_4b_4$ and $errh_4b_4$. *Phys. Rev. B*, 35:6597–6607, May 1987.

[148] Robert Cywinski. Muon Spin Relaxation Functions. PDF, 2005. http://www.isis.stfc.ac.uk/groups/muons/muon-training-school/2005-relaxation-functions-rc7912.pdf.

[149] Elvezio Morenzoni. Introduction to μSR Muon Spin Rotation/Relaxation. PDF, 2012. https://www.psi.ch/lmu/EducationLecturesEN/MuonSpinRotation-An-Introduction-print-em-2012.pdf.

[150] R Kubo and T Toyabe. *A Stochastic model for low field resonance and relaxation*, volume 810. Proceedings International Conference on Magnetic Resonance and Relaxation, 1966.

[151] Ryogo Kubo. A stochastic theory of spin relaxation. *Hyperfine Interactions*, 8(4):731–738, 1981.

[152] RS Hayano, YJ Uemura, J Imazato, N Nishida, T Yamazaki, and R Kubo. Zero-and low-field spin relaxation studied by positive muons. *Physical Review B*, 20(3):850, 1979.

[153] Stephen Blundell. Muon Relaxation Functions. PDF, 2008. http://www.isis.stfc.ac.uk/groups/muons/muon-training-school/2008-sjb-handout-two7889.pdf.

[154] Alain Yaouanc and Pierre Dalmas De Reotier. *Muon spin rotation, relaxation, and resonance: applications to condensed matter*. Oxford University Press, 2011.

[155] A. Suter and B. M. Wojek. Musrfit: A Free Platform-Independent Framework for μSR Data Analysis. *Physics Procedia*, 30:69–73, 2012.

[156] S. Kobayashi, S. Mitsuda, M. Ishikawa, K. Miyatani, and K. Kohn. Three-Dimensional Magnetic Ordering in the Quasi-One-Dimensional Ising Magnet $CoNb_2O_6$ with Partially Released Geometrical Frustration. *Phys. Rev. B*, 60:3331, 1999.

[157] Setsuo Mitsuda, Kazuhiro Hosoya, Tsuyoshi Wada, Hideki Yoshizawa, Takeshi Hanawa, Masayasu Ishikawa, Kazuo Miyatani, Kazuhiro Saito, and Kay Kohn. Magnetic ordering in one-dimensional system $CoNb_2O_6$ with competing interchain interactions. *Journal of the Physical Society of Japan*, 63(10):3568–3571, 1994.

[158] WA MacFarlane, O Ofer, KH Chow, MD Hossain, TJ Parolin, H Saadaoui, Q Song, D Wang, DJ Arseneau, B Hitti, et al. Longitudinal Field Muon Spin Rotation Study of Magnetic Freezing in Fe Rich $FeSe_{0.25}Te_{0.75}$. *Physics Procedia*, 30:254–257, 2012.

[159] TJS Munsie, A Millington, GM Luke, and HA Dabkowska. Oxide Self-Flux in Optical Floating Zone Crystal Growth of Nickel Niobate ($NiNb_2O_6$). *Preprints*, 2017.

[160] H. A. Dabkowska and A. B. Dabkowski. Crystal Growth of Oxides by Optical Floating Zone Technique. In Govindhan Dhanaraj, Kullaiah Byrappa, Vishwanath Prasad, and Michael Dudley, editors, *Springer Handbook of Crystal Growth*, pages 367–391. Springer Berlin Heidelberg, 2010.

[161] Takashi Kunimoto, Keigo Nagasaka, Hiroyuki Nojiri, Sebastian Luther, Mitsuhiro Motokawa, Hitoshi Ohta, Tomohiro Goto, Susumu Okubo, and Kay Kohn. Submillimeter Wave ESR Study of Magnetic Excitations in the Ising Ferromagnetic Chain $CoNb_2O_6$. *Journal of the Physical Society of Japan*, 68(5):1703–1710, 1999.

[162] CM Morris, R Valdés Aguilar, A Ghosh, SM Koohpayeh, J Krizan, RJ Cava, O Tchernyshyov, TM McQueen, and NP Armitage. Hierarchy of bound states in the one-dimensional ferromagnetic Ising chain $CoNb_2O_6$ investigated by high-resolution time-domain terahertz spectroscopy. *Physical review letters*, 112(13):137403, 2014.

[163] John A Hertz. Quantum critical phenomena. *Physical Review B*, 14(3):1165, 1976.

[164] Sudip Chakravarty, Bertrand I Halperin, and David R Nelson. Two-dimensional quantum Heisenberg antiferromagnet at low temperatures. *Physical Review B*, 39(4):2344, 1989.

[165] AJ Millis. Effect of a nonzero temperature on quantum critical points in itinerant fermion systems. *Physical Review B*, 48(10):7183, 1993.

[166] Andrey V Chubukov, Subir Sachdev, and Jinwu Ye. Theory of two-dimensional quantum Heisenberg antiferromagnets with a nearly critical ground state. *Physical Review B*, 49(17):11919, 1994.

[167] Allen M Goldman and Nina Markovic. Superconductor-insulator transitions in the two-dimensional limit. *Physics Today*, 51:39–44, 1998.

[168] Philipp Gegenwart, Qimiao Si, and Frank Steglich. Quantum criticality in heavy-fermion metals. *nature physics*, 4(3):186–197, 2008.

[169] Subir Sachdev. *Quantum Phase Transitions*. Cambridge University Press, 2nd edition, 2011.

[170] Subir Sachdev and Bernhard Keimer. Quantum criticality. *arXiv preprint arXiv:1102.4628*, 2011.

[171] P. W. C. Sarvezuk, E. J. Kinast, C. V. Colin, M. A. Gusmo, J. B. M. da Cunha, and O. Isnard. New investigation of the magnetic structure of $CoNb_2O_6$ columbite. *Journal of Applied Physics*, 109(7), 2011.

[172] R. Wichmann and Hk. Mller-Buschbaum. Synthese und Untersuchung von $NiNb_2O_6$-Einkristallen mit Columbit- und Rutilstruktur. *Zeitschrift fr anorganische und allgemeine Chemie*, 503(8):101–105, 1983.

[173] M.; Burdese, A.; Lucco-Borlera and P. Rolando. Phase Diagram of Nb_2O_5-NiO. *Ric. Sci., Rend.*, A7:454, 1964.

[174] I Yaeger, AH Morrish, and BM Wanklyn. Magnetization studies in transition-metal niobates: I. $NiNb_2O_6$. *Physical Review B*, 15(3):1465, 1977.

[175] C Heid, H Weitzel, F Bourdarot, R Calemczuk, T Vogt, and H Fuess. Magnetism in $FeNb_2O_6$ and $NiNb_2O_6$. *Journal of Physics: Condensed Matter*, 8(49):10609, 1996.

[176] TJS Munsie, A Millington, PA Dube, HA Dabkowska, J Britten, GM Luke, and JE Greedan. Crystal growth and magnetic characterization of a tetragonal polymorph of $NiNb_2O_6$. *Journal of Solid State Chemistry*, 236:19–23, 2016.

[177] Horst P Beck. A study on AB_2O_6 compounds, Part II: the branches of the hcp family. *Zeitschrift für Kristallographie-Crystalline Materials*, 227(12):843–858, 2012.

[178] Jonas A. Kjäll, Frank Pollmann, and Joel E. Moore. Bound states and E_8 symmetry effects in perturbed quantum Ising chains. *Phys. Rev. B*, 83:020407, Jan 2011.

[179] Ruoshui Ma, Feng Cao, Jian Wang, Guangrui Zhu, and Guangsheng Pang. Hydrothermal synthesis and phase stability of $CoNb_2O_6$ with a rutile structure. *Materials Letters*, 65(1920):2880 – 2882, 2011.

[180] Hyo-Jong Lee, In-Tae Kim, and KugSun Hong. Dielectric Properties of AB_2O_6 Compounds at Microwave Frequencies (A=Ca, Mg, Mn, Co, Ni, Zn, and B=Nb, Ta). *Japanese Journal of Applied Physics*, 36(10A):L1318, 1997.

[181] R. C. Pullar, J. D. Breeze, and N. McN. Alford. Microwave Dielectric Properties of Columbite-Structure Niobate Ceramics, $M^{2+}Nb_2O_6$. *Key Engineering Materials*, 224-226:1–4, 2002.

[182] Yingchun Zhang, Chaoyu You, Baojian Fu, and Jiangli Cao. Tailoring of Microwave Dielectric Properties in (1x)$ZnTa_2O_6$-(x)$NiNb_2O_6$ Ceramics. *Ferroelectrics*, 451(1):54–61, 2013.

[183] Shuijin Lei, Chuanning Wang, Donghai Guo, Xijie Gao, Di Cheng, Jianliang Zhou, Baochang Cheng, and Yanhe Xiao. Synthesis and magnetic properties of MNb_2O_6 (M = Fe, Co, Ni) nanoparticles. *RSC Adv.*, 4:52740–52748, 2014.

[184] H. J. Goldschmidt. An X-Ray Investigation of Systems Between Niobium Pentoxide and Certain Additional Oxides. *Metallurgia*, 62:211–218;241–250, Nov/Dec 1960.

[185] Oleg V Dolomanov, Luc J Bourhis, Richard J Gildea, Judith AK Howard, and Horst Puschmann. OLEX2: a complete structure solution,

refinement and analysis program. *Journal of Applied Crystallography*, 42(2):339–341, 2009.

[186] George M Sheldrick. SHELXT-Integrated space-group and crystal-structure determination. *Acta Crystallographica Section A: Foundations and Advances*, 71(1):3–8, 2015.

[187] Y Le Page. Computer derivation of the symmetry elements implied in a structure description. *Journal of Applied Crystallography*, 20(3):264–269, 1987.

[188] Y Le Page. MISSYM1. 1–a flexible new release. *Journal of Applied Crystallography*, 21(6):983–984, 1988.

[189] AL Spek. PLATON, an integrated tool for the analysis of the results of a single crystal structure determination. *Acta Crystallographica Section A: Foundations of Crystallography*, 46(s1):34–34, 1990.

[190] Hk Muller-Buschbaum and R Wichmann. Crystal Structure Investigation of $NiTa_2O_6$-Single Crystals. A Contribution About Ordered and Disordered Oxycompounds: AB_2O_6 and ABO_4. *Z. Anorg. Allg. Chem.*, 536:15–23, 1986.

[191] RK Kremer, JE Greedan, E Gmelin, W Dai, MA White, SM Eicher, and KJ Lushington. Specific Heat of MTa_2O_6 (M= Co, Ni, Fe, Mg) Evidence for Low Dimensional Magnetism. *Le Journal de Physique Colloques*, 49(C8):C8–1495, 1988.

[192] JM Law, H-J Koo, M-H Whangbo, E Brücher, V Pomjakushin, and RK Kremer. Strongly correlated one-dimensional magnetic behavior of $NiTa_2O_6$. *Physical Review B*, 89(1):014423, 2014.

[193] Sonja Maria Eicher. Quasi Two Dimensional Magnetic Properties of the TriRutile Phases MTa_2O_6, M: V, Fe, Co, Ni, 1984.

[194] GS Rushbrooke and PJ Wood. On the Curie points and high temperature susceptibilities of Heisenberg model ferromagnetics. *Molecular Physics*, 1(3):257–283, 1958.

[195] Michael E. Fisher. Relation between the specific heat and susceptibility of an antiferromagnet. *Philosophical Magazine*, 7(82):1731–1743, 1962.

[196] TJS Munsie, MN Wilson, A Millington, CM Thompson, R Flacau, C Ding, S Guo, Z Gong, AA Aczel, HB Cao, TJ Williams, HA Dabkowska, F Ning, JE Greedan, and GM Luke. Neutron Diffraction and μSR Studies of Two Polymorphs of Nickel Niobate ($NiNb_2O_6$), 2017. arXiv:1704.04043.

[197] Tian Liang, SM Koohpayeh, JW Krizan, TM McQueen, RJ Cava, and NP Ong. Heat capacity peak at the quantum critical point of the transverse Ising magnet $CoNb_2O_6$. *Nature communications*, 6, 2015.

[198] Theo Hahn. International Tables for X-ray Crystallography, Vol. A. *The International Union of Crystallography, D Reidel Publ Co, Dordrecht*, 1983.

[199] Ludovicus Josephus de Jongh. *Magnetic properties of layered transition metal compounds*, volume 9. Springer Science & Business Media, 2012.

[200] Mikio Takano and Toshio Takada. Magnetic properties of MTa_2O_6 (M= Fe, Co or Ni). *Materials Research Bulletin*, 5(6):449–454, 1970.

[201] E Ramos, ML Veiga, F Fernández, R Sáez-Puche, and C Pico. Synthesis, structural characterization, and two-dimensional antiferromagnetic ordering for the oxides $Ti_{3(1-x)}Ni_xSb_{2x}O_6$ ($1.0 \geq x \geq 0.6$). *Journal of solid state chemistry*, 91(1):113–120, 1991.

[202] E Ramos, F Fernandez, A Jerez, C Pico, J Rodríguez-Carvajal, R Saez-Puche, and ML Veiga. One-dimensional antiferromagnetic ordering for a novel nickel-antimony oxide. *Materials research bulletin*, 27(9):1041–1047, 1992.

[203] TJS Munsie, A Millington, PA Dube, HA Dabkowska, J Britten, GM Luke, and JE Greedan. Crystal growth and magnetic characterization of a tetragonal polymorph of $NiNb_2O_6$. *Journal of Solid State Chemistry*, 236:19–23, 2016.

[204] H Ehrenberg, G Wltschek, J Rodriguez-Carvajal, and T Vogt. Magnetic structures of the tri-rutiles $NiTa_2O_6$ and $NiSb_2O_6$. *Journal of magnetism and magnetic materials*, 184(1):111–115, 1998.

[205] Bryan C Chakoumakos, Huibo Cao, Feng Ye, Alexandru D Stoica, Mihai Popovici, Madhan Sundaram, Wenduo Zhou, J Steve Hicks, Gary W Lynn, and Richard A Riedel. Four-circle single-crystal neutron diffrac-

tometer at the High Flux Isotope Reactor. *Journal of Applied Crystallography*, 44(3):655–658, 2011.

[206] M.D. Lumsden, M. Yethiraj, and J.L. Robertson. Graffiti - SPICE Data Browser, June 2015. http://neutron.ornl.gov/spice/User_Downloads.html.

[207] Alexander Schenck. *Muon spin rotation spectroscopy: Principles and applications in solid state physics*. The University of California, 1985.

[208] AS Wills. A new protocol for the determination of magnetic structures using simulated annealing and representational analysis (sarah). *Physica B: Condensed Matter*, 276:680–681, 2000.

[209] Malcolm F Collins. *Magnetic critical scattering*. Oxford University Press, 1989.